AN IN VIVO BONE DENSITOMETER FOR USE WITH A DIAGNOSTIC X RAY SET

by

John Paul Nicholas Edwards, M.Sc., A. Inst. P.

A thesis presented to the

University of Aston in Birmingham for the

Degree of Doctor of Philosophy

April 1973.

Summary.

An invivo bone densitometer has been designed to be used with a full wave rectified X ray set. The densitometer has been constructed to give a fast and accurate scan of the ulna with a spatial resolution very much better than hitherto achieved.

The ulna was chosen so that a wide range of patients, who might have limited agility could be easily scanned for bone mineral content with a view to the early diagnosis of bone disease and to study progress and response to therapy.

To overcome the X ray output fluctuations due to variations of the supply voltage, an electronic compensation technique using two detectors was developed. One of the detectors samples the total incident X ray intensity over a portion of the every half cycle, and the other the X ray intensity transmitted through the ulna.

Tests to determine the performance of the compensation mechanism over a wide range of operating conditions were made. The reproducibility of the densitometer has been demonstrated by making scans using simulated dead and invivo bone.

Theoretical calculations using a simplified theory have been made to predict the accuracy of the compensation technique and the expected voltage signals. These calculations are compared with experimental observation.

Acknowledgements.

I should like to thank the following:-

Dr. P.E. Francois, my supervisor, for his constant guidance and encouragement given throughout the project.

Dr. J.A. Archer-Hall, for his prodigious and invaluable assistance given to me whilst at the University.

Dr. P.B. Carpenter, for suggesting such a challenging project and so willingly extending to me the facilities available at Dudley Road Hospital, Birmingham.

Professor S.E. Hunt, for the chance to tackle the project and his generous support.

The staff of the electronic and technical workshops for the equipment and helpful advice so readily given.

The staff of the X ray and Physics Departments at Dudley Road Hospital, for helping me to develop successfully the equipment at the hospital.

I should like to thank all my colleagues for the help they were always ready to give me. Discussion of my theoretical and experimental problems with them were always most fruitful and their cheerfulness and enthusiasm for hard work were most encouraging.

The joint effort of Mrs. V. Bailey and Mrs. S. Cousins, for the many hours of work in typing my thesis.

Finally, I would like to thank the Research Sub-Committee, Birmingham Regional Hospital Board, for a grant which made it possible for me to undertake this work.

CONTENTS

CHAPTER I.

1.1. Introduction. Invivo bone densitometry.

For a total mass of about 70 kg, the human body has a skeletal mass of about 10 kg of which 3 kg is bone marrow [1]. Examination of the skeleton may lead to the diagnosis of bone diseases as well as reflecting the biochemical state of the body. This is evident from Table 1.1, which shows the percentage whole body radical content which is present in bone [2].

TABLE 1.1

Radical	Percentage of whole body radical in bone
Ca	99
PO_4	88
C_6H_5O (Citrate)	70
CO_3	80
Mg	50
Na	35
H_2O	9

It is obvious from this table that normal bone contains a substantial fraction of the whole body radicals. The organic fraction of bone largely consists of collagen, whilst the inorganic fraction may be considered to be hydroxy-apatite $[Ca_3(PO_4)_2]_3 Ca(OH)_2$ [1,2]. Dallemagne and Fabry [3] have discussed other compositions and in particular the substitution of the hydroxyl radical by a carbonate radical. The structure and content of bone has also been discussed by Fourman [2].

To assess bone mineral content invivo a method must be used which causes minimal biological damage. Although such methods as ultrasonics have been used [4-10], atomic and nuclear radiations have proved up to the present to be the easiest and most reliable method. Methods involving radiation fall into three main groups according to the

source:-

(a) X rays generated from a conventional diagnostic X ray set,

(b) Low energy gamma radiation emitted from radioactive sources,

(c) Dual isotope techniques,

(d) Neutron activation analysis.

The methods will be discussed later in the chapter.

The absorption of X and Υ rays in a compound or mixture is preferentially greater in the higher atomic numbered elements and in the case of X ray absorption, the percentage of absorbed radiation which is absorbed by calcium and phosphorus in the bone has been estimated by Mack et al. to be up to 90%[11]. This large fractional absorption means that a measurement of X and Υ radiation absorption by bone is a useful diagnostic tool in those diseases of the bone in which the calcium or phosphorus content is disturbed. Two such diseases are osteoporosis and osteomalacia. Osteoporosis is the most common bone disease in the U.K.[2], whilst osteomalacia is much less common in those countries where an adequate diet is eaten.

In osteomalacia there is a lower calcium absorption from the intestine which is usually due to vitamin D deficiency. The bones become radio-translucent and fracture easily. The characteristic abnormality are pseudo fractures which are ribbon-like zones of decalcification extending radially to the long axis of the bone and was first described by Looser[12]. In the disease there is incomplete calcification of the bone matrix so that there is a reduction in the mineral content per unit volume of bone.

If there is too little bone matrix but with the matrix impregnated with the normal calcium salt content, the condition is called osteoporosis. The disease is often a manifestation of ageing (senile osteoporosis) and in women it is more common than in men and appears at an earlier age. The most important characteristic of the

disease is a thining of the cortex, with the bones appearing abnormally translucent. Unlike osteomalacia, pseudo-fractures are very uncommon, Pugh[13], and rarely does it occur in young people. Nordin[14] has suggested that the primary cause is a long term negative calcium balance.

Less common diseases affecting the bone, such as hyperparathyroidism, disturbances of the renal system and rickets, also result in a low calcium content of the bone. They are discussed in detail by Fourman[2].

(a) Methods using X ray generator sets.

Very often in this method a radiograph of the limb is taken using a conventional X ray set. Usually the limb is immersed in a bath of tissue equivalent liquid (water is often used) so that changes in the absorption of the X rays is solely due to bone. This is shown in Fig. 1.1.

Since visual inspection alone of a bone radiograph is liable to an error of about 30% when estimating its density[15], a standard absorber is radiographed alongside the bone and optical densitometry of the two images is carried out by equating bone absorption to a known thickness of standard absorber. A sketch of an optical densitometer trace is shown in Fig. 1.2.

In many cases the standard is made of aluminium, since the atomic number of aluminium (Z = 13) is close to the effective atomic number of bone ($Z \simeq 12$)[16]. Aluminium has the advantage of low cost, non toxicity and an ability to be machined. However, its density (2,700 kg m^{-3}) is substantially different from that of bone ($\simeq$1700 kg m^{-3}[17]). A closer approximation to bone is ivory (density$\simeq$1700 kg m^{-3}) and its use as a standard has been described by Mack[18,19]. The disadvantage of ivory is that it is slightly water absorbant and has a non uniform composition.

Fig.1.1.

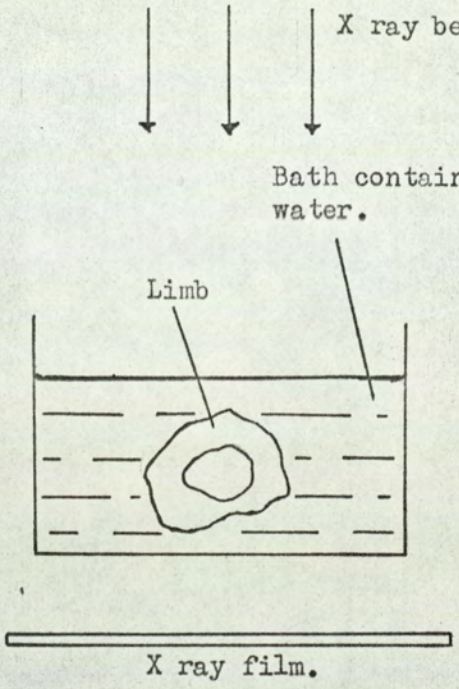

Fig. 1.2.

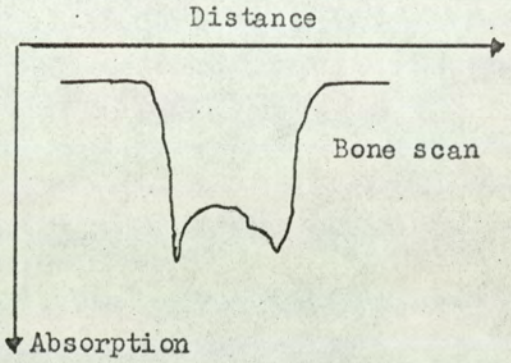

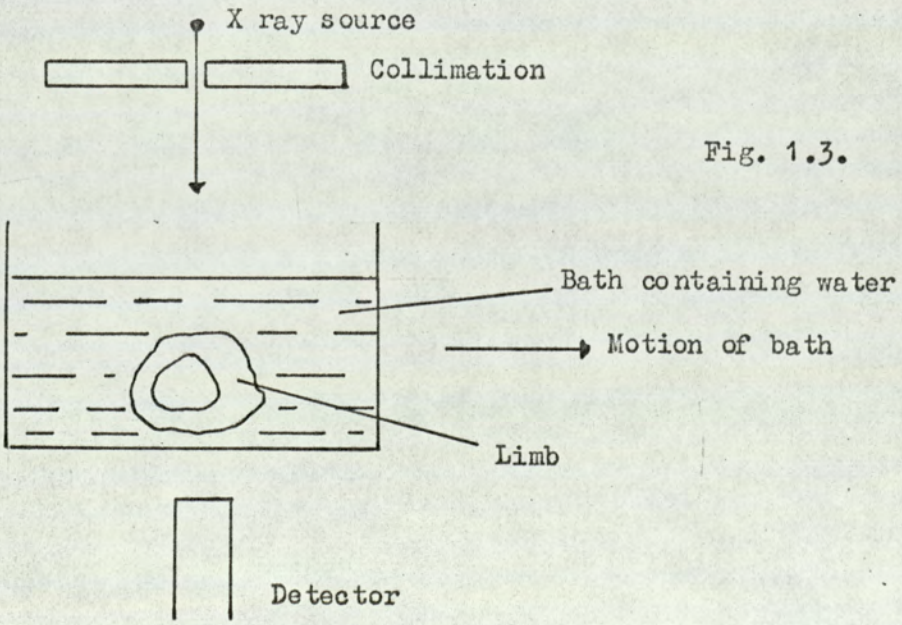

Fig. 1.3.

The task of radiographically determining bone mineral density has been pursued by many workers who have selected different skeletal bones for study:- the metacarpal[20-31], the ulna[32-37] and the radius[38-44], lumbar vertabrae[45-50] and femoral measurements [51-55] have also been made, but these latter measurements are more difficult because of the greater amount of surrounding soft tissue.

The chief advantage of the radiographic-densitometric method is the positional error as the exposure time is short ($\simeq$ 0.1 second) and therefore the limb can be regarded as being fixed with respect to the film and the X ray source for the time necessary to make the radiograph. With careful practise the error in assessing the bone density (in terms of a reference) by this method has been claimed to be about five per cent. Reduction of this figure is difficult to achieve since there are several inherent limiting factors, these being :-

(1) Variations in the photographic emulsion

(2) Variation in film development

(3) The variation in X ray intensity due to the angle of emergence of the X rays from the X ray generator (heel effect).

(4) Uncontrollable variations in the intensity and spectrum of the X ray beam due to beam current and anode voltage fluctuations.

The first two limitations are reduced by using high definition non-screened film and automatic film processing, whilst the third may be partially solved by standardising the X ray source-film geometry. Factor (4) can only be reduced by averaging out the X ray beam energy by exposing for many cycles of the mains. The effect of H.T. fluctuations is large, for the total X ray energy output varies as the square of the anode voltage [56], i.e. a 5% change in the voltage will give a 10% change in the X ray output energy.

Limitations (1) and (2) may be overcome by using a scintillation crystal , photomultiplier and counting system to replace the film[53] . The object to be scanned is carried through a narrow beam of X rays and the number of photons within a selected energy range is recorded. The principal of the technique is illustrated by the schematic diagram shown in Figure 1.3.

This method bears a similarity to the equipment constructed in this project in that the limb is moved through a beam of X rays generated by an X ray set and that the attenuated beam is detected by a scintillation crystal and photodiode.

Although this method, used by Meyer et al[53], overcomes the first two disadvantages, photomultipliers require a very stable EHT supply since the overall current gain M of the tube varies approximately as the eighth power of the accelerating voltage V, i.e. $M \propto V^8$. A 1% change in the EHT voltage will therefore cause about 8% change in photomultiplier current. The method also suffers from X ray beam intensity fluctuations.

(b) Methods using radioactive sources.

To overcome some of the disadvantages associated with X ray generators many workers (bibliography given in reference 58) have used low energy gamma radioactive sources. A collimated beam passes through a moving limb and a count of the transmitted photons is made by using a scintillation crystal and a photomultiplier system. The advantages of the system are:-

(a) The decay mode of the isotope is accurately known so that the spectral distribution of the emitted radiation is known,

(b) some isotopes, e.g. ^{125} I and ^{241} Am emits only one principal gamma ray so that the radiation can be considered to be monochromatic,

(c) the photon output for a long lived isotope is substantially constant.

A simple beam spectrum enables attenuation factors to be calculated easily unlike the hetogeneous spectrum emitted from an X ray set. For cases where the half life of the isotope is short, corrections allowing for its decay can be easily made.

The disadvantages of using radioactive isotope sources are:-

(a) A long scanning time is usually required (typically several minutes),

(b) A broad beam (a few mm) is needed to collect sufficient photons,

(c) even though a high strength source ($\sim$ 100 m Ci) may be used, there is considerable statistical error due to the low detected count rate,

(d) high strength sources cannot be made to occupy small volumes so that the isotope cannot be regarded as a point source.

The error mentioned in (c) will increase as the absorption becomes greater. For a count of 1000 the error will be $3\frac{1}{3}$ % (within one standard deviation), whilst for a count of 200 the error will be 7%. The technique has an error depending upon the registered count as well as an error associated with the movement of the limb during the time of scan. Such movement is important since the subject cannot keep his limb absolutely fixed for longer than about a minute even though the limb may be apparently securely fixed in a set position. In many cases the movement may be comparable to the spatial resolution of the detector system.

(c) Dual isotope techniques.

This technique involves the study and measurement of the beams transmitted through the limb when several radiactive isotopes with different γ energies are used separately. In this way more information may be gained regarding the nature of the filtration in the beam path, but at the cost of longer scanning times and higher doses. Many workers

have used this technique, an extensive bibliography has been given by Schrieling [57].

(d) Neutron activation analysis.

Following the studies of radioactivity arising from nuclear criticality accidents, it became apparent that by using low neutron fluxes many elements could be detected by employing whole body counters to measure the gamma radiation emitted from the induced radionuclides. Following the suggestion of Longham [58] and Gramerstfelder et al [59], neutron activation studies were carried out using animals and phantoms [60]. Anderson et al. [61] performed an experiment in which the total body sodium and chlorine were estimated in two subjects following irradiation with fast neutrons.

Palmer et al [62] and Chamberlain et al. [63,64] have developed this technique so that as many as six body elements could be measured. Comparative measurements in the changes of whole body composition are more accurate than absolute measurements since source-detector geometry is virtually impossible to define. For a total dose of about 1.5rem, it is possible to make comparative measurements to about 3% when estimating the whole body calcium content.

In whole body activation measurements a uniform irradiation of high energy (> 1 MeV) neutrons of sufficiently high flux (> 10^6 neutrons s^{-1} cm^{-2}) is necessary to irradiate a subject. Fast neutrons are used in order to obtain a uniform flux inside the body volume, the body thermalising the neutrons to give a predominently (n, γ) capture reaction. For calcium measurements, use is made of the $^{48}Ca(n, \gamma)^{49}$ Ca reaction. The characteristic γ rays (3.04 MeV for ^{49} Ca) are detected by scintillation counters and the counts stored by a pulse height analyser. The gamma spectrum is then usually analysed by computer. Because neutrons cannot be easily collimated, spatial distribution measurements are difficult to obtain.

Normally whole body elemental estimations or comparisons are made. However, neutron activation has the advantage that an estimation of the amount of a particular element present in the irradiated subject or specimen may be made by adjusting the pulse height analyser to count only the required characteristic gamma rays. Invivo measurement of radioactive iodine has been described by Boddy et al. [65,66].

1.2. The scope and development of the project.

The work undertaken in this research project was to design an inexpensive densitometer to scan the ulna with any diagnostic X ray set. The main policy in the design was to construct a densitometer whose spatial resolution, accuracy and speed of operation were very much better than existing bone scanning equipment. Additionally, the equipment had to be easy for hospital staff to operate with little or no adjustment.

1.3. The bone selected for study.

The bone chosen for study was the ulna, and the densitometer equipment was designed to obtain a high spatial resolution absorption scan of this bone. Although the lumbar vertabrae may give a more sensitive reflection of total skeletal calcium than the ulna[67], both the ulna and the radius have been found to reflect the degree of mineralisation of the remaining skeleton[40,68].

The ulna has the advantage of being a peripheral part of the body which can be moved without too much difficulty. This is important in the case of elderly people who might be arthritic. At about 30mm from the ulnar styloid the amount of subcutaneous fat and muscle surrounding the bone is small which is one advantage when small calcium differences between successive scans are sought. The bone was thought to have the additional advantage of having an approximately annular cross section.

While the equipment has been developed to scan the ulna, the scanning method developed is capable of adaptation to other bones by modification of the mechanical construction.

1.4. Outline of the problems associated with X ray generators.

General considerations.

It was known at the beginning of the project that the X ray output of a diagnostic X ray generator was heterogeneous and would be likely to fluctuate when in operation. This is because most generators are powered by a heavy duty transformer whose primary coil voltage is derived from the mains supply. Variations of this supply are caused by the operation of other heavy current equipment, such as lifts and other X ray generators and these variations will be reflected in an unknown way in the output of the X ray beam.

In the densitometric methods outlined in section 1.1(a) the extent of these fluctuations are mitigated as the radiographic exposure is made over many half cycles of the mains supply, thus averaging out the variations in spectra and intensity.

A knowledge or inference of the HT voltage V supplied to the anode is very important since the total unfiltered emitted beam intensity I is very nearly proportional to the square of the voltage[56],

$$\text{i.e. } I \propto V^2$$

so that a variation of 5% in the voltage will give a 10% change in the total emitted intensity of the beam. Since a voltage fluctuation will give twice the fractional change in the total X ray intensity, it was decided to investigate the intensity waveforms produced by a diagnostic set. To do this, a CsI(T1) scintillation crystal was coupled to a vacuum photodiode by a light guide. X rays impinging on the crystal are absorbed and these give rise to scintillations whose light intensity is proportional to the instantaneous X ray energy[69-71]. The light then causes a current in the photodiode, which was fed into a high input impedance source follower and amplifier. The waveform of the output voltage therefore represents the waveform of the X ray energy and this voltage may be viewed on an oscilloscope. In this preliminary

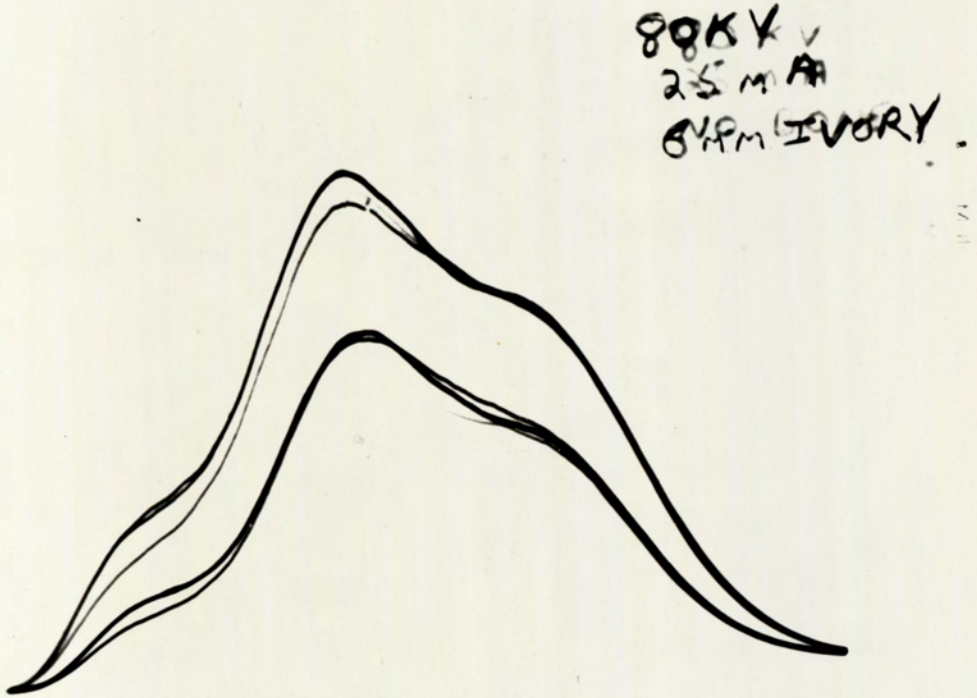

Fig. 1.4. The instantaneous X ray intensity waveforms recorded over several half cycles. Upper waveforms 1.5mm A1 filtration. Lower waveforms 1.5mm A1 + 6mm ivory filtration.

investigation photographs of several voltage waveforms given by a full wave rectified set were taken, a typical one being shown in Fig. 1.4. The camera was left open for $\frac{1}{8}$ second to allow the film to record several successive waveforms. The larger waveforms show the instantaneous intensity with no filtration of the beam, whilst for the smaller waveforms the X ray beam was filtered by a 6 mm thick ivory slab to simulate absorption in bone. It is obvious that there is a similarity between one half cycle and the next, and this similarity is retained when there is substantial filtration by ivory in the beam path.

1.5. Possible methods to deal with X ray fluctuations.

There are several possible methods to deal with the X ray fluctuations caused by voltage supply variations :

(a) Generation of a separate AC supply

(b) Passive devices to stabilise the transformer input with capacitive smoothing of the output.

(c) Two detector analogue compensation techniques.

These are discussed in turn.

(a) Generation of a separate AC supply.

To overcome the fluctuations in the mains supply it would be possible to generate an AC supply by a large motor alternator set. Such a set would have to be capable of generating about 10 kw at 240V and therefore would require a flywheel with a very large moment of inertia. The alternator set would be prohibitively expensive and bulky, as well as requiring connection to the generator, and for these reasons it was decided that this approach would be impractical.

(b) Passive devices to stabilise the input.

For a power of 10 kw the current in the primary coil of the transformer is about 40A and any stabilising equipment inserted into the circuit of this coil would have to be capable of stabilising such large currents.

It is not possible to make a passive device which will guarantee a supply voltage of constant amplitude and constant waveform from fluctuating mains. A passive system operating on a capacitor saturable reactor circuit can be made to give a substantially constant peak voltage, but only at the expense of waveform distortion. If such a stabiliser were used it would be necessary to smooth the rectifier output by using very large resevoir capacitors, so that the value of the stabilised peak voltage is maintained (to one per cent, say) throughout each half cycle. Capacitive smoothing will be discussed in the following sub-section.

Using passive devices, the difficulty of connecting such equipment to the transformer would have to be overcome. In view of these difficulties, input stabilisation was not attempted.

To smooth the transformer output a bank of capacitors would have to be connected to obtain a high and constant DC level. Such equipment would have to be immersed in oil in view of the poor dielectric strength of air to maintain a high standard of safety.

Using capacitive smoothing, the order of magnitude of the capacitive C needed to give a voltage ripple ΔV when a current is of 100mA is drawn for a time Δt seconds can be calculated. Suppose the peak voltage is 100kV then the charge Q coulombs stored by the capacitor will be

$$Q = CV$$

$$= C.\ 10^5 \text{ coulombs}$$

and $\Delta Q = i \Delta t = C \Delta V$

where ΔQ is the charge drawn from the capacitor. For a voltage fluctuation of 1% ,

$$\frac{\Delta V}{V} = 10^{-2} = \frac{i \Delta t}{CV} = \frac{10^{-3}}{10^5 C}$$

$$C = 1 \mu F .$$

This is extremely large capacitance for an operating voltage of 100 kV and a bank of such capacitors would occupy considerable space. There would also be difficulty in switching the X rays on and off because of

the charging and discharging of the capacitors.

Resistance-capacitive filter sections could not be used because the DC output voltage would fall with increase in beam current due to the voltage drop across the filter resistors.

Because of these difficulties associated with stabilising the power in the transformer, the more attractive possibility of performing an analogue operation was examined.

(c) Two detector analogue compensation techniques.

If no electrical connections are to be made to the X ray generator it is inevitable that a full wave rectified set will send information in samples every 10^{-2} second. To compensate the X ray intensity fluctuations every half cycle, two detectors could be used, one to monitor the X ray beam energy and the other to sample the beam after passing through the limb. Three methods were considered as to how the analogue results could be handled electronically or digitally :

(i) Determination of the X ray absorption in bone from an inverse function derived from the monitor signal,

(ii) Division of the monitor and detector signals.

(iii) Integration of monitor and detector signals over a portion of the half cycle.

The three alternatives are discussed in turn.

(i) It was seen from Fig. 1.4 how the X ray intensity waveform varies in every half cycle and in Chapter 4 it is shown that the waveform of the beam current remains almost exactly the same in successive half cycles. The variation of X ray output energy is therefore due to anode voltage fluctuations. By using two X ray detectors in the manner outlined earlier, one could determine the instantaneous voltage from an inverse function of the monitor signal

e.g. $E_1 = E_1(I,V,X)$

where E_1 = instantaneous X ray energy received by the monitor

I = electron beam current

V = H T anode voltage

X = effective target efficiency allowing for built in fixed filtration.

For I and X determined or fixed,

$$E_1 = E_1(V)$$

$$\therefore V = E_1^{-1}$$

i.e. the inverse function of E_1 .

E_1 could have been found and hence E_1^{-1} have been tabulated over a range of likely change in anode voltage. For the lower detector one could obtain

$$E_2 = E_2(I, V, X, x)$$

where E_2 = instantaneous X ray energy received by the lower detector,

x = X ray absorption in the limb.

With the previously mentioned constancy of I and X,

$$E_2 = E_2(V, x)$$

$$= E_2(E_1^{-1}, x)$$

$$\therefore x = (E_2, E_1^{-1})^{-1}$$

i.e. x is the inverse function of a particular E_2 .

The necessary operations needed to evaluate x might be carried out either by analogue or digital computer. It is possible that either of these systems of computation could be constructed for which the operation time on each pair of samples could be made less than 10^{-2} second. Alternatively, the information could be stored and the operations carried out over a period much longer than that required to perform the scan. However, it would be easier if an instantaneous analogue operation on the two sample pairs could be performed, even if the analogue operation is based on an approximation. For these reasons the other two possibilities were examined.

(ii) Division of the monitor and detector signals.

The observations of X ray energy waveform had shown that there was a similarity of the waveform for filtered and unfiltered beams, as well as for different peak anode voltages. If there were two detectors as sketched in Fig.1.5, then if there were a rise in the peak mode voltage or beam current the energies received by the two detectors would rise. The converse would be true if the peak voltage or beam current fell. From this emerged the idea that electronic division of the two signals might be a method of compensation, since both monitor and detector signals would rise and fall simultaneously with variation of each half cycle.

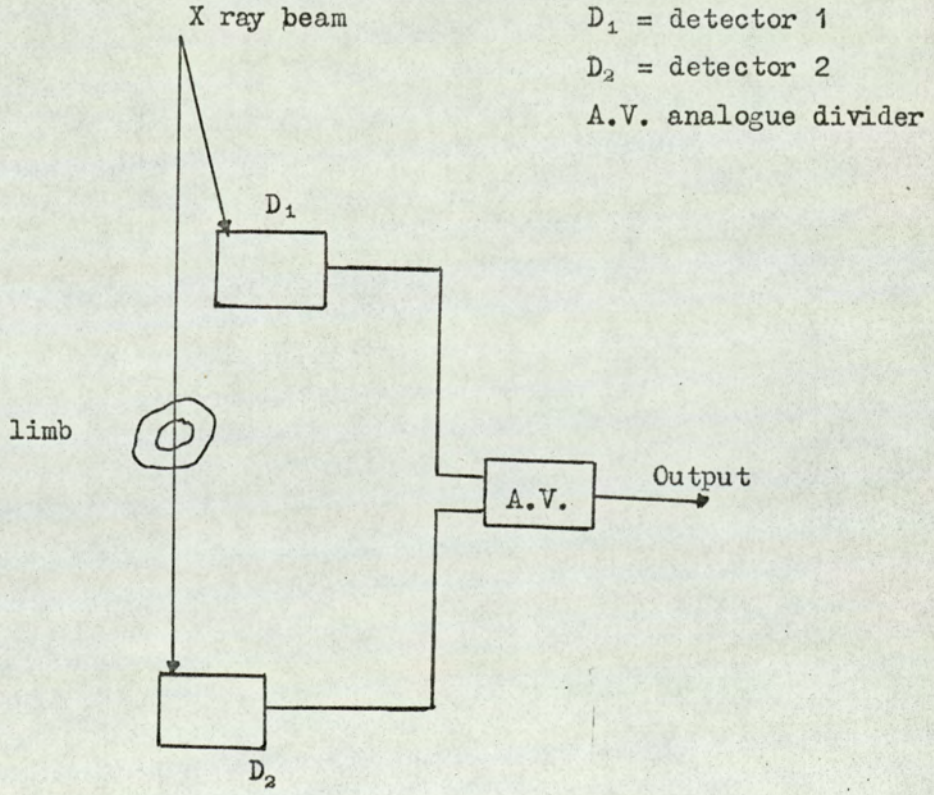

Fig. 1.5.

It was therefore necessary to evaluate the accuracy with which the compensation mechanism could work in practise. This obviously depends upon the similarity of the X ray spectra received by the two detectors. For the purposes of the calculation (appendix 1), a 10 mm layer of ivory and a water depth of 40 mm was considered to be in the path of the bottom scanning detector. This depth of water was considered to be sufficient to cover the arm near the ulnar styloid. For the monitor, the beam filtration was considered to be 45 mm water and 5 mm ivory. The 5 mm ivory represents the average thickness of the ulna. The additional filtration of 1.5 mm aluminium was allowed for in both beams as this is normally introduced to reduce skin dose when the X ray set is operated conventionally.

The calculation of the accuracy of the technique was made assuming peak voltages of 90 and 95 kVp and an X ray spectral distribution by Kramer's law[72]. The division was assumed to be carried out at the instant of peak mode voltage when the spectra would be hardest and the differences in spectral energy received by the two detectors would be a minimum.

The differences between the quotients for these two mode voltages was found to be 1.9% and represents the theoretical limit of accuracy of this compensation technique under these conditions. Following this result, practical tests were carried out on a Burr Brown divider (type 4095/15). It was found that the error increased for lower numerator and denominator voltages and was about 3%. The result of any instantaneous division would therefore be least accurate when there was the greatest amount of bone in the X ray beam, at which point there could be greatest clinical interest.

Assuming the error to be about 5%, this represents no significant advance upon other refined techniques e.g. optical densitometry. Because of this the idea of analogue division of the detector signals was abandoned. However, it was felt that use could be made of the similarity of the instantaneous X ray energy waveforms. One such method was to integrate

electronically the two detected signals over a portion of every half cycle. This idea was successfully pursued and a brief description of compensating by integration is given in the following section.

(iii) Integration of the monitor and detector signals.

X rays produced by an unmodified set are collimated so as to fall on two detectors D_1 and D_2 whose entrance slits accept beams separated by about 2° but are vertically separated by about 158 mm (Fig. 1.6). D_1 and D_2 are 350 mm and 578 mm respectively from the focus of the X ray beam when a Mullard Guardian 125 X ray table was used.

The first detector D_1 is used to sample the instantaneous X ray energy, whilst D_2 measures the instantaneous intensity of the X rays transmitted through the limb. Each detector has a scintillation crystal which gives a voltage proportional to the incident instantaneous X ray energy which is integrated over a portion ($\frac{1}{4}$ to $\frac{3}{4}$) of the half cycle. Both signals are amplified, and the output voltage from amplifier 1 is compared with a voltage in the level detector. When the integrated voltage signal reaches that of the level detector, the integration of the second detector is terminated and the voltage attained is given on the output terminal from which it can be stored or viewed on an oscilloscope.

If the anode voltage falls, the first integrator and amplifier will take fractionally longer to reach the preset voltage level, and the converse will be true if the anode voltage rises during the next half cycle. This method of compensation has been found to be very accurate. The theory is discussed in detail in chapter 2 and theoretical calculations have been made (chapter 6) to determine the accuracy of the integration technique.

1.6. Type of output required.

Consideration was given at this stage of the project to the most suitable type of result required from the densitometer. The 100 readings

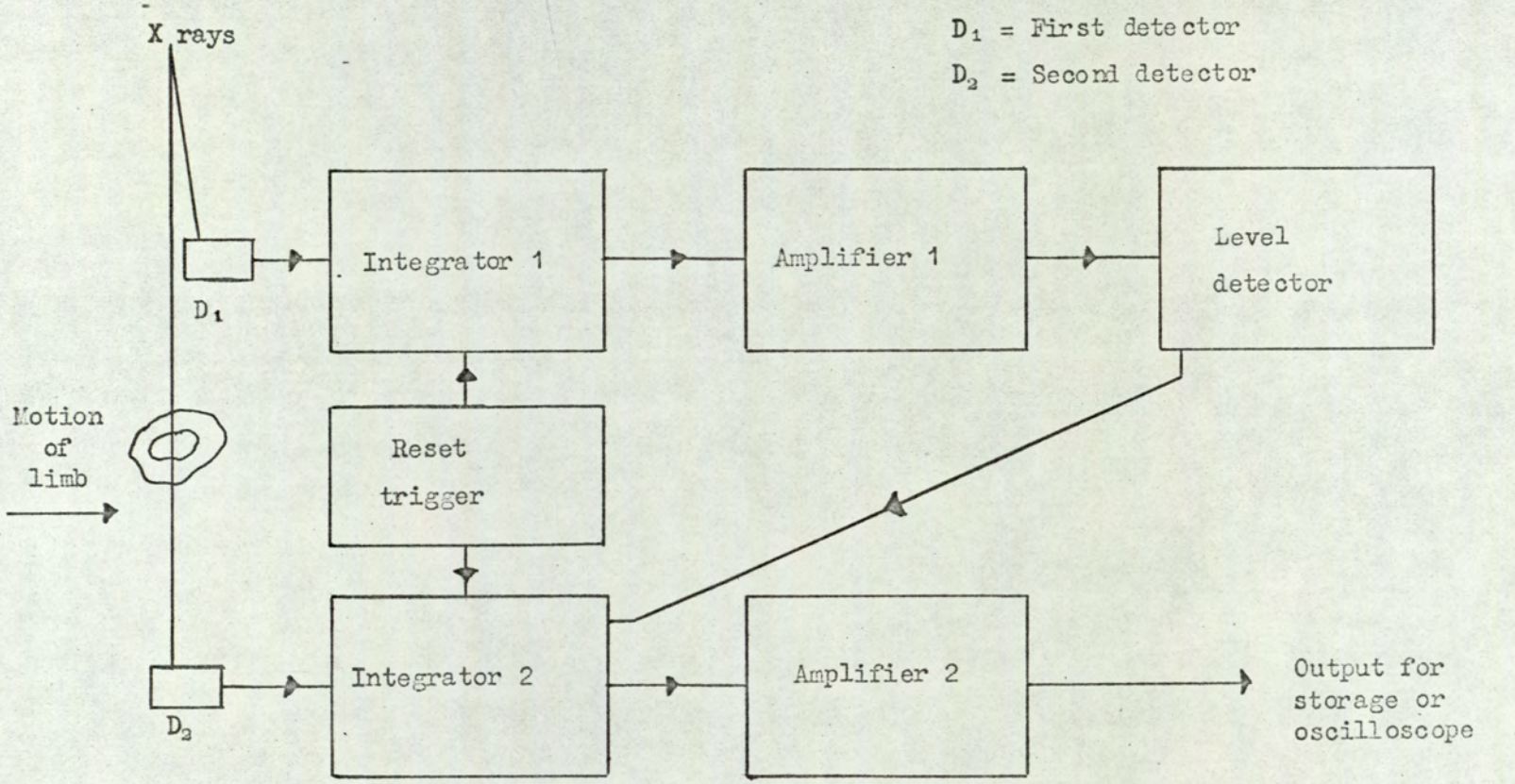

Fig. 1.6. Simplified schematic diagram of the electronic integration.

per second, derived from output voltage of the electronic equipment, could be stored on magnetic tape. Such a method would only really be of value if the bone passed through the X ray beam at a constant velocity, thereby obtaining absorption readings at regular intervals.

A constant rate of travel of the bone was obtained by the use of a synchronous motor to drive the carriage moving the arm. By employing a suitable gear ratio with the motor drive, the limb could be scanned at convenient intervals. The rate of travel of the limb through the X ray beam was chosen to be 10mm s^{-1}, thereby obtaining a reading every 10^{-1} mm. This velocity allows the ulna to be scanned in about one second, so avoiding difficulties of patient movement during the examination.

Magnetic tape storage would permit the retention of analogue voltage signals from both detectors and the results could be processed by a computer in some manner. It was realised that although the analogue results could be stored and handled adequately by magnetic tape, the analysis of the results could possibly take at least several minutes if a print-out result was required and possibly a day or two if an off-line digital computer had to be used.

A more convenient type of result would be to display the corrected analogue result on an oscilloscope as a vertical deflection and by making a horizontal time scan over a suitable interval a visual trace of the bone scan could be made. The trace could then be photographed. A photographic trace is a durable and permanent record which has the advantage that by superposition two or more results may be compared and changes in bone dimension and mineral content may readily be seen. By resting the negative on graph paper, measurements of the trace may be made.

The photographic method was chosen but it was found advantageous to have a horizontal deflection of the beam proportional to the position of the limb with respect to the X ray beam. The advantage of this method is

that the bone may be scanned in either direction and the horizontal position of the trace may be altered by adjustment of the oscilloscope controls. This was achieved by constructing a tracking potentimeter whose roller contact was connected to the moving frame carrying the limb. This provides a voltage to the oscilloscope which is proportional to the position of the limb with respect to the X ray beam. A negative film size of 5 x 4 in. was chosen to record the trace. Initially panchromatic film was used, but was discontinued in favour of X ray film which was sufficiently light sensitive and possessed the advantage that it could be processed automatically using the standard equipment of a radiology department.

CHAPTER 2.

Background theoretical analysis

2.1. Introduction

In order to understand the operation and limitations of the equipment it is necessary to know the physical conditions under which it operates. This involves consideration of

(i) The generation of X rays

(ii) Their attenuation

(iii) The analogue treatment of the electronic signals.

In practise all three items and especially items (i) and (ii) can only be treated approximately if the mathematics is not to become too complicated. Moreover, higher mathematical accuracy would not be an advantage in view of the broad assumptions made in this analysis about the operation of the X ray generator set.

2.2. The Generation of X rays

Electrons emitted from a filament are accelerated by a high voltage and are focussed on to a rotating tungsten target. When the electrons impinge on the target the main process of energy loss is by interaction with the atomic Coulomb field. Energy is lost by ionisation, excitation or bremssrahlung production. Several texts [73-76] deal with the theory of X ray production. Discussion here will be limited to a brief outline of the theory and to thick targets.

A thick target is one which absorbs all the kinetic energy of the incident electrons. All targets in diagnostic X ray sets are of this type. When an electron of mass m and charge $-e$ enters the field of a medium of charge ze the electron acceleration is proportional to z/m the bremsstrahlung radiation emitted is proportional to $(z/m)^2$. The intensity of the emitted radiation emerging from the target will depend upon several factors.

(i) Electron beam current

(ii) Accelerating voltage

(iii) Atomic number and density of the target

(iv) Attenuation of the X ray beam. This will in turn depend on (iii)

(v) Spectral and spatial distribution of the X rays and the efficiency of their production. This will also depend on (iii).

These factors are now considered in turn.

(i) The electron beam current.

The beam current of the tube is a measure of the number of electrons per second striking the target. If conditions (ii- v) remain constant, the X ray intensity will therefore be proportional to the beam current.

(ii) Anode voltage.

Early measurements were made by Ulrey [56] using a tungsten target at accelerating voltages from 20 to 50 kV. Even though his measurements were not corrected for anode absorption, he found that the energy I of the radiation was proportional to the square of the voltage, i.e.

$$I = kV^2 \qquad 2.1$$

where k is a constant.

Corrected measurements were made by Kulenkumpff and Schmidt [77], using a platinum target. They verified the intensity-voltage relationship given by Ulrey in equation 2.1.

(iii) Atomic number and density of the target.

As early as 1908 Kaye [78] had shown that the intensity emitted for a given voltage and beam current was proportional to the atomic number of the target material. In later work, Duane and Shimizu [79] reached the same conclusions.

(iv) Inherent filtration of the X rays.

Because the electrons penetrate the target, any useful radiation has to escape from its origin in the tungsten target into a direction where it can be used. There is therefore a probability that the generated X rays will interact with the target material. This inherent filtration will "harden" the generated beam as low energy radiation is preferentially absorbed. On most diagnostic X ray sets a thin(~ 1.5 mm) aluminium filter is usually added which further hardens the beam in order to reduce the patient skin dose.

If the spectral distribution of the generated X rays is known together with the filtration in the beam path, it is possible in principle to deduce the spectrum and intensity of the emerging beam. Unfortunately difficulties arise owing to the way in which electrons are scattered and diffuse in the target, as well as to the complicated variation of photon absorption cross section with energy. The accuracy with which the spectral intensity may be calculated is limited by accuracies in photon cross sections and bremsstrahlung theory. Such calculations have to be performed by numerical integration, although accuracy of theoretical results may be within those of experimental work. Self filtration by the target has been described by many authors[80-86] and Fig. 2.1. illustrates the changes in the spectral intensity due to this filtration.

The experimental work of Ham[87], Davey[88] and Hanson and Salem[89] suggest that for a continuous X ray spectrum there is an effective depth y below the surface of the target along the electron path at which the bremsstrahlung may be considered to be generated. The depth-energy relationship follows an equation of the form

$$y\rho \quad \alpha \quad E \qquad 2.2$$

where ρ = density of the material

E = energy of the incident electrons.

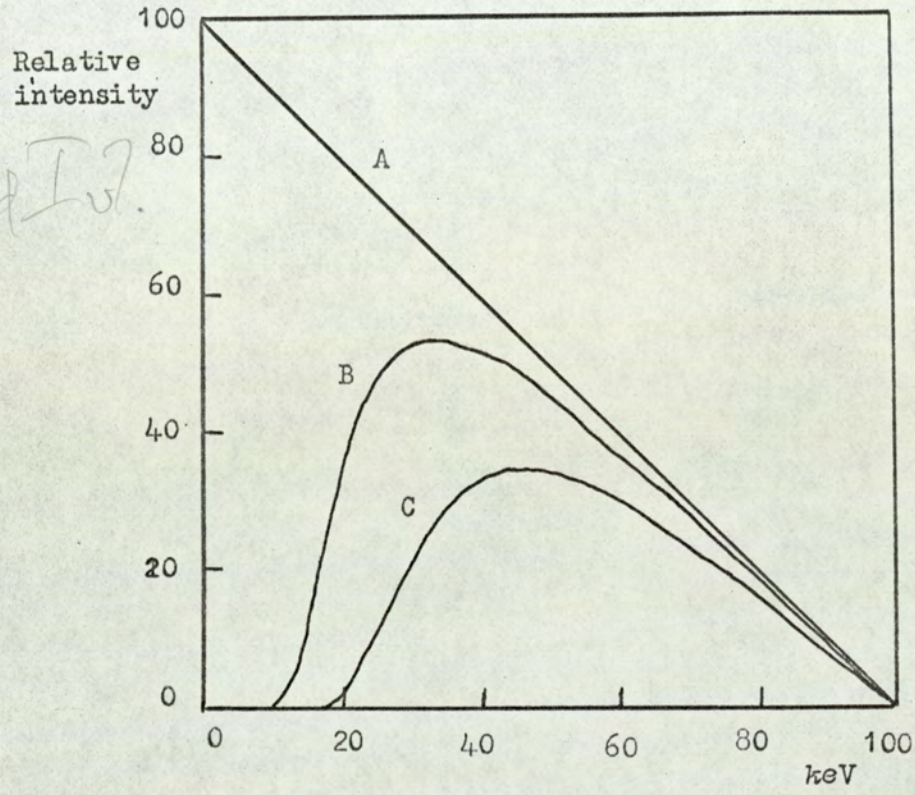

Fig. 2.1. X ray spectra at three locations at 100 kVcp (constant potential).

A. As produced within the target, before attenuation on the way out of the tube.

B. In beam leaving the tube, after traversing the inherent filtration of the tube and its housing.

C. In beam reaching the patient, after traversing both inherent filtration and external filter.

Taken from reference 99.

The results of Stoddard [90] and Farr [91] suggest that the effective bremsstrahlung production depth in high atomic number targets is about one quarter of the range of the bombarding electrons. Electron ranges have been tabulated by Berger and Seltzer [92] and have to be multiplied by a constant dependent upon the atomic number in order to estimate the range, as Cosslett and Thomas [93] have shown.

In Chapter 6 the ranges of the electrons in a tungsten target have been calculated as well as an effective depth of production of the generated bremsstrahlung. It has been shown that for photon energies above 40 keV the absorption of X rays in the target is small ($\sim 5\%$).

(v) Spectra emitted from the target.

Using quantum theory, Kramers [72] deduced that if an electron of energy eV impinges a thick target the spectral distribution at production is given by

$$dI_{\upsilon} = \frac{8\pi e^2 h}{3\sqrt{3}\, lmc^3} z(\upsilon_o - \upsilon)d\upsilon \qquad 2.3.$$

where dI_{υ} = intensity emitted in the frequency range υ to $\upsilon + d\upsilon$

υ = frequency of the X rays

υ_o = Duane-Hunt frequency limit

e = electronic charge

h = Plank's constant

m = mass of the electron

c = velocity of light

z = atomic number of the target

l = a constant whose value is about 6.

This agrees with the experimental work of Kulenkampff [80, 81] who obtained the equation

$$dI_{\upsilon} = Cz\,[(\upsilon_o - \upsilon) + z\,b]d\upsilon \qquad 2.4.$$

where b and C are constants independent of voltage. The term zb is small compared with the first term on the right hand side, so the equation simplifies to

$$dI_{\upsilon} = C_1(\upsilon_o - \upsilon)d\upsilon \qquad 2.5.$$

where $C_1 = Cz$.

Several workers have found departures from this law for the lower energies. Kulenkampff found departures below $0.4\upsilon_o$. For aluminium he observed a higher intensity at lower quantum energies, whilst the intensity of low energy X rays emitted from a platinium target was lower than predicted. The same conclusion was reached by Dyson[82], Endelsack et al[94] and Saylar[95] .

It has been suggested that the fall off at low energies which is observed for heavy elements is due to the greater number of back-scattered electrons.

The value of C in equation 2.4 has been given by Dyson[82] and Unsworth and Greening[83] and is $2.76 \cdot 10^{-6}$ (*keV* interval electron)$^{-1}$. The X ray intensity emission dI for a tungsten target is given by

$$dI = 1.02 \cdot 10^{11} (E_o - E)dE \qquad \begin{matrix} keV \\ mA^{-1}\ sr^{-1}\ s^{-1} \end{matrix} \quad \begin{matrix} keV\ \text{interval}^{-1} \\ \\ \end{matrix} \qquad 2.6$$

where dI = X ray intensity emission in the energy range

E to E + dE

E_o = maximum energy of the X ray.

The integration of equation 2.6 shows that the total intensity I is proportional to the square of the maximum voltage in agreement with the observations made by Ulrey[56].

Experimental measurements of X ray spectra are difficult to make in view of the high photon flux ($\simeq 10^{11}$ photons $mA^{-1}\ m^{-2}\ s^{-1}$ at 1 metre) and the complicated corrections (such as detector response) needed to establish the true spectrum from the observed spectrum. In order to overcome the first difficulty, low electron beam currents ($\simeq$ 0.5mA)

are used together with fast analyser detectors. By using a fine aperture slit and a large source-detector distance, the photon fluxes may be further reduced. Such methods have been described by Unsworth and Greening[83]. Owing to the finite detector resolution and corrections to the observed spectrum have to be made. If a photomultiplier gives an output pulse of magnitude V volts there is not a unique high V for an incident photon energy E. If R(V,E) is the response function for an incident photon of energy E and F(V) is the observed pulse height distribution, the true spectrum is given by

$$F(V) = \int R(V,E)\ T(E)dE \qquad 2.7$$

where T(E) is the true pulse height distribution.

Dixon and Aitken[96] have examined the problem of obtaining T(E) in considerable detail for scintillation detectors. Although the function may be found approximately, difficulties arise when the pseudosolutions are obtained from inverse transforms and trial and error methods.

Despite these difficulties, several spectral measurements have been made using diagnostic X ray machines. Peaple and Burt[97] have measured spectra in the range 40 - 100 *kVp*. Similar measurements have been made by Epp and Weiss[98] whose results are shown in Fig. 2.2. These measurements are discussed at greater length in section 2.2.1.3. Other measurements are given in references[100-105].

The Efficiency of X ray production.

As most diagnostic X ray sets can be operated at high power levels (typically 5 *kW*), it is useful to know the X ray conversion efficiency of the set. The efficiency of the X ray production has been investigated by Kramers[72] who found that

$$\text{Effeciency } \eta = \frac{\text{X ray energy}}{\text{Cathode ray energy}}$$

$$= k\,z\,V$$

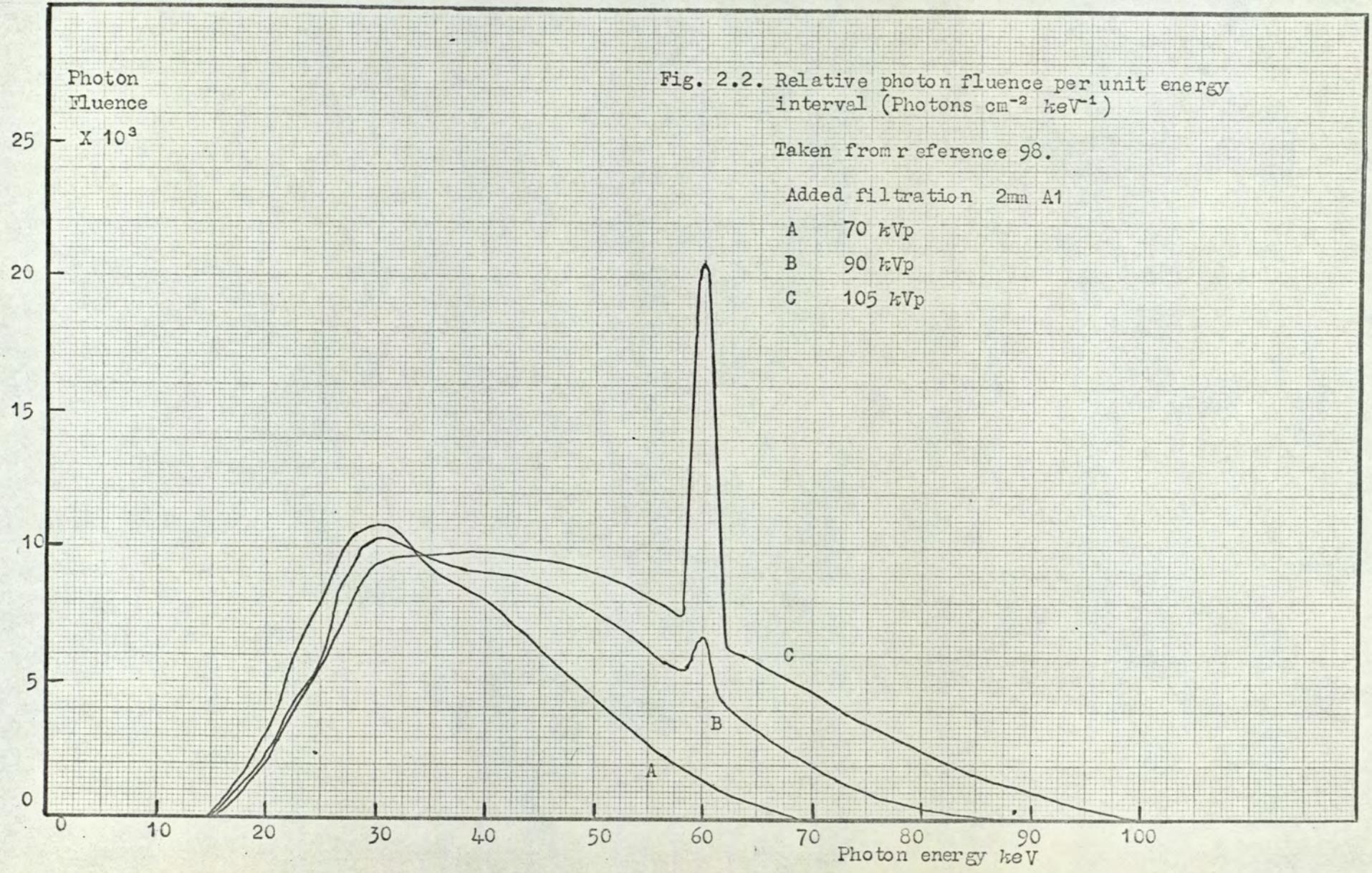

Fig. 2.2. Relative photon fluence per unit energy interval (Photons cm^{-2} keV^{-1})

Taken from reference 98.

Added filtration 2mm Al

A 70 kVp

B 90 kVp

C 105 kVp

where z is the atomic number of the target

V is the accelerating voltage (volts)

k is a constant

Kramer's value for k was $9.2\ 10^{-10}$ so that for tungsten, $\eta = 0.68\%$ at $100kV$.

This is a quantitative agreement with the value of $(1.5 \pm 0.3)10^{-9}$ given by Kulenkampff[81]. The efficiencies found by Dyson[82] yield a value of $k=1.3.10^{-9}$ in agreement with those of Kirkpatrick and Wiedmann[124], but were in excess of the earlier value of $1.1.10^{-9}$ given by Compton and Allison[76] by about 20%.

Spatial distribution and polarisation the generated X rays.

If an incident electron is retarded along its path then electromagnetic theory requires that the resultant X rays have to be plane polarised with a zero intensity at 0 and 180°, and have a maximum at 90°. A full description of the theory is given by Heitler[73]. Earlier Stokes[106] and Thomson[107] considered the spatial distribution but their equation describing this did not agree with the experimental results of Kulenkempff[81], Bohm[108] and Homerjäger[109] principally because of over simplification of the theory and neglect of relativistic effects.

Even at relatively small accelerating voltages the velocity of an electron is relativistic. Sommerfeld[110] gave the intensity I as a function of angle θ as

$$I = \frac{\alpha^2 e^2 \sin^2\theta}{4\pi^2 c^3 (1-\beta\cos\theta)^6} \qquad 2.9$$

where $\alpha = \frac{1}{137}$ the fine structure constant

$\beta = \frac{v}{c}$

v = velocity of the electron

c = velocity of light

r = classical radius of the electron

e = change of the electron

By integrating over the whole time of retardation the total intensity I_t is given by

$$I_\varepsilon = \frac{\alpha e^2 \sin\vartheta}{16\pi r^2 c^3} \left[\frac{1}{\left[1 - \beta\cos\theta\right]^4} - 1 \right] \qquad 2.10$$

Although this equation describes more accurately the spatial distribution than the equations derived by Stokes[106] and Thomson[107], it predicts a maximum intensity at an angle greater than which is found. Similarly the equation predicts a zero intensity at 0° which does not agree with experiment. The discrepancy may be explained by transverse motion of the electrons in the target.

Dyson[82] has measured the continuous X ray spectron emitted from electron opaque targets for low accelerating potentials (6 - 12 kV). Using a proportional counter, he found for energies above 0.5 of the maximum the intensity rises to a maximum at about 60°. The degree of isotropy was found to decrease with increasing quantum energy for a given fraction of the maximum energy E/E_{max}, there is only a small variation in anistropy with change of accelerating voltage. Dyson also found that radiation emitted from gold was much more isotropic than that emitted from beryllium or aluminium. This has been suggested to be due to different amounts of electron backscattering. Botden[111] has published the work of Oosterkamp and Proper who used a thick gold target and accelerating voltages between 10 and 25 kV. The total intensity was found to be a maximum at about 15° to the forward direction, being 10% higher at this angle than in the forward direction.

For characteristic radiations emitted from several elements, this has been confirmed by Green et al[112]. The anistropy will be more pronounced for lower energy photons and for smaller detector-target angles.

The intensity distribution of the emitted X rays at right angles to the electron beam path is affected by the inherent filtration of the bevelled tungsten target. This is known as the heel effect and is important in cases where large X ray field areas are used with comparatively small source-object distances. Kodak Ltd.,[113] have published the intensity variations at various angles with respect to a bevelled 20° tungsten target. It has been found that within 4° of the central ray (perpendicular to the direction of the electron beam) there is an intensity variation of about 5% which increases to 70% at 20° to the central ray.

For the densitometer constructed in this project, angular variations in intensity distribution are not important since the source-detector geometry can be very accurately repositioned by a locking device and the angle of divergence of the two detected beams is only 2° from the central ray where angular variation of intensity is small. Furthermore, the equipment can be used with the long length of the second detector slit (9.5 x 0.25 mm) perpendicular to the electron beam path so that the heel effect becomes minimal.

2.2.1. Characteristic radiation

Introduction.

Besides the continuous "white" X ray spectrum emitted from electron bremsstrahlung there is radiation emitted which is characteristic of the target element. This is due to the de-excitation and deionisation of those target atoms which have received energy. For this to occur, the incident energy required must be equal to or greater than the energy transitions under consideration.

As a tungsten target has an atomic number of seventy four there are many possible transitions of the orbiting electrons which are governed by energy considerations and quantum selection rules. Despite the many possible transitions the characteristic radiation

may be thought of as consisting of only originating from the K and L shells owing to the complete absorption of higher orbital transitions (which give rise to lower energy X ray emissions) by inherent and external filtration. Since both beams have to travel through a 1.5 mm aluminium filter and about 50 mm water, it is clear from the attenuation coefficients shown in Fig. 6.4 that little radiation below about 30 keV will be transmitted. Owing to the low energy of the tungsten L shell radiation (~10 keV), only K shell radiation (~ 70 keV) will be transmitted to the detectors. The discussion of characteristic tungsten radiation will therefore be limited to the K radiations. The energies and relative intensities are given in Table 2.1.

Table 2.1

Characteristic K emission	Wavelength nm	Energy keV	Relative intensity
α_2	0.0213	55.10	100
α_1	0.0209	59.44	
β_1	0.0184	67.38	20
β_2	0.0175	69.24	

2.2.1.1. Direct K radiation.

This is generated by direct ionisation of the target atom by the incident electrons. For K shell radiation emitted from high atomic number targets, Green and Cosslett [112] have given the number of direct K shell ionisations occurring per incident electron as

$$n_k = 9.535 \cdot \frac{10^4 R}{Af} \left[T_o \ln (T_o) - (T_o - 1) \right] \qquad 2.11$$

where n_k = number of direct K shell ionisations emitted per incident electron.

A = mass number of the target

R = a factor to allow for electron backscatter(usually taken as unity)

f = constant in the Thomson-Whiddington loss equation(reference 114)

$T_o = E_o/E_k$, the ratio of the energies of the incident electrons to the K shell ionisation energy.

Green[86] following earlier work[112] has extensively studied direct characteristic radiation generated within different target elements. By assuming that the continuous X ray spectrum is emitted isotropically, as did Webster[115], Green was able to define an effective depth below the target surface at which the characteristic radiation was generated. This was done by experimentally observing the anisotropy of the emerging radiation caused by target filtration. The product of this characteristic depth y and the target density ρ was found to be approximately proportional to the excess energy of the incident electrons, i.e.

$$y\rho \propto (E_o - E_k) \qquad E_o > E_k \qquad 2.12$$
$$\propto E_o \qquad \text{if} \quad E_o >> E_k$$

where E_o = energy of the incident electron

E_k = k shell absorption energy.

This is in agreement with the results of Ham[87], Davey[88] and Hanson and Salem[89]. The value of y is however, considerably less than the range of electrons given by the Thomson-Whiddington law[114]. Experimentally determined values of $y\rho$ for a silver target and a constant accelerating voltage of 40kV was found by Green[86] to be 380g m^{-2} which was in good agreement with the theoretical results.

2.2.1.2. Indirect K radiation

Indirect radiation is due to ionisation of the target material by bremsstrahlung photons and represents a small but significant fraction of the total emitted characteristic radiation. The theory of indirect radiation is complicated by electron straggling and diffusion inside the target material and the necessary corrections needed to account for the self filtration of the generated X ray spectrum. Experimental and theoretical work to establish the contribution to the total characteristic line intensity by indirect k radiation has been done by Hanson and Cowan[116] and Green[86].

Green[86] and Green and Cosslett[112] calculated the ratio

$$\frac{\text{Indirect K radiation}}{\text{Total K radiation (Direct + Indirect)}} = F_k$$

and found that F_k could be written as

$$\frac{F_K}{1-F_K} = \frac{9.4 \cdot 10^6}{Z^4} \qquad 2.13$$

$$= 31\% \text{ for tungsten.}$$

The constant of the equation 2.13, $9.4.10^6$, was fitted to the previous experimental results of Stoddard[90], Burbank[117], Webster[115] and Costing and Descamps[118].

It is obvious from equation 2.13 that indirect characteristic radiation is only important for high atomic number materials. Use was made of this by Green[86] to eliminate indirect K radiation when determining the effective depth of generation of direct characteristic radiation. The importance of K shell radiations emitted by the X ray set used in this project is discussed in the following section.

2.2.1.3. Total K radiation line measurements in the whole spectrum.

Experimental measurements of characteristic radiation emitted from tungsten targets has been carried out by many workers. Such measurements are very difficult to make in view of the high photon fluxes and complicated detector response corrections. An additional difficulty is the large amount of bremsstrahlung energy present compared with the characteristic radiation.

Despite these difficulties, measurements have been made, although no analytical formulation of the results has emerged. People and Burt[97] using an NaI(Tl) scintillation counter and low beam currents (0.5mA), have measured the spectra in the range 40 - 100 kVp for full wave rectified X ray generators. They found only a small amount of K radiation was emitted at 80kVp, although at 100kVp the presence of this radiation was evident. The same workers also established the

variation of spectral output with beam current. A significant drop of flux above 65keV was observed at 100kVp when the beam current was raised from 1 to 3mA owing to regulation. They found when comparing the X ray output of two X ray sets, that there was better regulation for the set having the longer EHT cable.

Similar measurements have been carried out by Epp and Weiss[98]. After correcting the detector response, they found that with 2mm aluminium filtration that K radiation was just evident at 80kVp, whilst at 90,98 and 105 kVp the radiation was comprised of 1.4%, 4.1% and 7.5% respectively of the total energy. The spectra emitted from tungsten targets with sinusoidal voltages of 65 - 100 kVp are shown in Fig.2.2. This figure shows that when the accelerating voltage is 90kVp (the peak voltage used with the densitometer) there are no X rays below about 18keV and a broad intensity peak at about 30keV, although this extends from 24 - 68keV for half maximum values. It is also apparent that by increasing the peak voltage the emitted characteristic radiation increases together with a broadening of the bremsstrahlung peak.

The results of Epp and Weiss are in agreement with those of Hettinger and Starfelt[100], who measured the X-ray spectra emitted from a tungsten target at various constant accelerating potentials. They found, as did Tothill[120], that with the equivalent of 2mm aluminium filtration the fractional incident energy of the K radiations rose from zero at 69.6kV to not more than 5% at 100kV accelerating potential. Even at 250kV this fraction was less than 12%.

Assuming the X ray mode voltage to be sinusoidal, the contribution of K radiation to the whole spectrum will be less than 5% at 100kVp. Because of this, the presence of any characteristic k radiation emitted by the X ray set was ignored in the theoretical calculations.

2.3 Absorption of X rays.

When electromagnetic radiation travels through matter there is a probability that radiation will interact with the material. The interaction mechanisms of X and Y rays has been dealt with rigourously in several texts [73-76, 121, 122] and only a brief reference to these mechanisms will be made here. The probability of interaction per unit path length of X ray photons will depend on their energy and the density and atomic number of the material.

In the simplest case of narrow beam of homogeneous radiation and a single elemental absorber, the intensity I of an X ray beam after travelling through a thickness x of absorber is given by the exponential equation,

$$I = I_o e^{-\mu_L(E)x} \qquad 2.14$$

where I_o = initial intensity

$\mu_L(E)$ = linear absorption coefficient, which is a function of energy E

The linear absorption coefficient may be expressed in terms of the total cross section per electron by

$$\mu_L(E) = \rho\, N_A (z/A)\, {}_e\mu\,(E) \qquad 2.15$$

where ρ = density of the element

N_A = Avogadro's number

z = atomic number of the element

A = atomic weight of the element

${}_e\mu(E)$ = total cross section per electron

From equation 2.15 the mass absorption coefficient $\mu_m(E)$ is given by

$$\mu_m(E) = N_A (z/A)\ {}_e\mu(E) \qquad 2.16$$

The total mass absorption coefficient is the sum of the partial absorption coefficients $\mu_{mn}(E)$ for all possible N absorption phenomena i.e.

$$\mu_m(E) = \sum_{n=1}^{N} \mu_{mn}(E) \qquad 2.17$$

In the energy region 10 - 100keV the predominent interactions are the photoelectric effect and the Compton effect. The total mass absorption coefficient is then the sum of the photoelectric and Compton mass absorption coefficients τ_m and σ_m respectively, so that

$$\mu_m(E) = \tau_m + \sigma_m \qquad 2.18$$

The latter two cross sections are given approximately by

$$\tau_m = \frac{N_A Z^5 E_\gamma^{-3.5}}{\rho} .10^{-33} \qquad 2.19$$

for gamma ray energies E_γ above the K shell energy[12 3].

$$\sigma_m = \left(\frac{N_A Z}{A}\right) 2\pi r_o^2 \left[\frac{1+2}{\alpha^2}\left(\frac{2(1+\alpha)}{1+2\alpha} - \frac{1}{\alpha}\ln(1+2\alpha)\right) + \frac{1}{2\alpha}\ln(1+2\alpha) - \frac{1+3\alpha}{(1+2\alpha)^2}\right] \qquad 2.20$$

where $\alpha = \frac{E_\gamma}{511}$ keV

$2\pi r_o = 2.818.10^{-15}$ m, the classical radius of the electron.

If an electron passes through a compound or mixture the probability of interaction will in general be the sum of the interactions from all the different elements. The effect of chemical binding on the interaction of X rays with valence electrons is very weak, except in the case of Bragg reflection where the atoms are in an orderly arrangement. For an absorbing material having a different element, each having a mass absorption coefficient of $\mu_m(E)$, $\mu_{m_2}(E)$ ... $\mu_{m_n}(E)$ and a mass of $m_1, m_2 \ldots\ldots m_n$ respectively, the total mass absorption coefficient $\mu_m(E)$ will be

$$\mu_m(E) = \frac{\sum_{i=1}^{n} \mu_{mi}(E)\, m_i}{\sum_{i=1}^{n} m_i(E)} \qquad 2.21.$$

The linear absorption coefficient $\mu_L(E)$ of the material is then related to the density ρ and $\mu_m(E)$ by the simple expression

$$\mu_L(E) = \mu_m(E)\,\rho \qquad 2.22$$

If there are n elemental absorbers in an X ray beam path each having a linear absorption coefficient $\mu_{Li}(E)$ and a thickness x_i, the transmitted intensity will be

$$I = I_o\, e^{-\sum_{i=1}^{n} \mu_{Li}(E) x_i} \qquad 2.23$$

In the case of a heterogeneous beam of X rays the last three equations become more complicated. If the flux of X rays in the energy region E to E + dE is $\phi(E)dE$, then the mean mass absorption coefficient for one elemental absorber will be

$$\bar{\mu}_m(E) = \frac{\int_0^\infty \mu_m(E)\,\Phi(E)\,dE}{\int_0^\infty \phi(E)\,dE} \qquad 2.24$$

whilst for an absorber composed of n elements the equation will be

$$\bar{\mu}_m(E) = \frac{\int_0^\infty \sum_{i=1}^{n} \mu_{mi}\, m_i\, \phi(E)\,dE}{\sum_{i=1}^{n} m_i \int_0^\infty \Phi(E)\,dE} \qquad 2.25$$

The X rays emitted by a diagnostic set are heterogeneous and equation 2.25 must be used to calculate the alteration due to a composite material such as bone or water. If the energy distribution of the emitted beam is taken to be that given by Kramer's law (equation 2.3), then equation 2.25 becomes

$$\mu_m(E) = \frac{D\int_0^{E_{max}} (E_{max} - E) \sum_{i=1}^{n} \mu_{mi}(E)\, m_i \, dE}{\sum_{i=1}^{n} m_i} \qquad 2.26$$

where D is a constant

E and E_{max} are the energy and maximum energy of the X rays.

Equation 2.26 has been used in the theoretical calculations (chapter 6) and the integral evaluated by numerical integration.

2.4. Theory of the equipment.

In chapter 1 mention was made of the guiding factors governing the design of the equipment. In this section the theory of the equipment is given.

To overcome the difficulties associated with using X ray machines for scanning, it was decided to use two X ray detectors, one to sample the beam and the other to measure the transmitted intensity through the specimen as shown in Fig.1.6. This was outlined in chapter 1 and details of the equipment are given in chapter 3.

Adjacent X ray beams emerging from the set are detected by two Cs I(T1) crystals housed in detectors I and II. The light output of the scintillating crystals is very nearly proportional to the instantaneous X ray energy except for very low energy photons[69-71]. The emitted light is reflected towards the surface of a photocathode which gives rise to a current which is proportional to the incident light intensity. For each detector, the two separate currents are fed into a small capacitor to integrate the signal currents with respect to time. After integration the signals are fed into a high input impedance source follower whose outputs are fed into the linear amplifiers I and II, shown in Fig. 1.6.

Let the instantaneous signals from the detectors be S_1 and S_2. If the signals were integrated between times t_1 and t_2 the resultant amplified signals G_1 and G_2 are then expressed by the equations

$$G_1 = A_1 \int_{t_1}^{t_2} S_1 \, dt \qquad 2.27$$

$$G_2 = A_2 \int_{t_1}^{t_2} S_2 \, dt \qquad 2.28$$

A_1 and A_2 are constants whose value depends upon the amplification and X ray beam admittance of the two detectors, as well as the electron beam current and the source-detector distance. Usually the integration commences from the start of every half cycle and $t_1 = 0$.

The integrations are carried out until the value of G_1 reaches a preset value W whereupon the integration of S_2 is electronically terminated and the value of G_2 attained is used to give a y deflection on an oscilloscope. The value of t_2 is not fixed but is governed by the generator voltage waveforms. If the peak mains amplitude varies from V to V + ΔV, G_1 will reach the value W in a shorter time $t_2 - \Delta t$. Conversely, if the mains amplitude is lowered the time of integration will be greater than t_2. This is illustrated in Fig.2.3 and the conditions will then satisfy the equations 2.29 and 2.30.

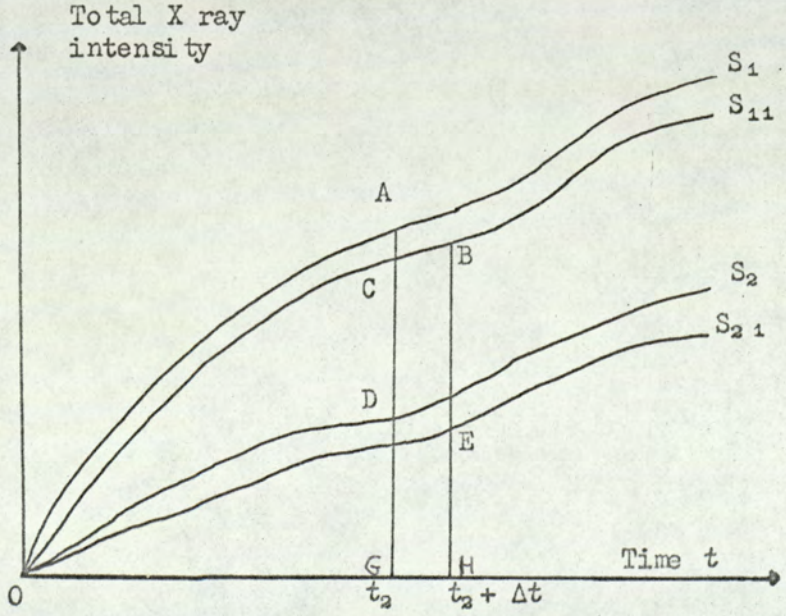

Fig.2.3.

If the two waveforms S_1 and S_{11}, S_2 and S_{21} are made approximately equal by similar filtration of the two X ray beams then

G_1 = Area OAG = Area OBH by electronic switching

and

G_2 = Area ODG $\simeq$ Area OEH.

G_1 may be written as

$$G_1 = A_1 \int_{t_1}^{t_2} S_1(V)dt = W \qquad 2.29$$

$$= A_1 \int_{t_1}^{t_2-\Delta t} S_1(V+\Delta V)dt = A_1 \int_{t_1}^{t_1+\Delta t} S_1(V-\Delta V)dt \qquad 2.30$$

The corresponding values of G_2 will then be

$$G_2 = A_2 \int_{t_1}^{t_2} S_2(V)\, dt \qquad 2.31$$

$$\simeq A_2 \int_{t_1}^{t_2-\Delta t} S_2(V+\Delta V)dt \simeq A_2 \int_{t_1}^{t_2+\Delta t} S_2(V-\Delta V)dt \qquad 2.32$$

Equations 2.31 and 2.32 are only rigourously equal if the aborption factors implicit in $S_1(V)$ and $S_2(V)$ are equal. A difference between $S_1(V)$ and $S_2(V)$ will mean that these equations are not exactly equal and therefore an error in G_2 will occur. This will be discussed later in this chapter and has been calculated in chapter 6.

The evaluation of G_1 and G_2 requires a knowledge of $S_1(V)$ and $S_2(V)$. These functions are the instantaneous signal currents from the two detectors and therefore depend upon the integrated energy incident upon the two CsI(T1) crystals. This energy will be dependent upon the filtration in the path of the two detectors.

Assuming a spectral distribution of X rays given by Kramer's law (equation 2.3), the X ray intensity of the unfiltered beam in the voltage range V to V + dV may be written as

$$dI = \alpha I(t) \left[V(t) - V \right] dV \qquad 2.33$$

where α = constant

$I(t)$ = electron beam current at time t

$V(t)$ = anode voltage at time t

The fraction of X ray energy transmitted at any one particular energy E has been given by equation 2.14 and for an absorber containing n different elements the fraction becomes from equation 2.21

$$I/I_o = \exp\left(-\left(\sum_{i=1}^{n} a_i \mu_{mi}(E)\, x_i \right) \rho \right) \qquad 2.34$$

where a_i is the fraction by mass of the ith element.

The total energy of the transmitted beam at any time t is therefore

$$\alpha\, I(t) \int_o^{V(t)} \left[V(t) - V \right] \exp\left(-\left(\sum_{i=1}^{n} a_i \mu_{mi}(E) x_i \right) \rho \right) V \qquad 2.35$$

so that after integration during the period $t_2 - t_1$ the signal G_1 will be

$$G_1 = K_1 \int_{t_1}^{t_2} I(t) \int_o^{V(t)} \left[V(t) - V \right] \exp\left(-\left(\sum_{i=1}^{n} a_i \mu_{mi}(E) x_i \right) \rho \right) dV dt \qquad 2.36$$

where $K_1 = \alpha A_1$.

G_2 will be similar but in general there will be different thicknesses of different absorbers in the X ray beam path i.e.

$$G_2 = K_2 \int_{t_1}^{t_2} I(t) \int_o^{V(t)} \left[V(t) - V \right] \exp\left(-\left(\sum_{i=1}^{m} a_i \mu_{mi}(E) x_i \right) \rho \right) dV dt \qquad 2.37$$

where $K_2 = \alpha A_2$.

The variation of absorption coefficients with X ray energy is illustrated in Fig.6.4. It is seen that the electron beam current $I(t)$ affects both G_1 and G_2 equally and variation of this will cause equal changes in the time scales of both integrals G_1 and G_2. In order to evaluate G_1 and G_2 the waveforms of $I(t)$ and $V(t)$ must be known or assumed. If the beam current is assumed to be constant and $V(t)$ to

vary simsoidally with angular frequency ω then $V(t)$ may be written as

$$V(t) = V_o \left| \text{Sin } \omega t \right| \qquad 2.38$$

where V_o = voltage amplitude

and the moduli signs have been introduced owing to the full-wave rectification of the voltage.

The electronic system ensures that

$$G_1 = W = \text{constant} \qquad 2.39$$

$$\therefore \left(\frac{\partial G_1}{\partial V_o}\right) \Delta V_o + \left(\frac{\partial G_1}{\partial t_2}\right) \Delta t_2 = 0 \qquad 2.40$$

Where ΔV_o and Δt_2 are the changes in voltage amplitude and upper limit of integration time respectively. This will cause a total change in G_2 of ΔG_2 where

$$\Delta G_2 = \left(\frac{\partial G_2}{\partial V_o}\right) \Delta V_o + \left(\frac{\partial G_2}{\partial t_2}\right) \Delta t_2 \qquad 2.41$$

From equation 2.40

$$\Delta t_2 = - \frac{\left(\frac{\partial G_1}{\partial V_o}\right) \Delta V_o}{\left(\frac{\partial G_1}{\partial t_2}\right)} \qquad 2.42$$

Substituting this into equation 2.41 we find

$$\Delta G_2 = \left[\left(\frac{\partial G_2}{\partial V_o}\right) - \left(\frac{\partial G_2}{\partial t_2}\right) \left(\frac{\partial G_1}{\partial V_o}\right) \Big/ \left(\frac{\partial G_1}{\partial t_2}\right)\right] \Delta V_o \qquad 2.43$$

Ideally we require $\Delta G_2 = 0$ for a non-zero value of ΔV_o

$$\text{i.e. } \left(\frac{\partial G_2}{\partial V_o}\right) \left(\frac{\partial G_1}{\partial t_2}\right) = \left(\frac{\partial G_2}{\partial t_2}\right) \left(\frac{\partial G_1}{\partial V_o}\right). \qquad 2.44$$

This is exactly true only in the special case when $G_1 = G_2$ i.e. when the filtration above the two crystals is exactly the same and they receive the same energy spectrum. Owing to the constant movement of the limb through the beam of X rays, G_1 and G_2 cannot be made equal throughout the scan. However, the error ΔG_2 may be made small by placing in the path of the monitor a filter which closely approximates to the mean filtration of thes econd X ray beam. This has been done

by using a 45 mm perspex water cell together with a 5 mm thick ivory slab as described in chapter 3.

Equation 2.43 gives the error in G_2 caused by a small peak voltage fluctuation ΔV_o. All the differential coefficients in the square bracket are positive and since $G_1 \simeq G_2$ to a close approximation

$$\frac{\partial G_1}{\partial V_o} \simeq F \frac{\partial G_2}{\partial V_o} \qquad 2.45$$

and

$$\frac{\partial G_1}{\partial t_2} \simeq F \frac{\partial G_2}{\partial t_2} \qquad 2.46$$

where F is a constant and is dependent upon K_1/K_2 .

2.4.1. Practical considerations.

For satisfactory operation we require that

(i) G_1 and G_2 be as large as possible for all absorber thicknesses.

(ii) There should be good bone/water discrimination.

(iii) The compensation technique should perform adequately.

These are discussed in turn.

(i) The values of G_1 and G_2 may be made large by using a high beam current, long integration time and a high peak anode voltage. However, the electronics and X ray generator have limited capabilities and a practical compromise must be sought. It will be shown in chapter 6 that if the value of G_2 increases with integration time, the fractional error $\Delta G_2/G_2$ increases. However $\Delta G_2/G_2$ decreases with the use of higher anode peak voltages.

(ii) Item (ii) suggests that a spectrum with a low mean energy be used because of the increasing difference between the absorption coefficients of water and bone at lower energies. A low peak voltage, besides giving a poorer signal, suffers the disadvantage that changes in the transmitted X ray beam caused by a given fractional change of anode voltage would be greater than if the X ray generator were operated at a higher voltage. This is because of the preferential absorption of softer radiation which will be

more predominant at low anode voltages.

If we assume in the simple case that the path of the second X ray beam passes through bone and water only having path lengths of b_x and w_x respectively, the equipment ensures that

$$b_x + w_x = K = 50 \text{ mm} . \qquad 2.47$$

If the parameters I and t_2 are regarded as constant within the limits of equation 2.47 then G_2 may be written as

$$G_2 = G_2(b_x, w_x, V_o)$$
$$= G_2(b_x, (K - f_x), V_o). \qquad 2.48$$

We therefore require that $\left(\frac{\partial G_2}{\partial b_x}\right)$ should be large in magnitude and $\left(\frac{\partial G_2}{\partial w_x}\right)$ be small over the ranges of b_x and w_x permitted by equation 2.47, because the absorption coefficients for bone and water are different

$$\left(\frac{\partial G_2}{\partial b_x}\right) \neq \left(\frac{\partial G_2}{\partial w_x}\right)$$

and therefore the bone/water discrimination may be defined as $\left(\frac{\partial G_2}{\partial b_x}\right) \Big/ \left(\frac{\partial G_2}{\partial w_x}\right)$ which should be as large as possible. As in (i), a practical compromise must be found.

(iii) The third item requires that the monitor which operates the switching electronics have sufficient signal to terminate the electronic integration of the second detector. Although the value W selected may vary over a large range, it is important that electronic signal to noise ratio be large and the switching time short. The waveforms of G_1 and $\left(\frac{\partial G_1}{\partial t_2}\right)$ as functions of time are determined by the anode voltage waveform, the filtration in the path of the monitor and the amplification of the signal. Large values of G_1 and $\left(\frac{\partial G_1}{\partial t_2}\right)$ are best achieved by sampling the X ray beam over a solid angle as large as conveniently possible.

Chapter 3.

3. The Experimental Equipment.

As described in Chapter 1 the densitometer was designed to give a fast, accurate scan of the ulna. Furthermore, it had to to be made as inexpensively as possible and capable of being used without adjustment by the hospital staff. Its use in a hospital also demanded that the equipment be compact and robust.

For simplicity this chapter has been divided into three main sections.

(1) The X ray detection system

(2) Mechanical equipment

(3) Electronic equipment.

3.1. The X ray detection system.

It was decided to detect the X rays by a scintillation crystal, and, via a suitable optical guide, lead the emitted light on to the cathode of a vacuum photodiode. The choice of a scintillation crystal in preference to other detection methods e.g. photoconduction, was made in view of the better efficiency and time response of scintillators in the 10 - 100 *ke*V photon energy region. The variable photo - conductivity of cadmium sulphide has been used to detect X rays, but it suffers from the disadvantage of a very long time response (> 10 seconds[125,126]). Lead sulphide has been used to detect ultra-violet radiation, but the response of the material falls off rapidly even for soft X rays. The choice of scintillator is discussed in the following section and the properties of the selected vacuum photodiodes are also outlined.

3.1.1. Choice of the scintillator detector.

In making this choice it was realised that the two detectors would receive X rays over a small area ($\simeq$10mm x 2mm) in the photon energy region 10 - 100 *ke*V. The factors governing the choice of scintillator were :

(1) Linearity and light output response in the energy range 10 - 100 keV,

(2) Spectral matching of the light output of the scintillator to the photodiode,

(3) Decay time, and translucence to its own emitted radiation,

(4) Cost,

(5) Special properties e.g. any hygroscopic nature, sensitivity to shock and temperature variations.

The most widely used scintillation crystal is NaI(Tl) and although its choice was not immediately ruled out because of its hygroscopic nature, it was realised that if it were selected because of its high light output compared with other crystals, e.g. CsF, KI, CsI, that shaping and airtight sealing would be difficult. Owing to the low energy range of the photons, the choice of covering material would have to be very carefully considered, particularly in view of the small size of the scintillation crystals required ($\simeq 5 \times 5 \times 10$mm or $\frac{1}{4} \times \frac{1}{4} \times \frac{3}{8}$ in.) In view of these complications, Na I(Tl) scintillation crystals were not chosen.

The thallium doped caesium iodide crystal has a light output lower than NaI(Tl) but higher than other solid scintillation crystals except CsI(Na)[127]. However, CsI(Tl) was chosen because the CsI(Na) crystal has a narrower peak emission spectrum (peak at 428 mm) which might give spectral mismatching with the photodiodes chosen.

3.1.2. The CsI(Tl) crystal.

Thallium doped caesium iodide crystals are non hygroscopic and almost colourless with a density of 4510 $kg\ m^{-3}$. This high density and the high atomic number of its main constituents (Cs = 55, I = 53) mean that the crystal possesses a very high stopping power for X and γ rays. The total linear absorption coefficient is shown in Fig.3.1.

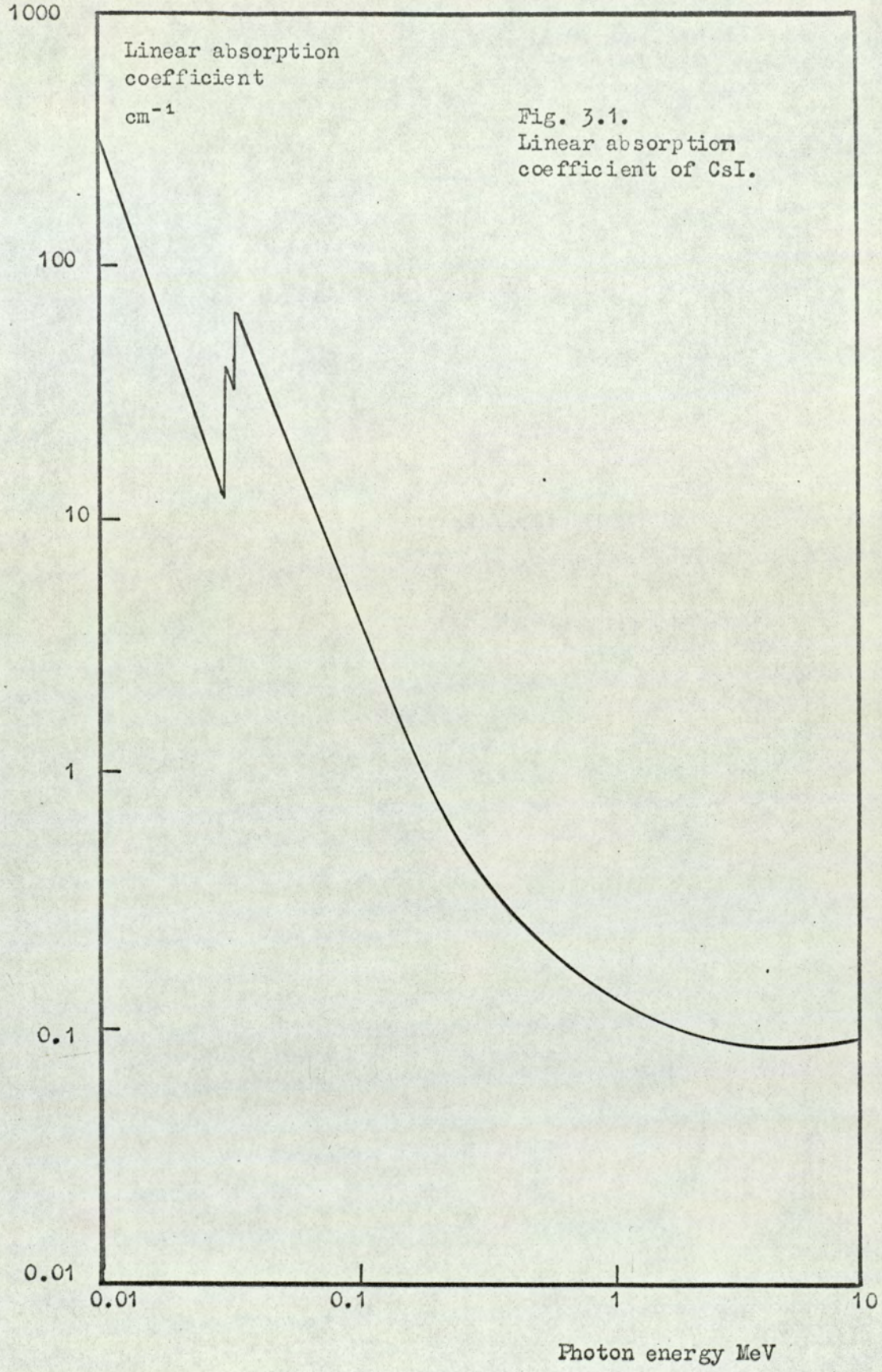

Fig. 3.1.
Linear absorption
coefficient of CsI.

as a function of photon energy. These measurements are given by Schmeling[57]

Time response characteristics

The integration of the X ray energy is carried out for about 5ms and at the end of every mains half cycle the integrator is discharged for about 400μs to reset the device. It is therefore important that they decay characteristics of the CsI(Tl) crystal (and the electronics) be much smaller than the discharged time.

Storey et al[129] showed that the effective decay time of the CsI(Tl) crystal depends upon the energy of the ionising particle. These workers found a decay time of (1± 0.05)μs for 660keV electrons, the decay time decreasing for particles having a higher differential energy loss, which means that for 100keV electrons the decay time will be less than 1μs. Plyavin[130] has measured the photoluminescent decay time of CsI(Tl) using a brief (10 ns) pulse of light to excite the impurity absorption energy band. A decay time of 0.8 ± 0.1 μs was found. For gamma excitation, Jones and Ward[131] have observed that the time taken for the light output to rise from 10% to 90% of its peak value was about 1μs and was independent of the thallium concentration. Owen[132] has found that when CsI(Tl) is irradiated by γ rays there is a relatively slow pulse rise of about 0.2μs, followed by a decay possessing two exponential components of 0.4 and 7μs. This response to γ irradiation is a common feature of NaI(Tl) and CsI(Tl) and may be associated with the electron hole recombination and saturation at high electron transfer rates[133].

Light output response of CsI(Tl)

This has been investigated by Guin and Murray [69,70] and Collinson and Hill[71]. These workers have investigated the light output of the crystal when irradiated by X rays in the energy region 10 - 100keV. Fig (3.2) shows the light output per unit energy of incident photons plotted against photon energy. The same authors have also considered

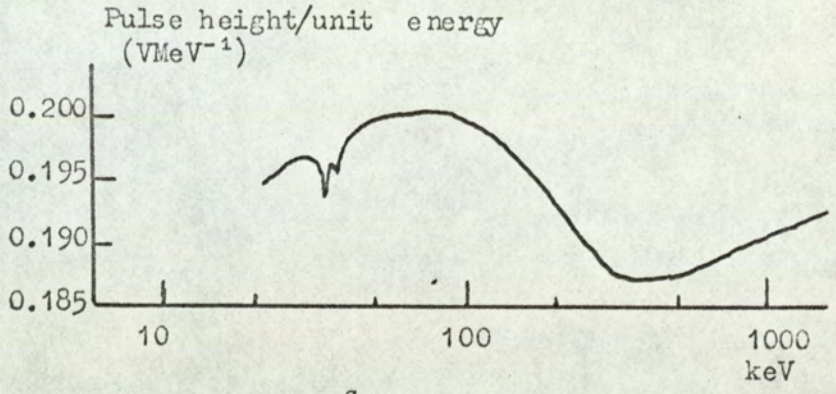

Fig. 3.2a. Pulse height per unit energy for 1 x 1 in CsI(T1) crystal. Taken from Collinson and Hill[71].

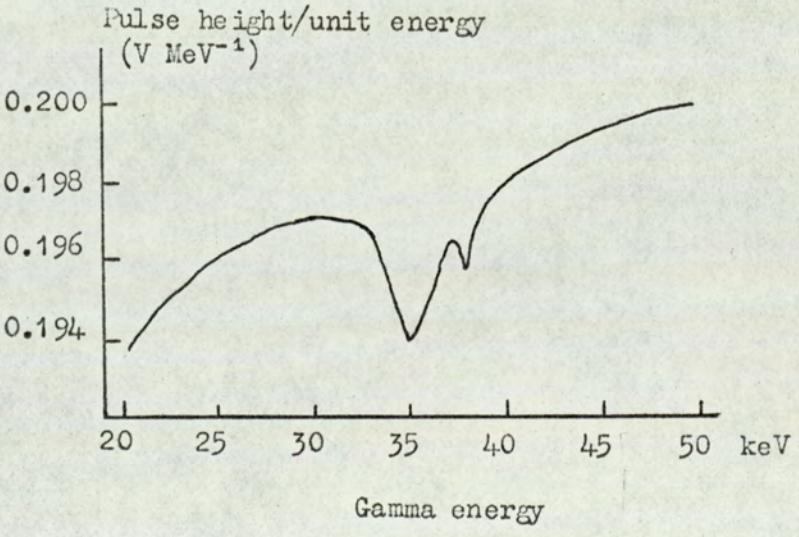

Fig.3.2b. Pulse Height per unit energy for 1 x 1 in CsI(T1) crystal. Taken from Collinson and Hill [71].

the escape of secondary X rays which give rise to an asymmetric pulse height distribution. These secondary X rays are produced in the crystal by the incident photon giving rise to the K escape peak. The magnitude of this effect will depend upon cyrstal size and crystal-source geometry. An estimate of the K escape peak was made by Axel[134] and the largest correction for this effect was about 2.5%.

Below 100keV the predominent photon interaction with CsI(Tl) is by photoelectric absorption (ratio of photo-electric to Compton absorption sections at 100keV = 8.5). When observing a low energy scintillation event the K and the L edges of the crystal must be taken into account, as absorption at these edges will give rise to the probability of K and L escape radiation. The K edges of iodine and calcium are 33.2 and 35.6keV respectively, while the L edges of both atoms are about 2.5keV.

In the assessment of the response of CsI(Tl) to γ rays, the response of the crystal to electrons is implicit. This is because of the K and L shell electrons ejected from the Cs and I atoms when an X or γ ray interacts with the crystal. Guin and Murray[69,70] have noted that the electron response has a maximum at 20keV and decreases for electrons above or below this energy. This means that there will be a maximum response to X rays. Hence when an X ray of 55keV energy ejects a 20keV electron, the resultant light output per unit energy will be a maximum. For X rays in the energy range (32 - 55)keV the ejected electron will possess less than 20keV kinetic energy and therefore the overall response measured by light output per incident photon energy is sub linear.

For interacting photons having an incident energy slightly lower than the K shell energy ($\sim$ 35keV), an L-shell electron is ejected with kinetic energy of 30keV which is on the "high" side

of the electron response peak. If the energies of the incident photons are lowered the overall light output response will pass through a second maximum and then fall for low energy electrons. The theoretical light output response is more difficult to analyse because of the similar atomic charge of the atomic constituents and therefore interaction cross sections. Collinson and Hill[135] have investigated the light output of the crystal theoretically and have given equations above and below the K edges. Despite complications due to the similarity of the atomic numbers of the caesium and iodine and the three L sub-shells of each atom, good agreement with experimental results were obtained except for low energy (< 20 keV) electrons. This may be partly attributed to the lack of information regarding M shell cross sections. In the calculations of Zerby et al[136], Jones[137] and Kaiser et al[138], it was assumed that for photons above the K absorption edge energy the fractional number of interactions resulting in a L shell photoelectron could be neglected. This assumption was examined by Collinson and Hill[71] who showed that for low energies this assumption was not valid.

3.1.3. The photodiodes

As the top detector is nearer to the spot source of X rays than the second detector and may sample a larger solid angle of incident X rays, this permits a less sensitive photodiode to be used with considerable saving of expense. For the monitor a Mullard 92AV vacuum diode was chosen whilst for the second detector an EMI 9524B photomultiplier was used initially as a photodiode by taking the signal off the first dynode and connecting the other dynodes to earth potential. The photomultiplier was changed to specially constructed photodiodes for reasons which are discussed later. Photomultiplier tubes were deliberately not used in their conventional mode because of their excessive gain and the necessity

for a separate and expensive EHT supply. Furthermore, a drift of 1% in the supply voltage to the photomultiplier tube will cause the final anode current to charge by about 8%. The output current of the vacuum photodiodes do not suffer the extreme sensitivity to voltage changes provided the diode is well saturated. The typical output impedance is $\geq 10^9\ \Omega$.

Gas filled photodiodes (e.g. Mullard 92AG) were not chosen despite the current gain they offered because of the uncertain long term behaviour characteristics of the gas. The current multiplication is also very sensitive to contamination and molecular degradation.[139, 14

The Mullard 92AV valve.

This is a small photoemmisive vacuum device having an S11 response. The photocathode has a caesium antimony surface of 210mm^2 and a sensitivity of about $45\mu A lm^{-1}$ at 85 volts. The maximum permitted anode voltage supply is 100 volts, but for low light intensities ($\simeq$ 0.02 lumen) there is electron saturation of the diodes at about +18 volts anode to cathode. The dark current is <0.05 nA with a anode to cathode capacitance of about 1 pF.

The diode is 54mm long and 19mm in diameter and has seven pins in a B7G base configeration. Pins 1,2,6 and 7 are connected to the cathode, whilst the other three pins join to the anode. It was noted that pins 3 and 5 were joined to the anode via very thin getter wires. Connection of these two wires to the sturdier anode connection (pin 4) depends upon the orientation of the photodiode. It is therefore prudent to connect pins 4,5 and 6 together so that there is a good anode connection with the getter wire at this potential. This wire, like a capacitor microphone, forms a variable capacitance between itself and the anode so that if there is a potential difference between the two charge may be stored. Even though such capacitance will be small ($\sim$ 0.1pF) it discharge

(or charge) would give a spurious current.

The EMI 9524B photomultiplier.

This is a high gain photomultiplier having a CsSbO photocathode surface which gives a S 11 response. The cathode sensitivity is about 70μA lm^{-1}. The overall length of the photomultiplier is 115mm and has a diameter of 29mm with a flat end photocathode window. The dark current was found to be about 0.05 nA with a capacitance of the anode to all dynodes of 6pF.

The main disadvantage of the photomultiplier was that it possessed a mechanical resonance at about 300 Hz which made it extremely microphonic. For this reason another vacuum tube was used in the bottom detector.

The Special Photodiode.

To overcome the unacceptability of the 9524 B photomultiplier to microphony a special rugged photodiode with a flat end photocathode window was ordered from EMI Ltd., The photodiode showed no mechanical resonance at low frequencies (< 600 Hz) and it was found to give a microphonic-free signal in operation. It also had the additional advantage of a lower anode to cathode capacitance (4pF). The photodiode had an overall length of 70mm and a diameter of 28mm. The sensitivity of the photocathode was about the same as the photomultiplier, but with a smaller dark current.

3.1.4 The CsI(Tl) crystal holder and light reflector.

Inside each lead-roofed dural detector boxes was housed the photodiode, the crystal with its housing and the electronic integrator. For the best light collection efficiency the crystal was designed to be as near to the photocathode as possible. The small crystal ($\frac{1}{4} \times \frac{1}{4} \times \frac{3}{8}$ in) was held in a perspex container, as shown in Fig 3.3. Inside the container was milled a central rectangular cavity for the crystal. The two crystals, when

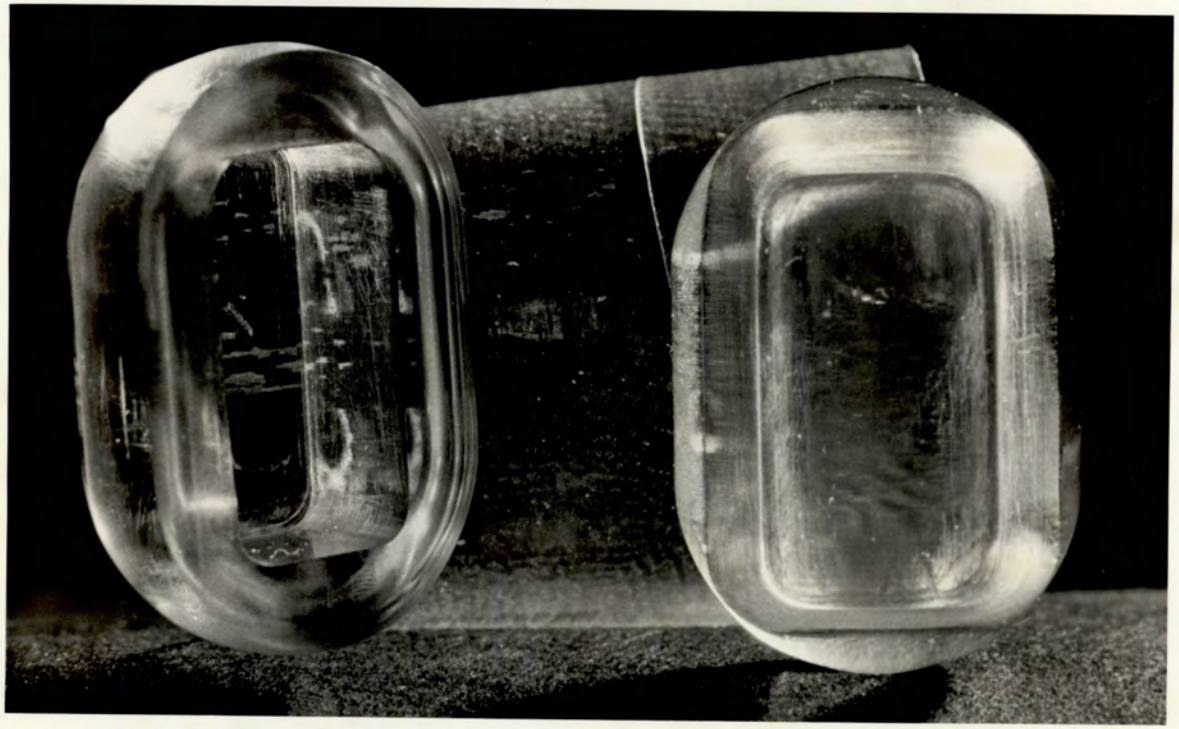

Fig. 3.3. The perspex holders for the CsI(T1) crystals

received from the manufacturers, Nuclear Enterprises, measured slightly more than the required size and were reduced by careful abrasion until they slid comfortably into the milled cavities.

The perspex holder possesses the advantage that if the outer curved surface is made reflecting, light emitted away from the photocathode in a scintillation event has a high chance of being reflected back into the photocathode. Furthermore, the total path length of any singly reflected ray still remains small ($\simeq$10mm), so that absorption in the perspex and the crystal is small.

The outer curved surface of the crystal housing was aluminised by evaporation in vacuo. Despite its higher light reflectance, a silver coating was not used because of its much greater absorption coefficient for low energy X rays. It was found best to hold the perspex by the inside of the cavity, with the outer curved surface facing the evaporating boat. The small flat annulus around the cavity had to be covered with mica to prevent aluminium being deposited on this surface. Several evaporations were required to obtain a uniform coating over the whole curved surface of the perpex. After aluminising the coating was inspected and the flat face of the holder carefully polished.

Upon comparing the photodiode currents with and without the reflector housing it was found that a seven fold increase in photocurrent was obtained and therefore, the crystal reflector housing was worth the trouble of making. For all optical couplings a gel with a high light transmission was used. Care was taken not to introduce air bubbles by placing the gel on one of the two surfaces and bringing the two surfaces together. In view of the small area of all the optical couplings, this point was considered to be important.

3.1.5. The Monitor light assembly

Inside the monitor the crystal housing is held in position by a small perspex holder which is secured to the middle cross piece of dural channel by 6BA nuts and studding. To hold the housing the supporting perspex holder was shaped to a similar curvature to that of the crystal reflector housing. To prevent scratching of the aluminised surface a small area of polyurethane foam was cemented to the inside cavity of the perpex holder.

Light leaving the crystal reflector was guided on to the curved surface of the Mullard 92AV valve by a small perspex cylindrical plane concave light pipe. The radius of curvature of the light pipe was machined to match that of the photodiode. A flexed piece of phosphor bronze mounted in two grooves of the perspex holder firmly secures the photodiode in its correct orientation with respect to the crystal and provides sufficient pressure on the light pipe and the crystal housing to make the complete assembly secure.

3.1.6. The detector light assembly

The detector photodiode has the advantage of having a flat end window as well as being situated in a more spacious box than the monitor. These two advantages have meant that the optical system was simpler in design and easier to manipulate should an examination of the system be required.

The inside of the end dural channel piece adjacent to the X ray collimator slit was covered with a sufficient thickness of polyurethene foam until with the back of the crystal holder pushed against the foam, the collimator slit was about 13mm from the external flat face of the perspex holder. To secure the photodiode in a central position (Fig.3.4) two pieces of perspex (50 x 25.4 x 10mm thick) were cemented to the antimonial lead roof and to the sides of the $7\frac{1}{4}$ in. long adjacent channel pieces. (The detector is described in section 3.2.3). The thickness of the perspex blocks was carefully finished

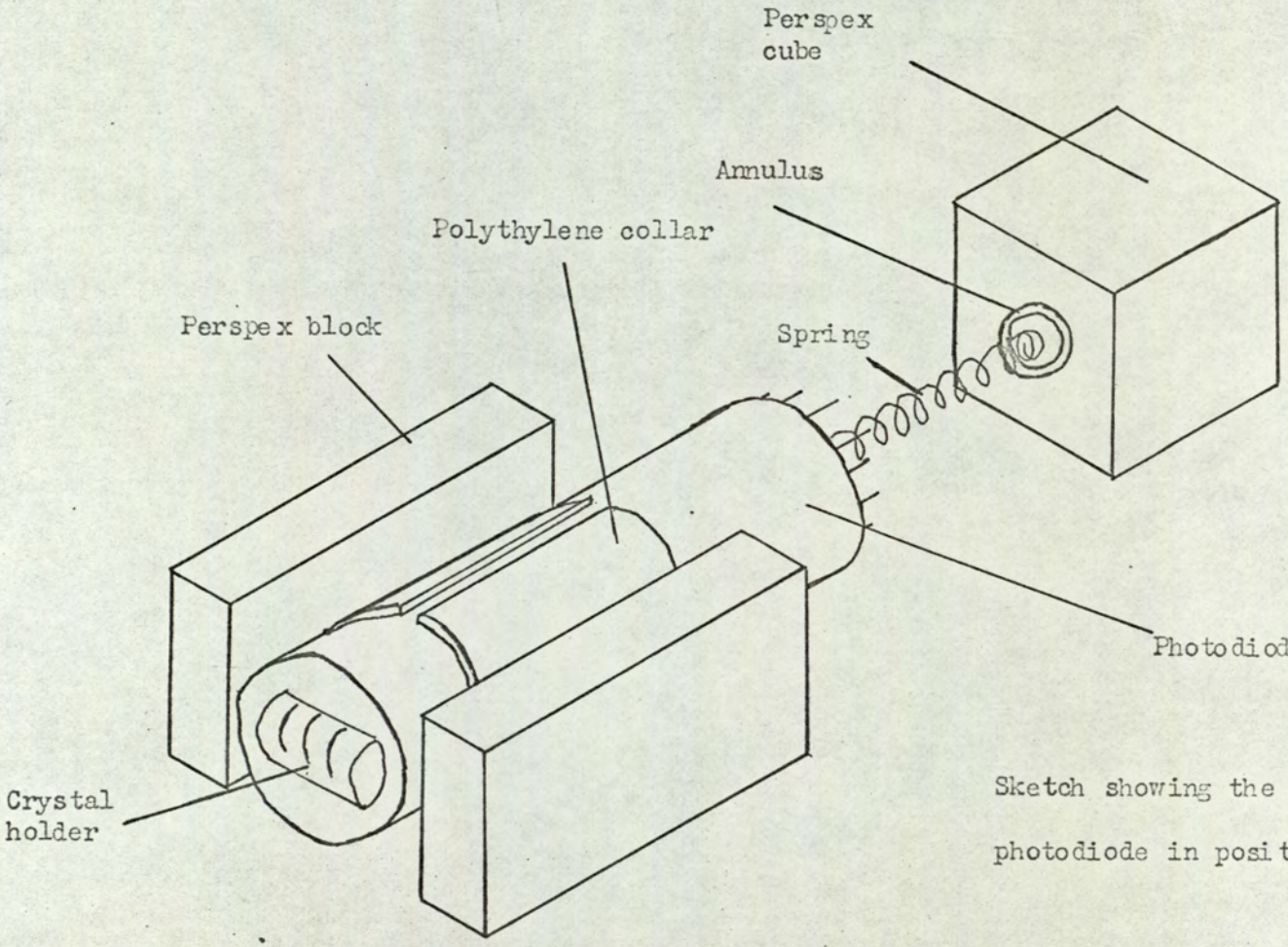

Fig. 3.4.

Sketch showing the detector photodiode in position.

until with a single layer of polyethylene forming a collar about 1 mm thick around the photodiode, it fitted firmly between the two blocks. The polyethylene collar was orientated so that it was midway around the tube with the two ends meeting at the "inverted" top of the detector box to face the observer. When in this position the dural cover lid pushes the two ends of the collar so that vertical movement of the photodiode is impossible.

Longditudinal movement of the photodiode is prevented by employing a steel spring to exert a force against a cemented perspex block and the pin end of the diode. The spring about 6 mm diameter and 30 mm long, was slotted over the glass vacuum seal to prevent risk of shorting the pins. A 25 mm perspex cube was centrally cemented to the antimonial lead roof about 25 mm away from the nearer end of the photodiode. A small annulus of 1 mm thick perspex having an inside diameter marginally greater than the outside spring diameter was stuck to the side of the perspex cube facing the collinating slit. This served to prevent the spring slipping from its set position once the detector box cover had been sealed.

3.2. The Mechanical Equipment.

The framework of the densitometer contains all the equipment except the camera, osilloscope and the three phase power supply for the motor. In most cases duraluminium was chosen as the construction material, being light, rigid, inexpensive and easily machinable.

The mechanical equipment may be broadly split into three separate parts for discussion:

(a) The bottom framework which has the rails for the moving frame and supports the other two sections,

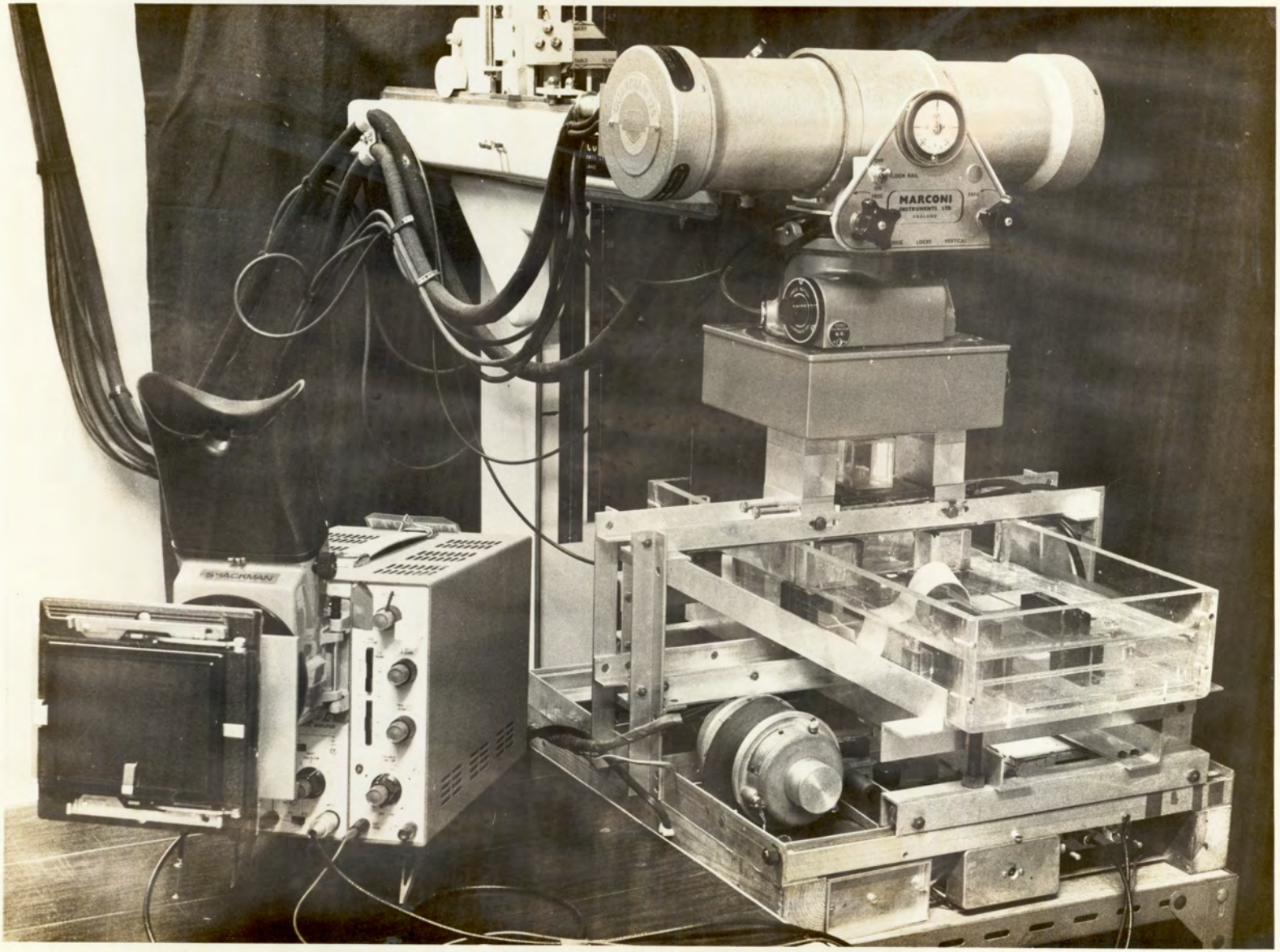

Fig.3.5. The densitometer.

(b) the trolley, which holds the perspex water bath and which is capable of being driven by the synchronous motor,

(c) the framework holding the monitor and the detector in the path of the X rays.

Since the initial construction of the three sections it was found necessary to make slight alterations. These modifications have been made in order to house the electronic equipment as it was thought desirable to have this contained within the main body of the machine.

The equipment is shown in Fig.(3.5).

3.2.1. The bottom framework.

This has an overall dimension of $20\frac{1}{4}$ x 24 in with the perimeter of the framework made from 24 x $1\frac{1}{2}$ angle and 20 x 1 in channel. Four pieces of channel were used in all, two pieces screwed back to back with five 2BA screws 4 in apart for rigidity. The bottom pair of channel pieces were rounded off at the corners so that the two vertical faces of the angle and the channel could fully abut when brought under tension. This was effected by using 3/8 in diameter silver steel rod of length $21\frac{1}{4}$ in and threaded at each end for 3/8 in Whitworth nut. The rod was mounted inside the channel pairs and also formed the guide rails on which the trolley runs. To ensure parallelism of the rod to the channel two small pieces of dural 1/8 in thick were forced into the channel on either side of the silver steel. This was done at both ends for the pair of channel members.

Support for the central driving shaft was made by screwing back to back $19\frac{3}{4}$ x $1\frac{1}{2}$ in angle. Six 2BA screws were used to join the common vertical side and the ends were then fastened to the outer 24 in angle by two 2BA continuous screws at each junction. The

Fig. 3.6.
Sketch of the bottom framework.

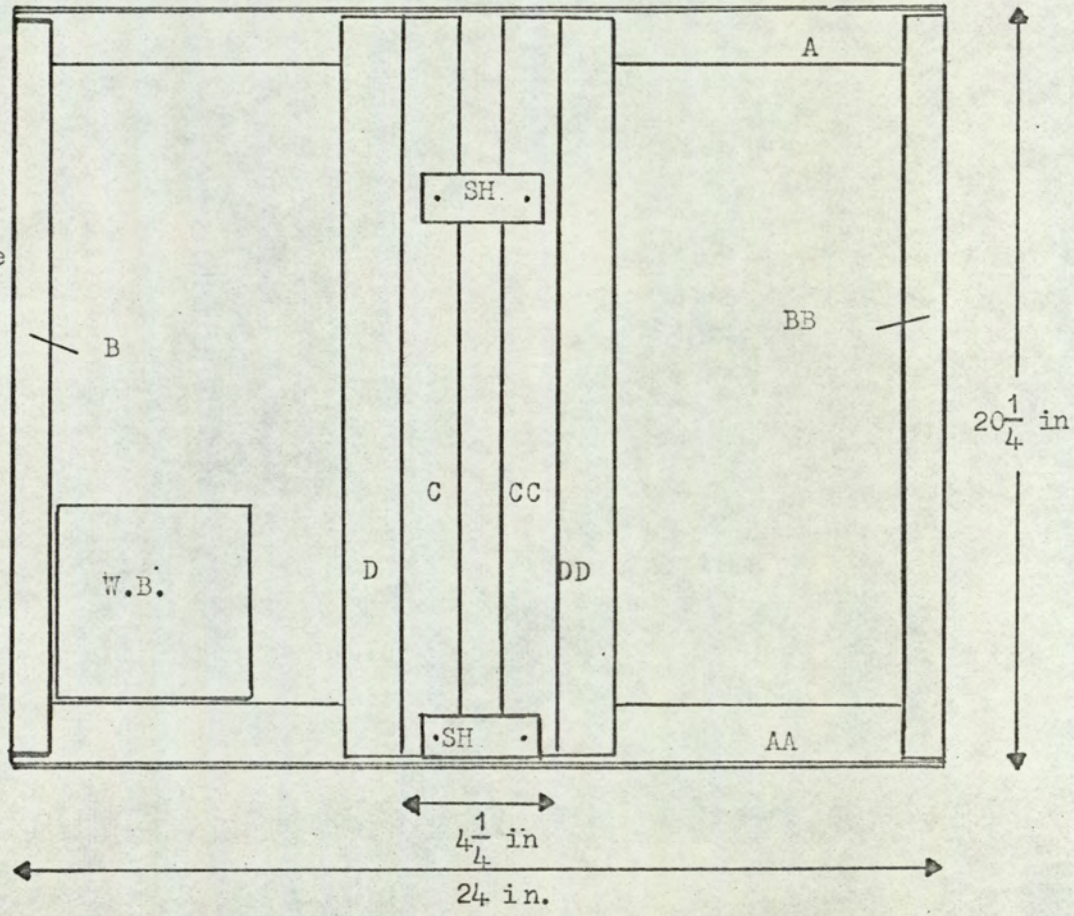

A, AA, C, CC,
D, DD $1\frac{1}{2}$ in angle

B,BB 1 in channel

SH Shaft holder

WB White coloured box containing electronics

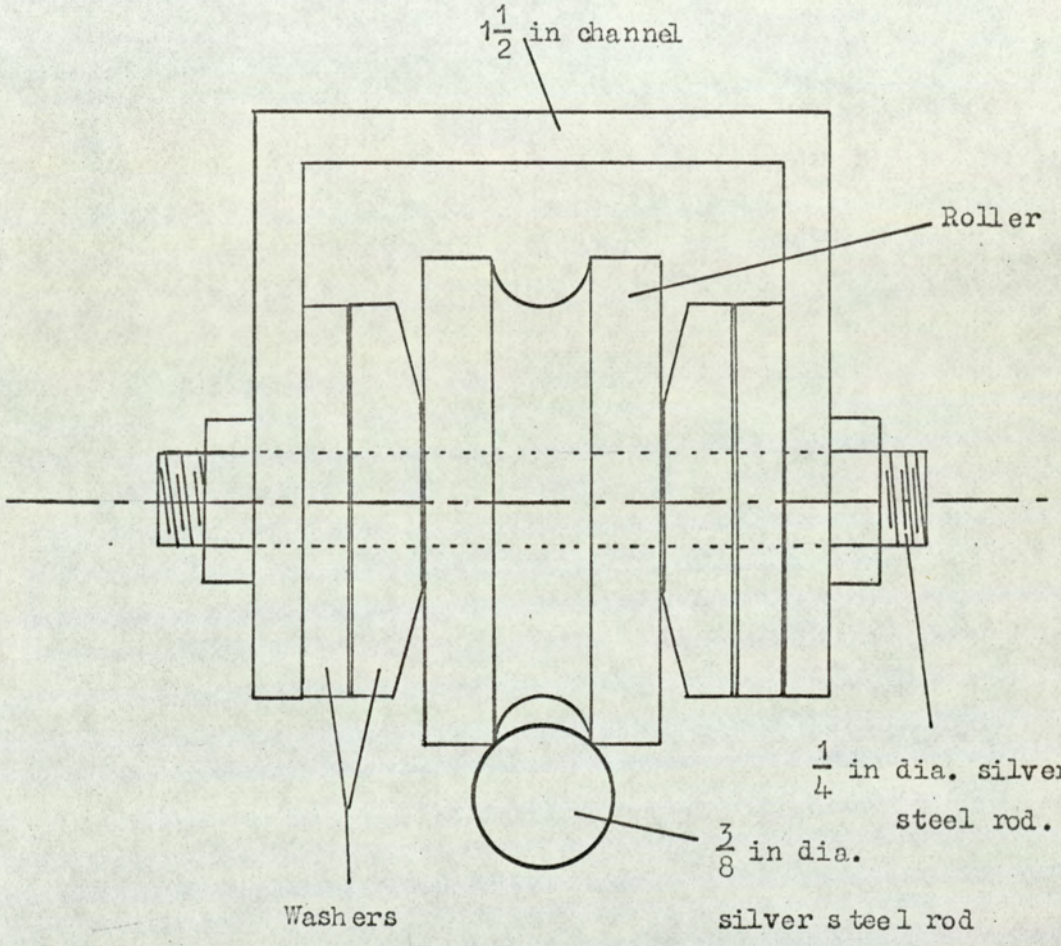

Fig. 3.7. Sketch to show the mounting of the trolley rollers.

distance between the vertical walls of the channel was made $3\frac{3}{4}$ in.

On top of the two pieces of channel C, CC, Fig.(3.6) was bolted the driving shaft holder. At the end nearest to the electronic box it was secured to just touch the inside dural member A and at the opposite end it was mounted $4\frac{3}{4}$ in from the inside of the dural angle. The shaft holder has a ball bearing mounting made to accept rod of 1/2" diameter.

The driving shaft.

This originally came from a metric lathe and was modified to suit the small travel length required for the moving trolley. The shaft has an overall length of $18\frac{1}{2}$ in and a diameter of 20 mm. The driving shaft has a square thread of 3 mm pitch. So that the moving trolley is not forced into the remainder of the frame at either end of its scanning range, sufficient thread was removed from the central part and one end of the shaft.

3.2.2. The moving trolley.

This piece of equipment serves to hold the bath for the limb and is driven by the synchronous motor to obtain a scan of the ulna. The trolley relies on two pairs of rollers to run freely on the 3/8 in diameter silver steel rods. These rollers have an outside diameter of $1\frac{1}{4}$ in and a width of 5/8 in in which there is a central 1/8" radius groove (Fig.3.7). Inside the 1/2" diameter hole of the roller was fixed a bearing which accepted 1/4 in steel rod.

Two pieces of $14\frac{1}{8}$ x $1\frac{1}{2}$ in channel house the two pair of rollers. The centre of each roller was mounted 3/4 in from the end of the channel and 1/2 in above the lip. Longitudinal movement of the roller inside the channel was prevented by employing two stainless steel washers on either side of the flat roller edges to ensure a tight fit. The face of the two washers touching the rollers was slightly bevelled to ensure that there was contact with only the

inner bearing which is free to rotate. A 2in length of 1/4 in diameter silver steel rod, tapped at both ends for 1/4 in Whit. screws, secures the rollers in the channel. The two channel roller holders were then fixed $22\frac{3}{4}$ in apart so that they could move together along the silver steel track. This was achieved by fixing the holders with two pieces of $24\frac{1}{2}$ x $1\frac{1}{4}$ in angle such that the vertical side of the angle was outmost. The distance between the end of the roller channel and the inside of the horizontal side of the angle was made $4\frac{5}{8}$ in and $5\frac{5}{8}$ in, an allowance of 1 in being made for the electric motor. Fixation at each junction was made by two 2BA countersunk screws and nuts. For extra rigidity two cross 1 in channel pieces were bolted to the $24\frac{1}{2}$ in long angle.

To carry the bath of water over the detector a top framework was connected to the lower by four corner supports. Three of the supports were fixed to the inside end of the roller channel but because of the motor in one corner this could not be done for the fourth support. The three supports were made from $5\frac{1}{2}$ x $1\frac{1}{2}$ in angle and was secured to the end of the roller channel with the two rounded common faces innermost. The fourth support was made from a mild steel bolt 1/2 in diameter and $3\frac{3}{4}$ in length with a flat hexagonal head turned down to just under 1/8 in thickness. For this support a 1/2 in diameter hole was drilled in the top of the channel $3\frac{3}{4}$ in from the nearest edge to the motor. Two nuts on either side of the channel roof could then secure the bolt, but this was left until the remainder of the trolley had been constructed and secured. The four vertical supports connected to the roller channel were then screwed to two $14\frac{3}{8}$ x $1\frac{1}{2}$ in angle pieces above and parallel to the pair of roller channels, so that the horizontal sides of the angle were vertically above the top of the channel. Fixation at every junction was again made by two 2BA screws.

To hold the perspex water bath (24 x 10 x 4 in high) two pieces of $1\frac{1}{2}$ in angle $24\frac{1}{2}$ in long were used. They rested centrally on the horizontal flat surfaces of the two pieces of angle situated above the roller channel and with the other face in full contact with the vertical face of the corner support. The 2 x 2BA screws at each junction were then tightly secured and the $\frac{1}{2}$ in diameter screw was then slotted downwards through the accommodating holes to form the fourth vertical support. Two nuts were fastened on, and a third on the underside of thec hannel. By tightening the three screws in order, the whole trolley could be made secure.

3.2.3. The framework holding the monitor and detector.

As has already been mentioned, this framework holds the monitor above and the detector below the perspex bath. The framework was constructed entirely from 1 in angle, for although rigidity is required, there is no necessity for great mechanical strength. It is centrally fastened to the outside of the 24 x $1\frac{1}{2}$ in bottom angle, and forms the central bridge-like structure above and below the bath. The two cross pieces holding the detector boxes were made from $22\frac{1}{4}$ in long 1 in angle and were fastened to the $10\frac{3}{4}$ in high vertical upright members of the framework. Underneath each junction of the cross-pieces and vertical supports was screwed a $4\frac{1}{4}$ in length of angle to make the bridge $4\frac{1}{4}$ in wide and to give rigidity to the framework.

In the case of the bottom detector mechanical decoupling was found to be necessary because of the susceptibility of this detector to microphony. A further pair of 1 in angle pieces were mounted back to back to the existing bridge angle pieces. With the monitor bridge supports screwed tight, the first inner bottom cross bridge supports were removed and a central portion cut away to give a generous allowance for the alignment and rubber mounting necessary to decouple the detector. The four end pieces were then replaced

and tightly screwed into position.

Finally the two pairs of vertical bridge supports were carefully centred on the two outer sides of the bottom 24 x $1\frac{1}{2}$ in angle with the bottom of the vertical supports and the angle pieces coincident.

3.2.4. The monitor and detector boxes

Both these were constructed using 1 in dural channel and had an antimonial lead roof to collimate the X rays on to the scintillation crystal and shield the photodiodes from the X ray beam.

The monitor box

This houses the CsI(T1) crystal together with its light guide, the photodiode and the integrator. The external measurement of the monitor box was made 4 x 3 x 1 in high with each piece of channel end cut at 45°. After the pieces were stuck to the lead roof, eight holes were drilled into the opposite face of the channel and tapped for 6 BA continuous screws. A small $2\frac{3}{4}$ in length of channel was cut and cmented to the two 4 in pieces to fix the position of the scintillation holder with respect to its collimation slit. The piece of channel also makes the larger section of the monitor lightproof, for a collimation slit must be cut in the lead roof and the screw cover to permit X rays to reach the lower detector. This cover was constructed from 4 x 3 x $\frac{1}{16}$ in dural sheet.

The detector box.

This houses the same components as the monitor box except for the different light guide and photodiode. The box was made 3 x $7\frac{1}{4}$ x 1 in high to fit the EMI 9534 B photomultiplier. The diameter of the photo multiplier (29 mm) meant that the 1/8 in thick dural screw cover could not be made flat. To overcome this a central 3/16 in depression 1 in wide was made in the dural cover to accommodate the photomultiplier. This cover was fixed to the box by

sixteen 6 BA screws to ensure a light, tight fit.

3.2.5. The antimonial lead roofs.

These serve to collimate the X rays on to the scintillation crystals and to shield the photodiodes and the electronics from the incident X ray beams. It was decided to make the thickness of the lead roofs about 1/4 in to ensure sufficient mechanical strength and adequate attentuation of the X rays (linear absorption coefficient of lead for 100 kV photons = 59 cm^{-1}). Sufficient protection of the photodiodes must be given from the very high photon flux ($\sim 10^{11}$ photons mA^{-1} sr^{-1} s^{-1}) must be given as X rays incident on the photocathode could have a deleterious effect.

To obtain the shape and thickness of lead required a brass casting trough was made and supported at the corners by four steel blocks of equal height. The collimation slits were made by clamping a vertical strip of metal 10 mm wide at right angles to the longer side of the trough and just touching the floor. Before casting the antimonial lead the mould was heated to a temperature a little higher than the melting point of lead so that there would be no sudden solidification when the cast was made. Immediately after casting, a stream of hot air was blown underneath the mould to cool the molten antimonial lead from the bottom as slowly as possible. Simultaneously a gas flame was directed on the liquid surface. It was found that this prevented solidification commencing from the surface which results in serious cavitation of the finished cast.

When cold the cast was radiographed at 100 keV and 5mA for 20 minutes. A close examination of the developed radiograph was made for cavitation of the cast and if the result was negative, the cast set aside for machining.

The underside of the cast was milled to obtain a flat face to cement to the dural detector boxes. For the bottom detector, two slabs of antimonial lead were needed because the brass casting trough

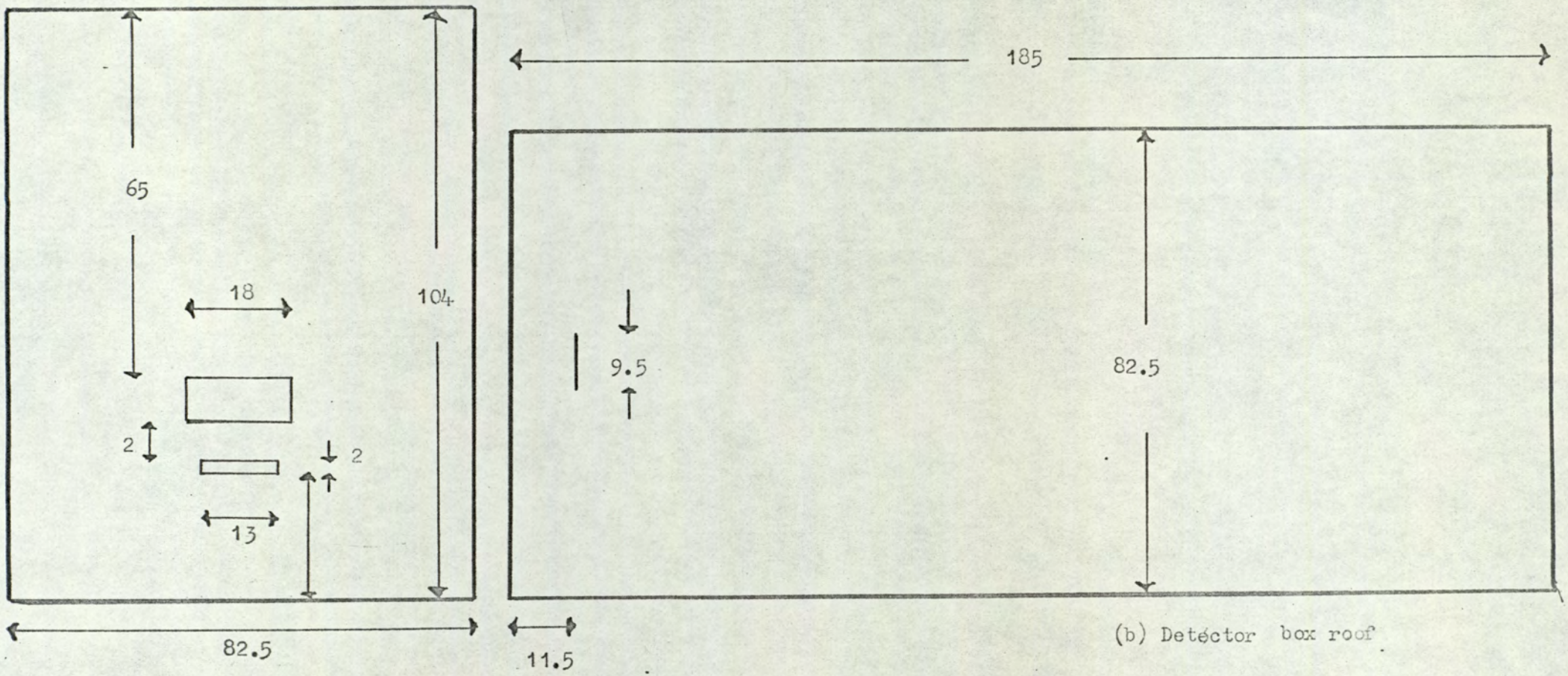

(a) Monitor box roof

(b) Detéctor box roof

Dimensions in mm.

Fig.3.8. Sketch of the anitomonial lead roofs.

was of insufficient length. After milling a flat face, one end of the 3 in. sides of both slabs were milled at 45° to the surface so that the edges were complementary. The two detector slabs were cemented together with Araldite. Soldering was not attempted in view of the large mass of lead to be heated and the possibility of irrevocably changing the shape of the slab. The bottom detector shield was cut to a total length of $7\frac{1}{2}$ in. and finally both detector lead roofs were cemented to the dural detector boxes. The arrangement of the collimation slits in the antimonial lead is shown in Fig. 3.8.

3.2.6. The lead collimation slits.

After the X ray beam passes through the smaller collimator in the antimonial lead roof of the monitor (Fig.3.8), the beam requires further collimation. This is because the area and divergence of the beam determine the area which irradiates the lower detector as well as the patient dose.

To collimate the beam two adjustable lead sheets 3 × $2\frac{1}{4}$ wide × $\frac{1}{8}$ in. thick were fitted underneath the monitor. These lead sheets rest between the $2\frac{1}{4}$ in. wide space of the two 1 in. bridge angle which hold the monitor. The small lead sheets rest on a much larger sheet (15 × $3\frac{1}{4}$ × $\frac{1}{8}$ in), cemented underneath the top bridge frame. Into this last sheet was cut a slit to allow the X rays to reach the bottom detector. Part of this shielding can be seen in Figs. 3.9 and 3.10.

By removing the monitor and adjusting the positions of the two lead collimators, the dimensions of the beam was reduced to 12 × 2mm at the lower detector.

3.2.7. Miscellaneous equipment.

The perpex bath.

The perspex bath was made 24 × 10 × 4in. deep to give it sufficient size and strength to accommodate a subject's arm and

hand with a sufficient depth of water to cover the arm over the examination area. The bath was constructed from $\frac{1}{2}$ in thick perspex except for the floor which was made $\frac{1}{4}$in. thick to minimise X ray absorption. Fig. 3.5. shows the bath in position.

The water cell.

This was constructed to provide a path of water over the monitor X ray entrance collimator slit so that the average filtration of the two detector beams would be equal with consequential little error in compensation.

The X ray path length through the water is 45mm, the roof and floor of the cell being made from $\frac{1}{8}$ in perspex to give a beam path through the perspex equal to the floor of the bath. The water cell has external dimensions of 60mm wide x 50mm x 51.3mm high and is shown in position in Fig.3.9. Two removable nylon screws, fitted into the cell but not in the X ray beam path, allow the cell to be filled and periodically recharged due to loss by radiolysis. The 5mm slot of ivory which forms the remainder of the composite monitor filter, rests on top of the water cell above the collimation slit in the X ray beam path.

The dural blocks.

Three dural blocks are mounted in either side of the top detector to support a brass flange used to ensure reproducable positioning of the X ray tank head with respect to the two detectors. The total height of the blocks is $3\frac{1}{2}$ in. and have a width of 3 in. They are shown in position in Fig. 3.5, 3.9, 3.10. The lower pair of blocks have two holes tapped with $\frac{1}{4}$ in. BSF thread to permit the fixation and locking of the two supports in the top bridge angle by four $\frac{1}{2}$ in long screws. The positions of the two supports are adjustable, and can be very accurately adjusted and relocated by three 3 in. long $\frac{1}{4}$ in BSF screws fixed to the bottom pair of dural

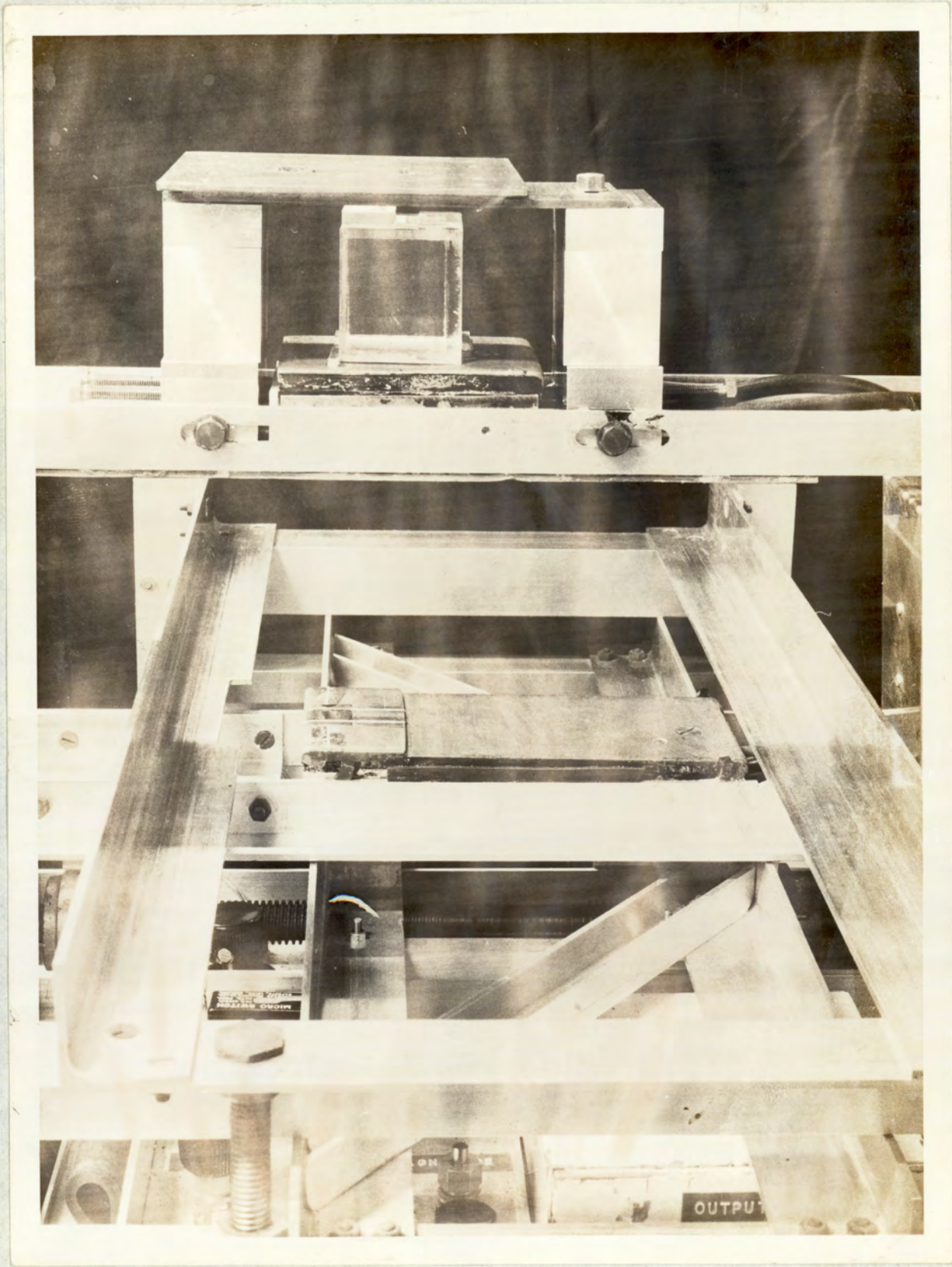

Fig. 3.9. Close up of part of the densitometer.

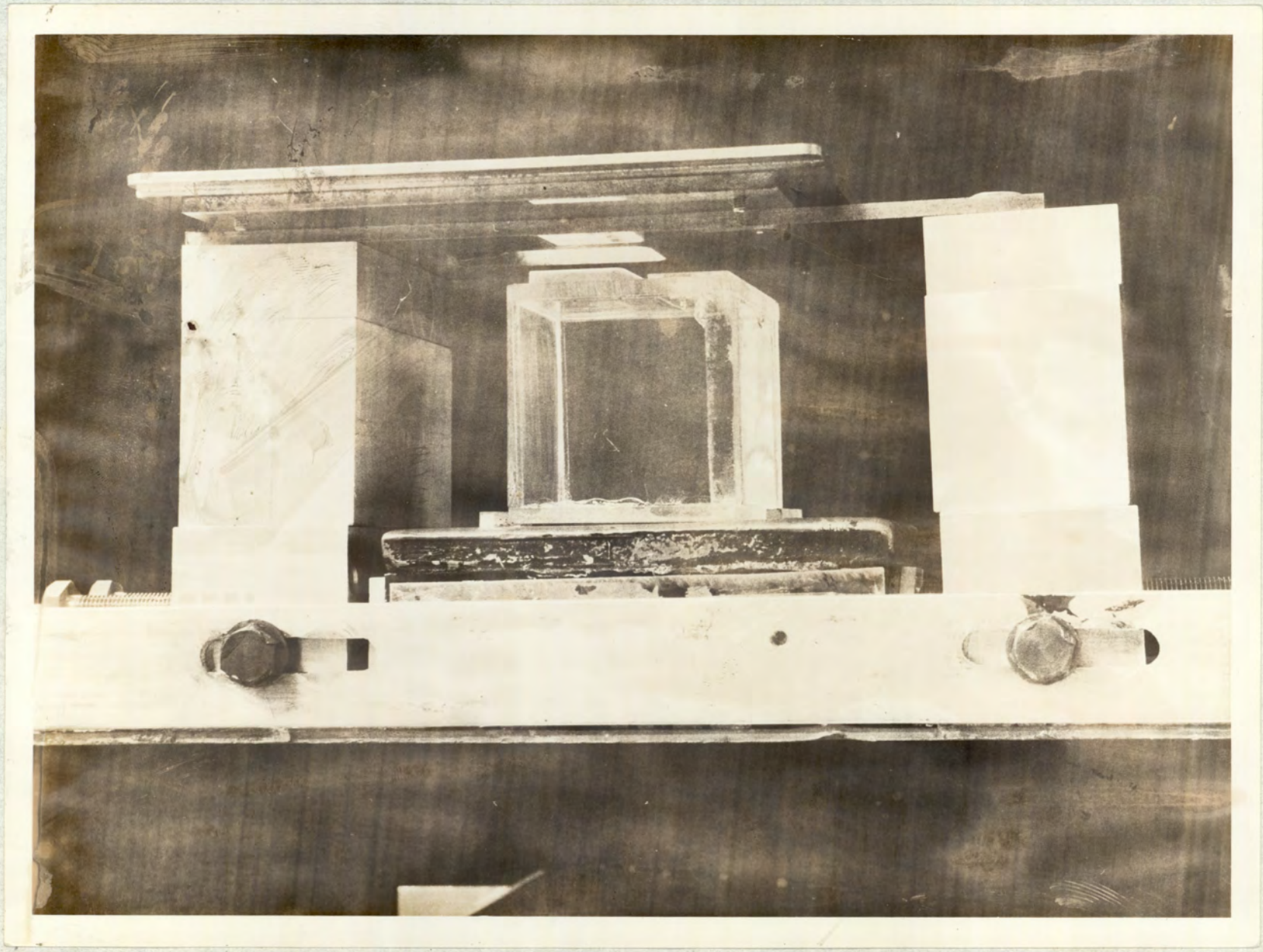

Fig. 3.10. The monitor, water cell and brass flange.

blocks with their axes parallel to the bridge angle. The ends of these screws abut on to an insulating piece of perspex cemented on either side of the monitor. If the dural blocks are locked into the bridge angle (by the four $\frac{1}{2}$ in. long screws) the three long screws will define and fix the position of the top detector.

A central OBA clearance hole through the three blocks nearest to the motor allows the studding connected to the brass flanges to be secured to the blocks. The opposite end of the flange is locked into position by a long OBA screw which engages a thread in the other bottom dural blocks.

The brass flange.

A brass flange was constructed to be mounted on top of the dural supports to ensure reproducible positioning of the X ray tube with respect to the two detectors. This is done by two opposite sides of the flange engaging a standard complementary flange fixed underneath the housing of the X ray tube. It is shown in position in Fig.3.9.and Fig. 3.10 shows the details of the construction.

The perspex arm or limb fixing frames.

Two frames were made (one for each arm) to secure the limb on to the floor of the perspex bath in a suitable position so that a scan of the ulna could be made about 30mm proximal to the ulnar styloid. Two photographs of the method of fixation of a subject's hand and arm is shown in Figs. 3.11, 3.12. To minimise rotational movement of the ulna the hand is secured in a supinated position by two adjustable straps which define the positions of the first and fifth fingers. Adjacent to the ulnar styloid is a 1 in. wide, 2 in. high fixed perspex block padded with firm rubber. Opposite this is a variable compression spring loaded padded block to press against the radial styloid so that the ulnar styloid is pushed against the fixed support. To keep the arm flat a 3 in wide

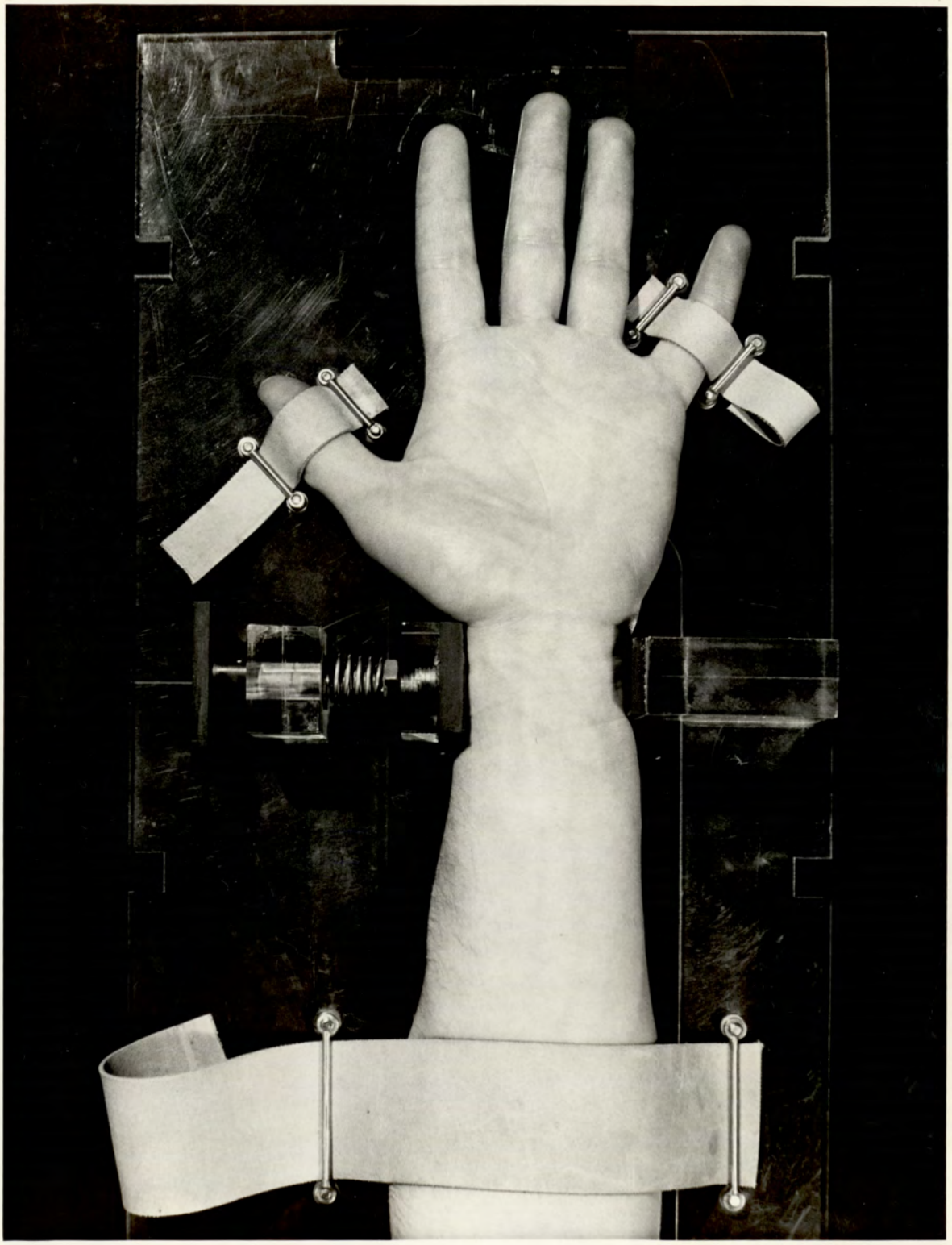

Fig. 3.11. Photograph showing a subject's arm fixed in the perspex frame.

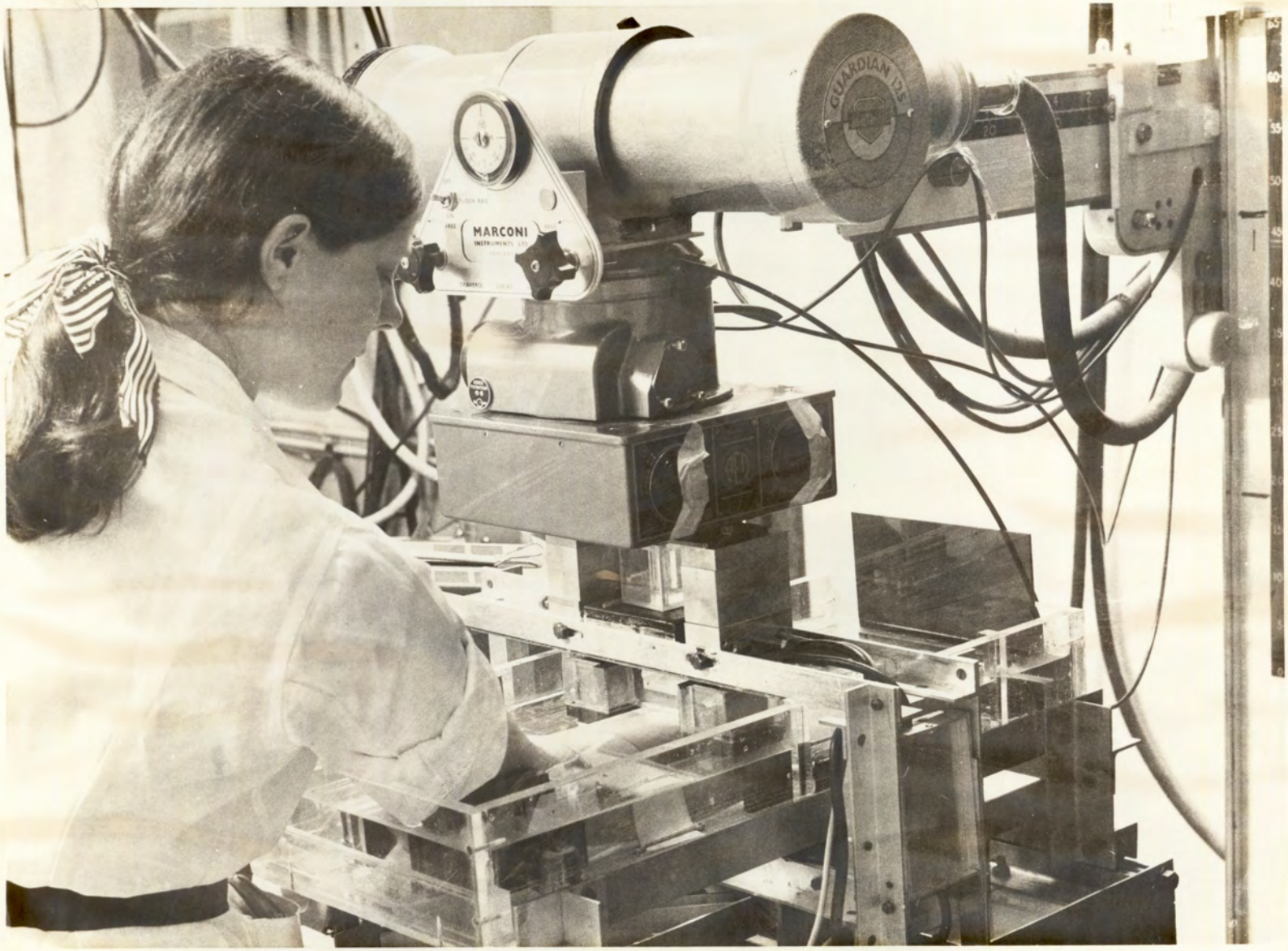

Fig. 3.12. A subject's arm in position for scanning.

strap is secured over the arm between the elbow and the wrist whilst two further adjustable padded blocks keep the elbow in a fixed position to help minimise rotational and lateral movement.

Four $\frac{1}{2} \times \frac{1}{2} \times 3\frac{3}{4}$ in perspex blocks were cemented vertically to the two opposite long inside walls of the bath to allow the fixing frame to be slotted in and secured against the floor of the bath so that an upward pull on the fixing straps by a subject would not separate the fixing frame from the bath. The frame is finally secured into position by three large perspex wedges, Fig.3.12, to take up the differences in dimensions between the frame and the interior of the bath. One wedge is pushed into place along the 10 in. side of the bath nearest the fingers, whilst the other two are place on the long 24 in. edge nearest the ulna.

The small bath tank.

To maintain a constant X ray path length of 50mm through the water and limb in the bath a small perspex tank was constructed to fit over the area of arm in which the ulna was to be examined. It is shown in position in Fig.3.5. Inside the tank at either end were cemented two large pieces of lead to ensure that sufficient pressure is exerted by the narrow 15mm wide central position of the tank on the subject's arm to keep the X ray beam path through the water and limb fixed.

If the tank is set in position to make a scan 30mm from the ulnar styloid, the tank may be placed into position by resting its supports on the perspex hand fixing frame and moving it until it abuts onto the sides of the radial and ulnar styloid perspex blocks of the frame.

The ivory step wedges.

The provide an absorption calibration of the X rays which may be easily compared with the ulna trace, two ivory step wedges were

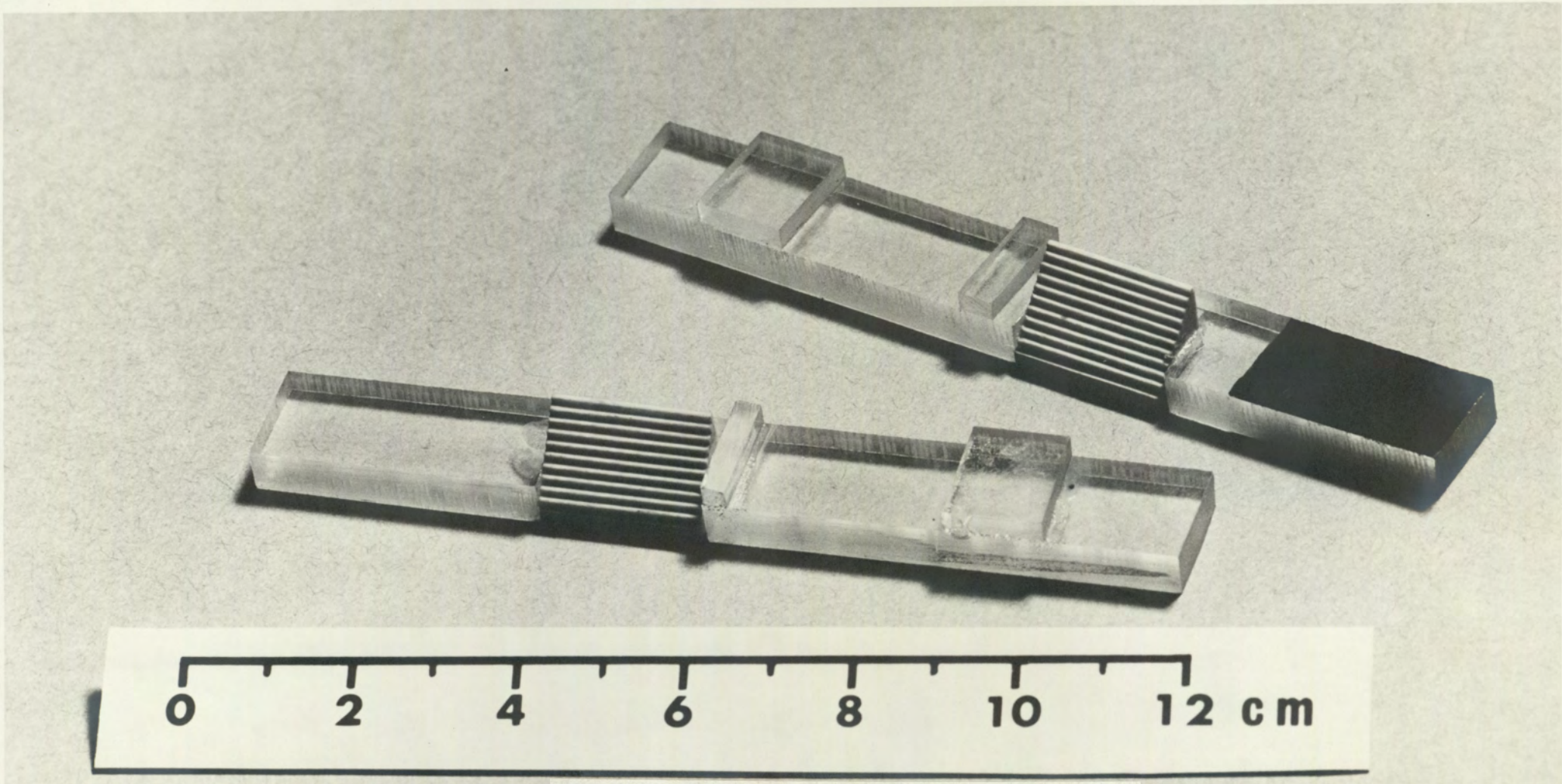

Fig.3.13. Photograph of the step wedges.

made from ivory having a density of 1.7 $10^3 kg\ m^{-3}$ and had a total width of 15mm. The steps were accurately cut so that with an initial step of height 3mm, each step was 1mm high and 1mm wide, the maximum step giving an X ray path of 13mm. The step wedge was cemented into a cut made in a strip of $\frac{1}{8}$ in. thick perspex which is also shown in Fig.3.13. Two smaller strips were cemented on top of the larger strip so that the step wedge could be accurately positioned in the scanning path by slotting the two small strips on either side of the ulnar styloid block. Perpendicularity of the steps to the motion of travel is ensured by pushing the step wedge until its supporting perspex strip abuts against the central edge of the hard fixing frame, with the 3mm step nearer the ulna.

3.3. The electronics

Introduction

To perform the electronic investigation of the photodiode currents in accordance with the theory given in Chapter 2, the integration was first carried out by amplifying the signal and using capacitive feedback. However, this method was found to be unsatisfactory due to DC thermal drift. A DC amplifier had to be used because of the low (100Hz) fundamental frequency of the signal.

By using an amplifier as the first stage, the high input resistance will vary with temperature. It will also generate electrical noise proportional to its resistance and this will be immediately amplified. Using high input resistances, any stray capacitance across the resistor will give an alternative path for the signals and this will become more serious the higher the value of resistance and the frequency of the signal. The stray capacitance will also lead to a phase change of the signal.

If the signal is fed into integrator circuit, shown schematically in Fig. 3.14, the following equations will be true if the gain of the amplifier is large.

Let V_o, V_1 and V_2 be the voltages at the positions of the integrator shown in the sketch and R and C be the values of resistance and capacitance respectively used in the integrator. Further, suppose the gain -A of amplifier be large.

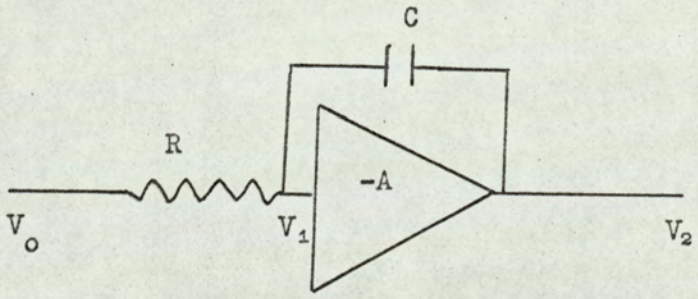

Fig. 3.14.

Then $$\frac{V_2 - V_1}{1/jw\,C} = \frac{V_1 - V_o}{R}$$

and $$V_2 = -AV_1 .$$

This gives

$$V_1 = \frac{V_o}{jwCRA}$$

and

$$V_2 = -\frac{V_o}{jwCR} .$$

The current i through C can also be written as

$$i = C\frac{d}{dt}(V_1 - V_2) \simeq -C\frac{dV_2}{dt}$$

so that $$V_2 = -\frac{1}{RC}\int V_o\, dt .$$

To approach ideal integration of the input signal V_o, large values of A,R and C are required so that the time constant ARC is very much larger than the time t over which V_o is integrated. The value of the output signal V_2 is inversely proportional to RC so that further amplification is necessary to obtain a result. This will add to the problems of thermal DC drift. It was found that a thermal drift was so bad that even when the electronics was allowed to stabilise for one hour there was still drift. This was despite the fact that high stability resistors and heat sinks for the transistors had been used.

These difficulties were met by first integrating and then amplifying the photodiode signals. This method, which was successfully developed, will be seen to have several important advantages.

A high quality capacitor generates no electrical noise and its fractional change in capacitance will be very small for small temperature variations. Furthermore, it may be obtained having a small physical size. From previous experiments it had been shown that the photodiode

current was about 10nA when the scintillation crystal was irradiated with X rays. If this current was fed into an input capacitance C the voltage developed would be $10^{-10}/C$ volts if the integration time was 10^{-2} second. The value of C was made 270 pF for reasons of integration and switching time constants which are discussed later. This means that the voltage change across the capacitor will be about 0.3 volt after an integration period.

When connected to the cathode of a photodiode (Fig. 3.15) having a driving anode potential of 90V with an effective impedance of $> 10^{11}\ \Omega$, the small potential developed across C would have a negligible effect on the photodiode current, assuming a constant light intensity falling on the photocathode.

The time constant associated with the photodiode tube and the integrator capacitor will be

$$\text{Time constant} = 10^{11} \cdot 270 \cdot 10^{-12}$$

$$= 27 \text{ seconds.}$$

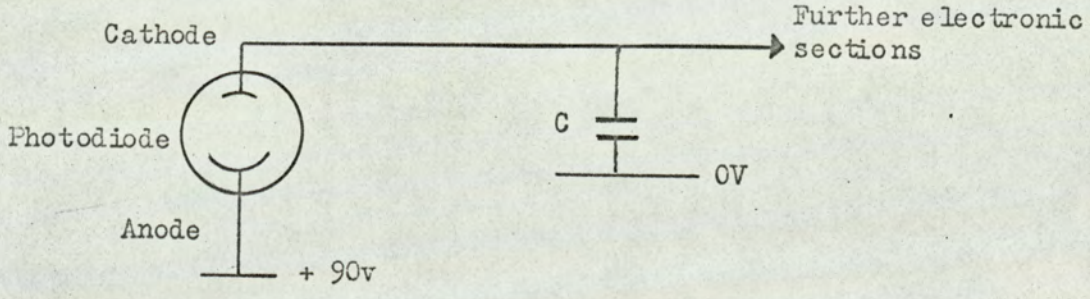

Fig. 3.15

To achieve this by the circuit shown in Fig.3.14, the time constant ARC must be equal to 27 seconds. If R = 100k Ω and A = 1000, C has to be 0.27 μF. The large value of RC will necessitate further amplification for reasons which were outlined previously.

When the idea of first amplifying the signal was attempted, the values of R,C and A were 100 k Ω , 3.3 nF and 1000 respectively, the value of C being chosen to give a useful output signal of about 10V. The product ARC has a time constant of 0.33 second, which is ninety times less than that of the photodiode and integrating capacitor. With an electronic switch placed in parallel with the capacitor, the time constant is $\geq$ 5.4 seconds, which is still about fifteen times better than what was previously achieved.

An additional advantage of integrating the signal first is that the effect of photodiode microphony will be reduced by a factor C_1/C

where C_1 = anode to cathode capacitance of the photodiode.

C = integrating capacitance.

C_1 was found to be 4pF so that if C = 270 pF the factor will be about 1/70 which is an important advantage in view of the very low photodiode currents.

Since we are only required to know the change in the DC level during an integration period, a large blocking capacitor may be used after integrating the signal provided that the lower frequency response of the following amplifier is satisfactory. Such a capacitor has been used and this virtually eliminates thermal DC drift problems, since only DC drift during an integration period ($\sim$ 5ms) will cause any error in the amplified output signal.

A schematic block diagram of the circuit is given in Fig. 3.16 and a full circuit diagram in Fig. 3.17. The important sections of the electronics are discussed and the appropriate diagram shown for clarity.

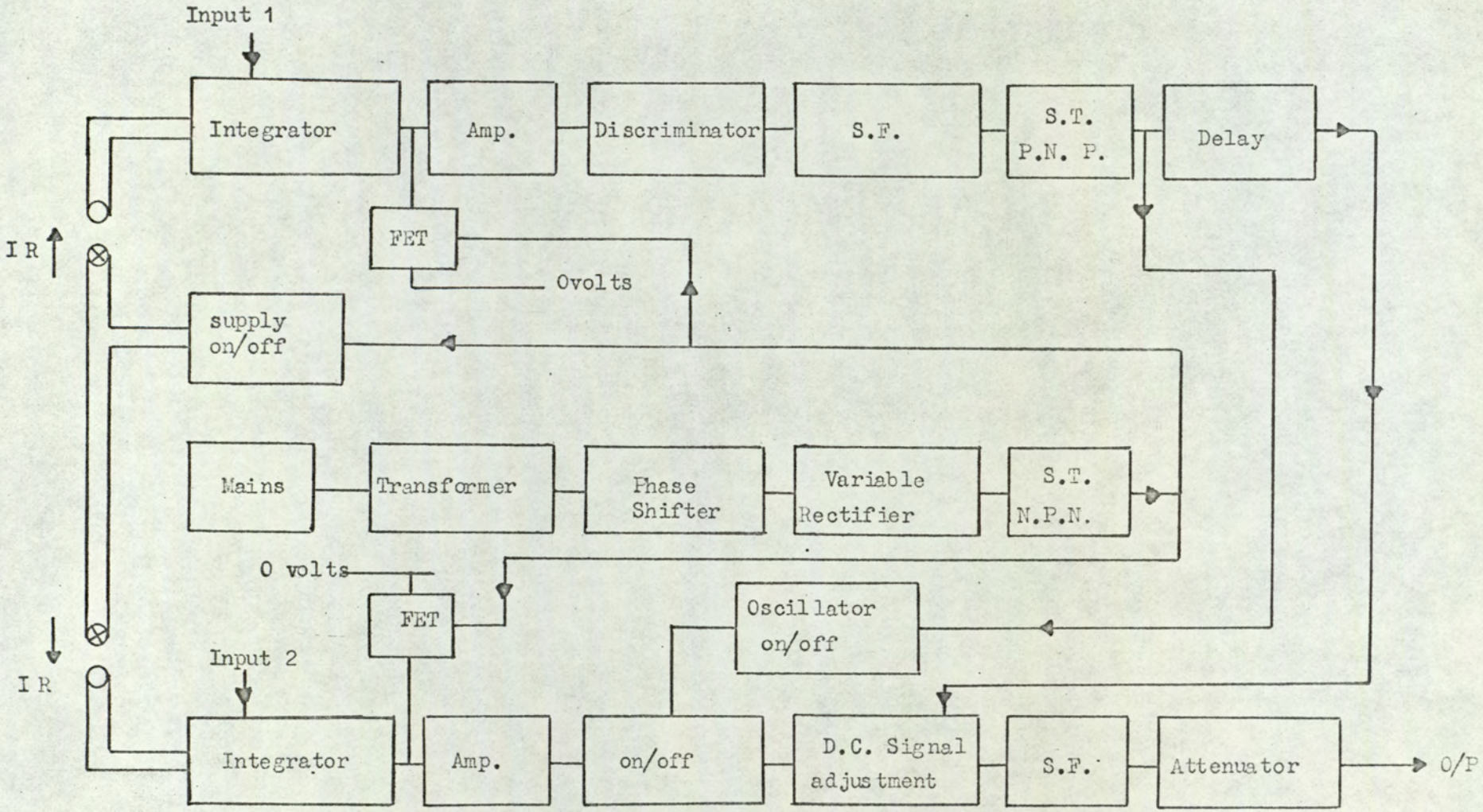

Fig. 3.16. Block diagram of the electronics.

⊗ Infra Red Transmitter

○ Infra Red Receiver

S.F. Source Follower

S.T. Schmitt trigger.

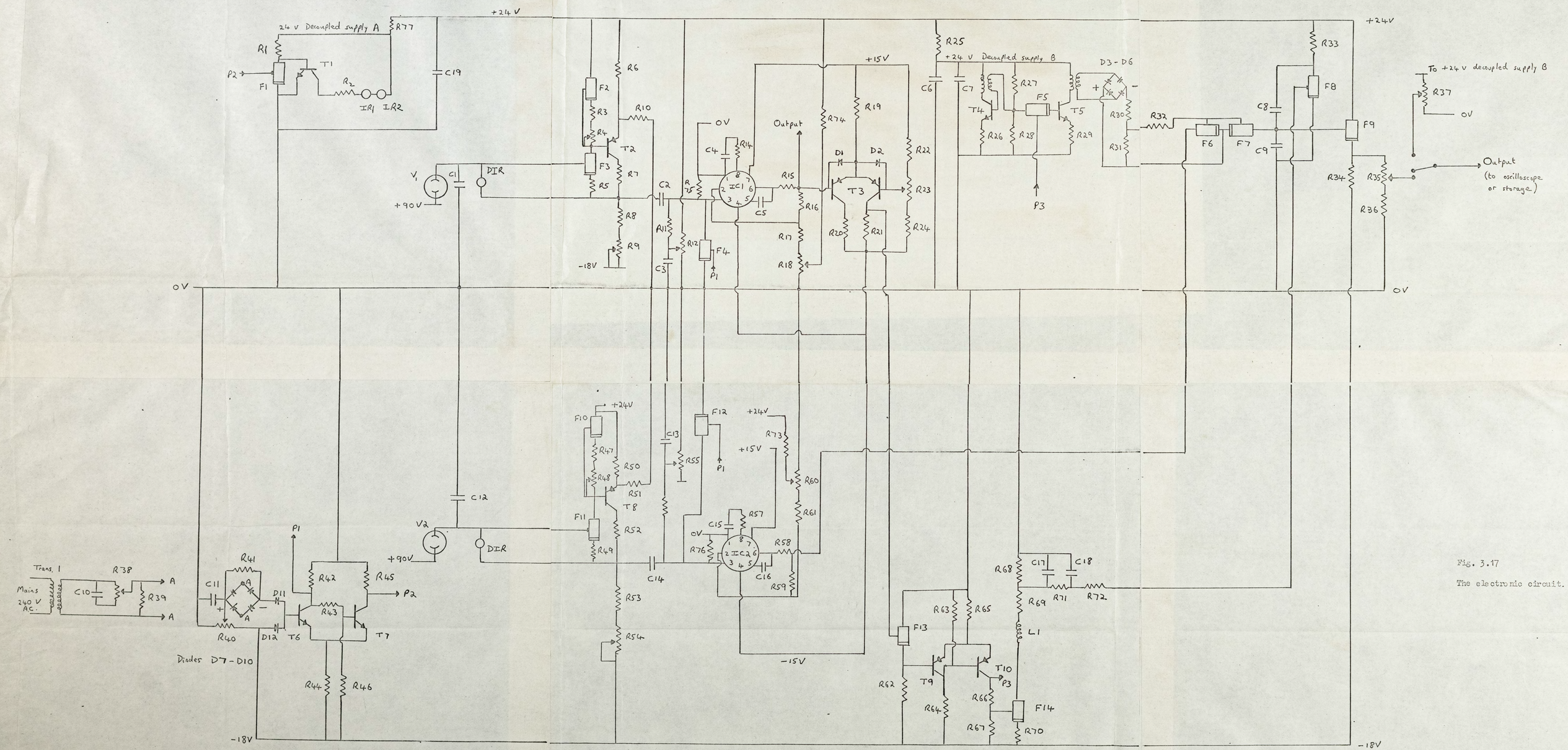

Fig. 3.17

The electronic circuit.

Fig.3.17

List of electronic components.

(a) Resistors and potentiometers.

R1	4.3k	R.28	10k
R2	50	R.29	1k
R3	220	R.30	330k
R4	10(variable)	R.31	560k
R5	280	R.32	100k
R6	180	R.33	4.7k
R7	10	R.34	22k
R8	5.6k	R.35	100k(potentiometer)
R9	2.0k(variable)	R.36	68k
R10	1.0k	R.37	5k(potentiometer)
R11	44M	R.38	5k(potentiometer)
R12	50k(potentiometer)	R.39	5k
R13	470k	R.40	10k(potentiometer)
R14	1.5k	R.41	56k
R15	47	R.42	4.7k
R16	4.7k	R.43	22k
R17	15	R.44	470
R18	10(potentiometer)	R.45	4.7k
R19	4.7k	R.46	10k
R20	4.7k	R.47	220
R21	4.7k	R.48	10(variable)
R22	820	R.49	280
R23	10k(potentiometer)	R.50	180
R24	22k	R.51	1k
R25	1k	R.52	10
R26	1k	R.53	5.6k
R27	43k	R.54	2.0k(variable)

Fig.3.17(Cont)

(a)

R.55	50k(potentiometer)	R.67	560
R.56	470k	R.68	5.6k
R57	1.5k	R.69	1k
R.58	47	R.70	220
R.59	4.7k	R.71	560k
R.60	10(potentiometer)	R.72	560k
R.61	15	R.73	1.5k
R.62	2.2k	R.74	1.5k
R.63	1k	R.75	1.5M
R.64	1.5k	R.76	1.5M
R.65	120	R.77	200
R.66	820		

(b) Capacitors.

C.1	270pF	C.11	1000μF
C.2	1μF	C.12	270pF
C.3	50μF	C.13	50μF
C.4	50pF	C.14	1μF
C.5	50pF	C.15	50pF
C.6	1000μF	C.16	50pF
C.7	0.1μF	C.17	5nF
C.8	5nF	C.18	5nF
C.9	8nF	C.19	1000μF
C.10	1μF		

(c) Inductances

L1 3mH

Fig.3.17(Cont)

(d) Bipolar transistors

T.1	BFX 98	T6.	2N2926
T.2	2N4062	T.7	2N2926
T.3	BFX 11	T.8	2N4062
T.4	BC 1842	T.9	V723
T.5	BC 184	T.10	V723

(e) Field effect transistors.

F.1	2N4859	F.8	2N4859
F.2	2N3821	F.9	3N139
F.3	2N3821	F.10	2N3821
F.4	2N4859	F.11	2N3821
F.5	2N4859	F.12	2N4859
F.6	2N4859	F.13	2N4859
F.7	2N4859	F.14	3N139

The FETs have been marked thus:-

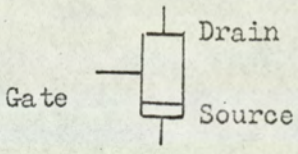

(f) Integrated circuits

IC1 μ709C

IC2 μ709C

(g) Diodes

D1 - D10 1GP7

D11,D12 DK 20STC

(h) Infra-red emitting diodes

IR1, IR2, ME 5A

(i) Infra-red switching diodes

DIR BPY 68

Fig.3.17(Cont)

(j) Photodiodes

V1 AV92

V2 Special photodiode(see text)

(k) Transformer

Trans 1 240V to 40V AC output

3.3.1. Detailed description of the electronics
The monitor and the detector.

The monitor.

After integration and amplification the positively increasing signal is passed into a dual transistor discriminator where it is compared with a preset voltage. When the signal is equal to the preset level, a positive pulse is sent from this stage through a source follower to activate a fast PNP Schmitt trigger. A positive rectangular pulse sent from the Schmitt trigger terminates the integration of the second detector by switching on an oscillator which supplies an earth free negative voltage to the gates of a pair of switching FETs. Simultaneously, the pulse from the Schmitt trigger passes through a 15 μs delay stage, after which time the constant DC level reached by the second detector after termination of integration is raised by a constant amount.

After every half cycle both the input and output of the integrator are shorted to reset the electronics for the next half cycle. This is done by an infra-red switch and a switching FET, activated by a signal derived from the mains supply.

The detector.

This possesses the same integration amplification and resetting stages as the monitor. Upon emerging from the amplifier the signal is presented to an FET switch which will only conduct the signal if the oscillator has not been triggered by the positive signal sent by the PNP Schmitt trigger. Upon receiving this pulse the voltage attained by the detector is raised by a constant amount and allowed to pass through a buffer source follower, The part of this last may then be stored or displayed on an oscilloscope.

3.3.2. The electronic resetting system

This has to reset the integrator and the amplifier at the end of each half cycle. To do this the inputs to these sections are shorted for a brief duration ($\sim$ 800 μ seconds) every half cycle of the mains supply.

When the electronic switching devices do not have to conduct, it is important that their conduction resistance is very high (> 10 MΩ) and what is more important, particularly in the case of the integrator stage, is that no current is allowed to leak into the proceeding stage by any voltage pulse which makes the electronic switch non conducting.

It was found when attempting to switch the integrator by using switching FETs that the gate source leak current was comparable to the photodiode current ($\simeq$ 1 $\wedge$ A). This was also true for MOS FETs. An infra-red switching system, consisting of a separate emitter and diode receiver was developed to act as a shorting switch for the integrator. For the amplifier, a switching FET was found to be satisfactory.

The IR switching system is shown in Fig. 3.18. The gate of F1 is connected to the first collector of the NPN Schmitt trigger, which when at -12V makes F1 non conducting. The base of T1 therefore goes positive causing the transistor to conduct and the IR emitters to emit radiation on to the duo diode receivers. The receivers then conduct, and short the integrator inputs.

The I.R. receiver.

The Mullard BPY 68 duo diode was chosen because of its very small size (9.5 mm long x 2.8 mm dia.) and its symmetrically diffused silicon construction enables it to operate with either positive or negative bias. Its spectral response, having a peak at 820 nm and a half maximum response width of 340 nm(640-950 nm);

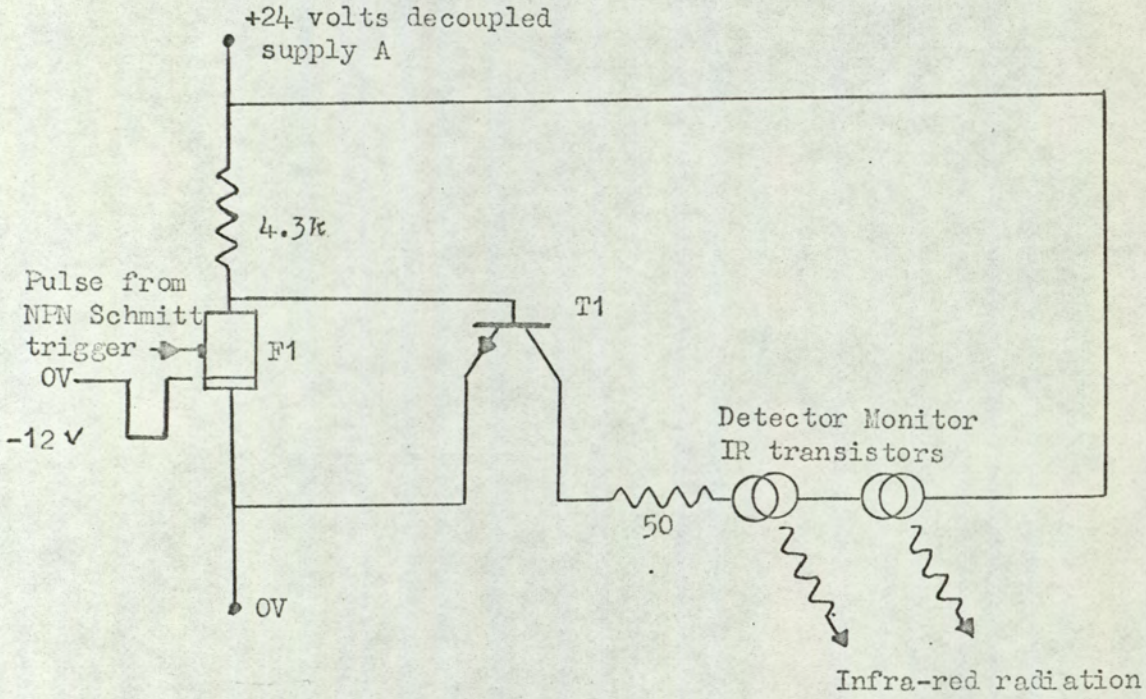

F1 2N4859
T1 BFX 98

ME 5A I.R. Transistors

Fig.3.18 The infra-red transmitter circuit.

ideally matched to that of the emitter.

The diodes were tested for their symmetrical conduction at all the bias voltages (~ 0.2 volt) at which it would operate in the integrator across the capacitor and found to have a conduction resistance of ~ 0.9 k Ω. It was also essential to know the resistance of the duo-diode in its non conducting state as this forms the input resistance of the integrator and therefore its value is directly related to the input impedance of the device. The non conducting state was investigated with a sensitive galvonometer with a $1\frac{1}{2}$ volt battery bias. No current was observed, but a lower limit of $\frac{1}{3}$ μ A was taken giving an effective resistance R of $R \geq 50$ M Ω.

Of equal importance is the capacitances of the duo-diode. The device has two capacitances lead to lead and body to lead. The first capacitance is in parallel with the instantaneous resistance of the device and the second is in parallel with the 270 pF integrating capacitor. Of the two the first is the more important as it represents a shunting path for signals across the non-conducting diode and therefore limits the high frequency response of the incoming signal. This capacitance was found to be 7 pF which means that at 500 Hz the input impedance is halved, assuming R = 50 M Ω.

The second capacitance increases the integrating capacitance and will merely increase the time constant by a small amount. It was found that the body-lead capacitance was about 2.5 pF, which represents an increase in integration capacitance of about 1%.

The I.R. emitters.

These are Monzonto ME 5A gallium arsenide diodes which emits infra-red radiation at a peak of 900 nm with a spectral half width of 40 nm. The two emitters are connected in series as shown in Fig. 3.18.

3.3.3. The integrators

This is situated in the dural boxes adjacent to the photodiodes. The circuit is shown in Fig. 3.20.

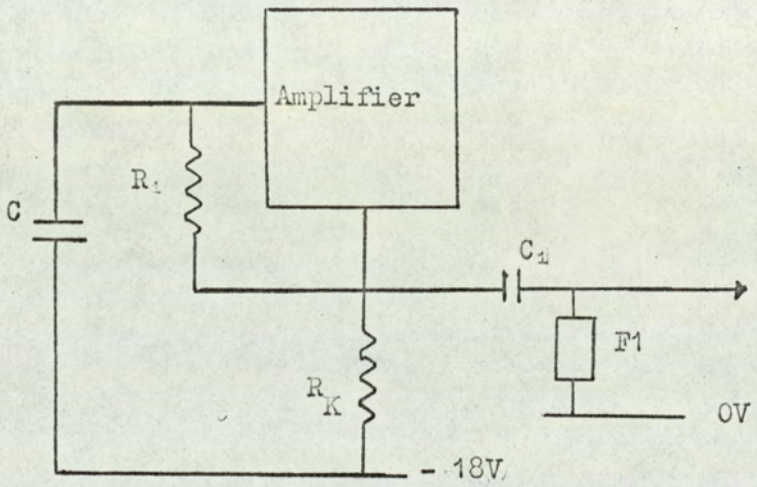

FIG. 3.19

R_1 = resistance of infra red diode when conducting ($\simeq 1 k\Omega$)

R_2 = resistance of F1 when conducting (20Ω)

R_K = biasing resistor ($18 k\Omega$)

C = integrating capacitor (270pF)

C_1 = blocking capacitor for the following amplifying stage ($1\mu F$).

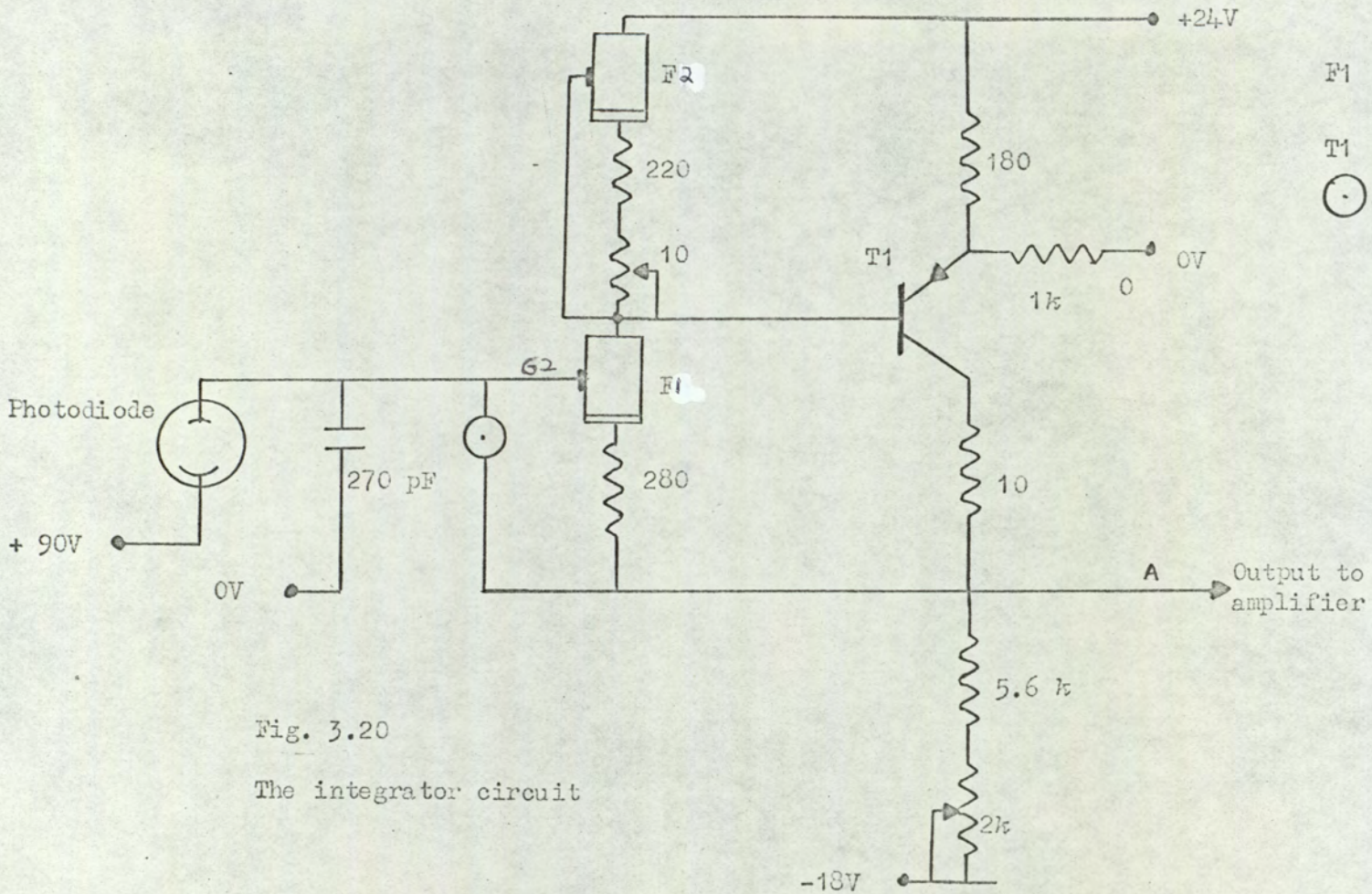

Fig. 3.20

The integrator circuit

The lower FET F1 acts in the normal amplifier mode with the top FET F2 as a voltage controlled drain resistor for F1. On emerging from the drain of F1 the negative siganl is passed into the base of the high gain transistor T1. From the point of view of an earthed input signal on the gate of F1, the transistor behaves as an emitter follower having a unity gain if the 10 Ω resistor is shorted

$$\text{i.e.} \quad \frac{\text{Output signal across A0}}{\text{Input signal across G20}} = 1$$

(10 Ω resistor shorted)

However, if an earth-free input signal is placed between G_2 and A the output signal gain across A0 without the 270pF and 10 Ω is a little over 10^3. Inclusion of the 10 Ω collector resistor lowers the gain to 400 but has the advantage of increasing the stability of the device. The currents travelling through F2 and the base of T1 were made about equal to a large range of operation of F2 and T1. The source resistance of F2 was made 220 Ω in series with variable 10 Ω which could be adjusted with a screwdriver through the lead roof of the dural housing. Its purpose was to adjust the bias of F2 and the DC level of the output point A.

The input impedence of the integrator stage will be $\geq 2.10^{10}$ Ω if the gain of device is 400 and the non conducting resistance of the duo diode is ≥ 50 MΩ. The integration time constant must be much longer than duration of electrical integration ($\simeq$ 5ms) and will be

$$\text{Integration time constant} = 270.10^{-12} . 2.10^{10}$$

$$= 5.4 \text{ s}$$

Conversely the resetting time constant of the input capacitor and the duo diode must be much shorter than the resetting time every

half cycle ($\simeq$ 800μs). If the conduction resistance of the duo diode is 1 kΩ then

$$\text{Resetting time constant} = 270.10^{-12} . 10^{3} \text{ s}$$

$$= 270 \text{ n s}$$

i.e. the resetting time is about 3000 times greater than the 270 n s time constant. This will ensure that there is absolutely no charge remaining in the capacitor.

The resetting time constant will only be as quoted if the intrinsic gain of the two FETs and the one junction transistor, which are in the integrator circuit, is made zero by shorting the output. This has been done with the switching FET F1 which is shown in the equivalentcircuit of Fig. 3.19.
The input impedance of the amplifier with R_1 if the output is not shorted will be

$$1000 (1 + G^{*}R_K)$$

where G^{*} is transconductance of the output transistor ($\sim$30 mmhos)

Hence input impedance 500kΩ , so that the resetting time constant t_c would be 135 μs, so that the resetting time is only six times greater than the 135 μs time constant.

The emitter of the transistor is biased by two high stability resistors between the +24V supply and earth. To ensure thermal stability each of the emitter resistors were mounted in small copper blocks into which had been drilled a central hole of sufficient diameter to admit the body of the resistor together with a thin insulating PVC cover. It was realised that the PVC cover would have a detrimental effect on the thermal conductivity, but it was felt that sufficient confidence could not be placed in the electrical insulating properties of the body of the resistance. Furthermore, if a short did occur to the earthed copper blocks, it would mean the likely destruction of the

transistor and a lengthy repair procedure to re-establish the correct D.C. bias for each component.

To minimise the effects of temperature variations the two metal capped FETs were mounted in a single copper block which was secured into contact with the antimonial lead roof of the housing. With this arrangement, no evidence of thermal drift found after the power supply had been switched on for a few minutes. By coupling the output of the integrator to the following amplifier stage by a large capacitor, any drift will have a negligible effect on the amplifier because only change in potential during the integration time (about 5ms) will effect the amplified signal.

3.3.4. The amplifiers.

Upon emerging from the integrators the positive signals are about 0.05 volt and therefore a gain of about 200 is required to obtain a reasonably sized output signal. To keep the physical dimensions of the amplifiers to a minimum, an integrated circuit (SGSμ709C) amplifier was chosen. This has an open loop voltage gain of about 45,000, but with the recommended feedback loop it may be reduced to any desired level. Using the recommended 50kΩ potentiometer in the feedback loop only allows the stable quiescent output voltage to be set at $\pm$ 1V within its $\pm$13V range. This was regarded as unsatisfactory because the signal from the integrator would always be positive so that only half of the operational range would be used. By biasing the inverting signal of the amplifier with a D.C. series feedback system the quiescent output voltage could be set by R_1 at any value within the operational range (Fig.3.21a). The full 26V range of the amplifier may therefore be used with the additional advantage that in the case of the monitor amplifier, the DC level of the signal may be

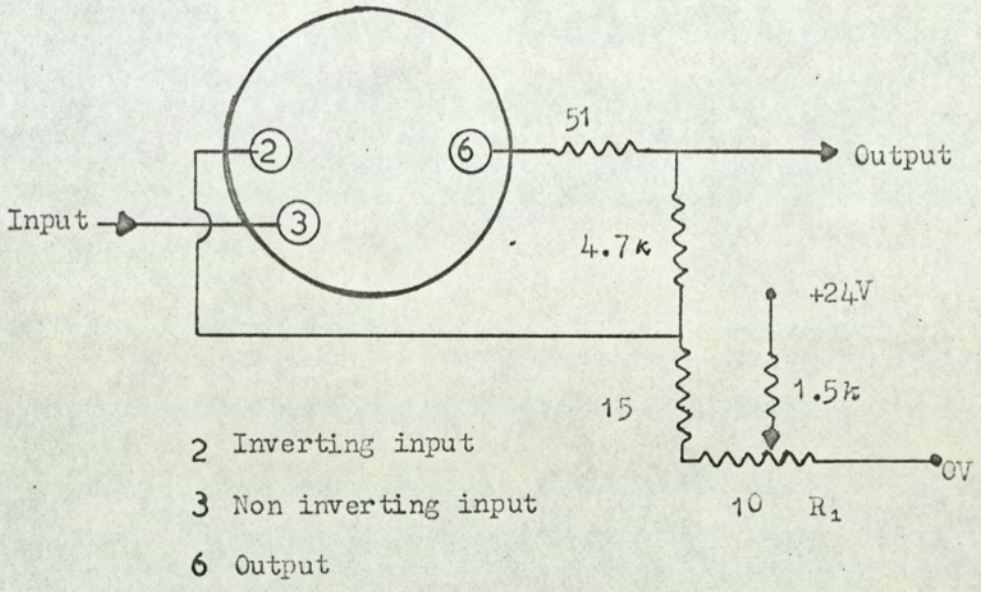

Fig. 3.21 (a) The external bias arrangement for the μ 709 amplifier.

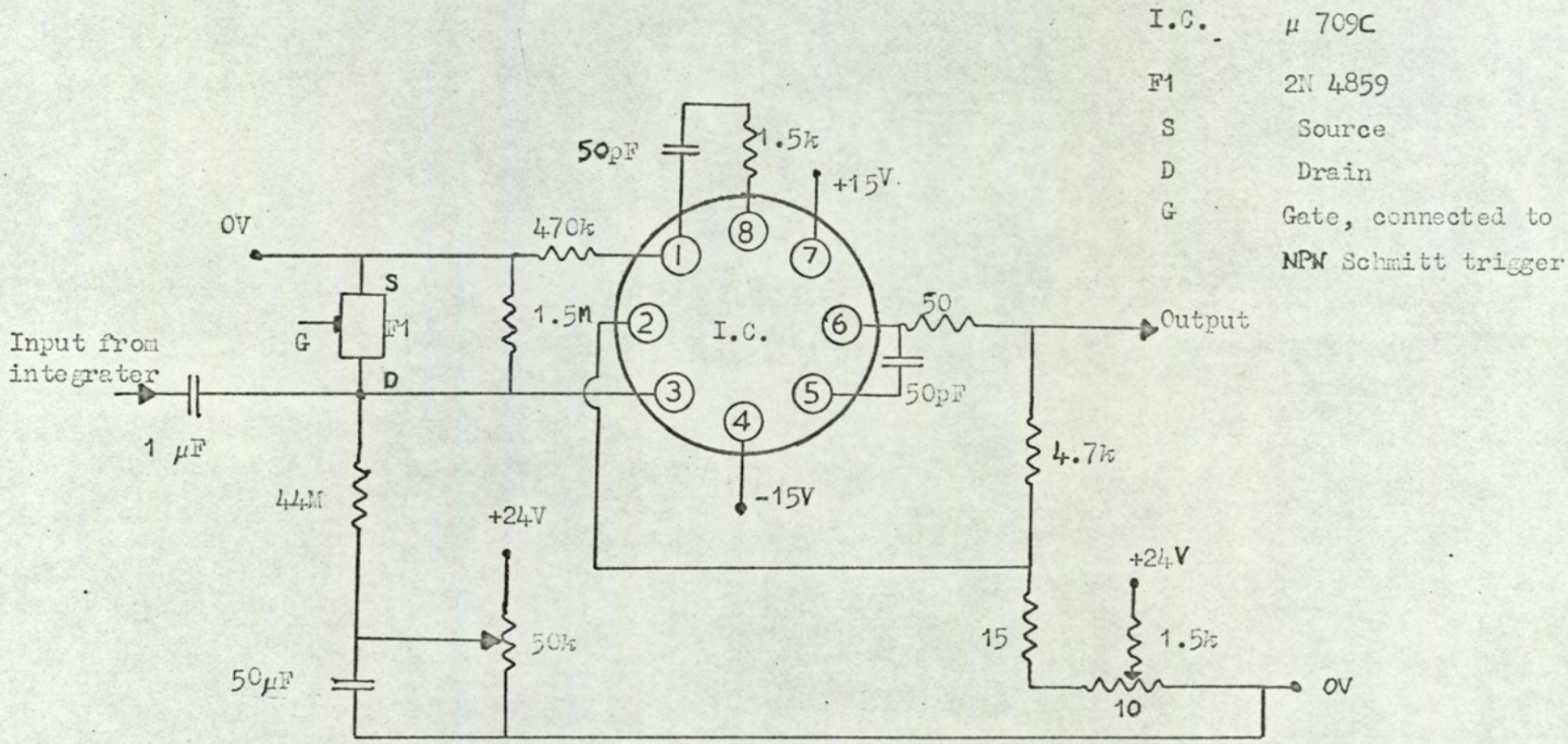

Fig.3.21 (b) The complete integrated circuit amplifier

raised or lowered. This will terminate the integration of the second detector signal sooner or later in the half cycle and so effectively extend the range of the discriminator.

The positive signal from the integrator is fed into the non inverting input of the amplifier via a high quality 1μF capacitor, Fig. 3.21b. To establish a DC level at the input a 1.5 MΩ resistor was fixed from this junction to ground. Without this resistance this quiescent voltage is not established and the amplifier will not operate. After every half cycle the input of the amplifier is shorted by the switching FET F1 upon receiving a positive signal 0V, from the second collector of the NPN Schmitt trigger. The conduction resistance of this device (when the gate to source voltage V_{gs} = 0) is only 20Ω, and gives a time constant of 20μs with the capacitor which is sufficiently small to ensure complete discharge in 800μs for which the FET operates in the conduction mode. The insulating resistance of the FET when V_{gs} = -10V is about 10^{10} Ω and therefore the drain-source conduction is negligible compared with the 1.5 MΩ resistor. When V_{gs} = -10V there is a gate to source leak in the FET which is proportional to V_{gs} and appears at the input of the amplifier. To offset this a very small current is fed into the input by a potentiometer so that with careful adjustment a null point could be obtained.

The time constant of input is 1.5s which is much larger than the integration time ($\simeq$5ms) every half cycle. With the value of components used the lower frequency limit is 0.2Hz. The upper frequency response is limited by stray capacitance and the characteristics of the integrated circuit amplifier. The voltage gain falls by 3dB at $\sim$500kHz. The wide bandwidth of the amplifier

will ensure that the signals with a fundamental frequency is 100Hz will be amplified with very little distortion.

3.3.5. The discriminator.

The discriminator, which is shown in Fig. 3.22, gives a positive output pulse when the value of the rising signal G_1 from the monitor amplifier reaches a preset value, which is determined by a potentiometer. This pulse operates the PNP Schmitt trigger in order to hold and display the instantaneous value of the signal G_2 from the detector amplifier. It is important, in order that the electronic system shall operate in accordance with the theory, that the discriminator performs rapidly and precisely. For this reason the discriminator is based on a dual PNP transistor in a single case, and high stability resistors have been used in the circuitry to give reliable action which is almost independent of temperature variation.

It is seen from Fig.3.22 that the bases of both transistors may be driven over a large voltage range. To prevent the bases going positive of the emitter a diode was added between the base and the emitter of each transistor to short the emitter-base junction should an attempt be made to drive the base to positive. The current through the transistor when conducting was made about 5mA to obtain a fast ($< 1\mu s$) positive output pulse when the discriminator is triggered. The pulse is fed into a source follower which acts as a buffer stage between the discriminator and the PNP Schmitt trigger.

3.3.6. The resetting pulse generator.

The two integrators and amplifiers are reset at the end of every half cycle from a rectified pulse derived from the mains supply. In view of the separate HT supply with the large power transformer needed to drive the X ray generator, it is important

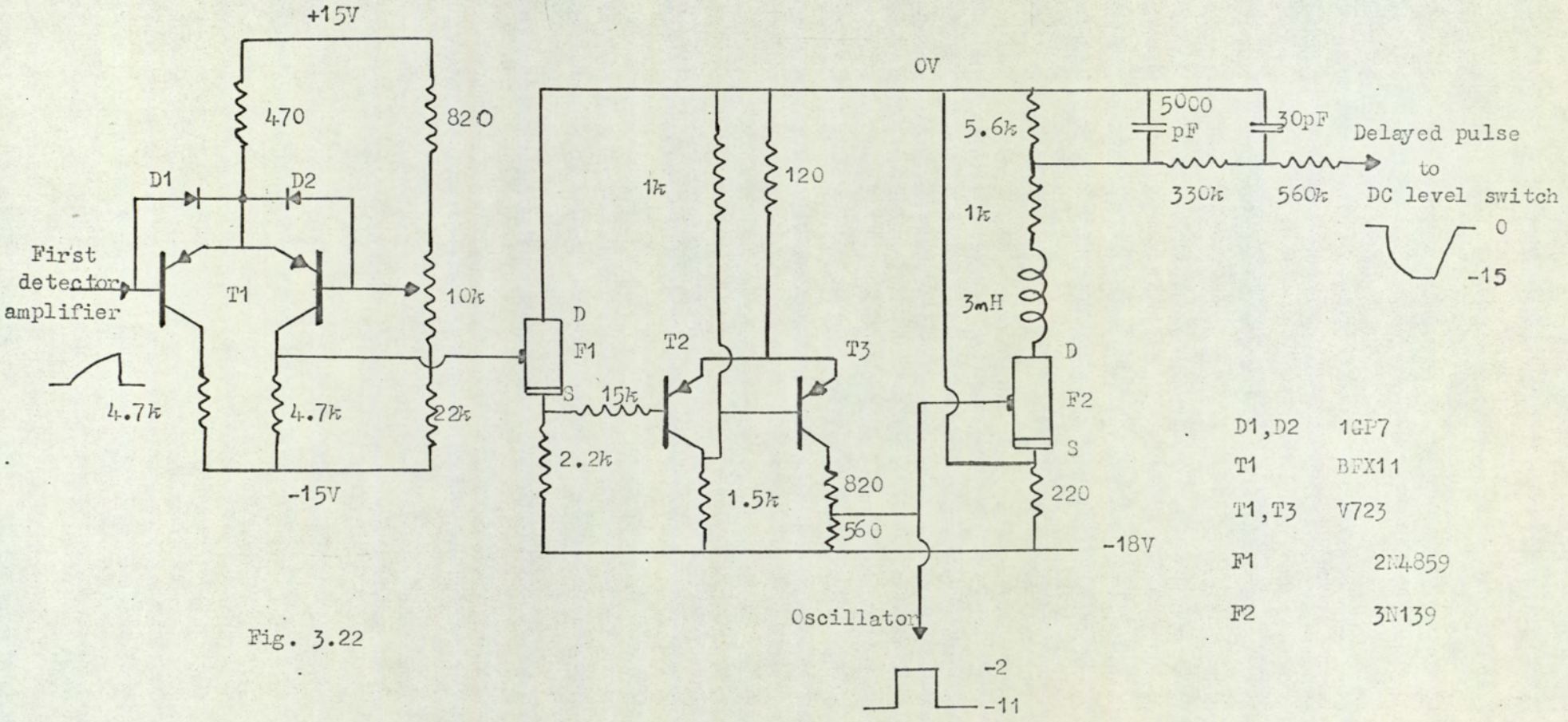

D1,D2	1GP7
T1	BFX11
T1,T3	V723
F1	2N4859
F2	3N139

Fig. 3.22

The discriminator, PNP Schmitt trigger and time delay circuits

that the resetting pulse be in phase with the minimum anode voltage of the generator. A phase shifting circuit was built so that the phase of the mains supply could be altered to trigger an NPN Schmitt trigger so that the pulse derived from this stage would reset the electronics at the correct time. The circuit is illustrated in Fig. 3.23.

A small 5:1 step-down transformer receives the mains supply and the 35V output across AA' is fed into a phase shifter consisting of a capacitor and potentiometer in parallel. The waveform at BB' is the same as that at AA' but with the phase capable of being changed up to ±45°. This waveform is then full-wave rectified and fed into a load resistor to give a mean DC voltage of 30V. The positive terminal of the rectifying bridge is connected to the mid point of a potentiometer whose ends are fixed, to the 0V and -18V DC supplies. A large capacitor across point C to ground ensures that AC signals at C are shorted but that the DC level of this point can be adjusted between 0 and -18V. Taking the signal from the negative terminal of the rectifying bridge inverts the waveform so that when the anode voltage on the X ray tube is a minimum the potential of D is rising so that it will correctly switch the NPN Schmitt trigger.

A positive going signal is allowed to conduct through diode D_1 to the input of the Schmitt trigger whilst diode D_2 presents the first input transistor base being driven more negative than -18V to safeguard the transistor. The duration of the triggering pulse fed to the Schmitt trigger is altered by adjusting the potentiometer at C which will raise or lower the DC level of the whole inverted pulse at D. Due to the poor conduction of the diodes at low forward voltages, the input pulse to the Schmitt trigger is trapezoidal in shape. The length of the flat top represents the

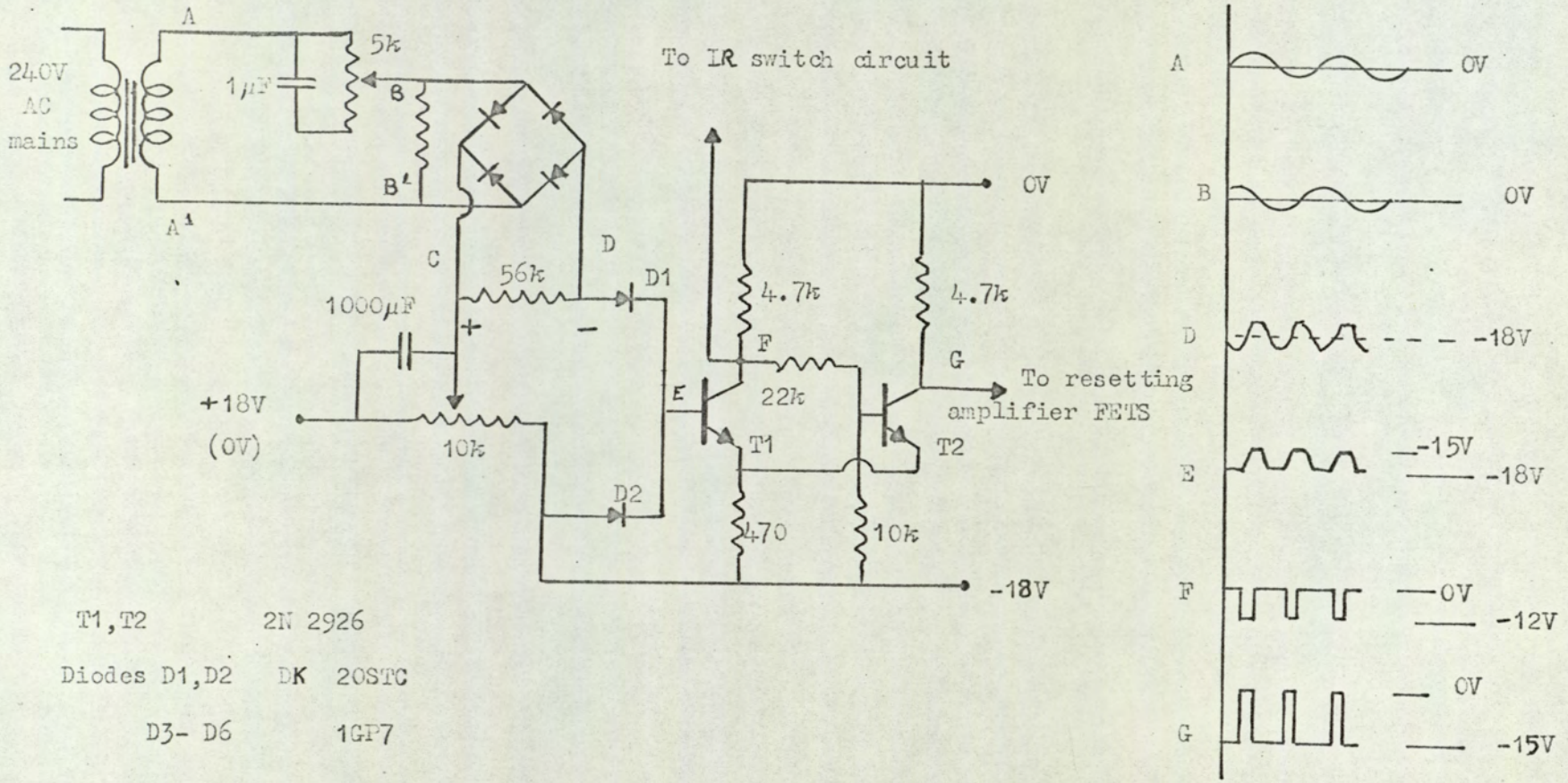

T1, T2 2N 2926

Diodes D1, D2 DK 20STC

D3- D6 1GP7

Fig. 3.23 The resetting pulse generator and NTN Schmitt trigger circuits.

minimum time for which the electronics may be reset and this was found to be about 500μs which is equivalent to about 10° in the cycle. The resetting time was $\simeq$ 830μs ($\equiv$ 15°) which ensures that the resetting operation is sufficient and that the integrator and amplifier have been completely discharged (the time constants of the infra-red and FET switches are 0.27 and 2.5μs respectively).

The positive resetting pulse (0V) from the NPN Schmitt trigger output has fast rise and fall times (< 1 μs) and a pulse height of 15V to ensure equally fast operation of the resetting electronics.

3.3.7. The PNP Schmitt Trigger and delay circuits.

Upon receiving a positive pulse from the preceding source follower, the PNP Schmitt trigger sends a large fast positive rectangular pulse to delay circuit and the oscillator (Figs.3.22 and 3.24). This causes the oscillator to operate and generate an earth free DC voltage which effectively terminates the integration of the second detector. The rectangular pulse, after a 15μs delay, raises the voltage attained by the second detector by a constant amount to give greater clarity to the oscilloscope trace. This procedure avoids the display of the integration process and only produces a short horizontal line on the oscilloscope screen which corresponds to the value of G_2 after the integration has been terminated. The length of the line is terminated when the electronics is reset to allow another integration. When the oscilloscope is used in its (x-y) mode the horizontal line appears as a dot having the same y deflection but whose x ordinate is proportional to the relative positions of the X ray beam and limb.

A large current (9mA) passes through the conducting transistors in the Schmitt trigger to obtain fast leading pulses (< 0.5μs). The delay circuit is necessary because if an attempt

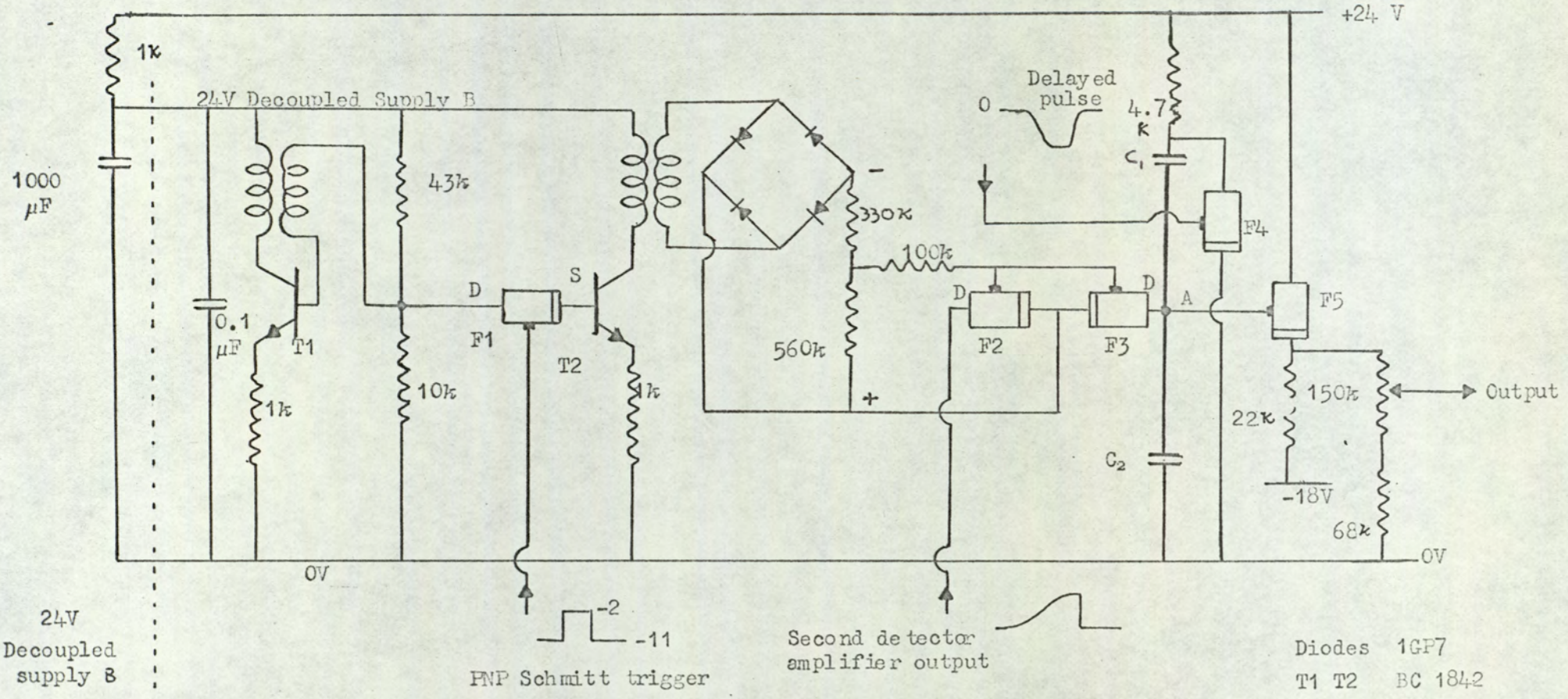

Diodes	1GP7
T1 T2	BC 1842
F1-F4	2N4859
F5	BN 139
C_1	3nF
C_2	5nF

Fig.3.24 The oscillator, terminal integration switch and and DC level adjustment switch.

is made simultaneously to terminate the detector integration and adjust the attained DC voltage level, the output is rendered unstable. The delay introduced by the circuit, as measured from the time of integration to the adjustment of the DC level of the signal is 15μs which is sufficient to ensure stability of the output signal. That is the displacement voltage, or throw out signal, is only applied to the F.E.T. after the sample and hold process is complete.

The Oscillator

This is required to provide an earth-free DC voltage for the switch which terminates the integration of the second detector, and is located in a separate housing to minimise interference. The circuit is shown in Fig. 3.24. This oscillator consists of a tuned 1MHz transformer which drives a second transformer oscillator via a switching FET F1 and the transistor T2. A signal will only be received on the base of T2 provided that F1 is in its conducting mode. This will depend upon V_{GS}, the signal on the gate of F1, which it derived from the PNP Schmitt trigger. A point worthy of mention is the way in which the FET is connected into the circuit.

The DC voltage of the drain is about 3.4 volts and when conducting there is only a small voltage drop across F1, so the source may be considered at the same potential as the drain. The pulse sent by the PNP Schmitt trigger varies between -2 and -11 volts so that in the conduction mode V_{GS} = - 5.3V. This negative bias does not seriously impair the conduction performance of the FET, as about V_{GS} = -10V is required to make itnon-conducting.

A full wave rectifying bridge was connected to the output of the oscillator. Initially a 1MΩ resistor was used as a load, but this was altered to a (560 + 330)kΩ potentiometer bridge load as the voltage across the 1MΩ was about 24V and which would damage the FET. By taking the signal across the 560kΩ the potential was found about 13.5V which is ample to switch the FETs in the terminal integration switch.

3.3.8. Terminal integration switch.

Previous experience had shown that difficulties had arisen when trying to terminate the detector integration by switching the HT supply, due mainly to capacitive effects and reverse current in the photodiode. These difficulties were overcome by employing a simple FET switch to isolate the detector amplifier output from the DC adjusting switch. The circuit is shown in Fig. 3.24.

There are three requirements for the FETs F2, F3.

(1) The drain-source resistance in the non-conducting state must be as large as possible.

(2) The conduction resistance must be as small as possible, and

(3) Gate current leak must be negligible.

The FETs chosen were the Texas 2N4859 with the following characteristics.

Gate leak at V_{GS} = -15V = 0.2 nA

Conduction resistance, V_{GS} = 0V = 25Ω

Non conducting resistance, V_{DS} = 15V, V_{GS} =-10V, $\simeq 3.10^{10}$ Ω

From the AC point of view the two capacitors C_1 and C_2 in the DC level switch are in parallel, together with the instantaneous resistance of the FETS F2 and F3. The two time constants associated with the non conducting and conducting resistances of

F2 and F3 must be long and short respectively compared with the integration time ($\simeq$5ms). With the component values chosen, the two time constants τ_{OFF} and τ_{ON} are

$$\tau_{ON} = 400 \text{ ns}$$

$$\tau_{OFF} = 480 \text{ s}$$

which satisfies the requirements.

It was found that the switching FET 2N4859 conducts equally well in both directions, so that the resistance of the back to back configeration may be taken to be twice the drain-source resistance of a single FET. The voltage signal applied to the gate and source has to be earth free in view of the varying DC level of the conducting switch. To terminate the second detector integration, a rectified DC signal of -13 volts, generated by the second oscillator pair coils is fed directly to the two gates and sources of F2 and F3. This makes F2 and F3 non conducting and isolates the second detector amplifier from the proceeding stages. To ensure the fast operation of this switch, which must cut off before the voltage level of the second detector is raised, the leads from the oscillator to the switch were made as short as possible.

The gate-source leak current in F2 and F3 may be neglected since this current ($\sim$ 0.1 nA) will be negligible compared with the current in the rectifier load of the oscillator ($\sim$10μA). However, the current must be considered in the operation of the DC level switch.

3.3.9. <u>The DC level switch</u>

The purpose of this device is to raise the DC level of the amplified second detector signal by a constant amount after the integration has been terminated so that the voltage signal appears as a dot on the oscilloscope screen when used in the

(x,y) mode. The circuit is shown in Fig. 3.24.

After the second detector integration has been terminated, a negative pulse from the delay circuit is applied to the gate of F4 making it non conducting. This raises the potential of C_1 from 0V to 24V and the junction of the two capacitors by $24\left(\frac{C_1}{C_1+C_2}\right)$ volts.

Three points of interest arise :-

(1) The effect of the non infinite off resistance of the FETs F2 - F3,

(2) The time constant of the DC level switch,

(3) The final potential of A.

Due to the non-infinite resistance of F2 and F3 in their non conducting state, a small current will flow through these FETs in a direction dependent upon the drain to drain voltage. This will cause the capacitors C_1 and C_2 to gain or lose charge and so the smaller the capacitances of C_1 and C_2 the greater effect will be a current through F2 and F3. However, the time constant associated with the adjustment of the DC level of the integrated signal, $4.7k\Omega \times (C_1 + C_2)$ must be much smaller than the integration time ($\simeq 5ms$). The values of capacitances chosen were $C_1 = 3$ nF and $C_2 = 5$ nF. A current of 1 nA for a duration of 5ms will therefore disturb the voltage at A by $625\mu V$, which is negligible.

The time constant associated with this stage, $4.7k\Omega \times (C_1 + C_2)$ seconds, need not be very short (say $< 1\mu s$) as the integration has been terminated and the DC level will not be adjusted again for about 10ms. This allows a limited flexibility in the choice of C_1, C_2 and R. With the values chosen the time constant is $35\mu s$.

The voltage by which the point A is raised when F4 is made non conducting has already been mentioned, but by measuring

this, a very effective check can be made as to whether the delay of the pulse sent by the PNP Schmitt trigger is sufficient. If it is not, then the signal at A will be raised before or during the termination of the integration and an examination of this signal on an oscilloscope will show it to be unstable.

To ensure minimal loading of the DC level switch a source follower was added after to this switch. In view of the wide range of potential which point A can take the FET F5 must give a linear output over both positive and negative gate potentials. The FET chosen was RCA 3N139 MOS FET which operates both in the enhancement and depletion modes.

The final stage of the circuit is an adjustable attenuator which permits the attenuation of the output signal up to 60%. It was included in the circuit because oscilloscope used (Telequipment D52) has a preset y amplification in the ratio 1,2,5 over the range 1.0. 10^{-2} to 50V cm^{-1}, and therefore a signal could be too large for one scale and only cover about half the screen on the next.

3.3.10. The voltage supplies.

(a) The Constant Voltage Transformer.

This is fed from the mains supply and gives a stabilised output of 240V AC to the two DC power supplies. The transformer chosen was the Advance CV150A which has a maximum output capacity of 150W and gives a stabilised output within ± 1% for an input variation of ± 15%.

(b) The ± 15V supply.

A Farnell A15 stabilised power unit was chosen and has a twin output supply, the output being connected in series to give a positive and negative output with respect to their common zero connection. The output voltage of either supply can be varied by means of preset potentiometers

(b) Cont...

between 12 and 17V at a maximum current of 100mA. For a 10% AC input variation the ripple voltage is less than 5mV peak to peak at full load.

(c) The +24V and -18V supply.

These DC voltage supplies is given by a Farnell STB power supply. It has a twin output supply (0 - 30V) and gives a stabilised output (± 0.05%) at a maximum load of 1A.

(d) 90V supply.

In the theory the photodiode current is taken to be proportional to the instantaneous total detected X ray energy and because of this importance was attached to the stability of this supply even though the current would be small and the photodiode driven well into saturation.

The circuit is shown in Fig. 3.25.

The stabilised mains supply was fed into a transformer to give an output of about 100V AC. To overcome an assymmetric ripple after rectification due to the distorted but high stabilised waveform of the CV150A transformer, the capacitor C_1 was added before the waveform was rectified. The last two smoothing components R_4 and C_6 were added inside the two detector boxes to reduce possible interference in the supply cables in the path from underneath the densitometer chassis to the photodiodes.

The final DC level is 89V and for a continuous current drain of 10 nA the ripple has been calculated to be 10 nV, which is negligible.

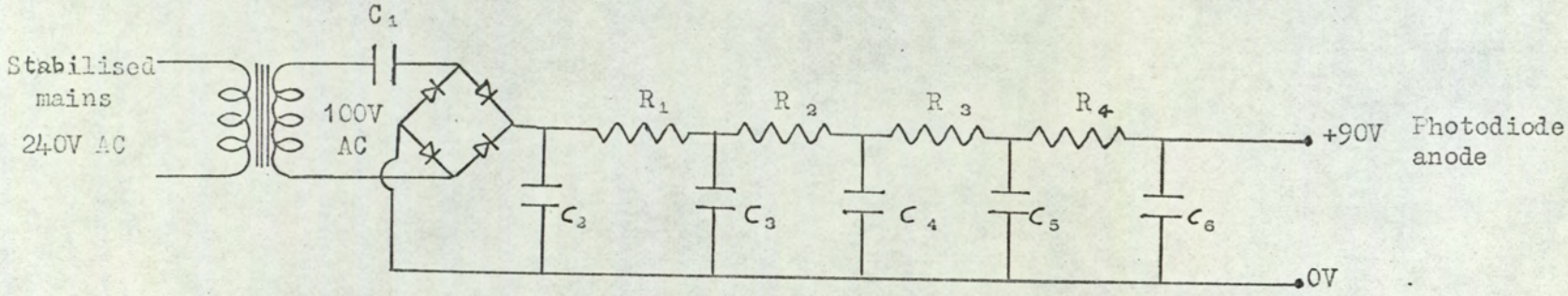

Diodes RS AS1

C_1	2μF	R_1	1.8k
C_2	32μF	R_2	5k
C_3	32μF	R_3	5k
C_4	12μF	R_4	2.2k
C_5	12μF		
C_6	0.1μF		

Fig. 3.25 The 90V supply circuit.

Chapter IV

Experimental procedures.

4.1. Investigations of beam current and X ray intensity waveforms.

4.1.1. Current waveform investigations.

In Chapter VI it is assumed that the beam current is constant with a value given by the control indicator. This current is derived from the passage of a large current (~5A) through a tungsten filament at the cathode. Usually this current is taken from a separate transformer whose output voltage is stabilised [141]. A photograph of an X ray tube assembly is shown in Fig. 4.1. whilst 4.2. shows detail of the tungsten filaments in relation to the tungsten anode target.

It was thought worth while to test experimentally the constancy of the beam current but to do so directly would mean measuring the current at very high potentials. Alternatively, the current in the primary of the filament transformer could be measured but this would entail interconnections with the equipment immersed in the insulating oil tank. The most convenient method was to detect any change in magnetic flux associated with the beam current by placing a toroid transformer around the cable carrying this current. The coil used (Fig. 4.3a) had a large internal diameter of 100 mm which enabled it to be fitted over the thick high voltage cables connected to the X ray tube head.

To detect the small induced voltages (which were found to be $\simeq 100\mu V$ when the beam current $\simeq 50mA$) it was found that additional amplification besides the oscilloscope was necessary. A low frequency AC amplifier with a gain of about 100 was found to be satisfactory.

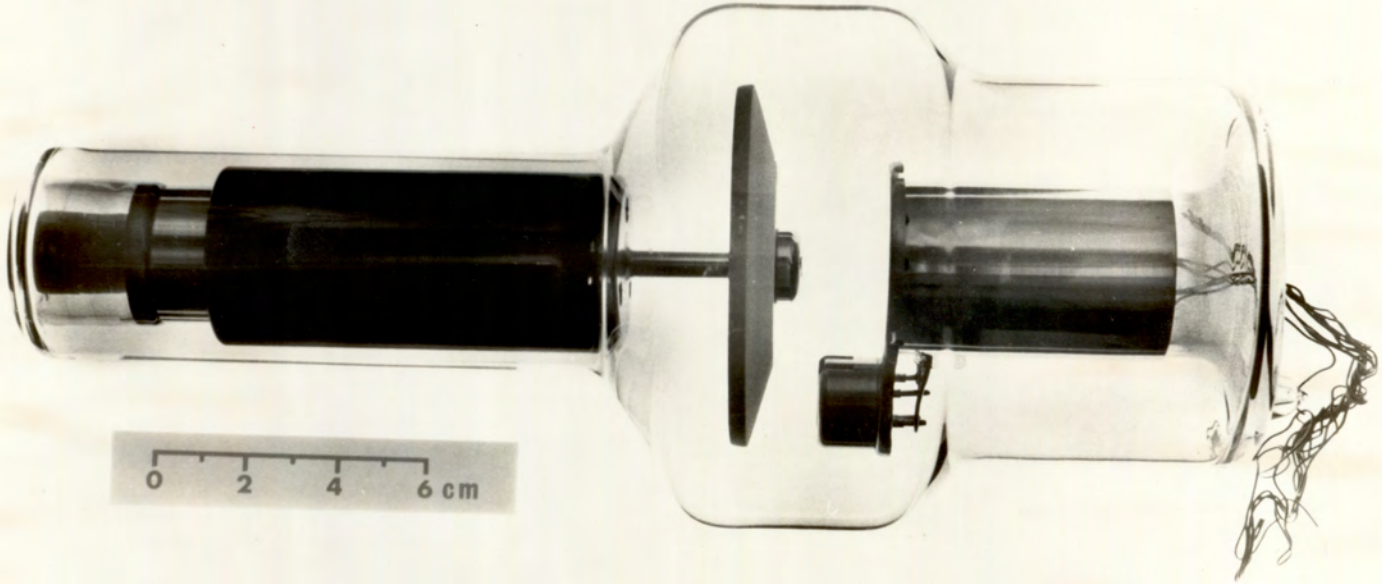

Fig. 4.1. A typical diagnostic X ray vacuum tube.

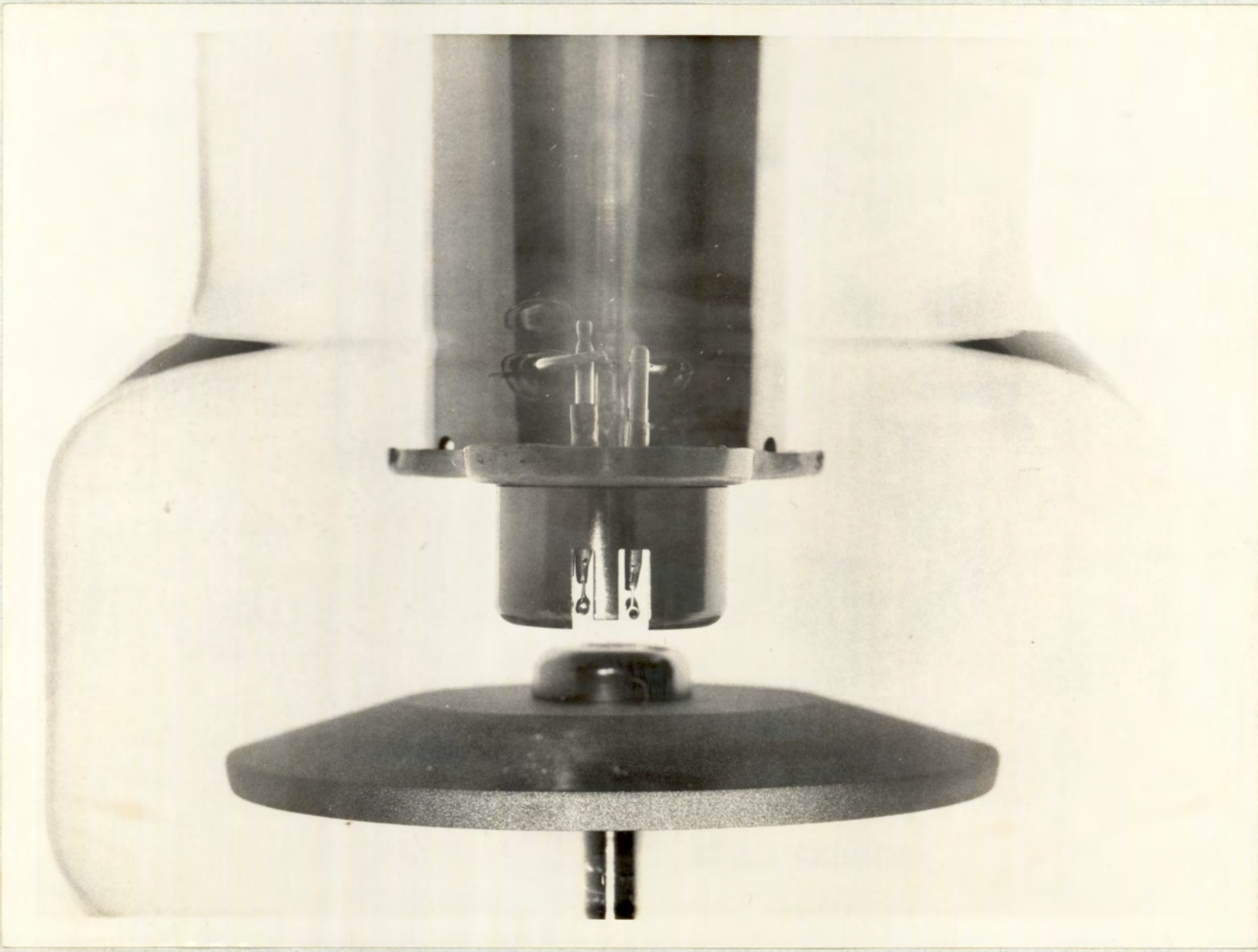

Fig. 4.2. The cathode heater filaments and anode tungsten target.

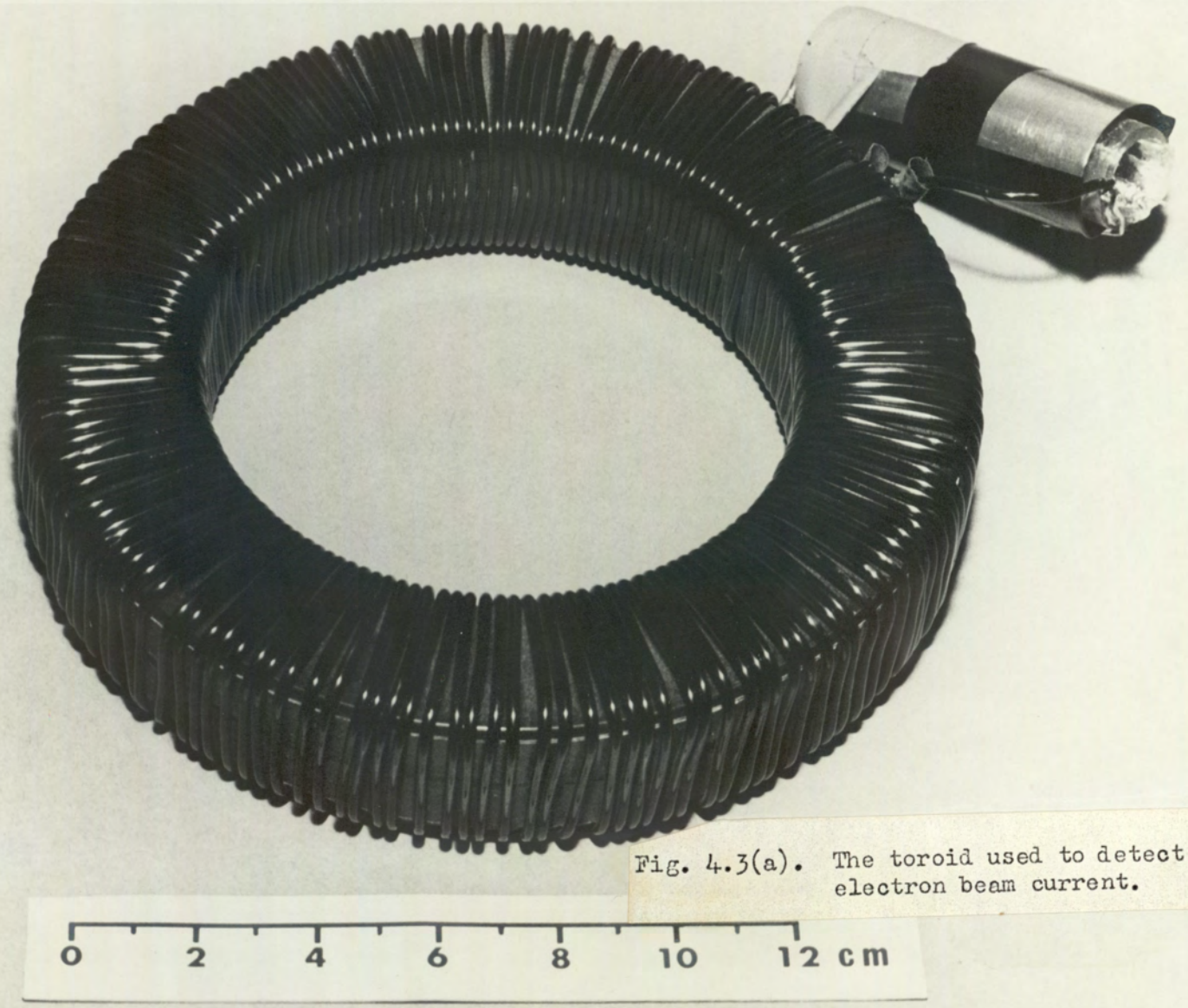

Fig. 4.3(a). The toroid used to detect changes in the electron beam current.

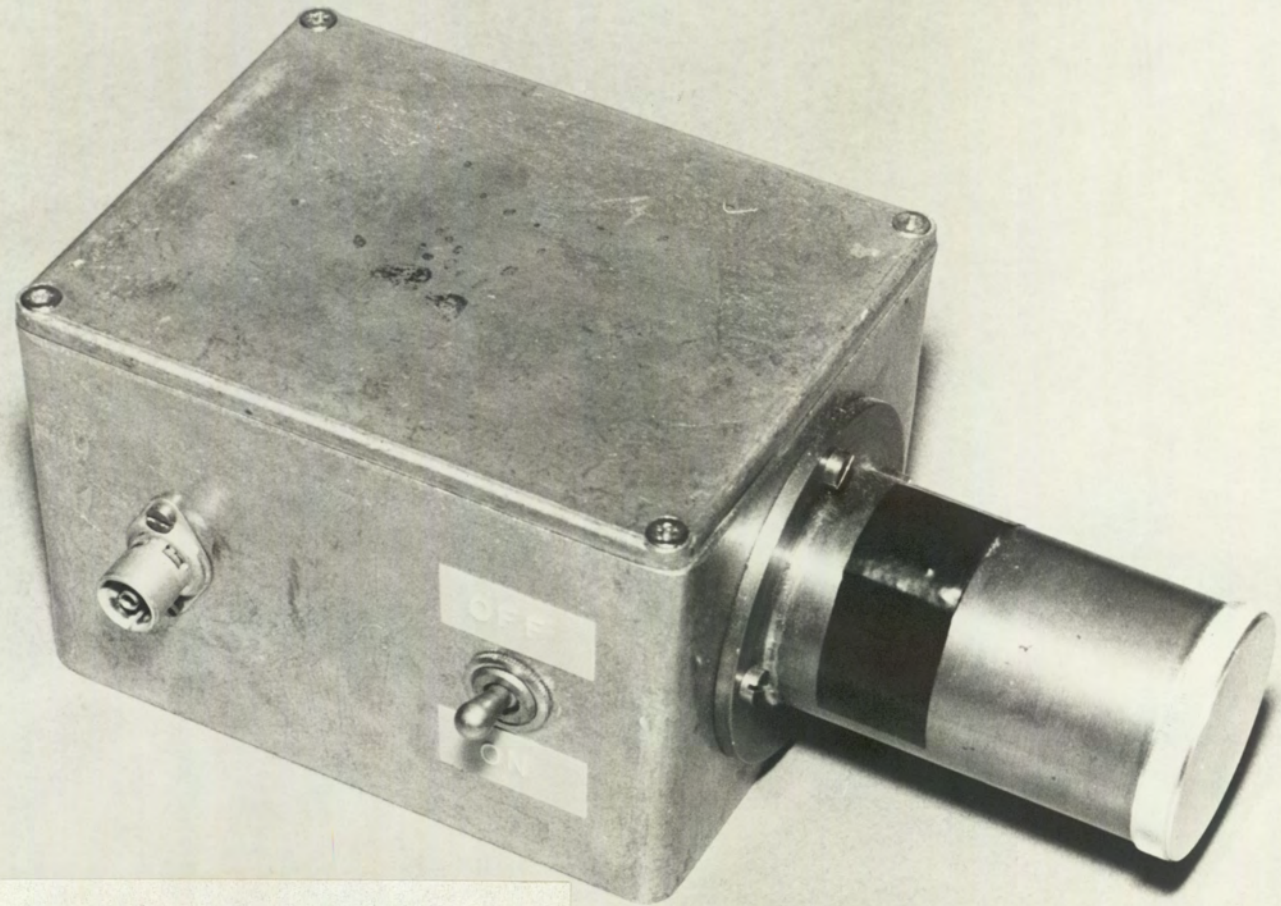

Fig. 4.3(b). The instrument used to measure the instantaneous X ray intensity emitted from a diagnostic set.

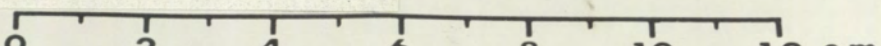

By passing a 50 Hz square wave current through a wire leading through the toroid, the waveform of the induced voltage was found to reproduce the current waveform, showing the the toroid would be suitable for the experiment. To simulate closely the expected beam current which was thought to fluctuate, a full wave rectified mains current was passed through the coil and amplified. Various RMS currents and peak output voltages were measured. The peak output voltage was found to be 0.66mV mA^{-1}.

By disconnecting the beam current cable from the X ray tube head the cable was fed through the toroid and reconnected. To minimise stray radiation in the experiments, the lead apertures in the X ray head were closed and the tube head orientated so that the normal X ray beam path was directed away from occupied areas of the room.

Traces were obtained for various combinations of peak anode voltages and beam currents, some of which are shown in Figs. 4.4 - 4.7. It is obvious that although the toroid can only detect the changes in beam current and not its value, the variation in the current is a substantial percentage ($\simeq$80%) of the indicator panel reading. It is evident from these traces that the current waveform is highly dependent upon the indicated panel beam current but not so dependent upon the peak anode voltage. A significant harmonic content is also evident.

4.1.2. Instantaneous X ray intensity.

Like the beam current, no method exists of directly measuring the high anode voltage waveform with single laboratory equipment. However, a good indication of the

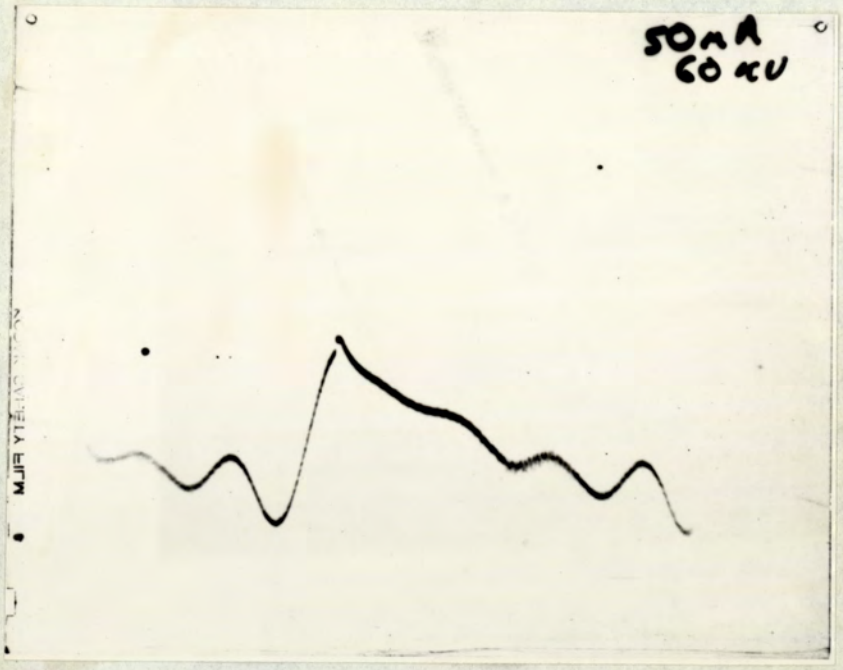

Fig. 4.4. Beam current waveform 50mA, 60kVp

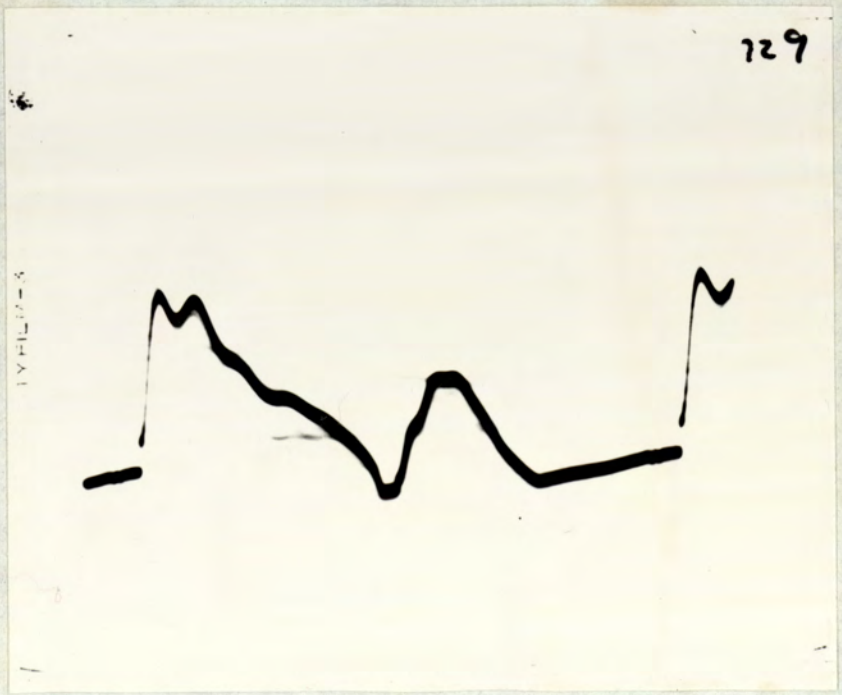

Fig. 4.5. Beam current waveform 50mA, 90kVp.

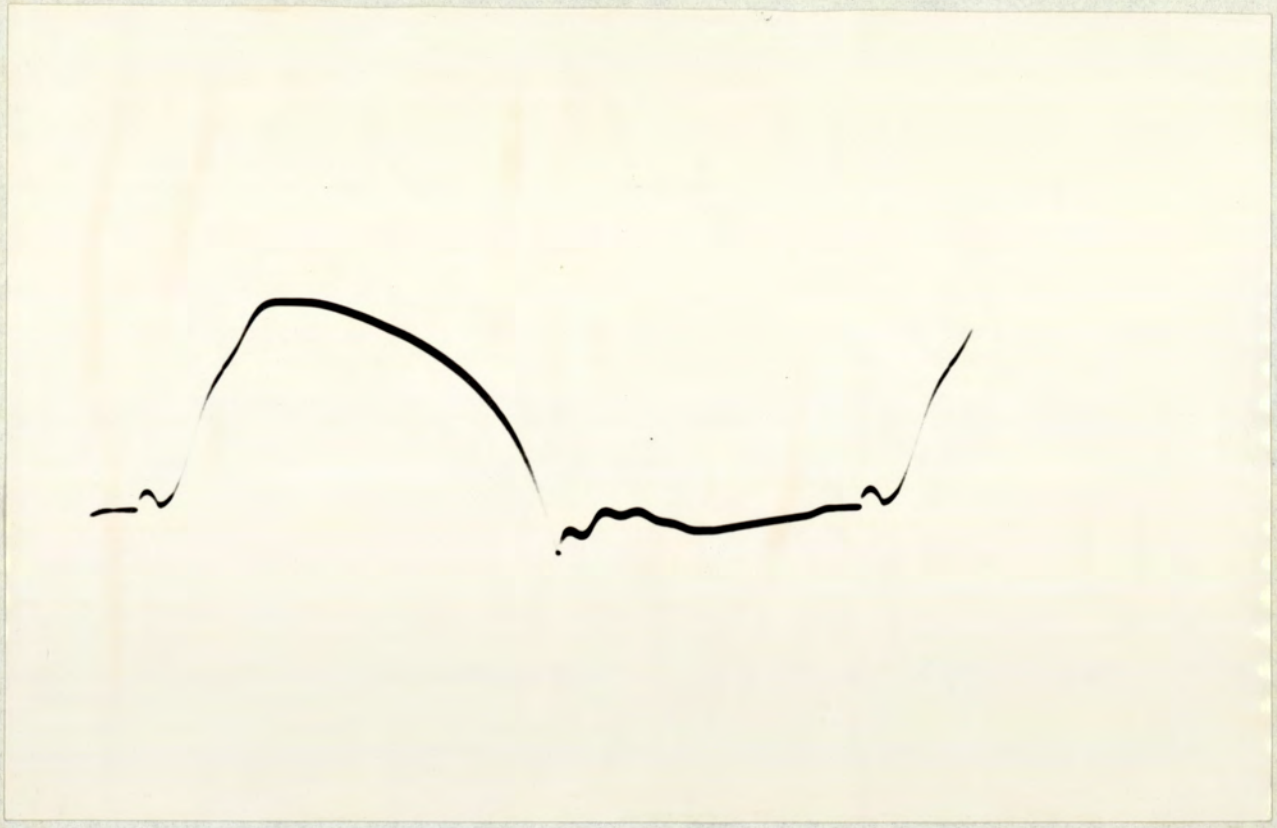

Fig. 4.6. Beam current waveform 200mA, 30kVp.

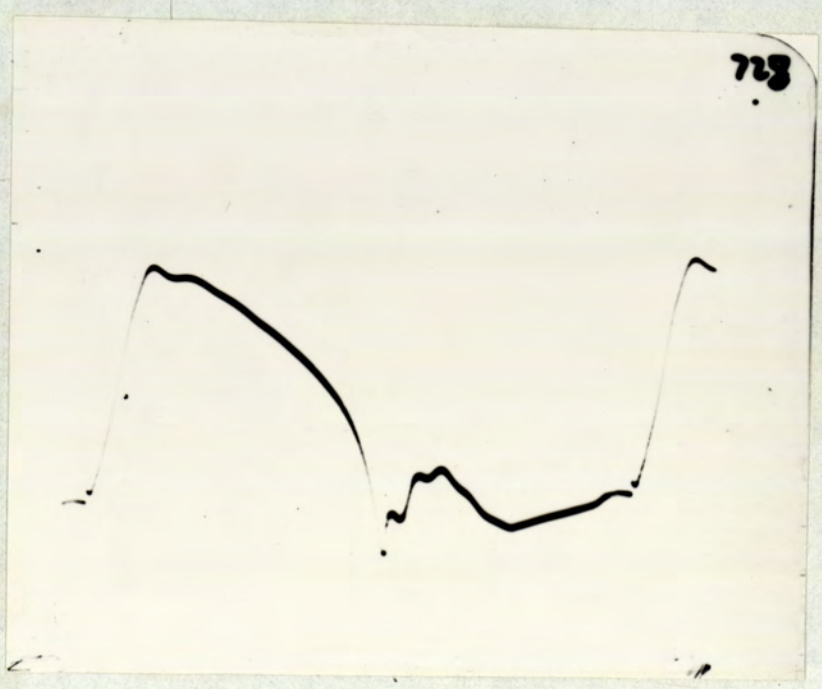

Fig. 4.7. Beam current waveform 200mA, 90kVp.

X ray generator performance may be made by measuring the instantaneous X ray intensity. This will depend upon the anode material, beam current, accelerating voltage and filtration of the beam.

To observe the instantaneous X ray intensity a CsI(T1) crystal was used with a 92AV photodiode. The current from the photodiode was fed into a high input impedance source follower and the signal amplified by a DC amplifier. The circuit is shown in Appendix A.2.6 and the equipment in Fig. 4.3b.

Various X ray waveforms were photographed three of which are shown in Figs. 1.4, 4.8 and 4.9. It is seen that the waveforms are assymetric. A comparison was made of the relative peak energy outputs of four diagnostic X ray sets in the hospital at the same nominal setting of anode voltage and beam current. Variations up to 25% were observed. Holloway et al[142] have conducted a much larger survey of X ray generator sets and found a correspondingly wider variation of beam energy output.

4.2. Investigation of observed signal fluctuations.

It is seen from the traces made with the densitometer that there is a small residual fluctuation of the signal for what should be constant absorption in the second detector beam path e.g. the 50mm water trace level in Fig. 5.7. To try and discover the cause of these fluctuations it was decided to test the theory which states that if there are equal filtrations above the two detectors then there should be no fluctuation in the signal no matter how large the peak anode variation. The filtration above the monitor was made 45mm water and 5mm ivory and so for this investigation the lower detector filtration was

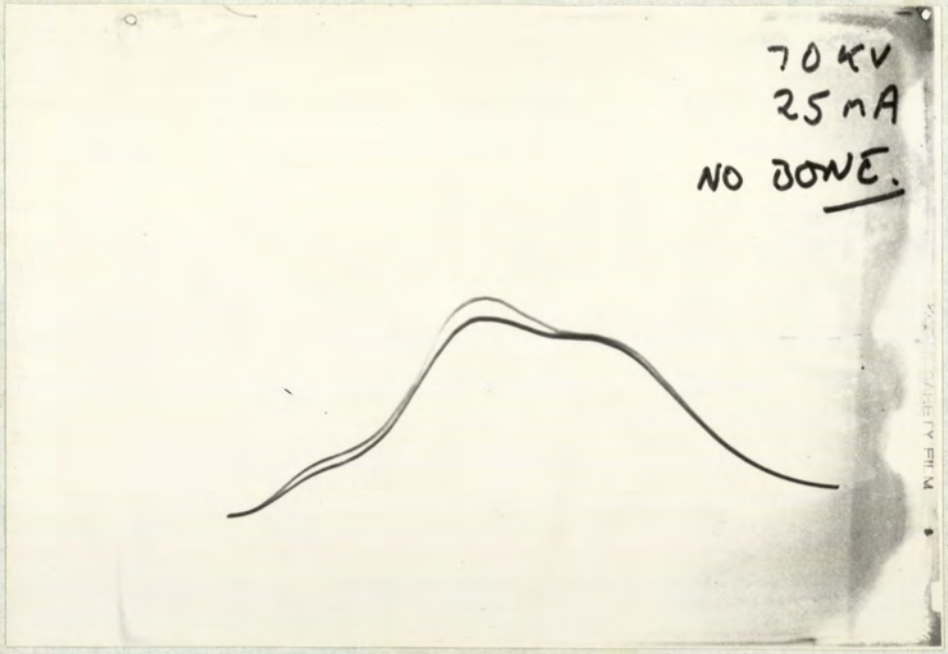

Fig.4.8. Instantaneous X ray intensity waveform over several half cycles. 70kVp, 25mA, 1.5mm filtration of aluminium.

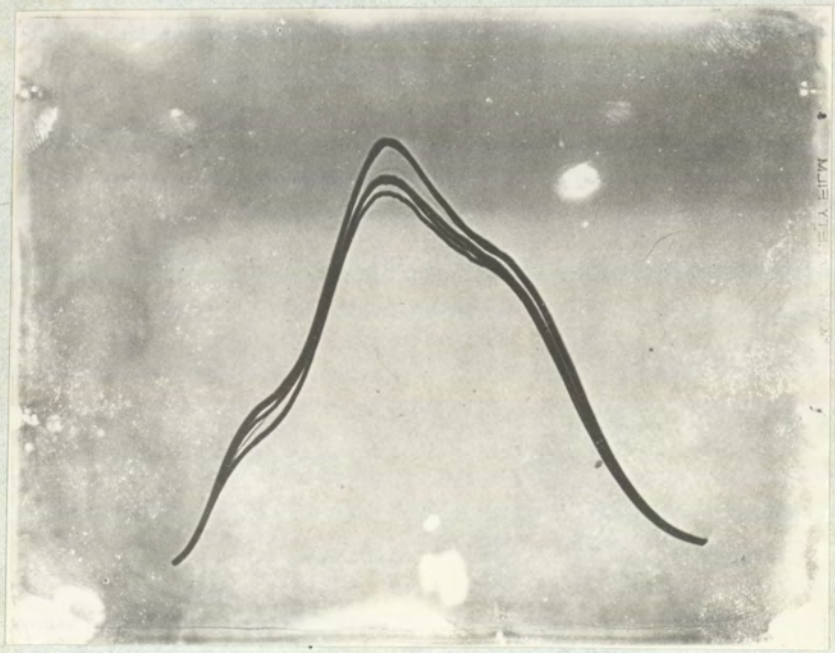

Fig.4.9. Instantaneous X ray intensity waveform over several half cycles. 90kVp, 50mA, 1.5mm filtration of aluminium.

made 46 mm water and 4mm ivory (there was no second 5mm ivory slab). To eliminate the possibility of microphonic interference from the synchronous motor and heterogeneity of the ivory, the signal from the second detector was observed on the time scan of the oscilloscope with the motor off and the ivory slab stationary. The small fluctuations ($\simeq 0.05$ volt) were still observed and a typical scan is shown in Fig.4.10. This shows the signal as a dot every half cycle and suggests a nearly periodic nature to the fluctuations. The same fluctuations were observed when the densitometer was rotated by 90° with respect to the X ray tube head.

The possibility of microphonic interference transmitted by the starter motor in the X ray tube head was eliminated by mechanically decoupling the tube head from the brass flange. The variations in the signal could be due to

(1) The electronics,

(2) movement of the focussed beam of electrons on the tungsten target

(3) gyration or movement of the target along its axis,

(4) some other cause.

As the electronics had been carefully designed together with fast switching times ($< 1\ \mu s$) it was thought that items (2) and (3) merited investigation by obtaining a pin hole image of the X ray spot source. It was also thought that in view of the "pitting" developed by well used tungsten targets (Fig.4.11), that small variations in the topography of the surface would give rise to large changes in the electostatic field very near to the surface which mught be sufficient to deflect slightly the incident electrons.

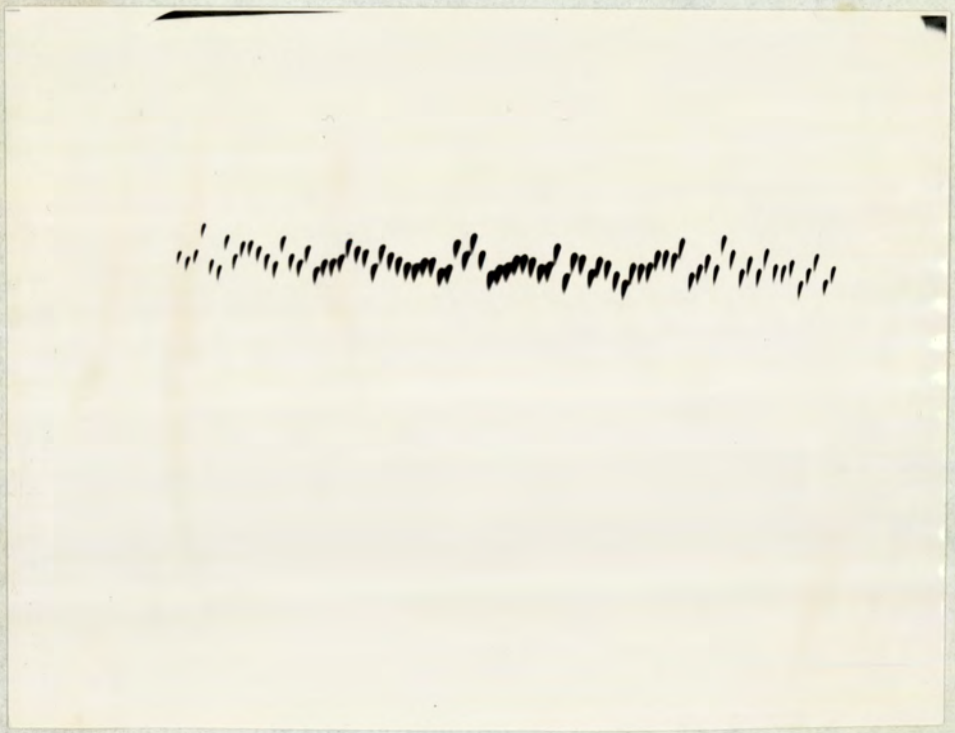

Fig.4.10. The small residual detector fluctuations ($\sim \frac{1}{20}$ V) present when a stationary object is scanned. Each dot represents the value of the signal received every 10^{-2} second.

Fig. 4.11. A well used tungsten target from a diagnostic X ray set.

A pin hole of about 0.1mm diameter was carefully punched into a 0.63mm thick sheet of tantalum, the experimental arrangement being shown in Fig. 4.12. A non-screened X ray film was placed in a thin light-proof polystyrene bag and laid on the floor of the perspex bath to minimise scattered radiation. A collimation tube was attached to the flange of the X ray head and the tantalum sheet was stuck with adhesive tape to the end of the tube, with the pin hole in the central beam (this was checked by using the optical guide). Distances d_1 and d_2 were made as equal as possible ($\simeq$450mm).

By switching on the X ray set with the bath in motion, an image of the X ray spot was obtained as a line about 60mm in length, corresponding to an exposure time of 6 seconds. Two exposures were made, the first with the bath travelling perpendicular to the electron beam and the second at right angles to the first.

A close examination of the first pin hole image revealed it to be in fact two parallel lines about 0.5mm apart. This is due to the separate electron beam filaments which separated by about 6mm and which can be seen in Fig. 4.2. The two electron beams therefore converge onto the anode target but do not coincide. The second exposure, with the bath travelling parallel to the two electron beams was found to be a single line having a width of nearly 1mm. The pin hole image lines in both exposures was as straight as could be visually ascertained, i.e. any movement of the focussed electron beam on the target was small (< 1mm).

The investigation was limited because the substantial transmission of the X rays through the thin sheet (even at low peak anode voltages) limited the image contrast on the X ray film.

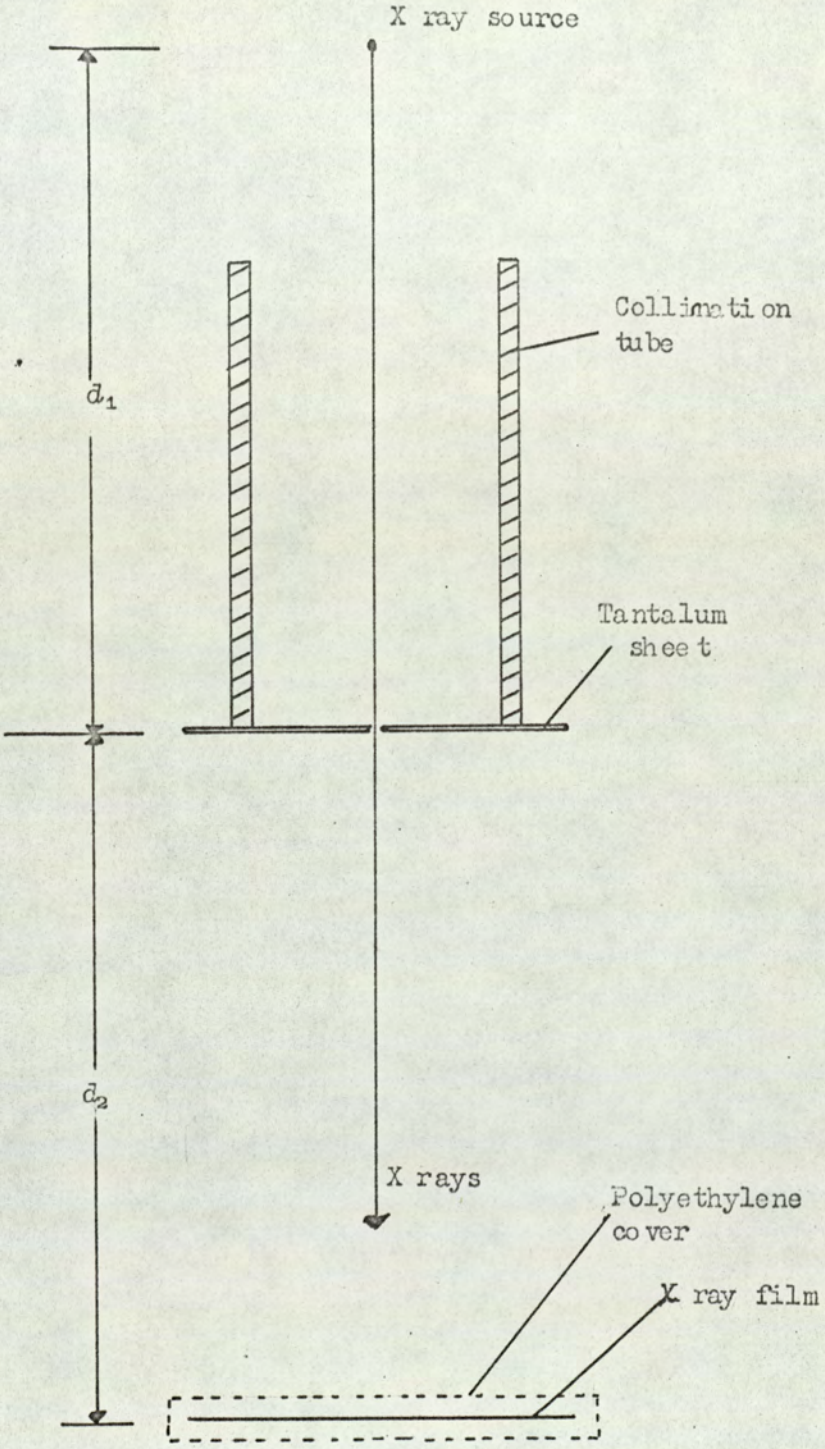
X ray source
Collimation tube
d_1
Tantalum sheet
d_2
X rays
Polyethylene cover
X ray film

Fig. 4.12

Possible magnetic interference with the electronics was eliminated as the two detectors and the remaining electronics were shown to be relatively insuceptible to an iron cored solenoid.

The cause of the signal fluctuations remains unknown and further investigation is merited because the fluctuations limit the accuracy with which a scan may be measured.

4.3. Scanning measurements

To assess the performance of the densitometer under different operating conditions, several experiments were carried out. To do these a simple setting up procedure was adopted. Those procedures which are infrequently required, such as the adjustment to the detectors and the electronics, are described in Appendix A2.

4.3.1. Setting up procedure.

This usually consists of four simple steps :-

1. The bath, perpex arm frame and ivory step wedge are fitted into position
2. The bath is filled with a warm 2% salt solution
3. The electronics is switched on, allowing five minutes warming up time
4. A scan is made of the ivory step wedge and the oscilloscope controls are adjusted as necessary.

It had been found that even when a constant layer of homogeneous material was scanned (e.g. 50mm water) the output was subject to the residual fluctuations mentioned in the preceding section. When comparing the 50mm water base line signal with a superimposed straight line it became clear that the negative film could not be aligned to better than a few degrees. In order to overcome this, a fixed potential voltage

was derived from one of the power supplies and used to define a reference line by a series of horizontal dots by using the tracking mechanism in the normal mode without the X ray beam. By using a potentiometer in conjunction with the DC supply, the height at which the reference trace on the oscilloscope screen could be adjusted (Appendix A2.5).

It was often found most suitable to adjust the potential until the DC level of the line was sixteen volts above the base line of the second detector amplifier. The line then defines the magnitude of the trace signal and the horizontal orientation of the photographic negative. This line may intersect the trace of the step wedge and ulna , depending upon the peak anode voltage and beam current selected. If this intersection is not desired, the DC level of the reference line can be raised so that it appears slightly above the 50mm water mark on the negative trace, i.e. clear of the traces of bone and ivory step wedge as sketched in Fig 4.13.

In exposing the film to the trace of the bone and reference line, it was found that the latter trace was more heavily exposed. By suitable adjustment of the oscilloscope brightness control a satisfactory compromise can be found. Even if the reference line has to be overexposed, there is no serious loss in the accuracy of correctly orientating the negative.

4.3.2. Scans made on the ivory cylinder.

Initial tests to asses the voltage signal and performance of the densitomer were made by scanning a hollow ivory cylinder. The radial dimensions (O.D.15mm and two I.D's of 9.5 and 10mm) were made so as to closely simulate the ulna. The use of ivory as a bone standard has been mentioned in Chapter 1.

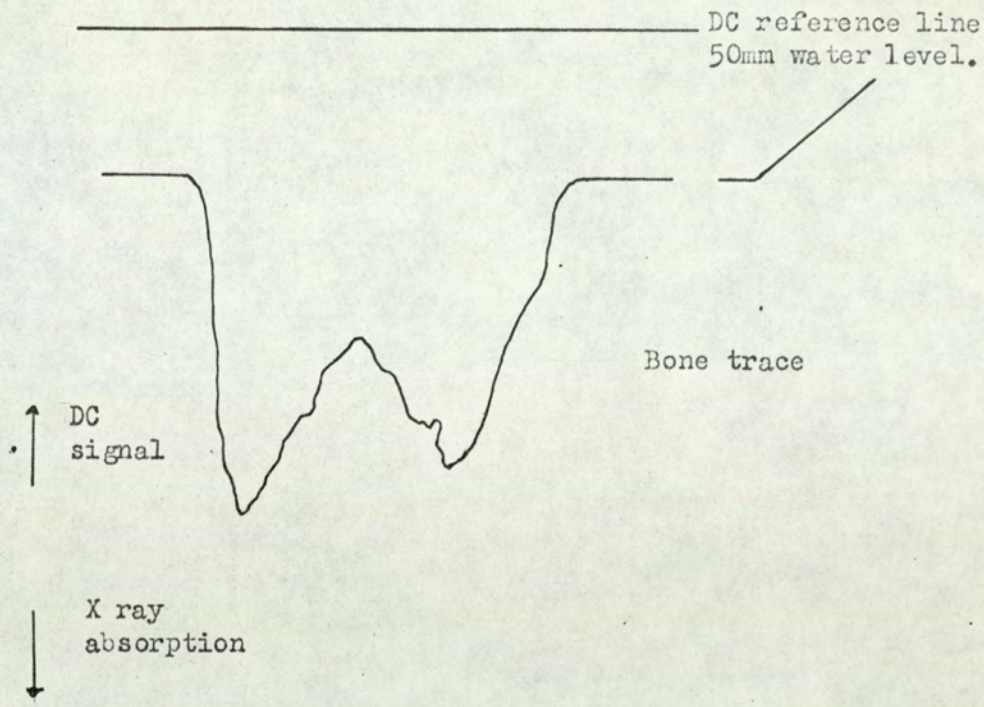

Fig. 4.13.

A scan of the ivory cylinder was made by placing it adjacent to the ivory step wedge in the bath of water. Care had to be taken to align correctly the central axis of the cylinder parallel with the ivory step wedge. It was found that this could best be done by securing the cylinder with adhesive tape to the floor of the bath, with the tape securing the cylinder at the opposite end to that to be scanned. Air bubbles were swept away by a small brush. The small perspex box was placed in position to ensure a constant beam path of 50mm in the ivory and water.

Measurements were made to asses the compensation afforded by the densitometer by making scans at 90 and 95 kVp. The results are given in Chapter 5. Dose measurements were made using LiF finger badges and the ivory cylinder to simulate the bone. The measurements are given in Chapter 5.

4.3.3. Method to obtain dead ulnae scans.

The hollow ivory cylinder can only simulate the ulna to a certain degree and to gain further experience with the X ray set and the densitometer dead ulnae were examined. The scanning of such bones offers the advantage that repeated scans on the bone may be made which is not possible in the case of in vivo measurements because of the radiation dose received.

The dead ulnae were taken from deceased geriatric patients and were about 80 mm long. In all cases the surrounding tissue had been removed and when not in use the specimens were kept in formalin in an air-tight container to avoid dehydration of the bone and marrow. If the bone becomes dehydrated, it may show an artificially low absorption compared with the 50 mm water level.

To overcome the problem of orientation and alignment of the specimen in the bath, a 50 mm rectangular wax block was moulded around the proximal end of the bone as illustrated in Fig.4.14. A small lead weight was placed on top of the wax so that the ulna could be orientated in four different stable positions with its axis parallel to that of the detector slit. An identification mark made in the sides of the wax block served to identify the orientation of the bone when in the bath. Furthermore, the bone could be scanned at any distance from the ulnar styloid.

With the ulna, ivory step wedge and perspex box in position, air bubbles were swept away by a small brush. Two scans of each ulna were usually made to check the reproducibility and if satisfactory, they were kept and recorded.

4.3.4. In vivo measurements.

These were carried out on volunteers to show any experimental difficulties in obtaining an in vivo scan before the densitometer was used for patients. The results also

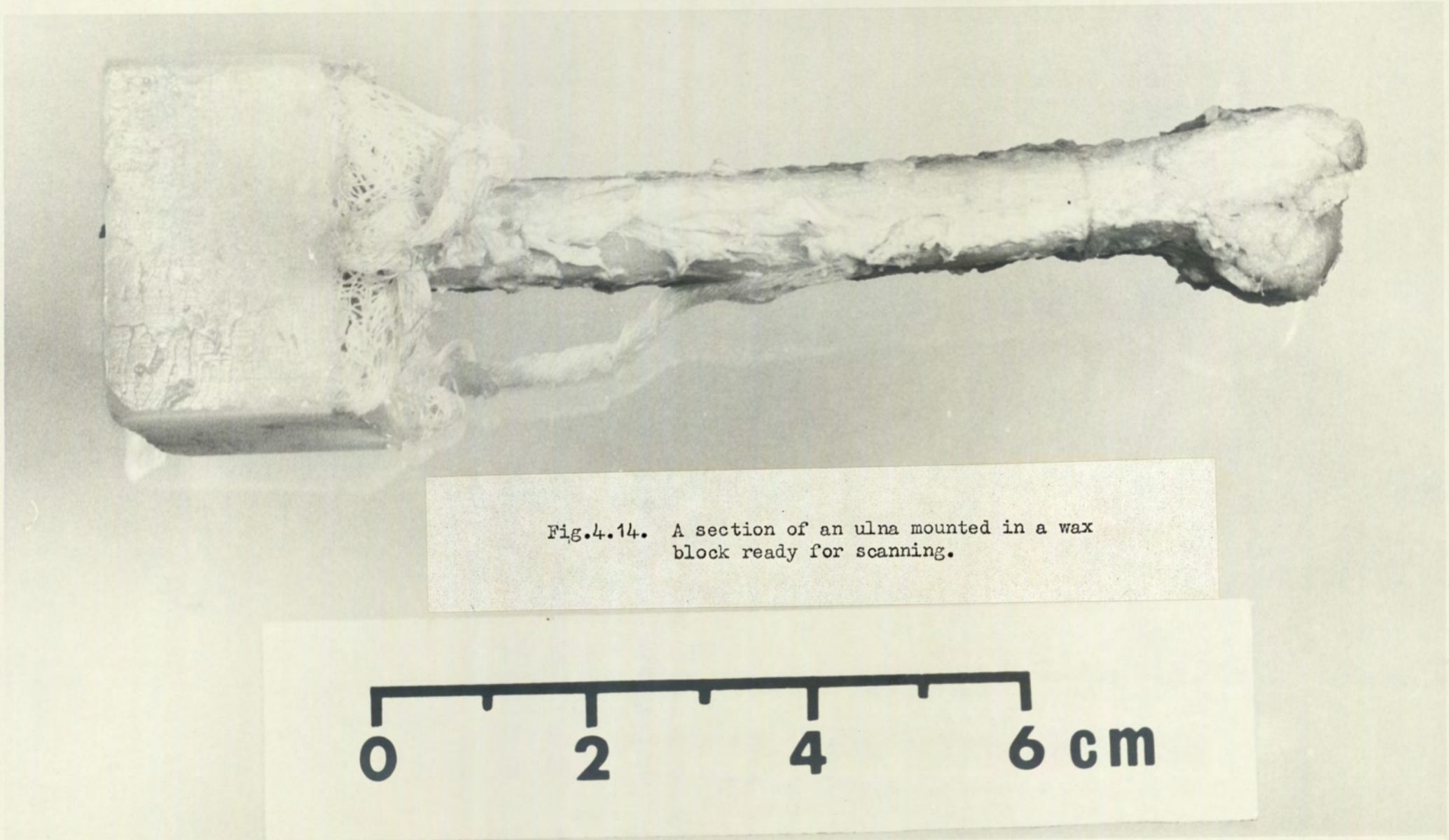

Fig.4.14. A section of an ulna mounted in a wax block ready for scanning.

indicate the reproducibility of in vivo measurement.

4.3.4.1. Tissue compensation.

Soft tissue has a mean composition of $(C_5H_{40}O_8N)$ [1] and a density close to that of water so that X ray absorption in these materials is very similar. In initial experiments to minimise the effect of varying amounts of soft tissue surrounding the ulna, the arm was immersed in a bath of water to a constant depth of 50 mm. This constant depth was ensured by placing the small perspex box over part of the limb to be examined. More ideally when an absorption scan is made, any variations of absorption are due to the bone alone. However, variations of composition or density of the soft tissue will give corresponding variations in the absorption trace.

It was found when making in vivo measurements that the average radiographic density of the soft tissue was slightly greater than that of water. Consideration was given to making the water radiographically denser by adding a suitable solute. Hine and Bowmell[1] have discussed glycerol-urea solutions, whilst Frigerio et al [143] have considered in detail tissue-equivalent liquids. There are several requirements for a soft tissue equivalent solution. It should be inexpensive, non toxic, stable and be readily available. The first two were considered to be particularly important as the whole arm is immersed in the liquid which is discarded after use.

In view of these considerations common salt solutions were tested and a 2% solution was found to be acceptable. Increasing the concentration from 2% to 2.4% did not significantly affect the trace. The absorption coefficient of the salt solution has been calculated to be about 6% greater than water at 60 keV. The absorption coefficient of the solution is given in Table A6.2 and shown graphically in Fig.6.6.

4.3.4.2. Scanning the subject.

This has to be done quickly and with the minimum dose and discomfort to the subject. The subject was first informed briefly and simply how the machine operated and what he was required to do. The subject's sleeving was them removed or folded away to expose the majority of the arm as shown in Fig.3.11. With the ivory step wedge in position, the arm was immersed into the bath until it was in a similar position to that shown in Fig.3.12 with the ulnar styloid resting firmly against the perspex block.

After allowing the subject to adopt the most comfortable position, the respective straps over the thumb and the fifth finger were carefully tightened until the arm was held firmly but comfortably in a supinated position. The perspex box was inserted over part of the arm to be examined and a note was taken of the position of the third finger. This permitted accurate repositioning of the arm.

To allow the subject to be accustomed to the motion of the bath the motor was switched on to move the bath in a dummy run. Finally one scan was made after which the arm was released from the bath and negative film developed.

Six subjects were scanned and a typical result which illustrates the in vivo reproducibility is shown in Chapter 5.

CHAPTER 5.

The Experimental Results.

5.1. Step wedge experiments.

To assess the performance of the densitometer X ray absorption trace measurements of the ivory step wedge were carried out under different operating conditions of anode voltage beam current and integration time. It was felt worthwhile to make two separate investigations:-

(i) The extent to which the densitometer compensated for nominal 5% voltage differences in the range (70-100)kVp for different integration times and X ray path lengths of ivory and water,

(ii) To determine the increase of voltage signal through a known path length of ivory and water with increase of peak anode voltage and integration time.

By making two scans of the ivory step wedge at nominal voltage differences of 5%, information for the first investigation can be determined whilst for the second only measurements obtained from the trace made at the first voltage are required. This is because of altering the anode voltage for the second trace the electronic integration will change from its preset value to compensate for the change in voltage. The results are discussed in section 5.5.

5.2. Errors in the trace measurements.

5.2.1. The reference voltage line.

The reference voltage line is a horizontal line on the oscilloscope screen which ensures the correct orientation when examining the photographic negative and defines a DC voltage above the baseline of second amplifier. It is described in detail in Section 5.5.

The reference line was set at 16 volts above the baseline of the amplifier to an accuracy of ± 0.05 volt, the accuracy being limited by parallax error due to the thickness of the oscilloscope glass screen. No difficulty was experienced in the DC setting of this line by the adjustment of the potentiometer shown in appendix A2.5

5.2.2. Errors in reading the photographic trace.

The photographic negative was laid flat on a sheet of graph paper and its orientation adjusted until the horizontal reference line was coincident with a convenient line on the graph paper. This was done to an accuracy of ± 0.25 mm for each end of the 80 mm line. The negative could therefore be aligned to ± 0.3°.

The photographic trace of an individual step is about 2 mm long (along the x axis) which corresponds to twice the actual physical size. The vertical thickness of each step on the negative should ideally be equal to the oscilloscope spot diameter but because of the non ideal compensation mechanism of the densitometer and the hetrogeneity of the ivory, the photographic image of a step is about 1.5 mm in height. The sensitivity of the densitometer is, however, sufficient to show if any part of an adjacent step is above the collimator, for in such a case the vertical position of the oscilloscope beam spot is evidently different from the remainder of the step. When making a measurement from the photographic negative, the average ordinate of the step trace was used.

5.3. Error in the integration time.

The setting of the integration time is described in appendix A2.4. As described in A2.4, the adjustment of the integration control involves the use of a strip of graph paper with the oscilloscope screen, and it is important that there

should be minimal parallax error.

One half cycle was made 90 mm on the horizontal time scan on the oscilloscope screen to obtain the convenient scale of 2^{o} mm^{-1}. To adjust the integration time the X ray generator set has to be switched on and in setting this time it could be seen to vary by about $\pm 2^{o}$ as the densitometer compensated for peak anode voltage fluctuations. The mean integration time was noted and the error involved was about $\pm 3^{o}$.

5.4. Beam current.

This was selected to give a suitable signal from both detectors to ensure the satisfactory operation of the compensation mechanism and an adequate output signal for any chosen value of peak anode voltage and integration time. The voltage signals obtained from the step wedge traces have been normalised to 50 mA beam current to allow an easier interpretation of the results. In normalising it has been assumed that the voltage signal is directly proportional to the beam current, other parameters remaining constant. It is shown in chapter 4 that the beam current is not constant and that its variation is a substantial fraction of the indicated value ($\sim$ 80%). In view of this it is therefore not surprising that the experimental points in Figs.5.5. and 5.6 do not follow the drawn curve more smoothly.

5.5. General interpretation of the step wedge results.

These results are given in tables A3.1 - A3.12 in appendix 3. Tables A3.1 - A3.4 show the voltage signals obtained from filtration by the step wedge for the conditions of operation given in tables A3.5 - A3.8. The results were compared by normalising the signals to 50 mA beam current and these are given in tables A3.9 - A3.12. Some of the normalised results are shown graphically in Figs.5.1 - 5.6.

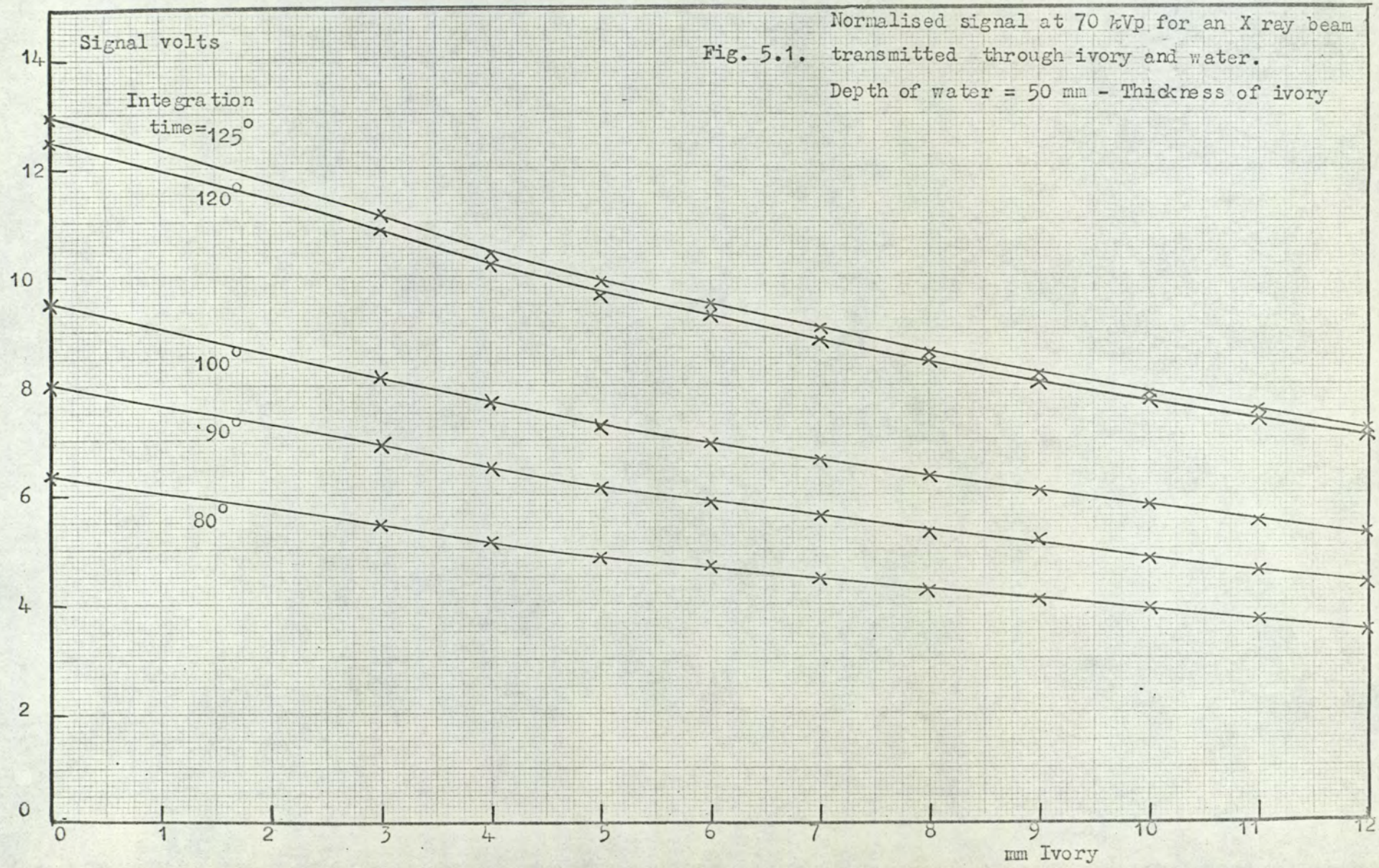

Fig. 5.1. Normalised signal at 70 kVp for an X ray beam transmitted through ivory and water.
Depth of water = 50 mm - Thickness of ivory

Fig. 5.2.

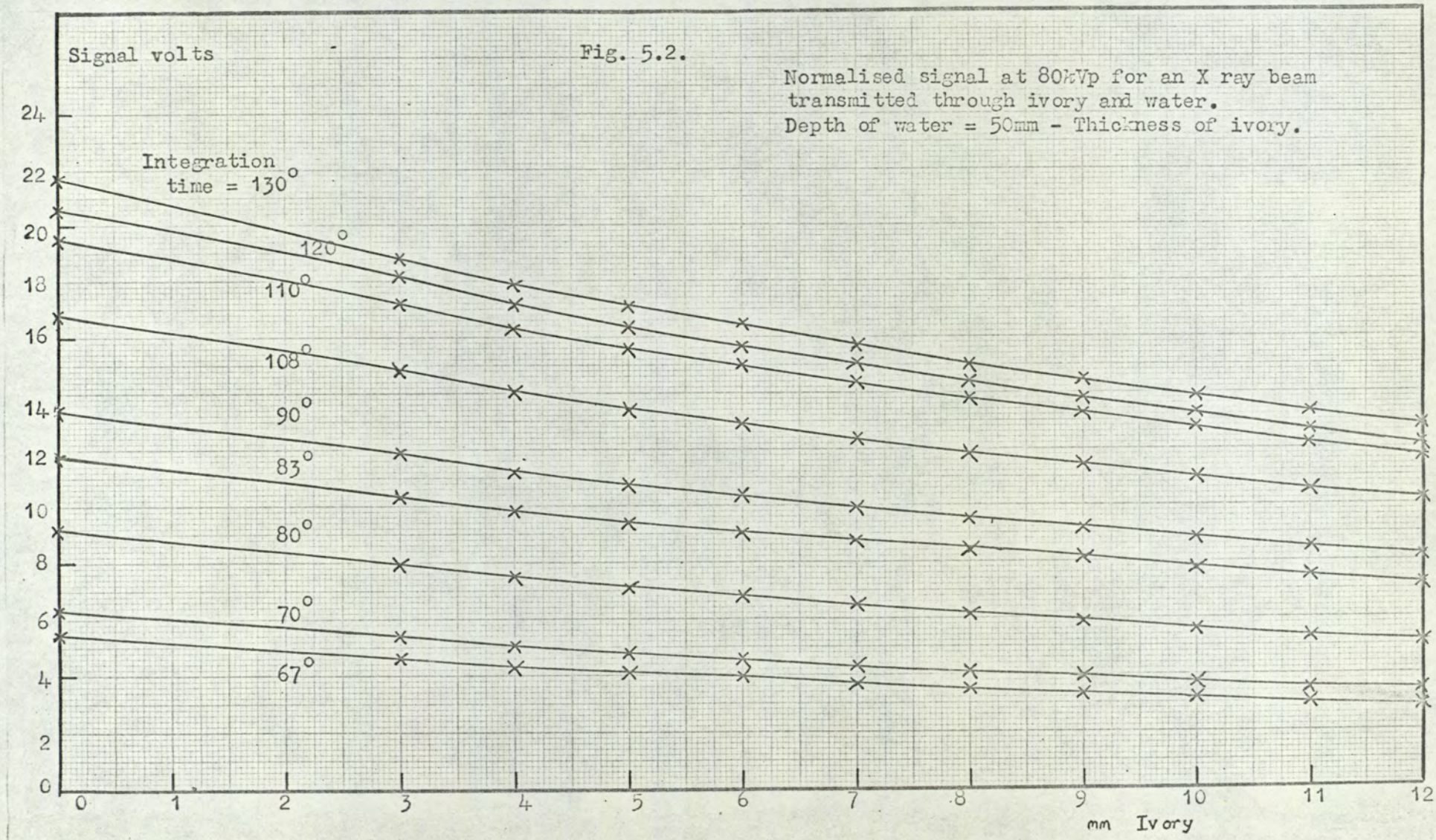
Signal volts
Normalised signal at 80kVp for an X ray beam transmitted through ivory and water.
Depth of water = 50mm - Thickness of ivory.
Integration time = 130°
120°
110°
108°
90°
83°
80°
70°
67°
24
22
20
18
16
14
12
10
8
6
4
2
0
0
1
2
3
4
5
6
7
8
9
10
11
12
mm Ivory

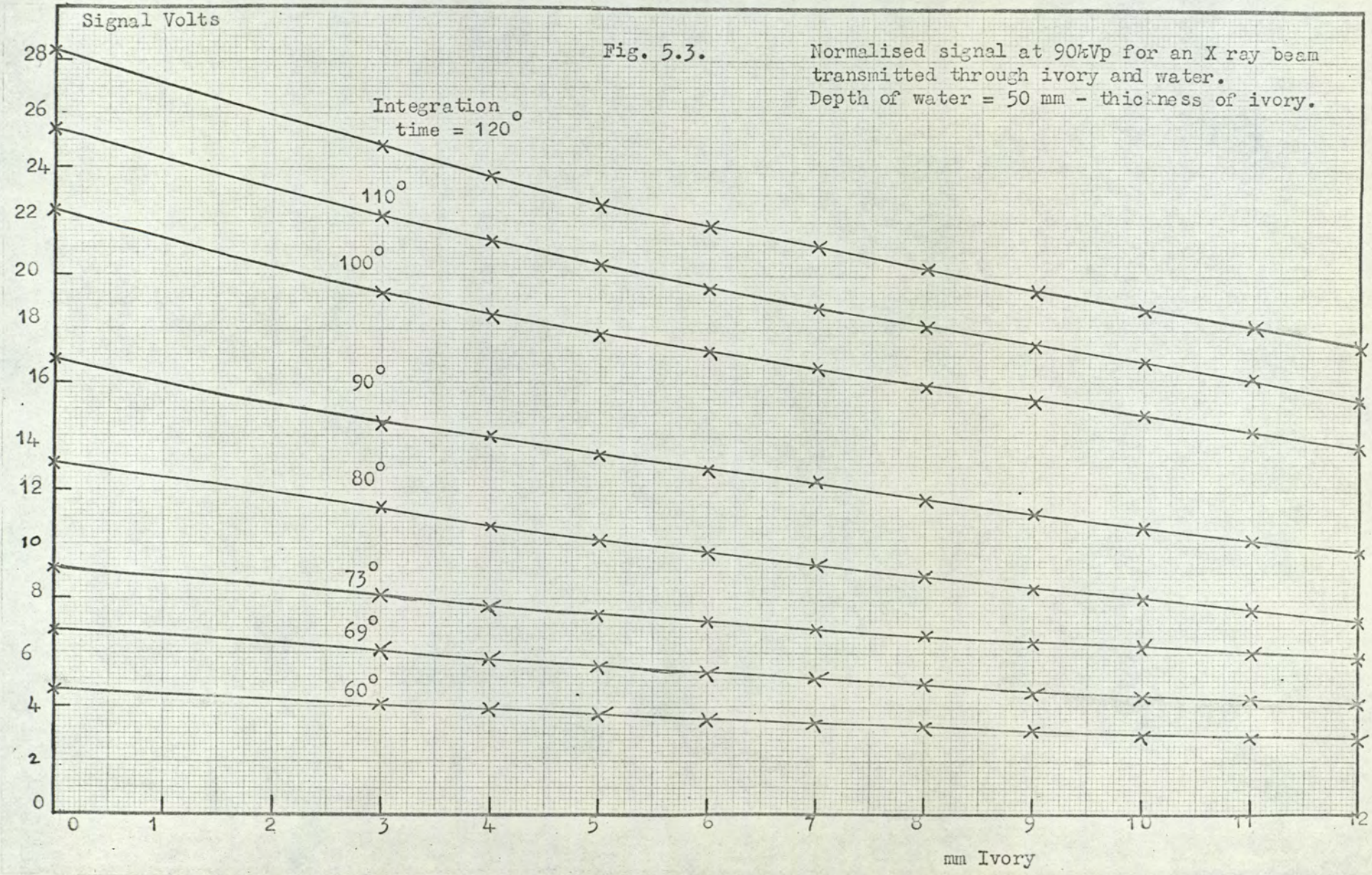

Fig. 5.3.

Normalised signal at 90kVp for an X ray beam transmitted through ivory and water.
Depth of water = 50 mm - thickness of ivory.

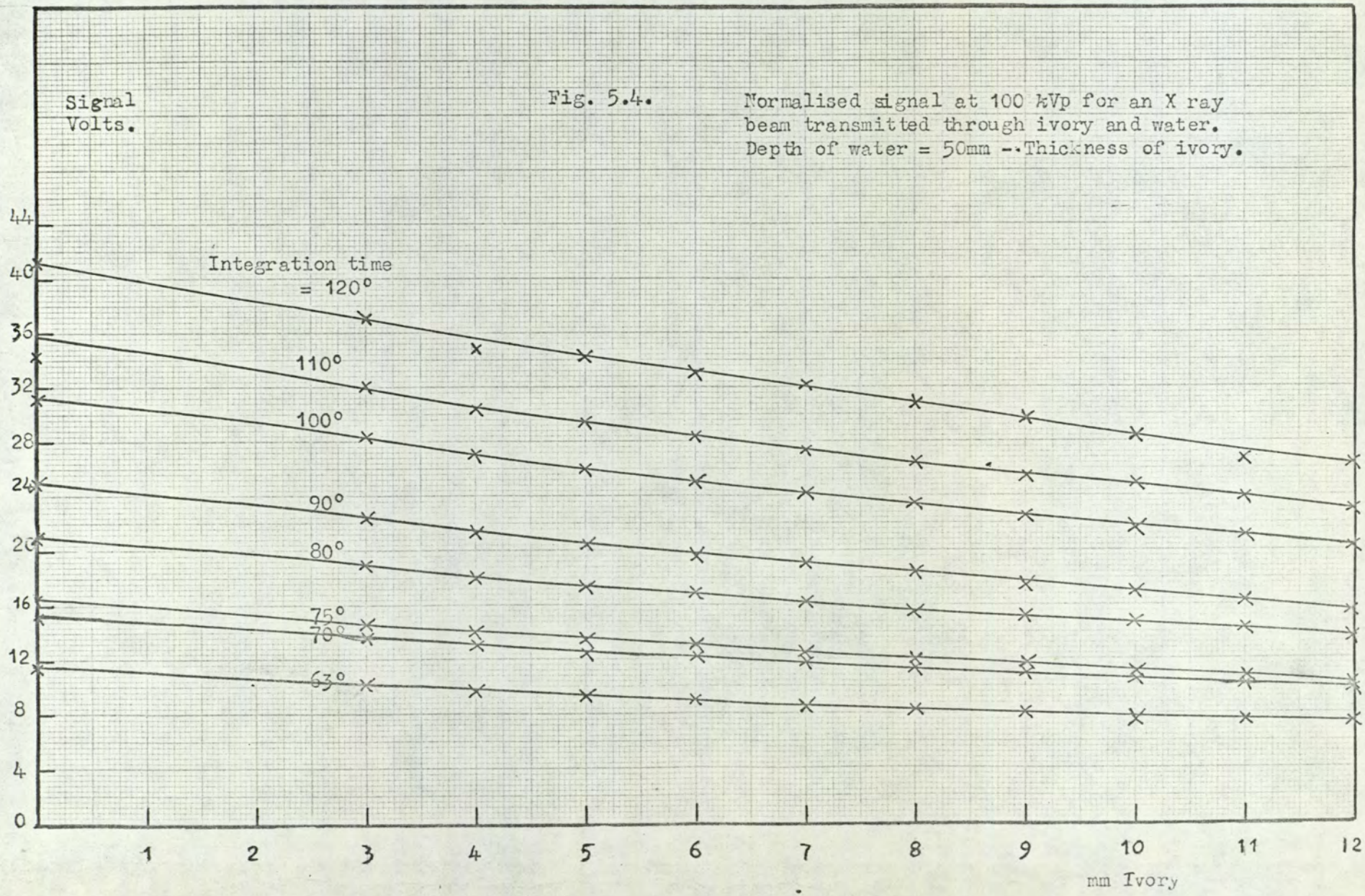

Fig. 5.4. Normalised signal at 100 kVp for an X ray beam transmitted through ivory and water. Depth of water = 50mm -- Thickness of ivory.

Fig. 5.5.

Normalised signal transmitted through 5mm ivory and 45mm water.

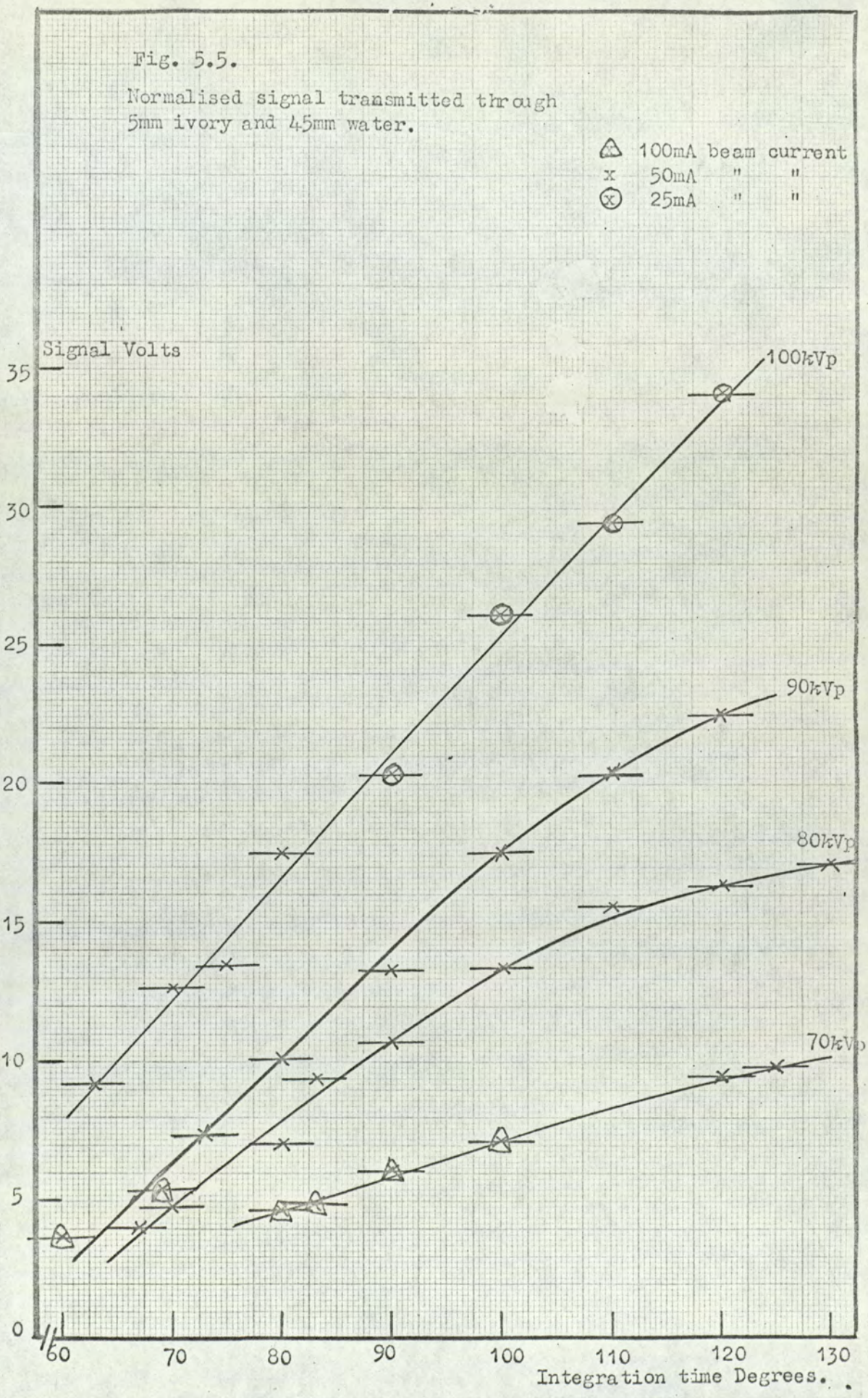

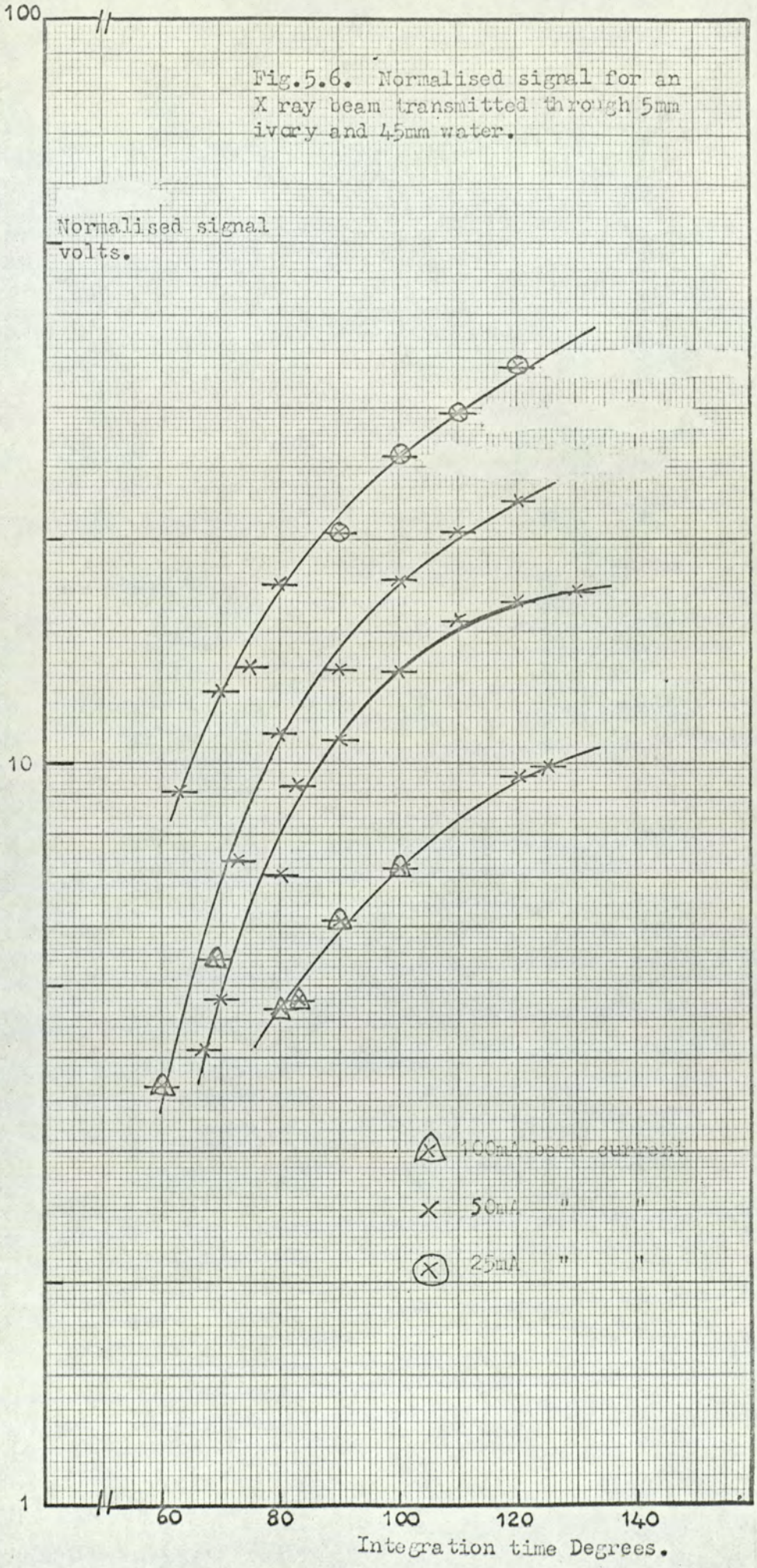

Fig.5.6. Normalised signal for an X ray beam transmitted through 5mm ivory and 45mm water.

The experimental results show that the output signal rapidly increases with peak anode voltage and integration time. In tables A3.1 - A3.4, Δ is the difference in mm between two step wedge traces obtained for a 5% difference in peak voltage setting. This signal voltage difference will depend upon the oscilloscope amplification and the beam current. For all settings Δ is small which shows that the densitometer operates satisfactory over a very wide range of conditions. Because the experimental error is larger than the theoretical error (Chapter 6), a detailed comparison between theory and experiment cannot be made to assess the accuracy of the compensation mechanism. As has been remarked in the previous paragraph, the experimental error in the compensation mechanism is small, which is in agreement with the theory.

The graphs shown in Figs. 5.1 - 5.4 have a similar shape with nearly identical decrements in signal for equal increments in the X ray path length of ivory traversed. For any peak anode voltage and integration time, it is seen that this decrement is largest when there is no ivory in the X ray beam path, i.e. when the transmitted beam is softest. However, this decrement does not significantly change owing to the beams appreciable hardening by the aluminium filter and water.

From the same graphs it is also evident that for a particular anode voltage and path length of ivory, that the discrimination increases continuously with increase of integration time. This is in disagreement with the simple theory which predicts only a very small increase in the discrimination if the integration period is long (> 130°). This is discussed further in Chapter 6.

The discrimination offered at 90kVp 80° integration time is about 0.5 volt mm^{-1} ivory for a 5mm path length of ivory.

This enables a bone profile to be measured to within about 0.3mm ivory equivalent if the error in assessing the position of the trace is 0.15 volt.

Figs 5.5 and 5.6 show the variation of signal voltage as a function of integration time for X rays transmitted through 5mm ivory and 45mm water. The results were normalised to 50mA beam current. The voltage signals do not follow more smoothly because of the error in integration time (± 3°) and the variation of the beam current waveform as was described in Chapter 4.

5.6. Ivory tube measurements.

Initial scans were made of a hollow ivory tube which was used to simulate the ulna. A typical scan, made at 90kVp anode voltage, 50mA beam current and 80° integration time is shown in Fig.5.7 together with the ivory step wedge.

To assess the compensation afforded by the densitometer for peak anode voltage fluctuations, a second trace was made at 95 kVp and compared with the first. This is shown in Fig.5.8 and the two traces are shown superimposed in Fig.5.9. The two traces were normalised corresponding to 5mm ivory in the X ray beam path because corresponding to this level there is theoretically zero error as the filtration above the two detectors are equal (chapter 2).

The two superimposed traces show that the compensation afforded by the densitometer is very good except when there is no ivory in the bottom detector beam path i.e. when the transmitted beam is softest. The traces also show the high resolution given by the densitometer which is evident by the cusps at the two maxima absorption peaks. The slight asymmetry of the peaks in the trace is caused by a slight off centring of the central hole. However, the right-hand peak is seen to correspond very well to the calculated level of 10.2 mm on the ivory step wedge.

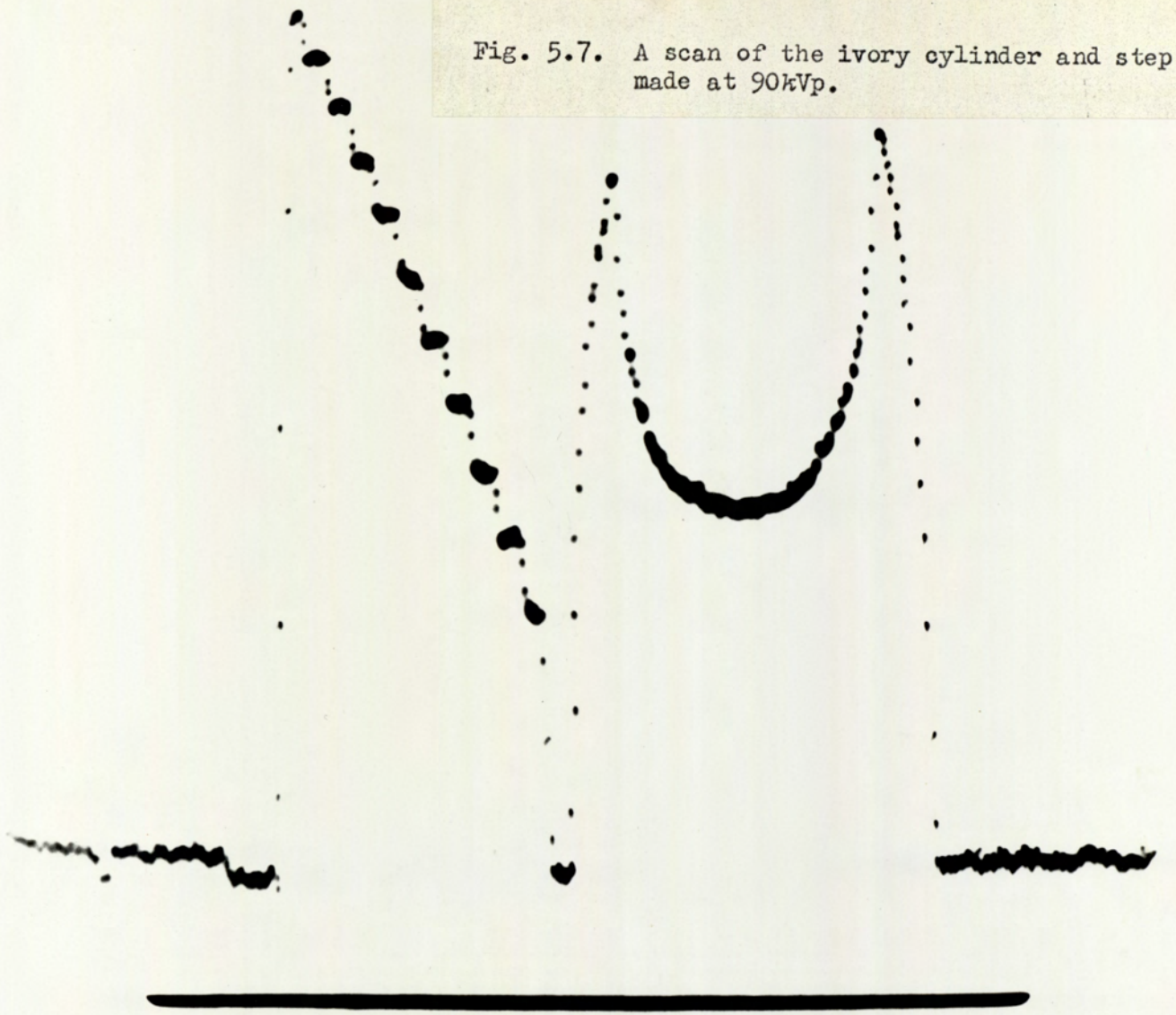

Fig. 5.7. A scan of the ivory cylinder and step wedge made at 90kVp.

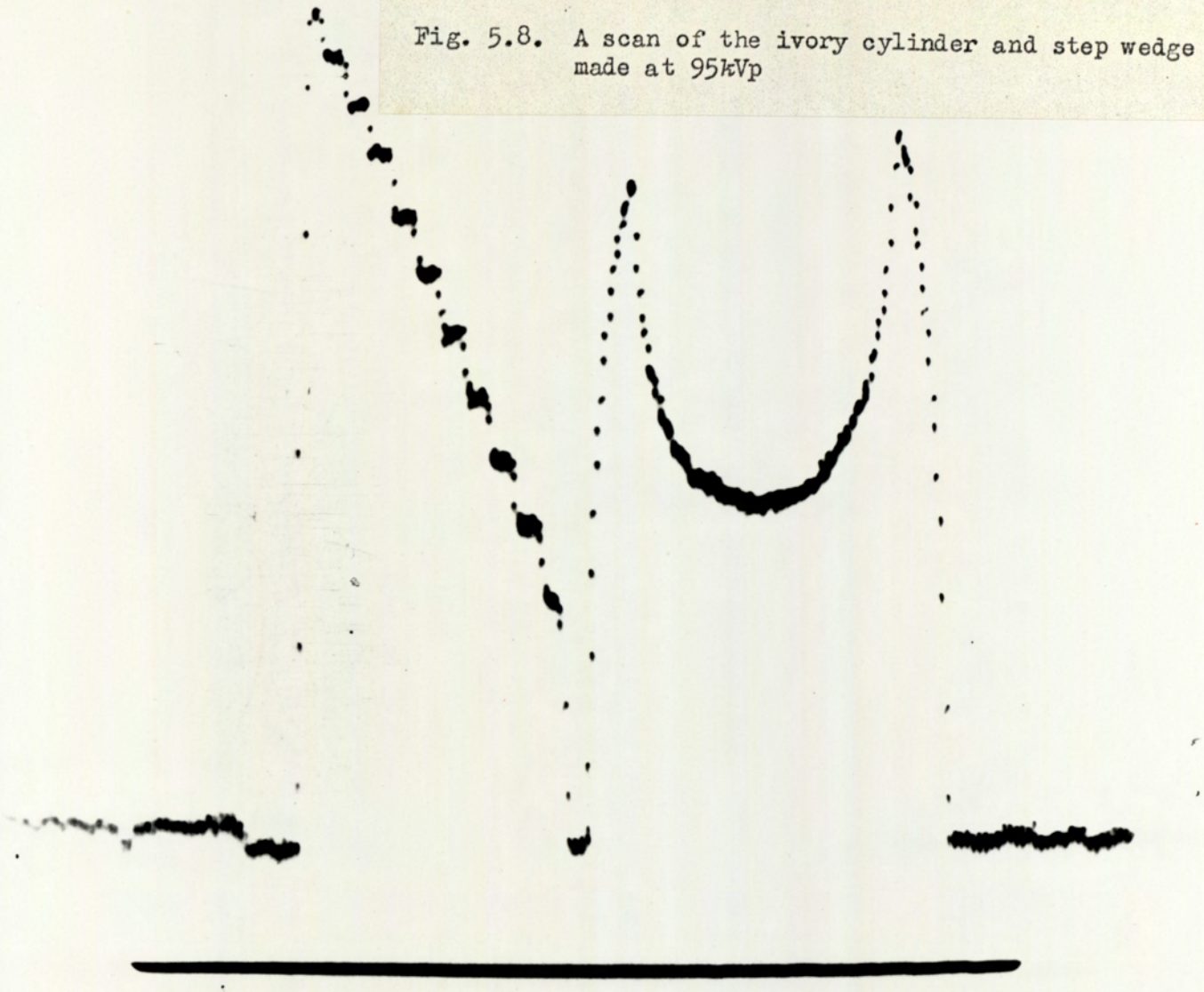

Fig. 5.8. A scan of the ivory cylinder and step wedge made at 95kVp

Fig. 5.9 Figs 5.7 and 5.8 superimposed.

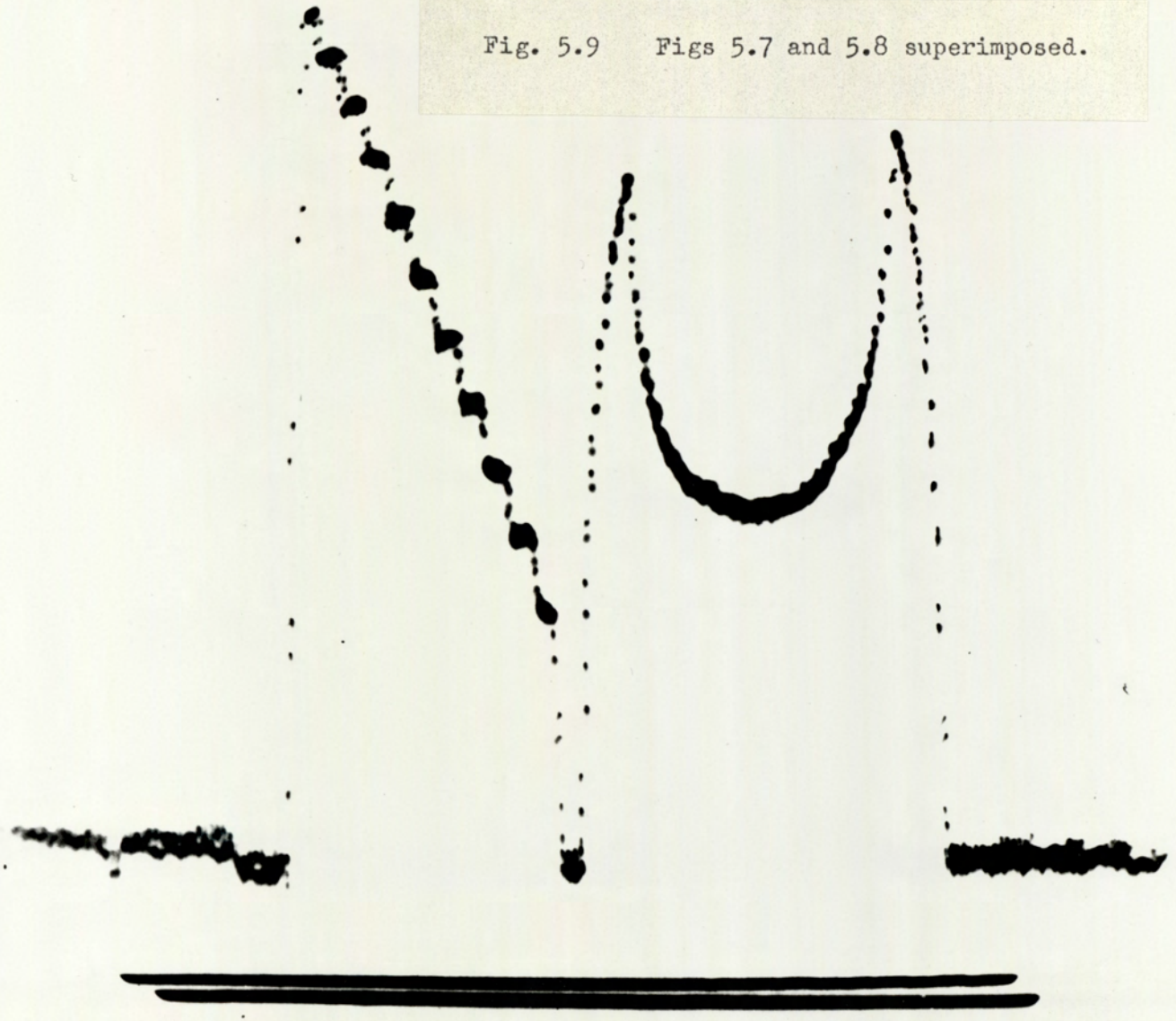

SAF.L

5.7. Dead ulnae measurements.

Scans were made of about fifteen ulnae removed from deceased geriatric hospital patients. The scans were taken at 10mm intervals from the ulnae styloid and a second set of traces were made with the ulnae rotated by a right angle.

In making scans of the ulnae repeat scans were made in order to check the reproducibility. A typical pair of observations is shown in Figs.5.10 and 5.11. They are shown superimposed in Fig.5.12. It is seen that the considerable structural detail is reproduced well on the two traces. To make a quantitative assessment of the reproducibility the two peaks on each trace were measured by reference to the ivory step wedge. This was done on two traces for each of four specimens. The measurements were made by the same observer but with a time interval to avoid recollection of previous readings. The average value of the difference between observations as a fraction of the mean is 1.7%. This is shown in table 5.1.

An assessment of the ease and accuracy with which a trace can be measured was obtained by several observers making measurements independently on the same trace. Again the heights of the peaks were assessed in terms of mm of ivory by reference to the step wedge. The variation expressed as a standard deviation was 1% of the mean and is shown in Table 5.2.

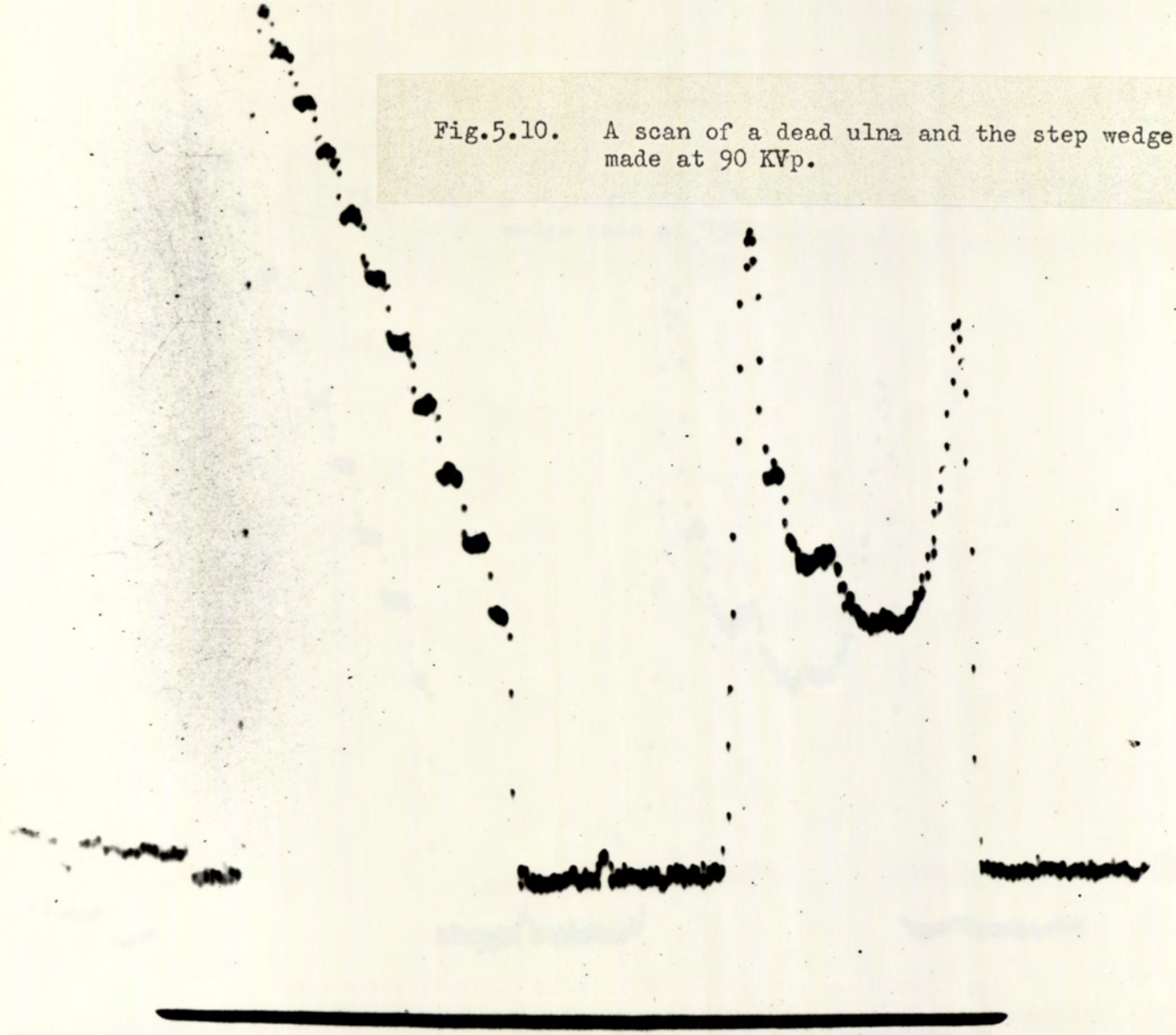

Fig.5.10. A scan of a dead ulna and the step wedge made at 90 KVp.

TABLE 5.1.

	1st Peak		2nd Peak	
	1st Trace	2nd Trace	1st Trace	2nd Trace
Specimen A	8.73	8.70	7 .83	7.69
Specimen B	6.25	6.15	9. 00	8.92
Specimen C	12.66	12.87	10. 73	11.11
Specimen D	10.45	10.20	8. 15	8.08

Peak heights measured on two peaks for each specimen. The observations are in mm of ivory measured by reference to the step wedge. The average value of the difference between observations as a fraction of the mean is 1.7%.

TABLE 5.2.

	1st Peak	2nd Peak
Observer A	10.3 ± 0.2	10.1 ± 0.2
Observer B	10.4 ± 0.2	10.2 ± 0.2
Observer C	10.2 ± 0.2	10.0 ± 0.2
Observer D	10.5 ± 0.2	10.3 ± 0.2
Observer E	10.3 ± 0.25	10.15 ± 0.25

Peak heights measured on two peaks for observer. The observations are in mm of ivory measured by reference to the step wedge.

Average of 1st peak = 10.35

Standard deviation = 1%

Average of 2nd peak = 10.15

Standard deviation = 1%.

5.8. In vivo reproducibility.

The reproducibility of in vivo measurement represents the limit of accuracy with which subject measurements can be made. In vivo measurements have been made on several subjects and to test reproducibility a scan of a subject's left ulna was made and is shown in Fig.5.13. After taking the trace the arm was removed from the bath and replaced after an interval when a second trace was taken. The second trace is shown in Fig.5.14 and the two traces are superimposed in Fig.5.15. It will be seen that the reproducibility is comparable with that achieved by scans made on dead bones. The small differences between the traces shown in Figs.5.13 and 5.14 are due to the limits of longditudinal and rotational precision with which the arm and the hand may be repositioned in the bath. The first limitation can almost be overcome by noting the extremity of the third finger of the supinated hand with a suitable marker placed in the bath. The second, which is responsible for the larger part of the error can be minimised by asking the subject to keep the axis of his whole arm parallel to the travelling bath. This limitation is discussed further in Chapter 7.

5.9. Choice of operating conditions.

To make a scan the operator has three parameters which contribute to the accuracy and size of the output signal - the beam current, peak anode voltage and the electronic integration time. In chapter 2 the factors which give a good performance were outlined, and the experimental and theoretical results are given in chapters five and six respectively.

To obtain reasonable signal (~10V) with low error in compensation technique a peak anode voltage of 90 kVp was chosen with an integration

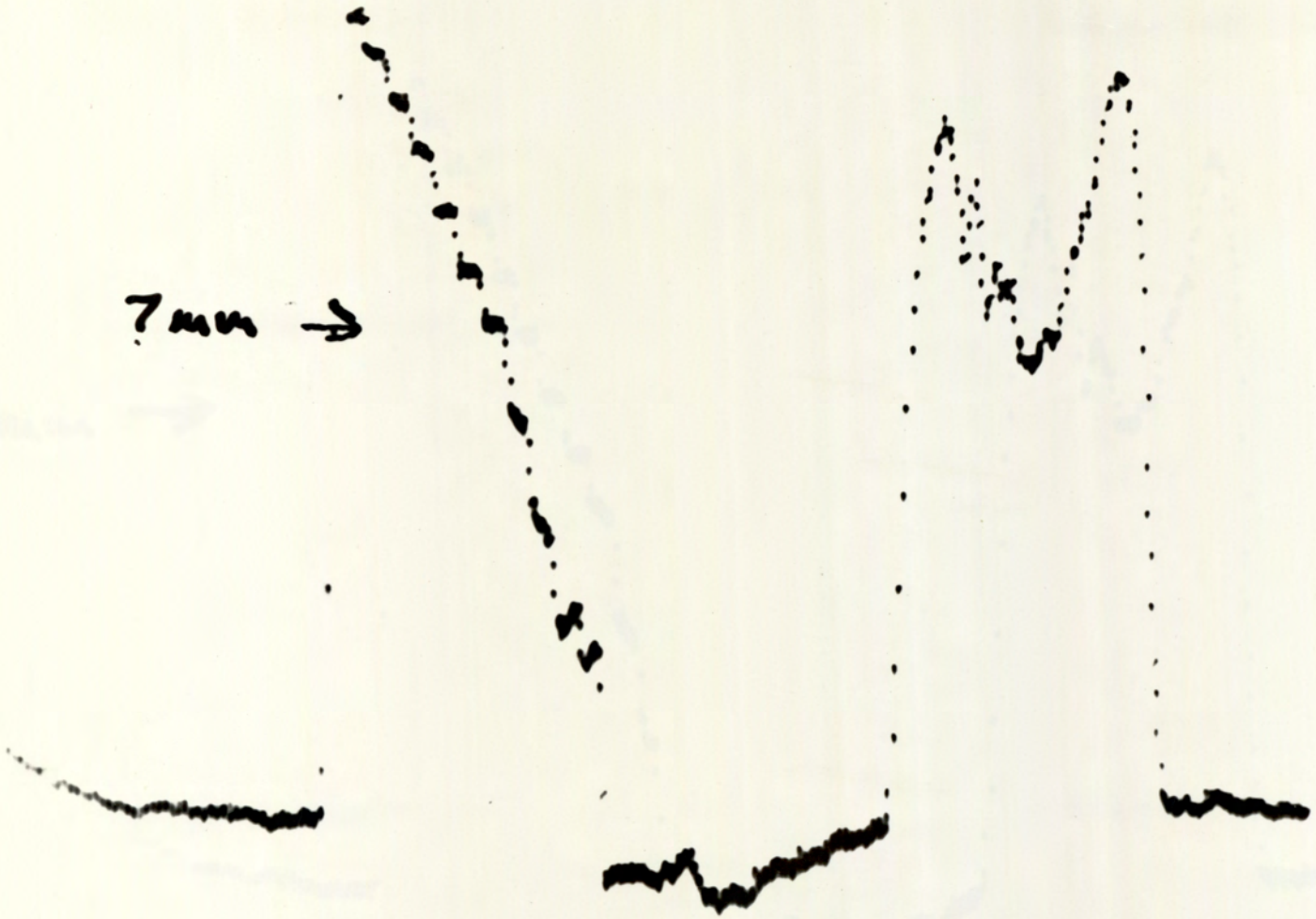

Fig.5.13. A scan of an invivo ulna and the step wedge made at 90KVp.

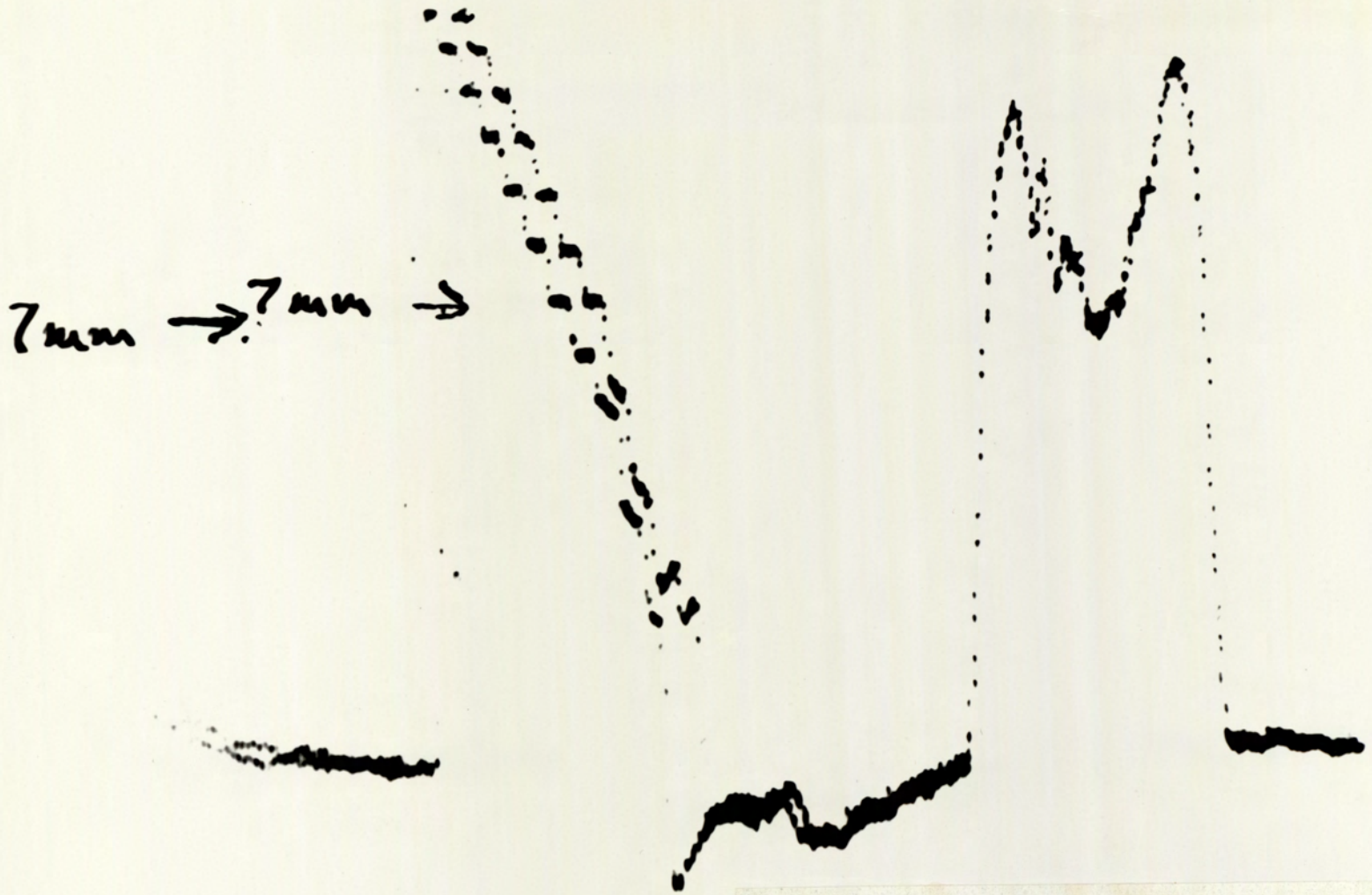

Fig.5.15. Figs 5.13 and 5.14 superimposed.

time in each half cycle of 80° and an electron beam current of 50 mA. For a scan lasting about six seconds, the Mullard Guardian 125 X ray generator is run at about half of its maximum permitted rating and the patient dose has shown to be small.

5.10. Dose measurements.

If repeated measurements are to be carried out on the same sample of bone it is necessary to know the radiation dose received during the examination scan. The X ray beam area is about 20 mm^2 (10 x 2mm) and the total area of irradiated tissue during clinical investigation is about 350 mm^2. For an average path length of 20 mm the total volume of tissue will be about 7 cm^3.

In the dose measurements LiF TLD finger badges were chosen principally because of their small size, tissue equivalence and waterproof covering. Other properties are described in reference 144.

To simulate the ulna the ivory cylinder was used as a phantom in the bath of water. The dose was measured by placing the ivory cylinder on the floor of the perspex bath with the bath filled with water to a depth of 50 mm. The water surrounding the ivory was assumed to be tissue equivalent for the purposes of dose assessment. A finger badge was positioned at A, Fig. 5.16, care being taken to ensure that the full sensitive area of the badge was in the X ray beam path. In measuring the dose, only one badge was used during a scan so that X ray beam perturbation was minimal. The badge was exposed by moving the bath through the X ray beam in the normal way. Three runs were made in one position in order that a reasonable dose measurement be obtained.

This procedure was repeated for the positions in Fig. 5.16 and the badges were then dispatched for processing. The dose readings for 90 kVp and 50mA exposure are given in table 5.3.

Two additional measurements were made without the ivory

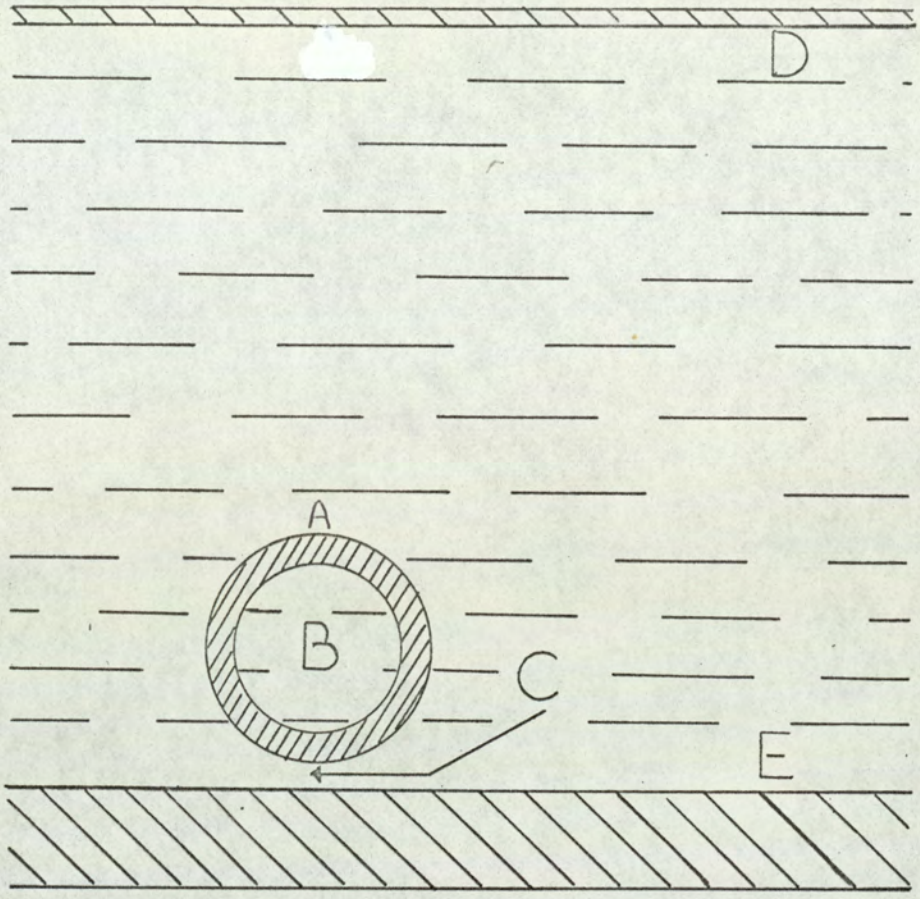

Fig. 5.16.

Positions of the LiF TLD badges in the bath of water

Water

Ivory

Perspex

cylinder in the bath of water. The first (Fig.5.16) was underneath the perspex box at the perspex-water interface and the second at the full depth of the water. The average of three exposures is given.

The scattered dose to the subject's and operator's body is believed to be less than 10^{-3} of that recommended by the I.C.R.P.[145]. This is discussed at greater length in chapter 7.

TABLE 5.3.

Position in Fig.5.16	Dose for 3 scans m rem	Dose per scan m rem
A	610	303
B	410	137
C	300	100
D	1500	500
E	380	127

CHAPTER 6.

Theoretical assessment of densitometer performance.

6.1. Introduction

In Chapter 2 the theory of the densitometer was described and equations were derived for the magnitude of the signals expected from the two detectors. It was seen that the signal strength is dependent upon four variables.

(1) The anode voltage,

(2) Electron beam current,

(3) Electronic integration time,

(4) The absorbers in the path of the two beams.

There are also several fixed factors which determine the magnitude of the signal. These are detector sensitivity, electronic amplification and source detector geometry.

In order to asses the limitations of the experiment it was decided to investigate the performance of the densitometer theoretically making the assumptions outlined in Chapter 2. Initial calculations were carried out to asses the correction afforded by the densitometer switching technique to the error which would result from fluctuations of the X ray tube voltage in a system using only a single detector to measure the density of the beam after passing through the limb. This was done for different anode voltages, integration times and bone thicknesses in the path of the second detector. Although the densitometer can only measure the total X ray absorption relative to a standard, calculations were made to estimate the effects on the output signal which would be caused by bone density changes and those caused by changes in the calcium content, Finally, calculations were made to test the idea that a scintillation detector

responding linearly above a fixed low energy limit would further improve the accuracy of the densitometer. The calculations are discussed in later sections in this chapter.

6.2. The assumptions made in the theory.

In order to avoid excessively complicated mathematics the following assumptions have been made :

6.2.1. Voltage.

The instantaneous anode voltage $V(t)$ was regarded as having a rectified sinusoidal with an amplitude V_{max} and an angular frequency ω of 100π radians sec^{-1} ($\equiv$ 50 Hz). No harmonics were introduced, and the anode voltage was regarded as being in phase with the electronic switching of the integrator and amplifier. The instantaneous voltage may be simply represented by

$$V(t) = V_{max} | \text{Sin } (\omega t) | \qquad 6.1.$$

where t = time.

6.2.2. Electron beam current.

The electron beam current is generated by the passage of a large current (few amperes) through a tungsten filament inside the X ray vacuum tube. An X ray tube with its tungsten filament is shown in Fig. 4.2. The thermal time constant of the filament was thought to be sufficiently long to treat the instantaneous current $I(t)$ as being time independent i.e.

$$I(t) = I \qquad 6.2.$$

where I = constant beam current.

Although investigations into the validity of equation 6.2 have shown the current not to be constant (Chapter 4), the equation has been used in the theory as a first approximation.

6.2.3. Spectral Distribution of the X rays.

When high energy electrons are quickly retarded in the

tungsten anode the spectral distribution will be given by Kramers law[72]. Characteristic X ray lines of tungsten may also be emitted if the incident electron energy is sufficiently high.

The spectral distribution of the emitted X rays is changed by the preferential absorption of low energy X rays in the tungsten target and any external filtration placed in the beam path. Although the calculation of the attenuation caused by external filtration is relatively easy, it is not the case for inherent filtration owing to the very complicated mechanism of bremsstrahlung and multiple electron scattering inside the target. An electron may lose up to half of its initial energy in an electron-electron scattering interaction, and hence there will be a large statistical spread in the depth of production of X rays. This has been discussed in greater detail in Chapter 2.

Since the depth of penetration of the electrons in the tungsten target is small ($\simeq 10^{-5}$ mm) as calculated from the Katz-Penfold equation[146], the attenuation of the emerging X ray will be small except for low energies. The equation is

$$R = 412E^{(1.265 - 0.0954\ln(E))} \text{ mg cm}^{-2} \qquad 6.3.$$

where R = range of electron (mg cm^{-2})

E = incident electron energy (MeV)

The range of electrons in the energy region 10 - 100keV has been calculated using this equation and the results are given in Table A6.1 and shown graphically in Fig. 6.1. Also shown is the distance perpendicular to the beam through which the X rays have to travel to escape from the tungsten in the direction of the detector. The effective depth of bremsstrahlung generation has been taken to be one quarter of the electron range, following the

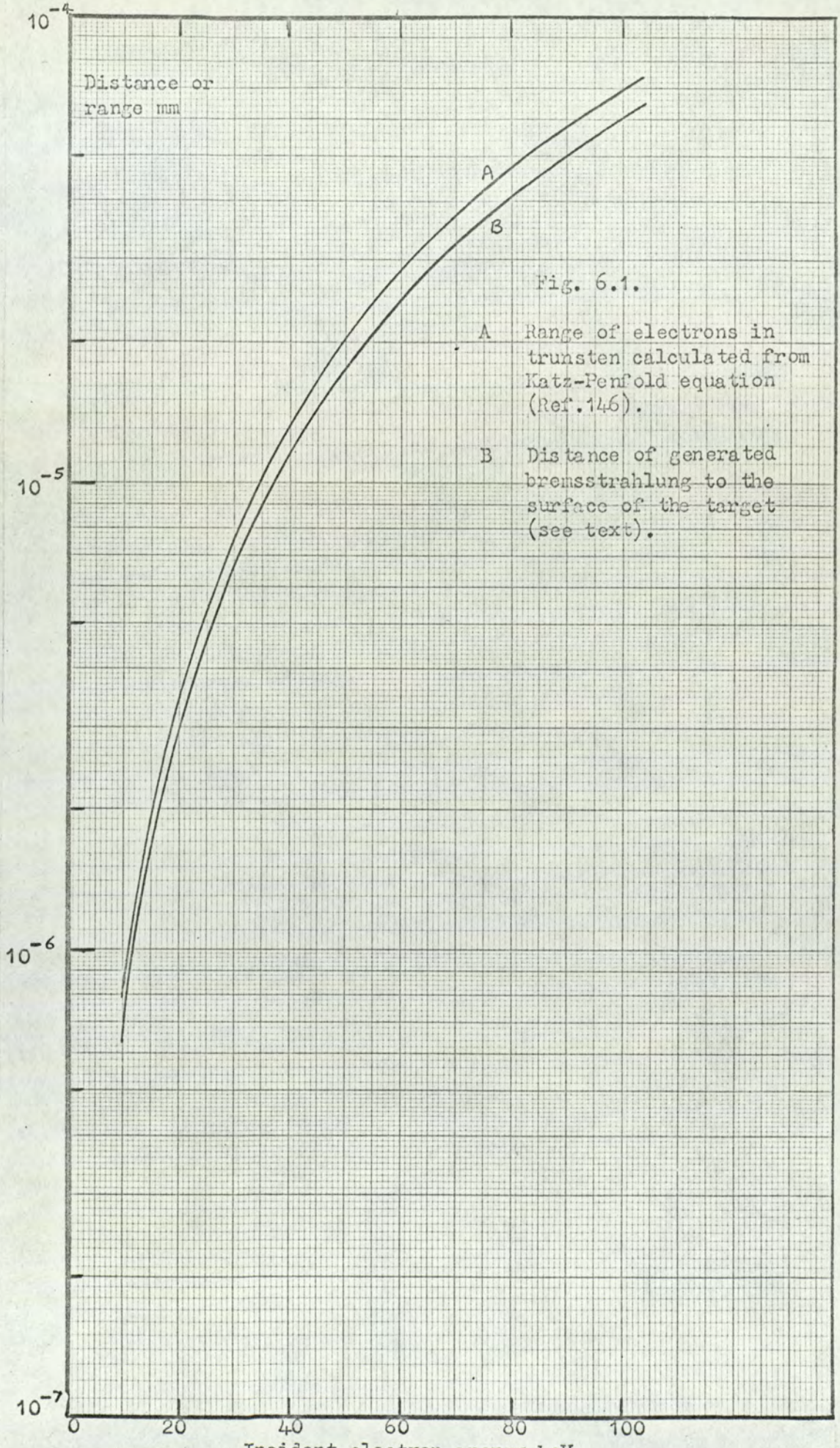

Fig. 6.1.

A Range of electrons in trunsten calculated from Katz-Penfold equation (Ref.146).

B Distance of generated bremsstrahlung to the surface of the target (see text).

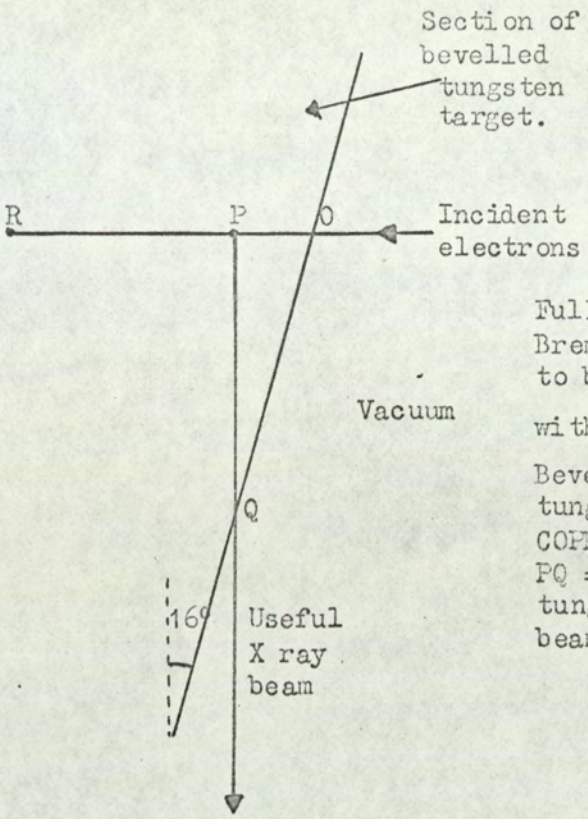

Fig. 6.2.
Diagram showing the assumptions made regarding the inherent filtration of tungsten target.

Full range of electrons=OR
Bremsstrahlung considered to be generated at point P with $\frac{OP}{OR} = \frac{1}{4}$
Bevelled angle of the tungsten target = 16°
COPR is a straight line
PQ = distance through the tungsten which a useful beam has to travel.

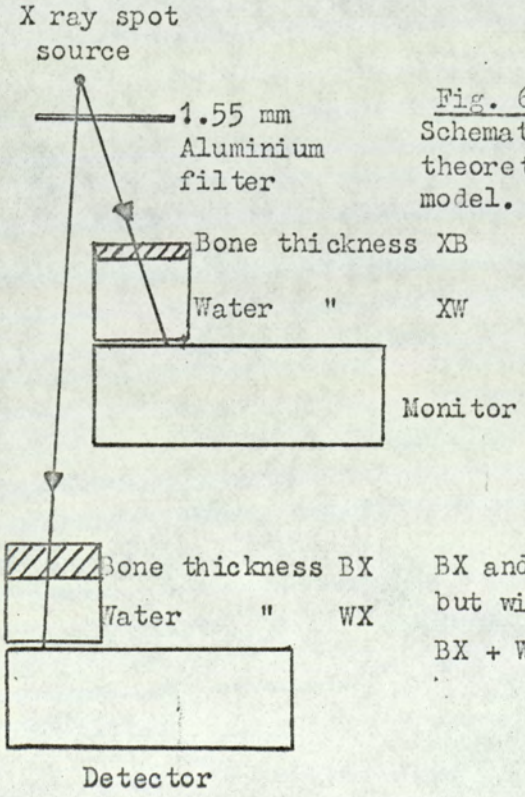

Fig. 6.3.
Schematic diagram of the theoretical filtration model.

XB = 5 mm
XW = 45 mm

BX and WX are variable but with the condition
BX + WX = 50mm

work of Stoddard[90] and Farr[91], and the calculations were made for a target bevelled at 16°. Fig. 6.2. illustrates the assumptions made.

In view of the small range of photons through the tungsten target it was decided to ignore the self filtration. The filtration in the boro-silicate vacuum-tube glass was also ignored in view of its low effective atomic number and the small thickness of the glass ($\simeq$1.6mm).

6.2.4. The attenuation coefficients.

The attenuation coefficients given by McMaster et al[147] were used in the computation as they are accurate to about 2% except at the lowest energies (< 10keV). The authors fitted a polynomial equation to the cross section for every element so that intermediate energy cross sections may be easily calculated. The polynomial has the form

$$\sigma_{mr} = \frac{1}{C_r} \sum_{p=0}^{3} a_p \left[\ln(E) \right]^p \qquad 6.4.$$

where σ_{mr} = rth partial mass absorption cross section ($cm^2\ g^{-1}$)

C_r = a constant relating the cross section in 6 per atom to that in $cm^2\ g^{-1}$.

E = energy of the X ray(keV)

a_p = pth Polynomial coefficient.

Equation 6.4. gives the cross section for one atomic effect, e.g. K. shell absorption. The total mass absorption cross section σ_{mt} will therefore be the sum of all the partial cross sections σ_{mr} i.e.

$$\sigma_{mt} = \sum_{r=1}^{R} \sigma_{mr} \qquad 6.5.$$

for R partial cross sections.

Each partial mass absorption cross section is given by an equation similar to equation 6.4 and in general four phenomena were taken into account

(i) and (ii) K and L shell absorptions

(iii) and (iv) Coherent and incoherent scattering.

The total mass absorption cross section for one element σ_{mt} therefore becomes

$$\sigma_{mt} = \frac{1}{C_r}\left[\sum_{r=1}^{4}\sum_{p=o}^{3} a_{rp}\ [\ln(E)]^p\right] . \qquad 6.6$$

For n elements, σ_{mt} will be

$$\sigma_{mt} = \sum_{i=1}^{n} \frac{w}{C_r}\left[\sum_{r=1}^{4}\sum_{p=o}^{3} a_{rpi}\ [\ln(E)]^p\right] \qquad 6.7$$

where C_r is the constant defined by equation 6.4 for the ith element w_i is the fraction by mass, of the ith element.

Multiplication of equation 6.7 by the density of the compound or mixture will give the linear absorption coefficient μ_L .

6.2.5. Attenuation of the beam.

Fig. 6.3 illustrates the external filtration model considered in the calculations. Above the monitor is situated a 5 mm slab of ivory together with a perspex cell containing 45 mm water. Over the second detector is the specimen of bone under examination in the bath of water. The total path length of perspex in the two beams was made equal (6.3 mm) so that spectra of the two X ray beams would be as similar as possible. In the calculations the attenuation due to the perspex was ignored. The absorption was considered to be due to five elements, hydrogen, oxygen, aluminium, phosphorous and calcium, having total mass absorption cross sections given by the polynomial expressions of McMaster et al (147). The

composition and density of the bone and ivory are discussed in the next section.

6.2.6. The composition of the bone and ivory.

It was stated in chapter 1 that many workers have regarded hydroxyapatite, $[Ca_3(PO_4)_2]_3\ Ca(OH)_2$, as being representative of the inorganic composition of bone. In the equations to calculate the attenuation coefficient of bone this same assumption was made and the density of hydroxyapatite was adjusted to 1500 $k_g\ m^{-3}$ to take into account the percentage of organic bone material. Most (>90%) of the organic matter is collagen [1]. The density of the ivory used was 1700 $k_g\ m^{-3}$ which is about the same as human bone [148-151]. In later calculations, the effective density and the calcium content of the bone were changed in order to assess the sensitivity of the densitometer. The linear absorption coefficient of bone used in the calculations is shown in Fig. 6.4 and given in table A6.2.

6.2.7. The water attenuation.

The absorption coefficients for muscle tissue and fat have been given by Spiers [151] and are shown in Fig. 6.5. together with the coefficient for water. It was noted in chapter 4 that a 2% common salt solution was more tissue equivalent than pure water, but in order to keep the mathematics simpler the tissue equivalent liquid in the bath was taken to be water. The calculated differences between the salt solution and water are given in Table A6.2 and shown in Fig.6.6. By considering only water in the bath, the advantage of testing the numerical accuracy of double integration is offered in the special cases where the filtration of both beams is equal. This is discussed in Section 6.3.

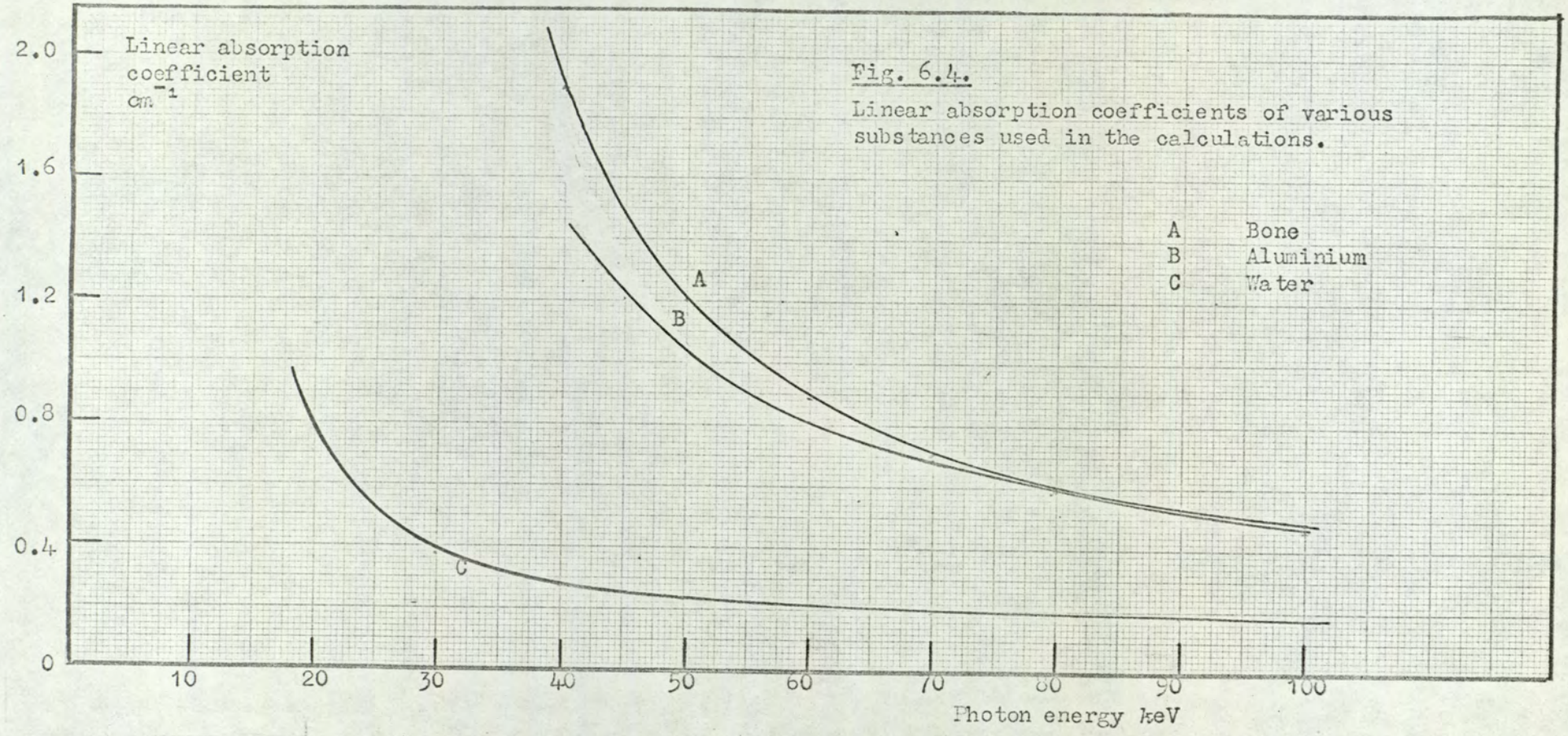

Fig. 6.4.

Linear absorption coefficients of various substances used in the calculations.

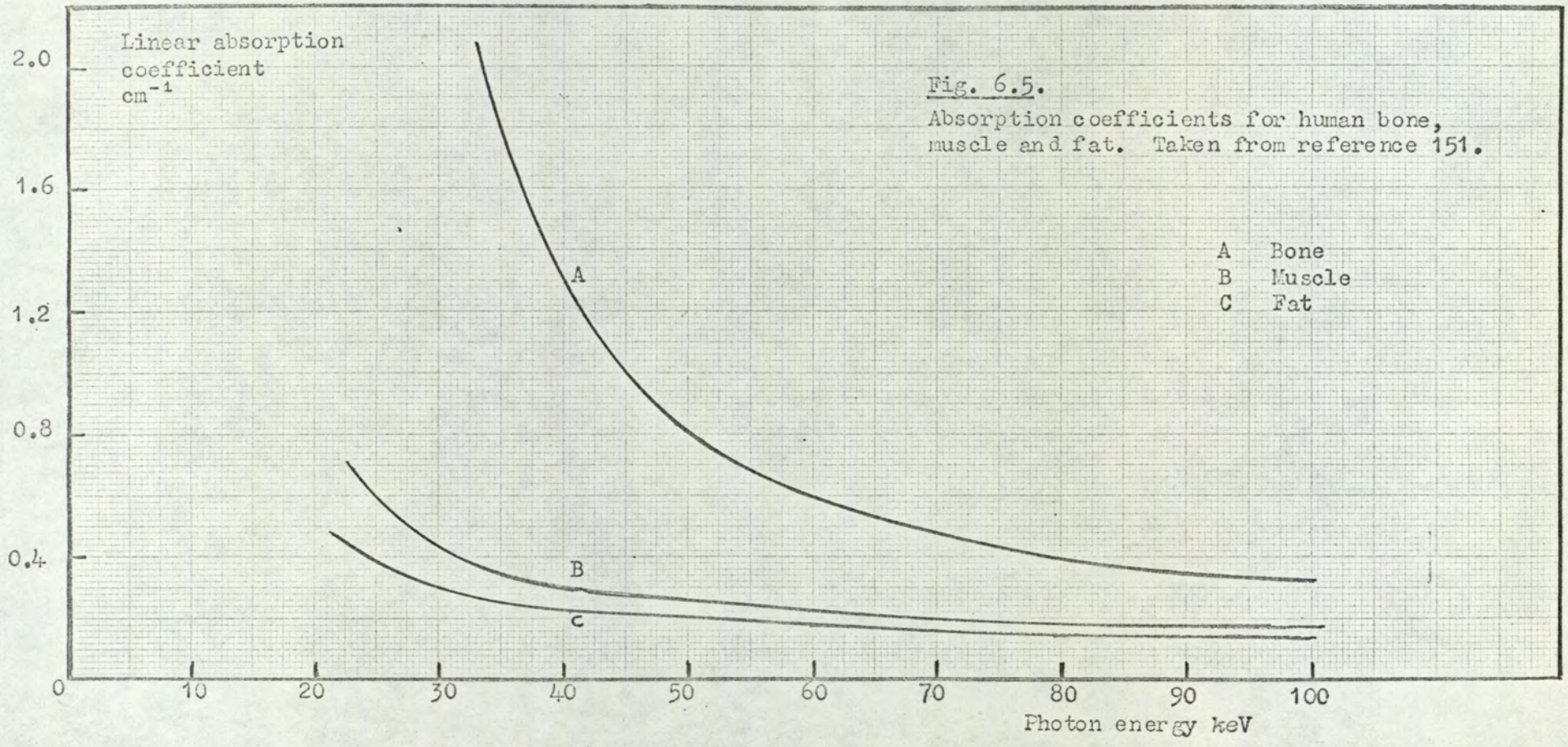

Fig. 6.5.
Absorption coefficients for human bone, muscle and fat. Taken from reference 151.

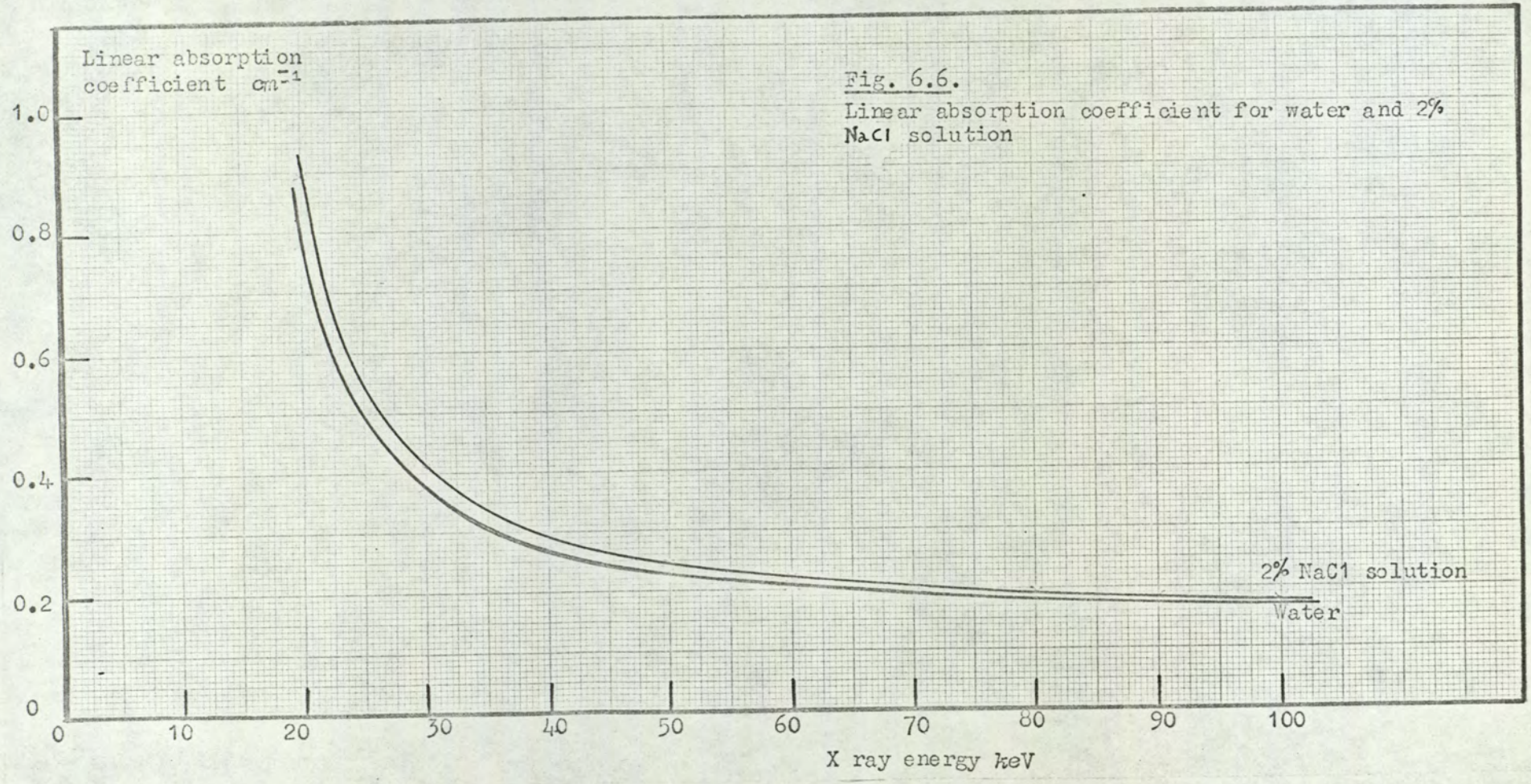

Fig. 6.6.
Linear absorption coefficient for water and 2% NaCl solution

6.3. Theoretical calculations.

6.3.1. Calculations to assess the performance of the densitometer.

These were carried out on the University's digital computer, the programme being given in Appendix 5.

The double integrations needed to evaluate the relative magnitude of the two detector signals were carried out using a modified Simpson integration procedure, the original being given in reference 152. This was chosen because it was found to be the fastest computationally. Other procedures, such as those given in references 152 and 153 were found to be too slow for the accuracy required ($\leq 0.1\%$). The calculated signals were not adjusted for the constant factors mentioned in Section 6.1.

The monitor and detector signals were calculated using the polynomial expressions describing the attenuation coefficients.

Writing equations 2.36 and 2.37 with the sinusoidal voltage $V(t) = V_{max} \sin wt$ and simplifying the exponential term to that given in equation 2.23, then

$$G_1 = \int_0^{t_2} I(t) \int_0^{V_{max} \sin wt} (V_{max} \sin wt - V) e^{-\sum_{i=1}^{n} \mu_i x_i} \, dV \, dt \qquad 6.8$$

$$= W$$

and

$$G_2 = \int_0^{t_2} I(t) \int_0^{V_{max} \sin wt} (V_{max} \sin wt - V) e^{-\sum_{i=1}^{m} \mu_i x_i} \, dV \, dt \qquad 6.9$$

where μ_i replaces $\mu_{Li}(E)$ for clarity and $\mu_i = \sigma_{mt}/\rho$ in equation 6.6, where ρ is the density of the absorber.

G_1 and G_2 may be found if the lower limits of both integrals are made non-zero, otherwise the absorption coefficients become infinite which leads to obvious difficulties. The lower time and energy integration limits were made t_1 and V_{min} respectively with

$$V_{max} \sin wt_1 > V_{min} \qquad 6.10$$

otherwise the computation failed. The precise value of t_1 and

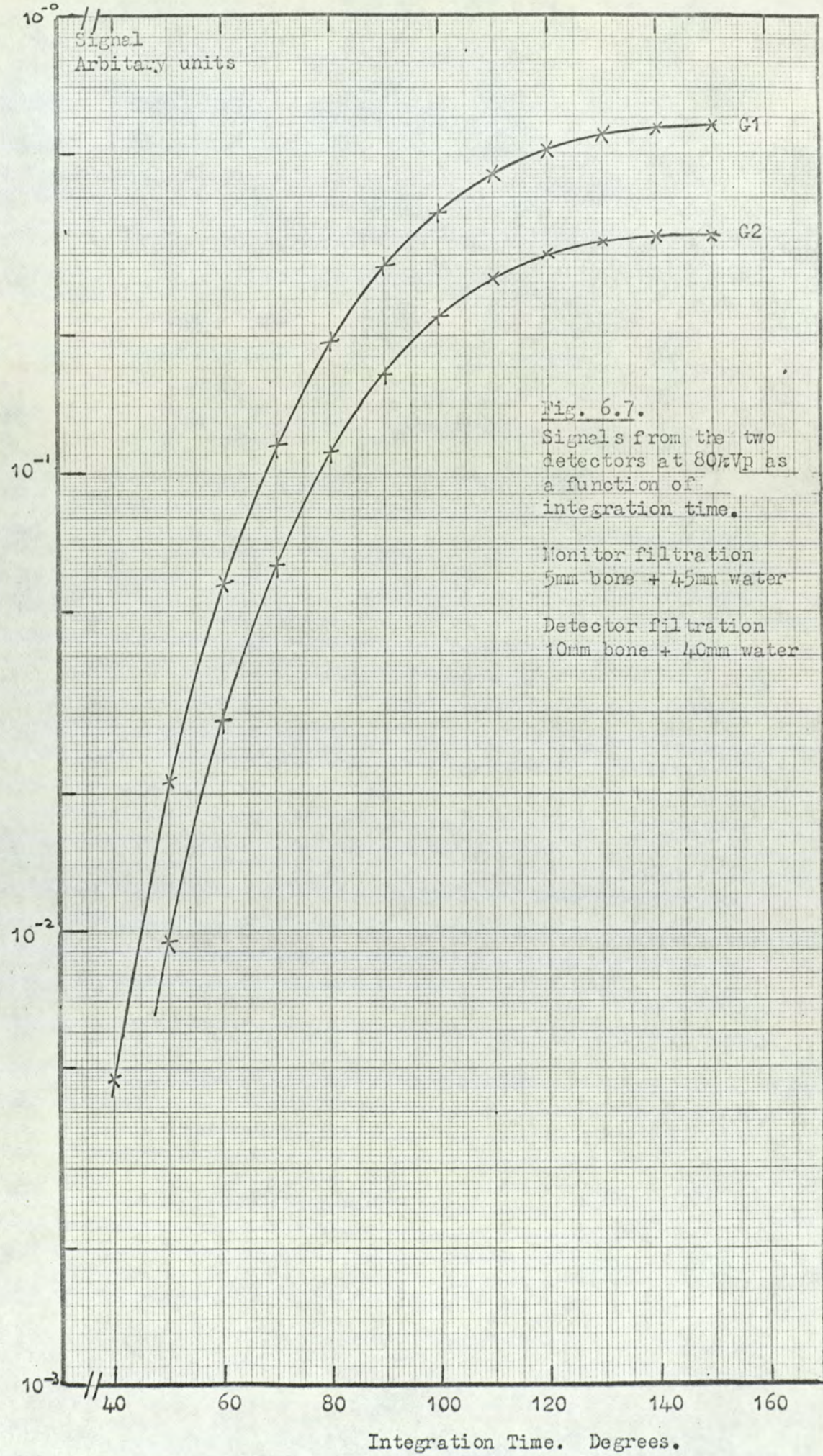

Fig. 6.7.
Signals from the two detectors at 80kVp as a function of integration time.

Monitor filtration
5mm bone + 45mm water

Detector filtration
10mm bone + 40mm water

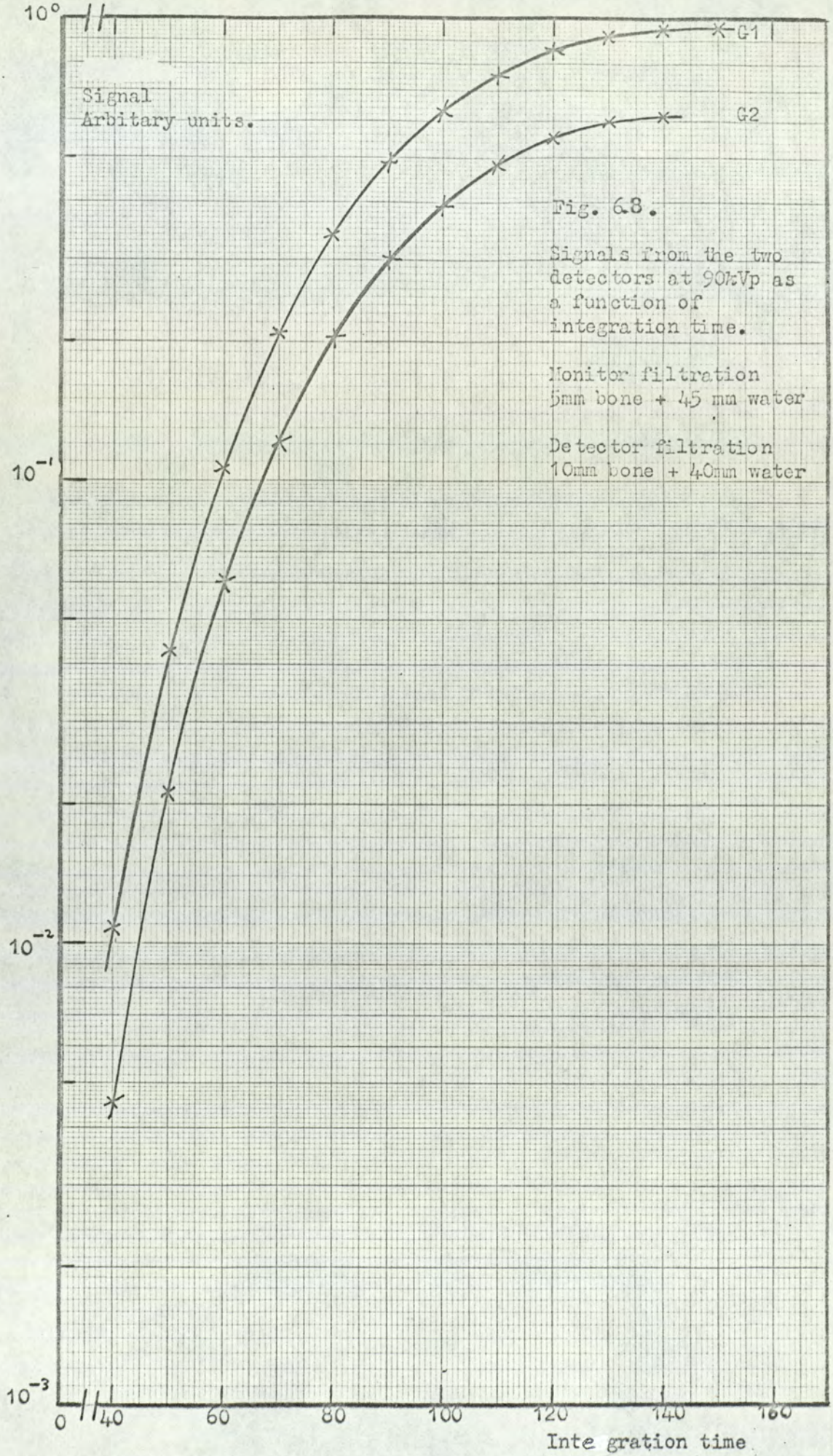

Fig. 6.8.

Signals from the two detectors at 90kVp as a function of integration time.

Monitor filtration
5mm bone + 45 mm water

Detector filtration
10mm bone + 40mm water

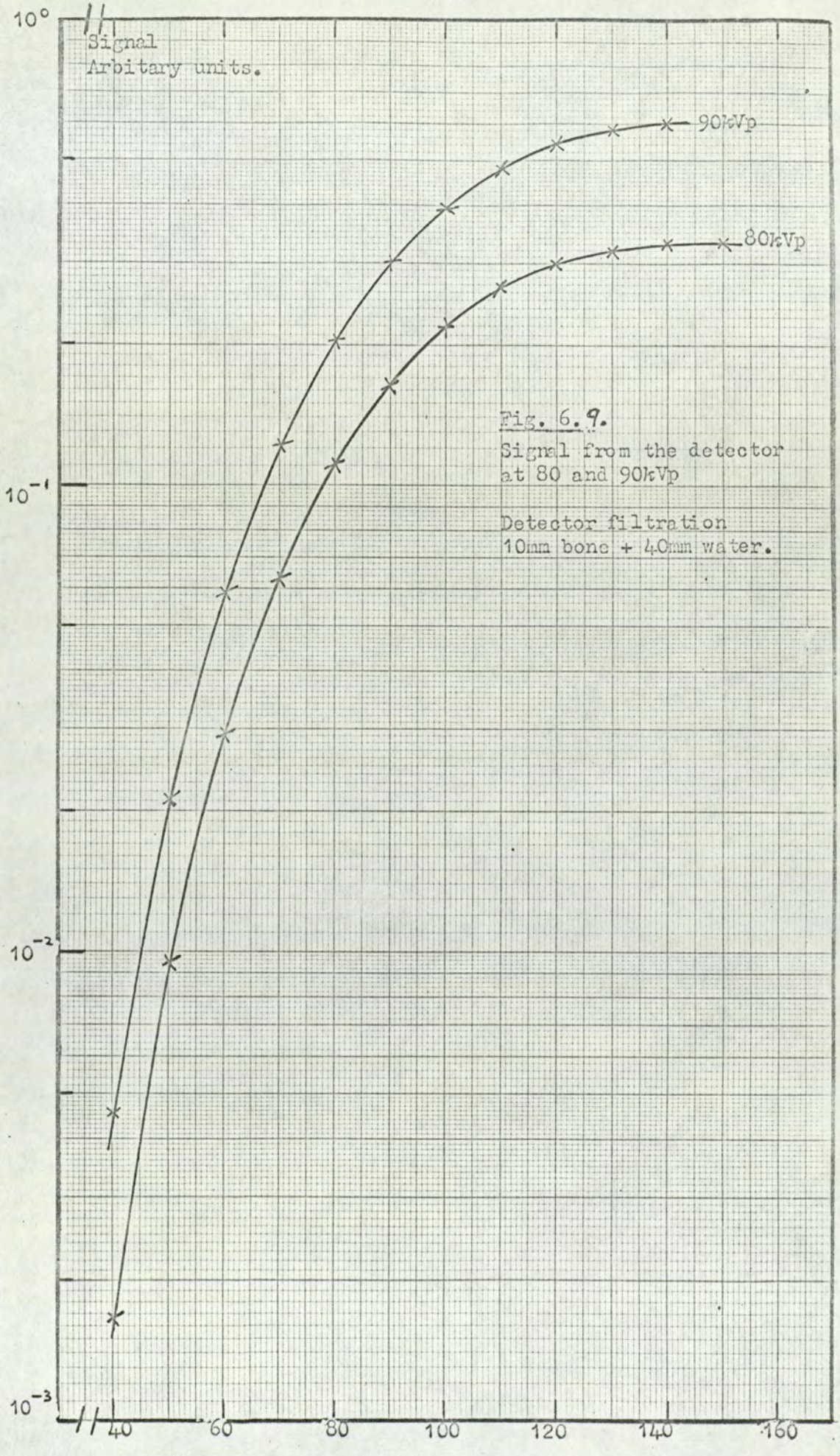

Fig. 6.9.
Signal from the detector at 80 and 90kVp

Detector filtration
10mm bone + 40mm water.

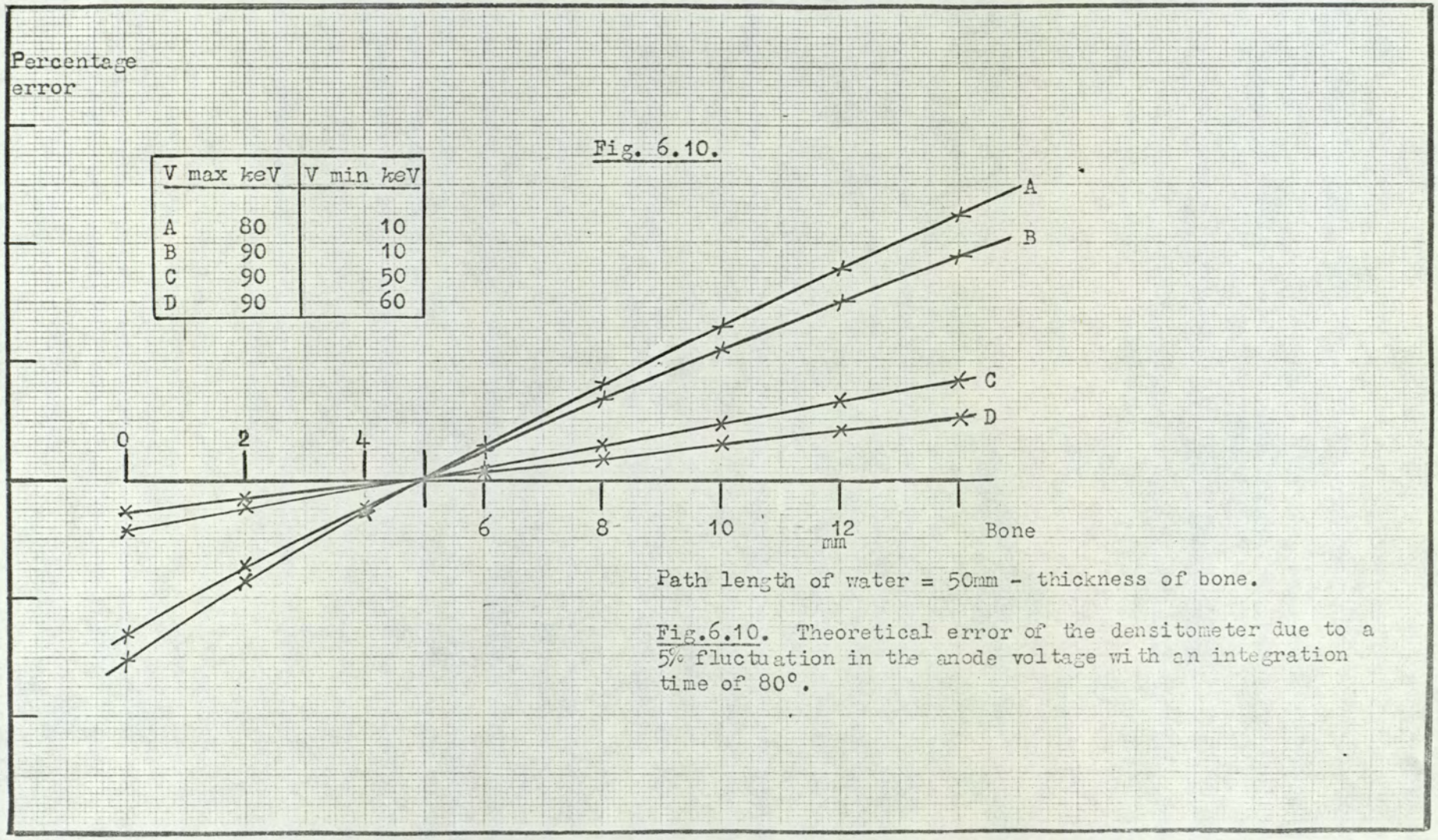

Fig.6.10. Theoretical error of the densitometer due to a 5% fluctuation in the anode voltage with an integration time of 80°.

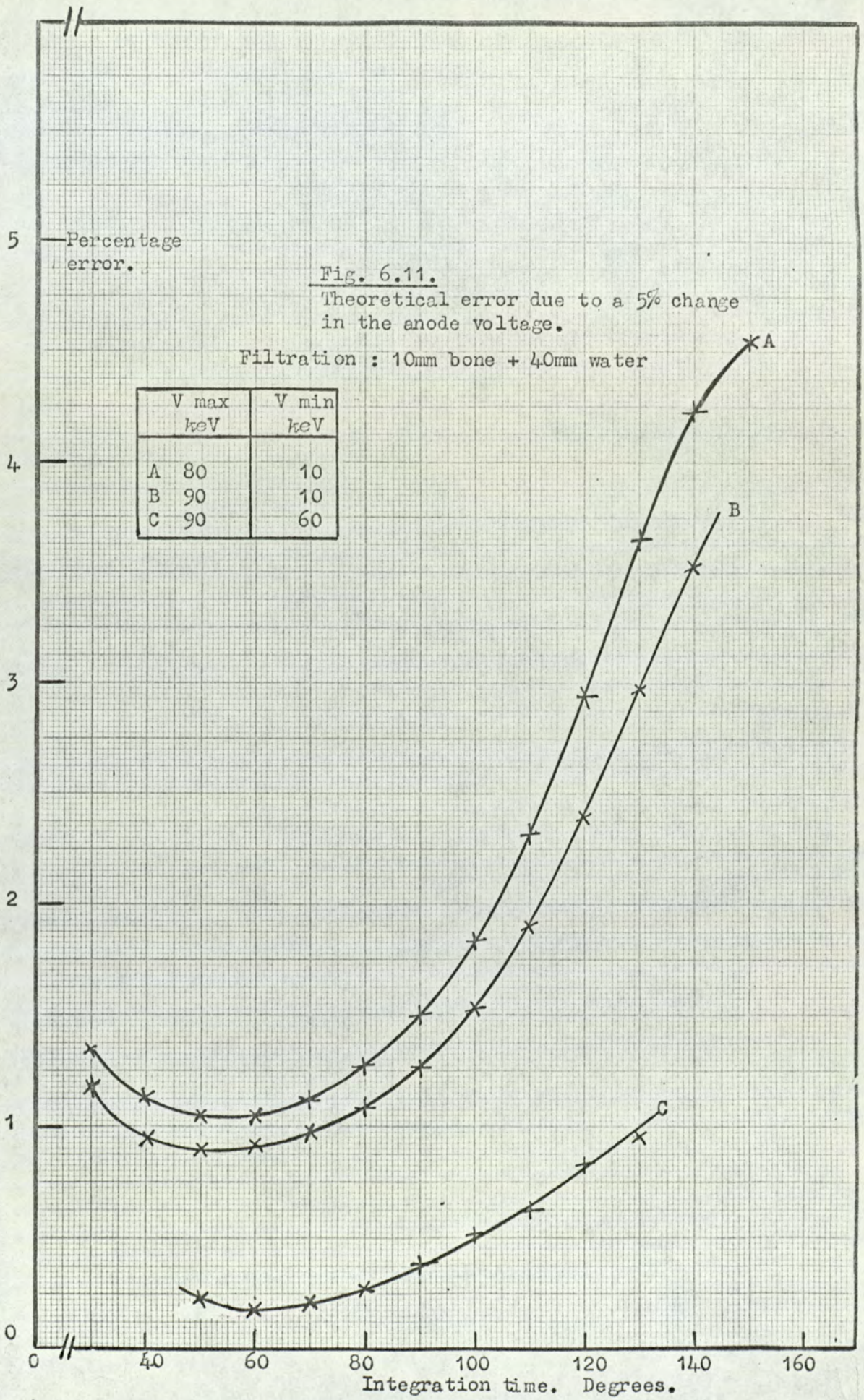

Fig. 6.11.

Theoretical error due to a 5% change in the anode voltage.

Filtration : 10mm bone + 40mm water

	V max *keV*	V min *keV*
A	80	10
B	90	10
C	90	60

V_{min} is not important since below about 15 keV all the photons will be absorbed. V_{min} and t_1 were made 10 kV and $5.555.\ 10^{-4}$ seconds respectively.

The value W (equation 6.8) was found by choosing the anode voltage amplitude and fluctuation, V_{max} and ΔV_{max} respectively and the upper limit of integration time t_2. To calculate the error in G_2 caused by a peak anode voltage fluctuation ΔV_{max} a new upper integration time t_2' was found by using the procedure Bisec (reference 152) to solve the equation

$$\int_{t_1}^{t_2} \int_{V_{min}}^{V_{max} \sin wt} (V_{max} \sin wt - V)\, e^{-\sum_{i=1}^{n} \mu_i x_i}\, dV\, dt$$

$$- \int_{t_1}^{t_2'} \int_{V_{min}}^{V'_{max} \sin wt} (V' \sin wt - V) e^{-\sum_{i=1}^{n} \mu_i x_i}\, dV\, dt$$

$$= 0 \qquad 6.11$$

where $V'_{max} = V_{max} + \Delta V_{max}$. 6.12

The beam current term, I(t) has been omitted in equation 6.11 because of its assumed time independence.

The upper and lower time limits of search used by the procedure Bisec to find t_2' were related to t_2 by the following equations for positive values of $(\Delta V_{max}/V_{max}) = 0.05$.

$$ULT = T2 \qquad (= t_2) \qquad 6.13$$

$$LLT \doteq 0.7 \times T2 \qquad 6.14$$

where

ULT = upper time search limit

LLT = lower time search limit.

Failure to fix a sufficiently low value of LLT leads to a non-sensical solution of t_2'. The accuracy with which t_2' was sought was made 1 μs , which corresponds to the switching time of

the electronics. It should be noted, however, that the accuracy of the solution of equations 6.11 is limited by the number of summations used in the Simpson procedure. In the calculations, 10^3 summations for each double integral were made. Increasing the number of summations rapidly slows down the speed of computation.

To test the accuracy of t_2' found in the solution of equation 6.11 the value of a new monitor signal G_{11} was found by evaluating the equation

$$G_{11} = \int_{t_1}^{t_2'} \int_{V_{min}}^{V'_{max}\,Sin\,wt} (V'_{max}\,Sin\,wt - V)\, e^{-\sum_{i=1}^{n} \mu_i x_i}\, dV\, dt \quad . \quad 6.15$$

Ideally the value of G_{11} should equal G_1 and therefore any difference between the two values represents numerical errors in the Simpson and Bisec procedures. The percentage numerical error ϕ was evaluated from the relationship

$$\phi = 100 \left(\frac{G_{11} - G_1}{G_1} \right) \quad . \qquad 6.16$$

The detector signals were found in a similar way. Normally, two detector signals were evaluated. The first, G_2 , using the anode voltage and upper integration time values V_{max} and t_2 respectively, and the second, G_{22}, by using the values V'_{max} and t_2' , i.e.

$$G_2 = \int_{t_1}^{t_2} \int_{V_{min}}^{V_{max}\,Sin\,wt} (V_{max}\,Sin\,wt - V) e^{-\sum_{i=1}^{m} \mu_i x_i}\, dV\, dt \qquad 6.17$$

$$G_{22} = \int_{t_1}^{t_2'} \int_{V_{min}}^{V'_{max}\,Sin\,wt} (V'_{max}\,Sin\,wt - V) e^{-\sum_{i=1}^{m} \mu_i x_i}\, dV\, dt \quad . \qquad 6.18$$

The percentage error X due to the voltage fluctuation ΔV_{max} was calculated using the relationship

$$X = 100 \left(\frac{G_{23} - G_2}{G_2} \right) . \qquad 6.19$$

Values of ϕ and X are given with the calculated values of G_1 and G_2 in tables A6.3 - A6.10.

6.3.2. Sensitivity of the densitometer to changes in bone density and composition.

In metabolic bone diseases there may be changes in bone density and composition which would be impossible to detect radiographically until such changes become large. To assess the sensitivity of the densitometer, it was decided to theoretically investigate such variations to the signal caused by simulated changes in density and composition.

6.3.3. Density changes.

In all previous calculations an effective density of 1500 $kg\ m^{-3}$ was assumed for the hydroxyapatite. It was thought initially that a linear change in density would give rise to a non-linear variation of the output signal. To test this, the transmitted X ray energy through 10 mm ivory and 40 mm water was calculated for an integration time of 30° in the half cycle for densities ranging from 1300 - 1800 $kg\ m^{-3}$ at 80 kVp. The short integration time was chosen because the integrated spectrum would be particularly soft and would therefore be most sensitive to non-linear changes of signal with density. The result is shown in Fig.6.12 and tabulated in tables A6.11. It is evident from these results that there is a nearly linear relationship between density and signal.

To estimate the sensitivity of the densitometer, the signal through 10 mm bone and 40 mm water was calculated for bone densities of 1300 and 1800 $kg\ m^{-3}$ for peak voltages of 80 kV and.

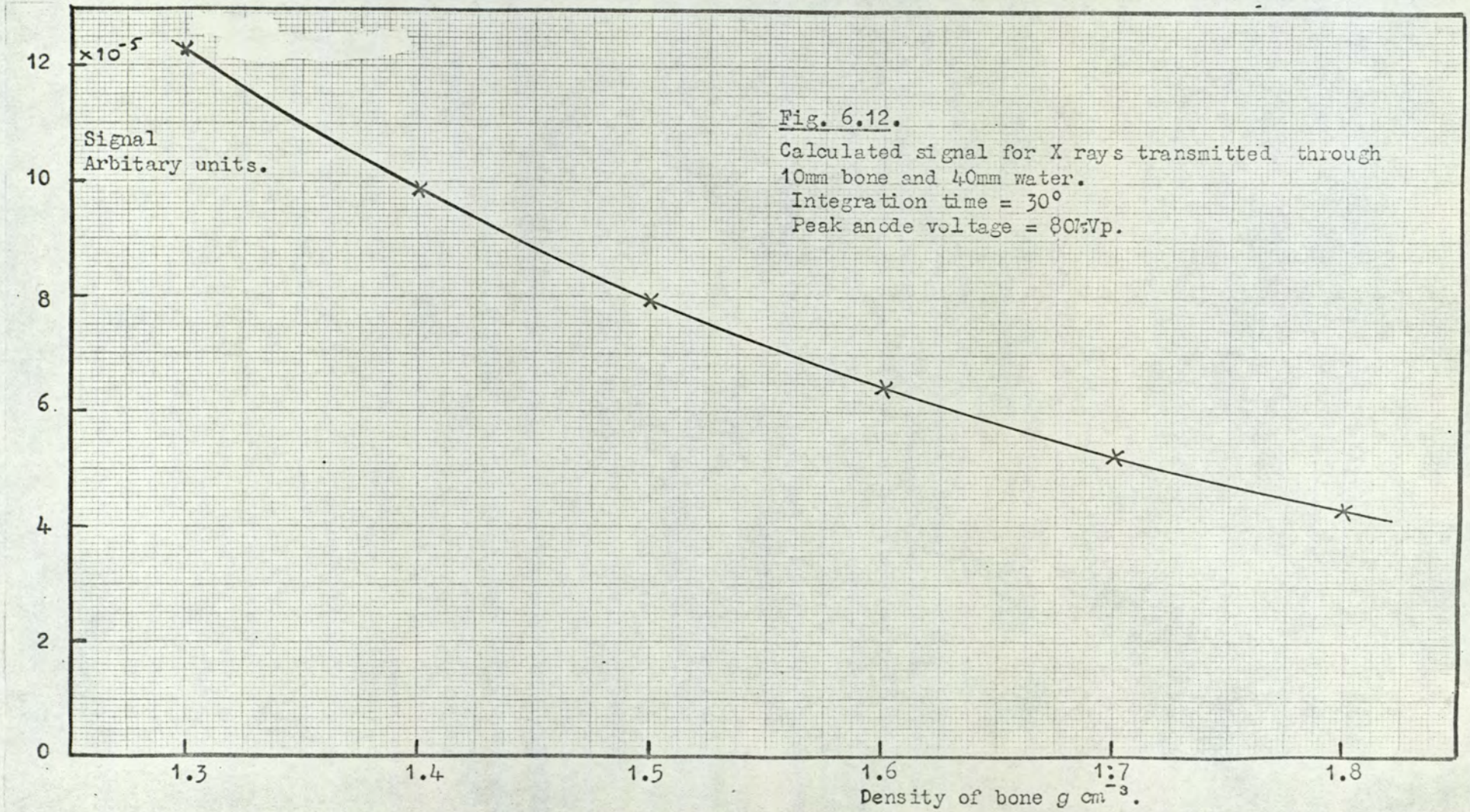

Fig. 6.12.

Calculated signal for X rays transmitted through 10mm bone and 40mm water.
Integration time = 30°
Peak anode voltage = 80kVp.

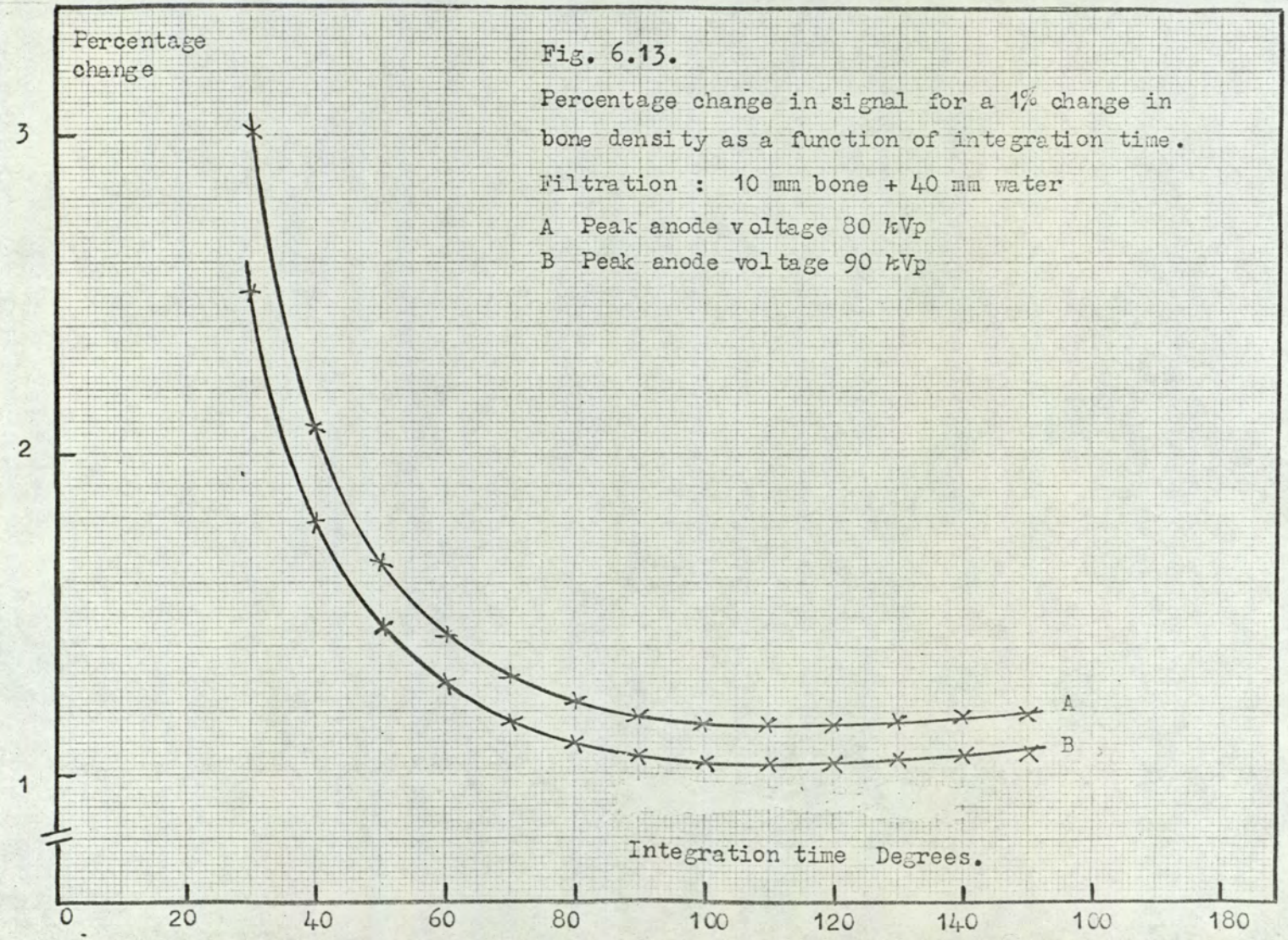

Fig. 6.13.

Percentage change in signal for a 1% change in bone density as a function of integration time.

Filtration : 10 mm bone + 40 mm water

A Peak anode voltage 80 kVp

B Peak anode voltage 90 kVp

90 kV between the integration times 30° - 150° in the half cycle. The percentage change (P.C.) was calculated from the equation

$$P.C. = 100 \left[\frac{G(\rho_1) - G(\rho_2)}{(\rho_1 - \rho_2)} \right] \frac{\Delta\rho}{G(1.5)} \qquad 6.20$$

where $G(\rho_1)$, $G(\rho_2)$ and $G(1.5)$ are the signals corresponding to bone densities of ρ_1, ρ_2 and 1500 $kg\ m^{-3}$ respectively and Δ_ρ is a small change in bone density.

In the calculations $\Delta\rho$ was made 15 $kg\ m^{-3}$ which is 1% of the assumed normal density of bone. Tables A6.12, A6.13 and Fig.6.13 show the variation in the P.F.C. as a function of integration time for different peak anode voltages. As would be expected, the discrimination falls as the integration time initially increases owing to the harder spectrum emitted. However, late in the half cycle when the instantaneous voltage is low and decreasing, the soft spectrum emitted is responsible for a small increase in sensitivity which is much less in magnitude than the initial decrease.

6.3.4. Calcium content changes.

Hydroxyapatite has the composition $[Ca_3(PO_4)_2]_3Ca(OH)_2$ and this has been assumed to represent the inorganic content of bone. Rewriting equations 2.21 ans 2.22, the linear absorption coefficient $\mu_i(E)$ can be written as

$$\mu_i(E) = \left[\frac{\sum_{i=1}^{n} \mu_{mi}\, w_i}{\sum_{i=1}^{n} w_i} \right] \rho \qquad 6.21$$

where μ_{mi} and w_i are the mass absorption coefficients and mass of the ith element respectively

ρ = density of the mixture or compound.

For hydroxyapatite the weighting factors for the elements H,O,P and Ca are 2.016, 416, 185.85 and 400.8 respectively with

$$\sum_{i=1}^{4} w_i = 1004.67 \quad . \qquad 6.22$$

If the mass of calcium present w_4 in one gram mole of hydroxyapatite is charged by T percent then the weighting factor for the element will change by an equal percentage and the new weight summation becomes

$$\frac{Tw_4}{100} + \sum_{i=1}^{4} w_i = 4.008\ T + 1004.67 \quad . \qquad 6.22$$

In a similar manner to section 6.3.2, it was found by calculation that there was a linear relationship between the signal and the calcium content of the bone. This is given in Table A6.14 and shown in Fig. 6.14. for an overall variation of 20%(± 10%), for bone and water path lengths of 5 mm and 45 mm respectively. The calculation was carried out for an anode voltage of 90 kVp and an integration time of 40° in the half cycle.

The relative transmitted intensities through bone and water for various integration times (30°- 150°) were calculated for calcium changes of -10, 0 and + 10% at 80 and 90 kVp and for bone and water path lengths of 5 mm, 45 mm and 10 mm, 40 mm respectively. The percentage change (P.C.) was calculated from the relationship

$$P.C. = 100 \left(\frac{G(-10) - G(+10)}{20} \right) \frac{\Delta Ca}{G(0)} \qquad 6.23$$

where G(-10), G(0) and G(+ 10) are the relative signals corresponding to calcium changes of -10, 0 and + 10% respectively. ΔCa is a small percentage change in calcium content of the bone.

ΔCa was made equal to one percent in the calculations. The results are given in Tables A6.15-A6.18 and are shown in Fig.6.15. It is

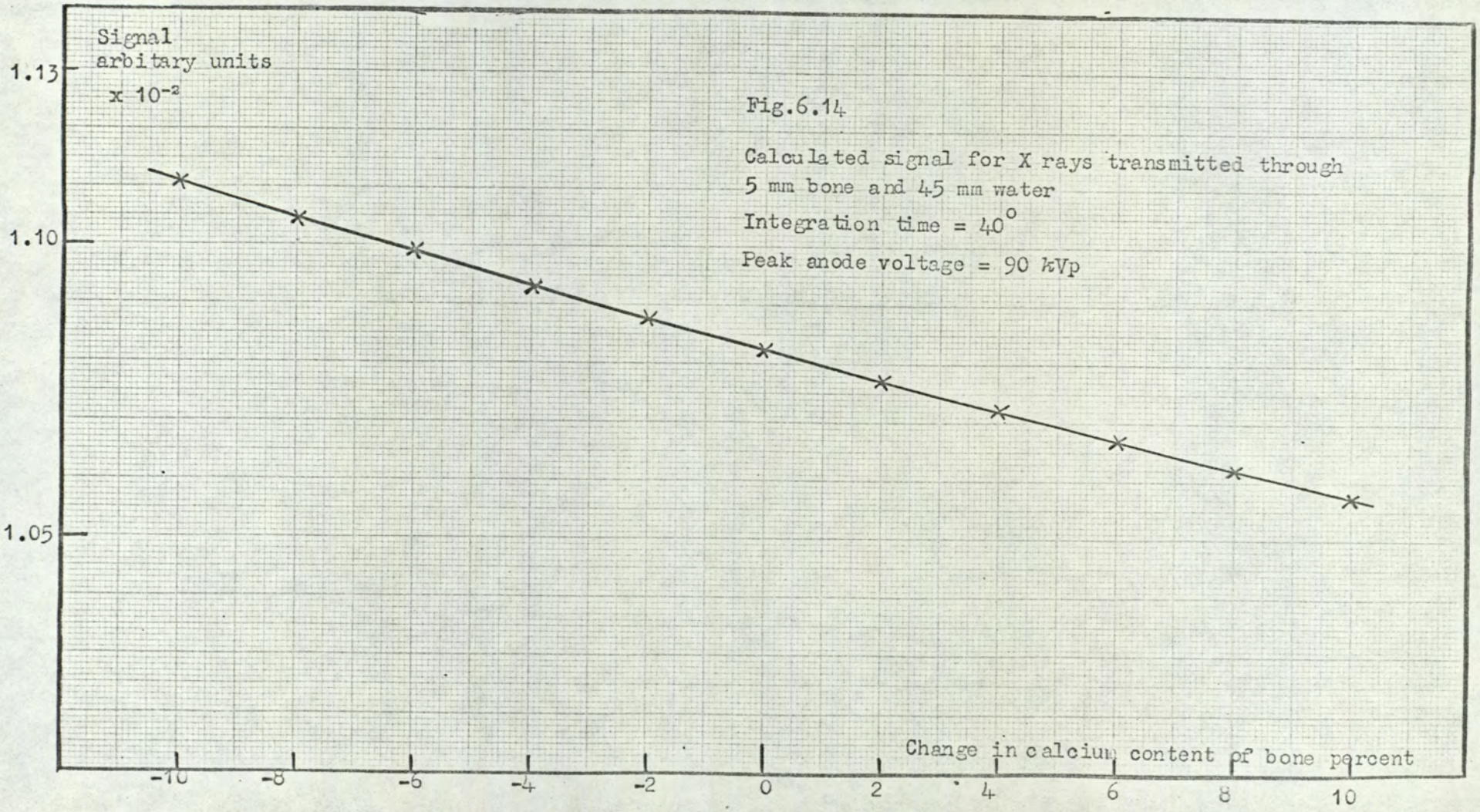

Fig.6.14

Calculated signal for X rays transmitted through 5 mm bone and 45 mm water

Integration time = 40^{o}

Peak anode voltage = 90 kVp

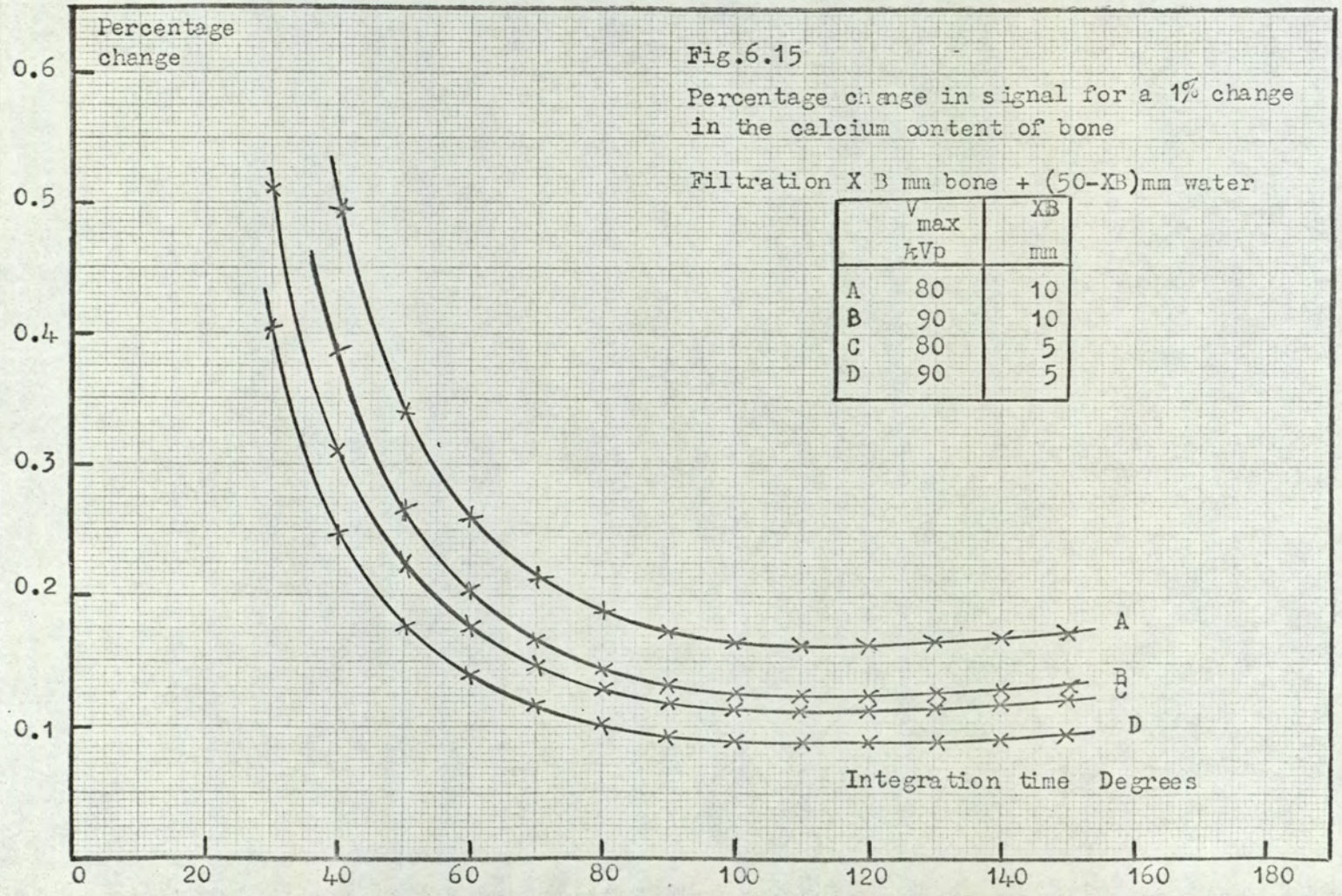

Fig.6.15

Percentage change in signal for a 1% change in the calcium content of bone

Filtration X B mm bone + (50-XB)mm water

	V_{max} kVp	XB mm
A	80	10
B	90	10
C	80	5
D	90	5

seen from these results that there is a sharp initial fall in the sensitivity followed by a very small increase. This is due to energy spectral distribution changes as outlined in the previous section.

6.4. Discussion of the theoretical results.

6.4.1. Introduction.

The relative output signals of the two detectors as a function of terminal integration time is given in Tables 6.13 and 6.14 and shown in Figs.6.7-6.9. It is seen that the signal is very small at the beginning of the half cycle due to the very heavy attenuation of the soft spectrum emitted by the X ray generator. The magnitude of the signals increases rapidly due to the increasing hardness of the beam and because the unfiltered X ray beam energy is proportional to the square of the instantaneous anode voltage. Towards the end of the half cycle the rate of increase of signal falls because the X ray beam is becoming softer as the anode voltage falls. Little additional X ray energy reaches the detectors and so the gradient of the integrated signal curve decreases and will become zero at 180°.

6.4.2. Error resulting from voltage fluctuations where there is unequal filtrations of the two X ray beams.

In Chapter 2 it was noted that if the filtrations above the two detectors was not identical there would be an error in the output of the second detector if there were a variation in the amplitude of the anode voltage. This error has been calculated for a 5% change in the anode voltage for thicknesses of bone 0 - 14mm in the X ray beam path of the second detector. Anode voltages of 80 and 90kVp were considered, and a terminal integration time of 80° was chosen. This was done for two reasons.

The first was that on experimental operating condition of 50mA beam current, 90kVp and 80° termination of integration time was chosen for the densitometer, and the second was that it was known that if the integration time was increased the accuracy of the compensation for voltage fluctuations decreased (section 6.4.1). The hypothesis that a scintillation detector having a higher quantum energy threshold response would improve the accuracy of the compensation was also tested.

The results are given in Tables A.6.6 - A.6.9 and shown in Fig. 6.10. The error shown in Fig. 6.10 is $\alpha - \phi$, which is the numerical error in the solution of equation 6.16 subtracted from the calculated densitometer error due anode voltage fluctuations. Although the numerical error has been estimated from calculations involving different bone and water filtrations, the energy and time ranges over which the integrals are calculated are very nearly the same. This method offers a sensitive test of the assessment of the errors in the special case where the two X ray filtrations are identical. In such a case the theoretical error is zero.

The results show a very nearly linear increase of error with increase of bone thickness in the X ray beam path except where there is very little bone filtration. This is due to the greater initial and additional hardening of the X ray beam by the bone which will absorb softer radiation to a greater degree than the water it has displaced.

The linear increase in error with increase of bone thickness allows the simple relationship to be written.

$$\text{Percentage error} = A(BX - 5) \qquad 6.24$$

where A = constant given in Table A6.10

BX = bone thickness(mm)

It is observed that the value of A increases by 19.3% when the peak voltage is lowered from 90 to 80kVp for a scintillation detector crystal which responds to all energies of incident radiation. If a scintillation crystal could be found which had a lower quantum energy threshold of 60keV the error would decrease by a factor of 3.6 when the peak anode voltage was 90kVp. This possibility is discussed further in sections 6.6 and 7.6.

6.4.3. Error resulting from voltage fluctuations for unequal filtration and variation of integration time.

Although the detector signal increases when the integration is allowed to continue for a longer time, it is thought worthwhile to calculate the error of the compensation technique as a function of terminal integration time for fixed X ray beam filtrations. This filtration was considered to be 10mm bone and 40mm water, for second detector and that for the first 5mm and 45mm water and bone respectively. For identical filtrations the error in the compensation technique due to anode voltage fluctuations will be zero for any terminal integration time.

The results are given in Tables A6.3-A6.5 and shown in Fig. 6.11. As in the previous sub-section, the error $\chi - \phi$ has been plotted. The results shown an initial fall in the percentage error of the densitometer compensation technique as the terminal integration time is increased followed by an increase after the curve has passed through a minimum at about 55°. The rate of increase of error is therefore initially negative, then zero and finally positive.

$$\text{As} \qquad \chi = \left(\frac{G_{22} - G_2}{G_2} \right) \tag{6.25}$$

$$\text{then} \qquad \frac{\partial \chi}{\partial t_2} = \frac{1}{G_2} \cdot \frac{\partial G_{22}}{\partial t_2} - \frac{G_{22}}{G_2^2} \cdot \frac{\partial G_2}{\partial t_2} \tag{6.26}$$

There are then three ranges of interest.

(1) $\frac{\partial \chi}{\partial t_2} < 0$ $\quad 0 < \omega t_2 < 55°$ 6.27

(2) $\frac{\partial \chi}{\partial t_2} = 0$ $\quad \omega t_2 \simeq 55°$ 6.28

(3) $\frac{\partial \chi}{\partial t_2} > 0$ $\quad 55° < \omega t_2 < 180°$ 6.29

The results were checked by calculating

$$\frac{\partial G_2}{\partial t_2} \text{ and } \frac{G_2}{G_{22}} \cdot \frac{\partial G_{22}}{\partial t_2}$$

in the three terminal integration periods,

(1) 30 - 40°

(2) 50 - 60°

(3) 120 - 130° .

by partial derivations being calculated by assuming that the average gradient in each tone range was the same as the gradient at the lower energy time. The results are tabulated.

ωt_2 Degrees	G_2 volts	G_{22} volts	$\frac{\partial G_2}{\partial t_2}$ volts s^{-1}	$\frac{\partial G_{22}}{\partial t_2}$ volts s^{-1}	$\frac{G_2}{G_{22}} \frac{\partial G_{22}}{\partial t_2}$ volts s^{-1}
30	$3.198\ 10^{-2}$	4.5415 -3	7.599	7.659	7.5644
50	$2.1199\ 10^{-2}$	2.1383 -2	67.64	68.39	67.81
120	$5.4269\ 10^{-1}$	5.5582 -1	67.66	75.02	73.25

It can be seen that the equality of

$$\frac{\partial G_2}{\partial t_2} \text{ and } \frac{G_2}{G_2} \frac{\partial G_{22}}{\partial t_2}$$

is in agreement with the equations derived for the three terminal integration periods considered. The shorter time in which G_1 reaches the preset value W for a 5% increase in anode voltage has been given in Tables A6.3 - A6.5. The differences between the preset and compensated terminal integration times are shown for a crystal responding to all X ray energies in Fig.6.16 for a nominal

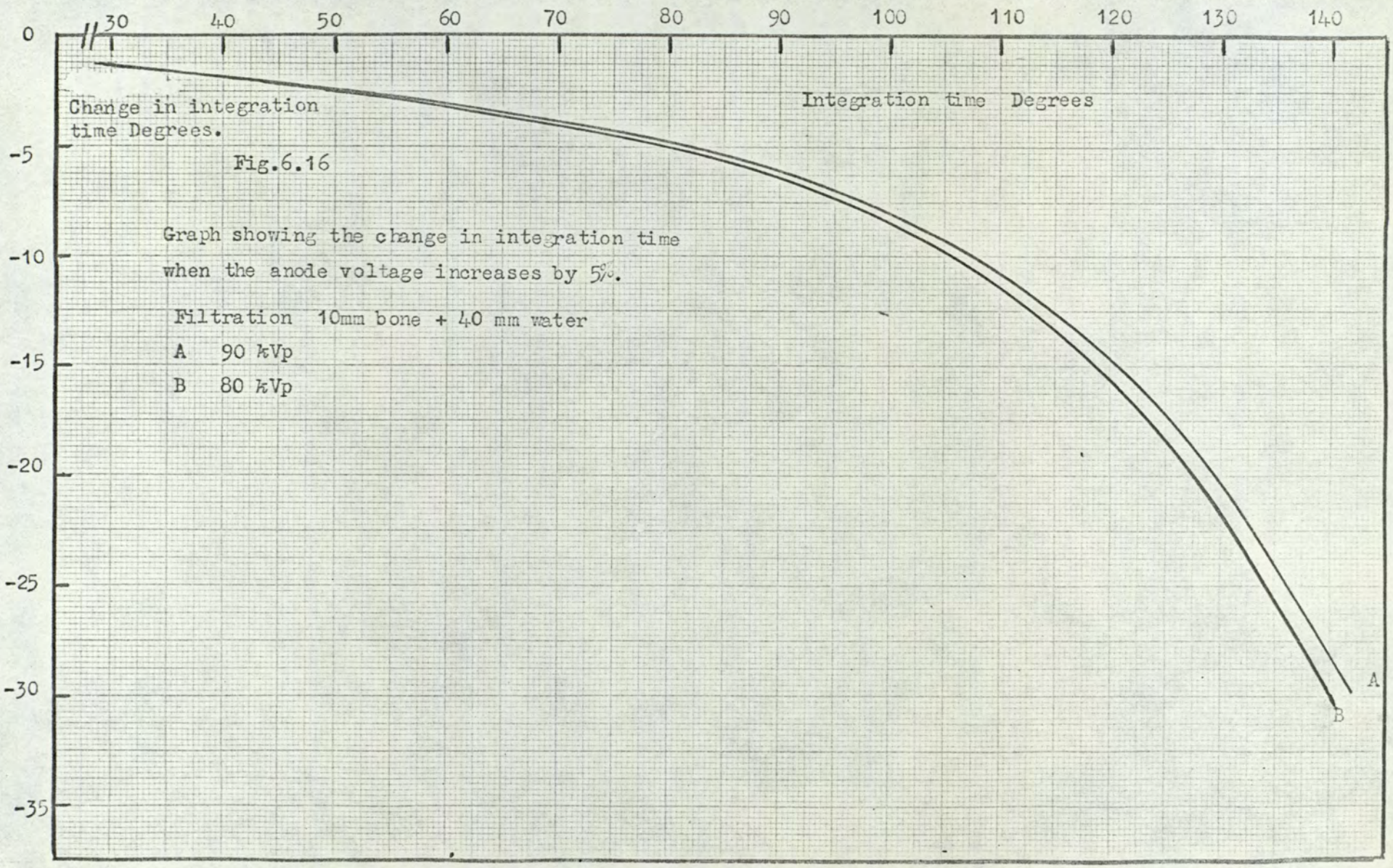

Fig.6.16

Graph showing the change in integration time when the anode voltage increases by 5%.

Filtration 10mm bone + 40 mm water

A 90 kVp

B 80 kVp

anode voltage settings of 80 and 90kVp. From this graph it is seen that for moderate integration times ($\simeq 90°$), the compensation is small ($\simeq 6°$) but increases rapidly for longer periods of integration.

6.5. Comparison between theory and experiment.

The calculations given in Tables A6.3-A6.5 show the relative magnitude of signals expected from the output of the second detector by making the assumptions discussed earlier in the Chapter.

If the theoretical results are to be compared with experiment, the former results must be normalised at some experimental operating condition. The results obtained have allowed two sets of experimental and theoretical data to be compared.

(1) The detector signal for various bone and water thicknesses in the X ray beam for termination of integration at 80° at 80 and 90kVp.

(2) The variation of detector signal as a function of terminal integration time for various bone and water thicknesses in the X ray beam at 80 and 90kVp.

In the first case the theoretical results were normalised to the experimental results corresponding to a beam attenuation of 50mm water. The results are given in Tables A6.19-A6.20 and shown in Fig. 6.17. For the second set of data, the theoretical results were normalised to the experimental data corresponding to a terminal integration of 90° in the half cycle. The results are given in Tables A6.21-A6.24 and shown in Figs. 6.18-6.21.

6.5.1. Detector signal for various ivory and water filtrations.

Fig.6.17 shows that at 80 and 90kVp for 80° integration, the calculated decrement in signal with an increment of bone thickness in the X ray beam is much greater than what is experimentally

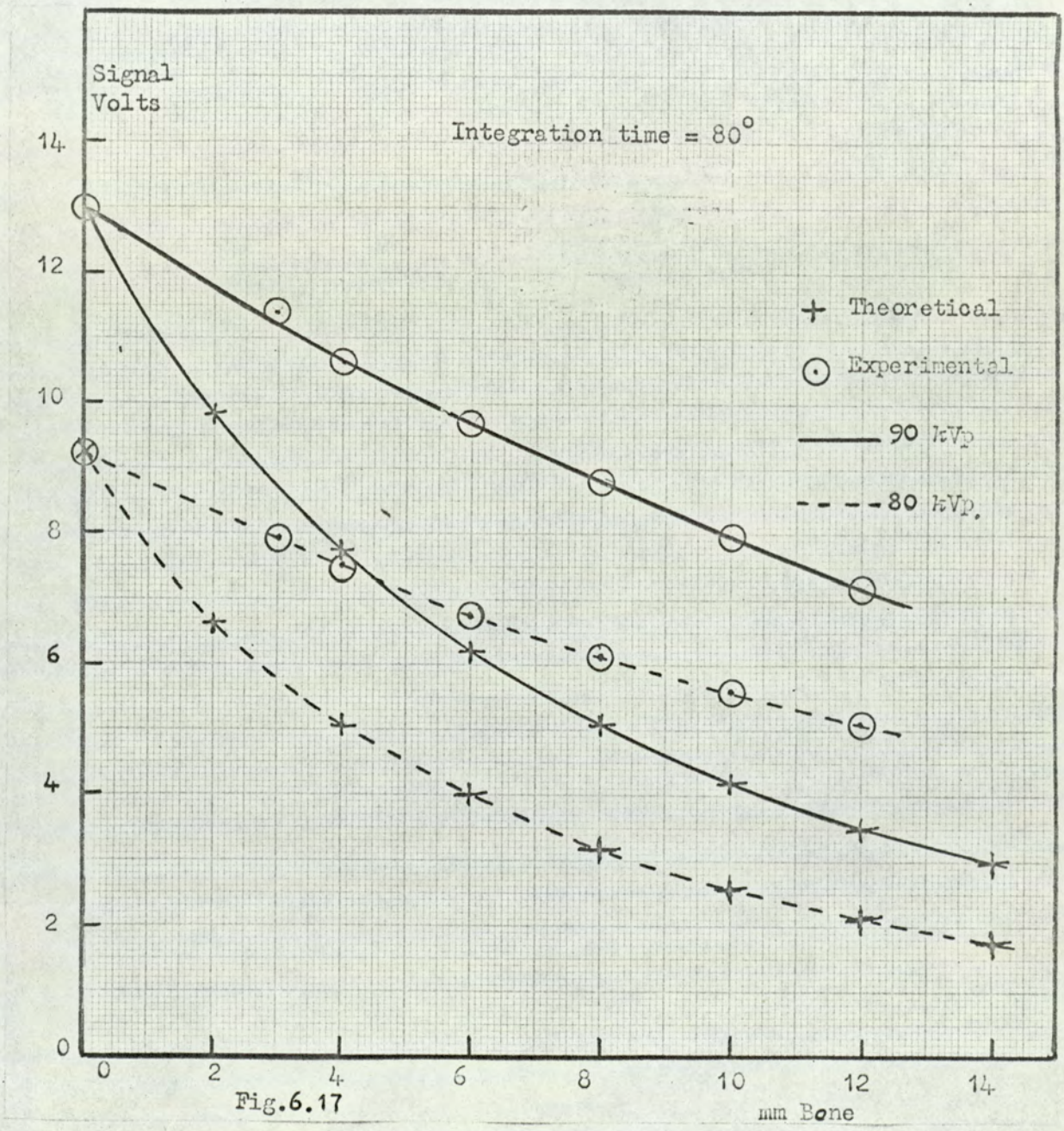

Fig.6.17

Comparison of normalised experimental and theoretical results.

observed. The X ray beam is therefore harder than what has been calculated. There are several possible explanations and the theory could be modified for these factors which are listed and discussed.

(1) Anode voltage waveform

(2) Electron beam current waveform

(3) Inherent filtration of the X ray beam

(4) External filtration of the X ray beam

(5) The composition and density of ivory.

These possibilities will be considered in turn.

The anode voltage waveform.

To obtain a harder quality spectrum the anode voltage would initially have to increase more slowly than the assumed sinusoidal waveform and then possibly increase at a faster rate later in the half cycle when $\omega t \sim 90°$. Unfortunately, as has been mentioned in Chapter 1, there is no convenient method of verifying this.

Electron beam current.

In the calculations the beam current was assumed to be constant. However, it has been shown in Chapter 4 that this current is not constant but has a waveform whose fundamental frequency is twice that of the mains supply. The beam current can therefore be represented by a Fourier series

$$I(t) = a_o + \sum_{n=1}^{\infty} b_n \text{ Sin } n\omega t \qquad 6.30$$

where a_o = constant

b_n = coefficient of the nth harmonic

w = fundamental angular frequency

t = time

If the beam current were higher at a time when the anode voltage was at or near the peak voltage, this would give a greater weighting to the harder spectrum emitted. Unfortunately, the degree of modulation cannot be found from experiments using the transformer coil (Chapter 4), because the transformer will not indicate the constant value a_o, of the Fourier series.. However, the variation of the beam current has been shown to be a substantial fraction ($\sim$ 80%) of the value given by the X ray generator control panel. Such a variation would probably explain the apparent hardness of the observed X ray beam. Any theoretical calculations made to account for the variation of beam current would necessitate the assumption of a Fourier series or a tabulated value for I at I(t).

Inherent filtration.

Inherent filtration would only harden the X ray beam by a small amount owing to the very small distance which the bremsstrahlung emitted in a useful direction has to travel to the surface of the tungsten target. This distance has been calculated for the range-energy relationship given by Katz and Penfold[146] and is shown in Fig. 6.1. and given by equation 6.3.

Considering a 80keV electron, this will generate bremsstrahlung in the energy region 0-80keV. At 80keV, the distance which a photon has to travel through the tungsten target is about $4.0.\ 10^{-5}$ mm and the total absorption coefficient for a 60keV photon is about $704 mm^{-1}$. Hence the fractional attenuation (I/I_o) will be

$$(I/I_o) = \exp(-\ 4.0.10^{-5}.\ 704)$$

$$(I/I_o) = 0.97$$

Considering a 40keV photon generated by the deacceleration of a 60keV electron, the tungsten having an attenuation coefficient of

$2.065.10^3$ mm^{-1} at this energy,

$(I/I_o) = \exp(-2.065.10^3 . 2.5 . 10^{-5})$

$\simeq 0.95.$

It is seen that only a very small fraction of the X rays are absorbed in the tungsten target, even for moderately low energy photons. The Katz-Penfold equation[146] could be used in computer calculations to allow for the inherent filtration of the target, but it is believed that such a correction would be small in view of the calculations shown above.

External filtration.

In the calculations the filtration of the X ray beam due to the glass envelope of the vacuum X ray tube and the floor of the perspex bath has been neglected. The thickness of the glass wall of the X ray tube is about 2 mm, whilst the X ray beam path length through the perspex is 6.3 mm(0.25 in). The effect of these two filtrations could be allowed for in future calculations, but would be small compared with the filtration of 1.5 mm aluminium and 50 mm water. It is believed that this correction would not harden the beam sufficiently to account for the observed differences between theory and experiment.

Composition and density of the ivory.

The assumptions made about the composition and density of the ivory have been outlined, and the small differences of the detector signal due to different compositions and densities have been calculated.

It is seen from Figs. 6.14 and 6.15 that a 1% change in calcium content will change the detector signal by only 0.1% (for a 5 mm X ray bone path at 90 kVp and 80° terminal integration time) whilst for the same operating conditions the percentage change in signal for a 1% change in bone density is 1%. Since the

experimental result is about 45% larger for an X ray beam path of 5 mm bone and 90 kVp, the necessary increase in either calcium content or density of the bone must be much larger to account for this difference. Such a large percentage is in disagreement with the assumptions made by other workers [148-150] and therefore any real underestimate of calcium content or density of the bone would not explain the large difference between theory and experiment.

6.5.2. Detector signal as a function of integration time.

Figs. 6.18- 6.21 show the similarity of the theoretical and experimental detector signal results as a function of terminal integration time. The conditions of peak anode voltage and X ray beam filtration have been given. The curve drawn through the experimental points indicates the general behaviour of the detector signal as the integration time is varied. In normalising the experimental results to 50mA beam current, it was assumed that the beam current was constant and had a value given by the control panel. It is therefore not surprising that these results do not follow the curve more closely.

The terminal integration time at which the theoretical results have been normalised is arbitary ; any such normalisation will not change the gradient of the curve (for any particular integration time) but merely alter the vertical position of the curve. It is seen from Figs. 6.18-6.21 that the gradient of the curve drawn through the experimental results is less than for the theoretical curve over the complete range of terminal integration time investigated. If the subscripts exp and th refer to experiment and theory respectively,

$$\left(\frac{\partial G_2}{\partial t_2}\right)_{exp} < \left(\frac{\partial G_2}{\partial t_2}\right)_{th.} \qquad 0 < wt_2 < 180^\circ \qquad 6.31$$

We may rewrite equation 6.9 as

$$(G_2)_{exp} = \int_0^{t_2} I(t) \int_0^{V(t)} (V(t)-V) e^{-\sum_{i=1}^{m} \mu_i x_i} \, dV \, dt \qquad 6.32$$

$$(G_2)_{th} = \int_0^{t_2} K \int_0^{V(t)} (V(t)-V)\, e^{-\sum_{i=1}^{m} \mu_i x_i} \, dV \, dt \qquad 6.33$$

where $I(t)$ = experimental electron beam current

K = constant electron beam current assumed in the theory

$V(t)$ = instantaneous waveform of the anode voltage.

From these two equations

$$\left(\frac{\partial G_2}{\partial t_2}\right)_{exp} = I(t) \int_0^{V(t)} (V(t)-V) e^{-\sum_{i=1}^{m} \mu_i x_i} \, dV \qquad 6.34$$

$$\left(\frac{\partial G_2}{\partial t_2}\right)_{th} = K \int_0^{V(t)} (V(t)-V) e^{-\sum_{i=1}^{m} \mu_i x_i} \, dV \qquad 6.35$$

If $\left(\frac{\partial G_2}{\partial t_2}\right)_{exp} < \left(\frac{\partial G_2}{\partial t_2}\right)_{th} \qquad 0 < wt < 180^\circ. \qquad 6.31$

then

$$\left[I(t) \int_0^{V(t)} (V(t)-V) e^{-\sum_{i=1}^{m} \mu_i x_i} \, dV \right]_{exp}$$

$$< \left[K \int_0^{V(t)} (V(t)-V) e^{-\sum_{i=1}^{m} \mu_i x_i} \, dV \right]_{th} \qquad 6.36$$

From equation 6.36 it is seen that there are several factors which could account for this inequality. They are listed and discussed.

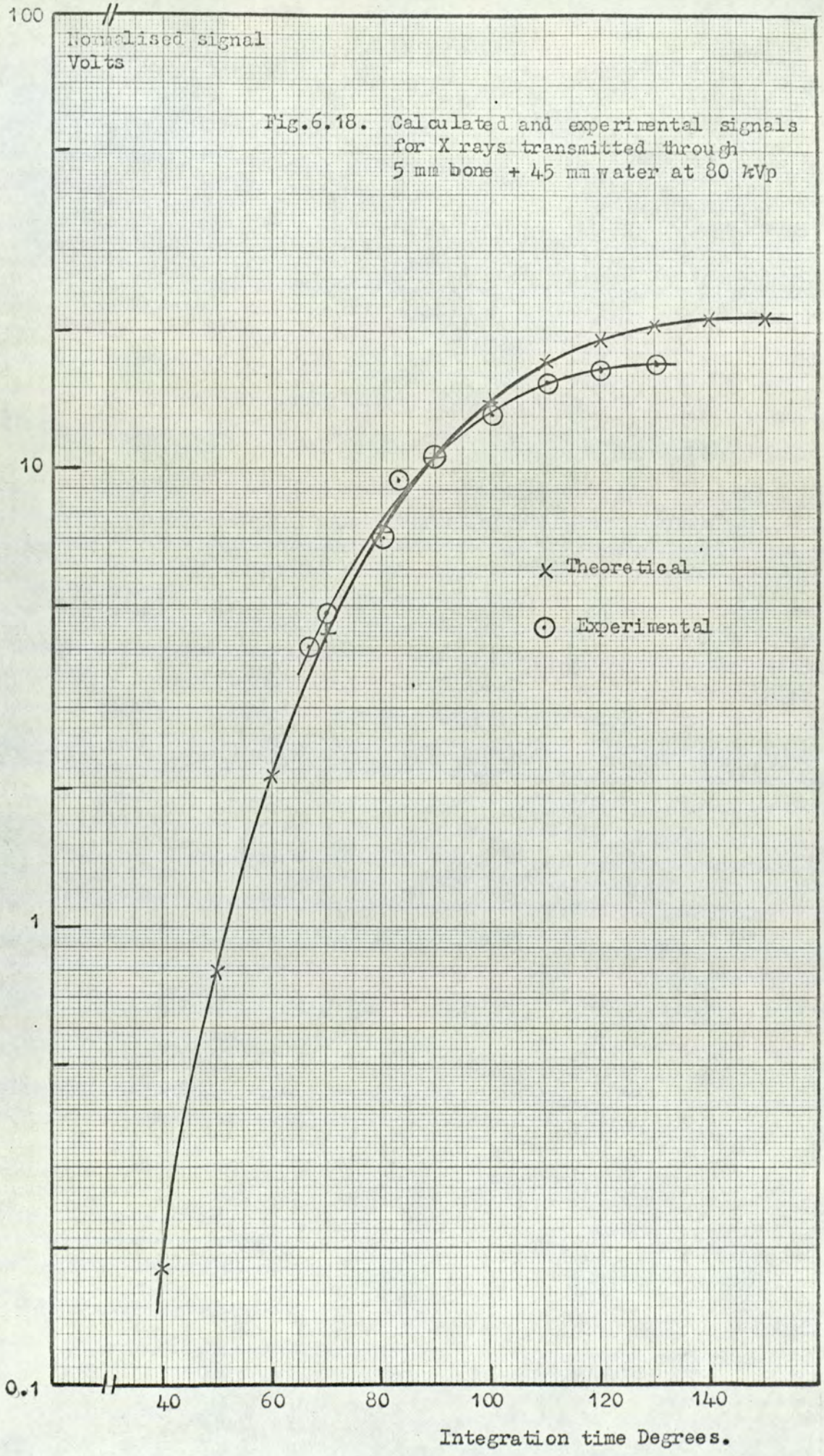

Fig.6.18. Calculated and experimental signals for X rays transmitted through 5 mm bone + 45 mm water at 80 kVp

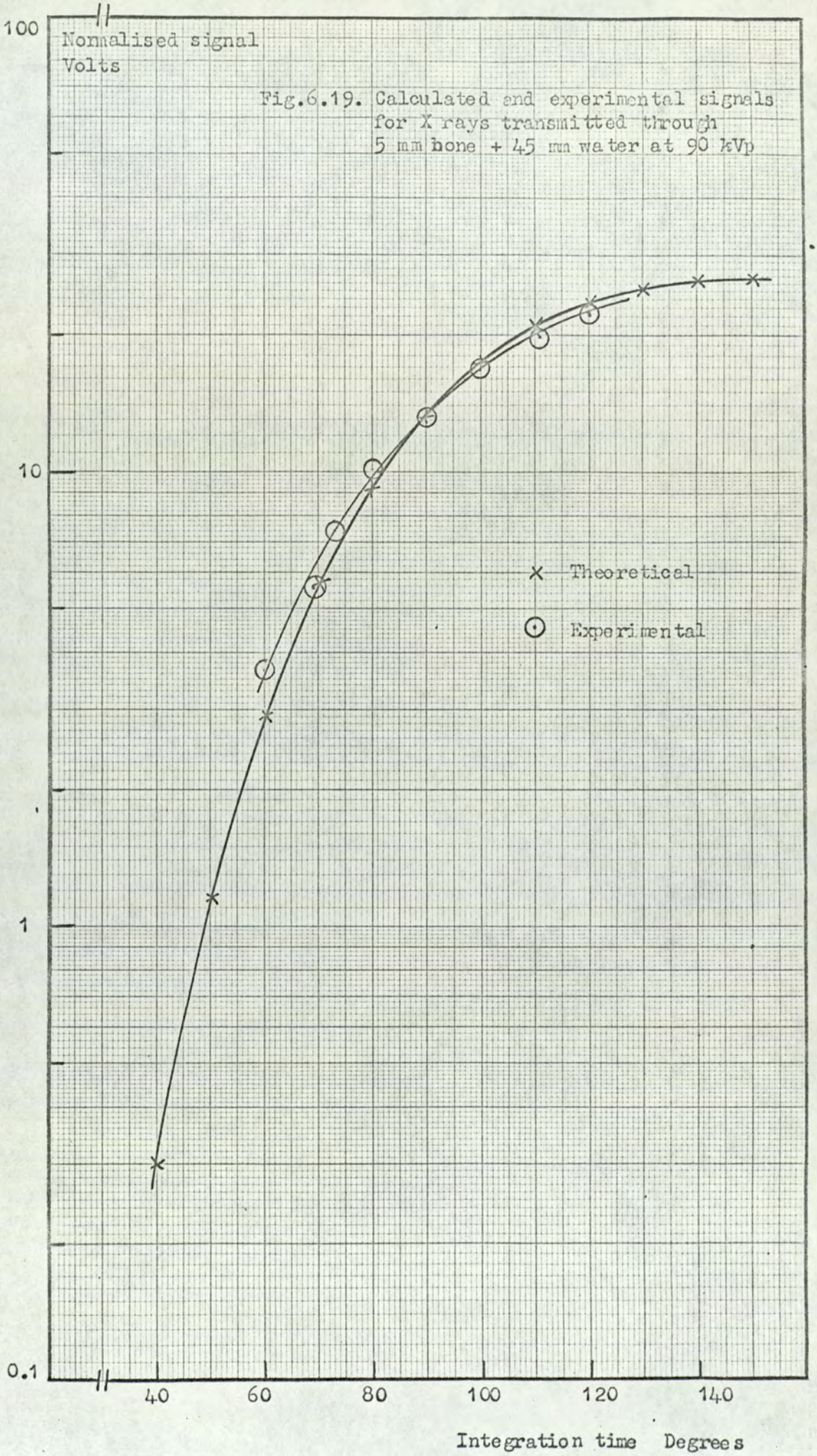

Fig.6.19. Calculated and experimental signals for X rays transmitted through 5 mm bone + 45 mm water at 90 kVp

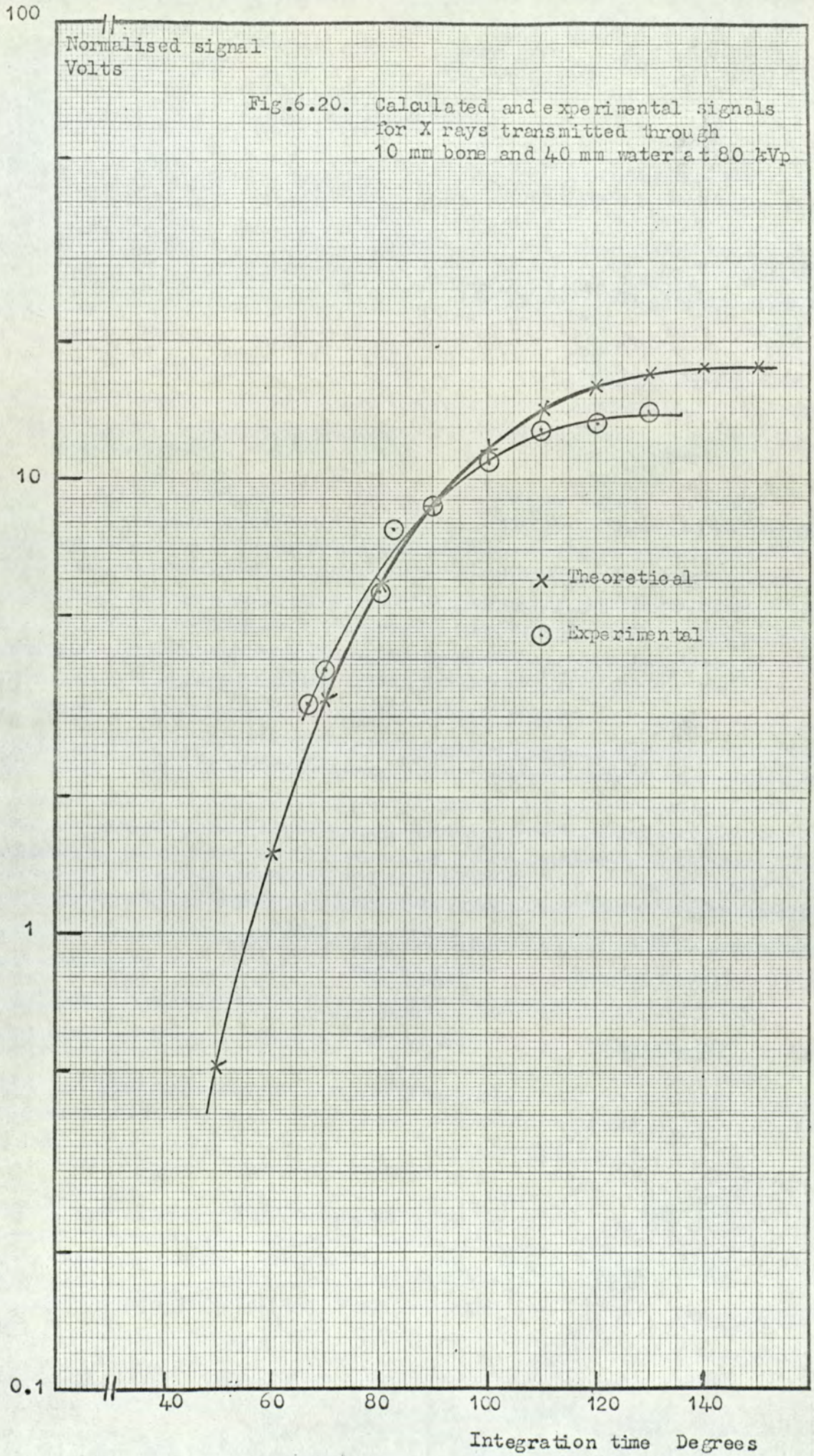

Fig.6.20. Calculated and experimental signals for X rays transmitted through 10 mm bone and 40 mm water at 80 kVp

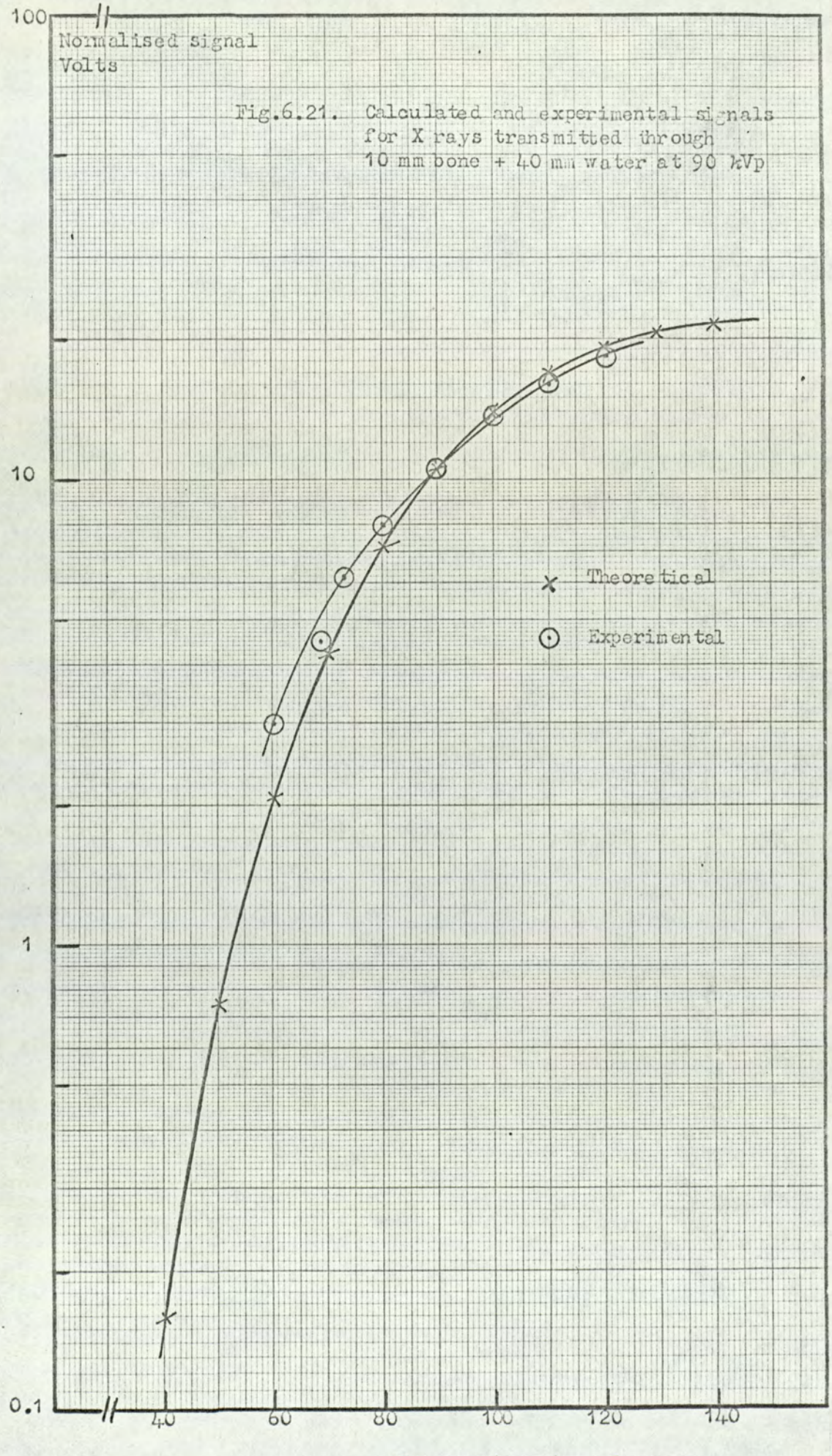

Fig.6.21. Calculated and experimental signals for X rays transmitted through 10 mm bone + 40 mm water at 90 kVp

$$(1)\quad I(t) < K \qquad 0 < \omega t < 180^{\circ} \qquad 6.37$$

$$(2)\quad \left[\int_{0}^{V(t)} (V(t)-V)\,dV\right]_{exp} < \left[\int_{0}^{V(t)} (V(t)-V)\,dV\right]_{th} \qquad 0 < \omega t < 180^{\circ} \qquad 6.38$$

$$(3)\quad \left[\sum_{i=1}^{m} \mu_i x_i\right]_{exp} < \left[\sum_{i=1}^{m} \mu_i x_i\right]_{th} \qquad 6.39$$

1. This factor states that the time varying beam current is less than the assumed constant value throughout the whole half cycle. The difficulties of investigating the electron beam current experimentally has been discussed.
2. The second inequality implies that the voltage waveform is non-sinusoidal and the possible reasons for this have been outlined in this section.
3. Equation 6.39 means that the amount of filtration of the X ray beam is greater than has been allowed for in the calculations. This includes both inherent and external filtration of the beam and this has also been discussed in this section.

6.6. Calculations with a scintillation crystal having a high response threshold.

The large reduction in the compensation error to be gained (at the cost of reduction of signal) by using a scintillation crystal with a higher energy threshold of 60 keV has been calculated(Table A6.5) and shown in Fig.6.11. The same filtration and peak voltage of 90 kVp has been assumed. The results show that with such a scintillation crystal the error would be reduced

by a factor of 4.2 for a terminal integration time of 80^{o}. A possible method how such a crystal could be made has been outlined in Chapter 7.

CHAPTER 7.

Recommendations and General Conclusions.

Introduction.

It has been demonstrated that the densitometer constructed in this project performs satisfactorily within the guidelines of Chapter 1. The equipment has evolved in various stages and further improvements can be made. These will be discussed in this chapter together with the conclusions drawn about the project.

7.1. Mechanical construction.

The mechanics and framework of the densitometer have generally proved to be of sound design. However, it has been found that when salt solution from the bath is accidentally spilt onto the dural frame, it becomes slightly corroded unless the frame is washed and dried. This problem could be overcome by coating the exposed parts of the framework with a waterproof varnish. An alternative would be to replace the dural framework by stainless steel but this would be considerably more expensive and would make the equipment heavier.

The scanning procedure would be simplified if there were an automatic return of the bath to its original position after making the scan. The camera cable release might also be linked to the switch so that only the on/off motor switch and the time delay switch need be operated.

7.1.1. The monitor.

The 92 AV photodiode used in the monitor detector is relatively insusceptible to microphony and mechanical decoupling is not necessary. To give more room for the electronics the monitor box could be made a little longer.

7.1.2. The detector.

Considerable improvement could be made to the alignment of the lower detector and its method of fixation. At present the lower detector is held between the lower bridge pieces of dural angle by rubber strips which provide mechanical decoupling and electrical insulation from the surrounding frame. A superior arrangement would be to support the detector by four nylon screws fitted into tapped holes in the dural angle. A thin sheet of rubber about 1.5 mm thick, would afford sufficient mechanical decoupling. The advantage of this method would be that the setting of the detector slit in the X ray beam could be fixed with much greater precision in order to obtain the maximum signal.

7.1.3. Collimation of the X rays.

The width of the X ray beam reaching the bottom detector has been made about 2 mm to guarantee that the detector slit is irradiated by the X ray beam. This large beam width is responsible for most of the X ray dose received by the patient and could be reduced by a factor of about four to give a beam width of 0.5 mm which would be sufficient to irradiate the 0.25 mm collimating slit. With the present arrangement, however, this is not practical because the monitor and the brass flange have to be removed in order to adjust the beam collimation. Although the monitor may be replaced very accurately by using the locating grub screw(Appendix 2) the brass flange cannot be replaced with equal precision. To overcome this disadvantage use could be made of the $\frac{1}{8}$ in. gap between the floor of the monitor and the top lead cover cemented to the underneath the dural bridge to provide a fine screw adjustment for the two lead slits.

7.1.4. The bath and moving trolley.

The possibility of obtaining an ulna scan with the arm held at a downward angle of 45° has been considered. This would be a little more comfortable for the patient, but would mean that the bath would have to be redesigned. Although the present equipment could be tilted to accommodate an arm in such a position, there would be an extra strain on the motor bellows. A better solution would be to redesign the moving trolley. One disadvantage with this arrangement would be that scans could be made using one end of the bath as opposed to both ends at present.

7.2. Scanning the subject.

Although a scan of a subject's ulna may be made with the aid of one person, practical experience has shown that inconvenience to the subject is minimised if two people are employed. The time taken to secure the subject's hand and arm in the bath is less than half than would be taken if only one operator were present.

It has been noted in Chapter 5 that the limit of reproducibility of invivo measurements is anatomical repositioning and in particular the rotational movement of the ulna. This movement could be substantially reduced by moving the patient with the same speed and direction as the ulna. To do this a small chair mounted on a trolley and driven by a synchronous motor would need to be constructed. Although the construction would present no difficulty, the possibility of electrical interference generated by the motor would have to be carefully considered.

7.3. Electronic equipment.

7.3.1. The detectors.

In view of the very small photodiode currents (~1 μA) it

is necessary to integrate and lead the current into source followers which are adjacent to the photodiodes. Little change is therefore envisaged, although with the recommended larger detector boxes a mu-metal screen could be usefully employed to shield the photodiodes and the electronics from any magnetic fields.

7.3.2. Main electronics.

With the present arrangement the electronics occupies the minimum space and is all within the framework of the densitometer. Normally the accessible controls offer a sufficiently large range of operation, but if adjustments to the gain of the amplifiers or the range of the discriminator are to be made the procedure becomes tedious and time consuming. This is because the leads from the main electronic box to the oscillator have to be disconnected. In such circumstances it would be advantageous to house all the electronics in a larger box. By using screening plates between sections of electronics as done at present in the main box induced interference should not be detectable. Special consideration would have to be given to the oscillator as this would have to be totally enclosed. The present oscillator enclosure has been found to be satisfactory.

The main disadvantage of using one large electronics box would be that it could no longer be permanently attached to the framework of the densitometer. However, by situating the two DC power supplies near the electronics box (which would lighten the densitometer) a composite enclosure, including the electronics could be made. Connection between the detectors and the power supplies and electronics could be arranged by a multi-pin socket which would facilitate the easy removal of the equipment.

7.3.3. The resetting pulse generator.

With the diagnostic X ray set used for the majority of the project, the observed phase difference between the maxima of the X ray intensity and mains supply is about 40°. Although the present range of phase shift of ± 45° is adequate, it might be necessary with some X ray sets to extend this range. The construction of an optional additional phase shift of ± 45° would then cover ± 90°.

7.4. Experimental work.

7.4.1. Dose measurements.

The measurements described in Chapter 4 were carried out using 90 kVp anode voltage and 50 mA beam current. If different operating conditions are to be used then the bone marrow dose will be altered. A series of measurements with LiF TLD badges would enable the dose to be stated for any different anode voltage and beam current combination. In making these measurements it would be necessary to state the width and length of the X ray beam reaching the lower detector.

In was unfortunate that attempts to measure the long term dose received by the operator were spoilt due to the unauthorised use of another X ray generator in the same room. The level of stray radiation is believed to be small because of the fine collimation of the X ray beam. It is felt that the majority of the operator dose is due to radiation leakage through the shielding of the tube head. With the present tube (Mullard Guerdien 125) the manufacturers quote a maximum possible leakage dose of 10 mrem h^{-1} at one metre distant from the tube head. Because the exposure time is only six seconds, even if 150 patients were scanned per week the operator dose would still be less than 1/40 of the maximum permitted (2.5 mrem h^{-1} whole body dose for radiation workers).

The dose to the patient may be calculated in a similar way. Assuming the patient's body to be 1 metre from the tube head, then the annual whole body dose will be 0.2 mrem if a monthly scan is made. This is much less than the background level of radiation (100 mrem y^{-1}) and so the densitometer may be safely used to observe calcium changes in the ulnae of pregnant women. However, measurements should be made to confirm these figures.

7.4.2. Pin hole traces of the X ray spot image.

Mention has been made (Chapter 4) of the fluctuations observed in the output when the beam filtrations were made equal. It was also noted that investigation of the size and possible movement of the position of the X ray beam spot was limited by the thickness of tantalum sheet available. An improvement would be to use a casting of antimonial lead.

A pinhole sheet, about 1 mm thick, would attenuate 60*keV* X rays by a factor of about 250 which would enable a better image to be obtained. The small hole could be made by making a plaster of Paris cast through which there was suspended a very thin tungsten or steel wire.

After making the cast the wire could be pulled through the antimonial lead to give a very small collimation hole. Problems associated with antimonial lead casting have been discussed in Chapter 3.

7.4. 3. The peak anode voltage.

This cannot be conveniently checked by interconnection of experiment with the HT anode supply. However, by observing the transmission of X rays through layers of various elements whose *k* absorption edge is in the energy range of interest (40-100 *keV*)

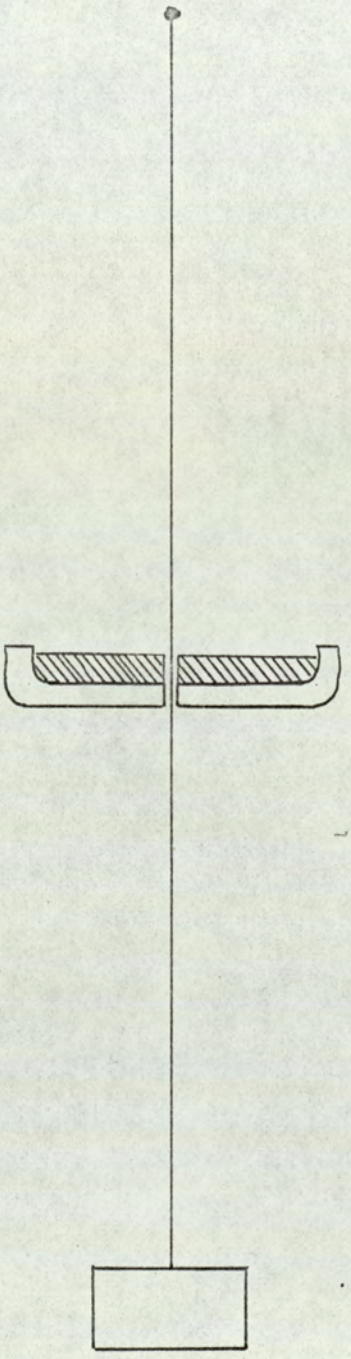

Fig.7.1. Method to obtain a thick pin hole collimator. See text.

the peak voltage may be determined. The method is described in references[154 -157]. Alternatively, lithium drifted germenium detectors could be used with a pulse height analyser.

7.5. Theoretical work.

In Chapter 6 it was stated that there was reasonable agreement between the experimental and theoretical results regarding the magnitude of the output voltage and integration time. Because the experimental error is larger than the theoretical error, a detailed comparison between theory and experiment cannot be made.

Improvement of agreement between the experimental and theoretical results could be obtained by taking into account the time dependence of the beam current and the filtration in the tungsten anode by assuming a Fourier series from an analysis of the beam current traces (Chapter 4). Inherent attenuation of the X rays in the tungsten target has been described by Soole[84] and Soole and Jaeger[85].

Complication of the programme would inevitably result owing to the inclusion of the inherent tungsten filtration. This is because the effective depth below the tungsten surface at which the X rays are generated will be energy and time dependent.

With greater speed of computation, the effect of both positive and negative variations in peak voltages different from 5% could be calculated together with the error of compensation. This would be particularly applicable in those cases where one or more of the HT diodes had substantially

different properties from the remaining diodes. Such differences are likely to be encountered in old X ray generator sets.

7.6. The scintillator crystals.

No difficulty has been experienced with the CsI(Tl) crystals whose nearly linear light output response, high stopping power and non hygroxopic properties make them eminently suitable for X ray detection. In view of the not too different emission spectra emitted by the thallium and sodium doped crystals, an increase in signal might result by using sodium doped crystals. This is because despite the narrower emission spectrum (peak at 420mm) the light output of the sodium doped crystal; about twice that obtained by thallium doping[127].

It has been shown in Chapter 6 that it would be advantageous to employ a scintillator which responded linearly above a lower threshold quantum energy of about 50keV. Such a crystal would have a time independent response and would totally discriminate against X ray quanta below this energy limit.

One method by which this idea could be approached would be to dope heavily a crystal whose constituent atoms have low atomic numbers with an element whose K shell absorption edge is at the required energy threshold. Such a crystal might be a rare earth doped lithium fluoride crystal which would substantially begin to absorb X rays about its K shell energy of $\simeq$50keV (we are only concerned with X rays in the energy range 10 - 100keV). The problem of substitial and interstitial receptance of the large rare earth atoms in the small alkali halide crystal would have to be experimentally tested. Other factors, such as a reasonable X ray to light conversion efficiency with a useful emmission spectrum would only be a few

of the many considerations which would have to be taken into account before the proposition became practical.

7.7. Subject measurements.

The high accuracy of invivo measurement of several subjects has been demonstrated and the equipment is ready for clinical use. Obviously the scanning of confirmed or suspected osteoporotic patients is the logical step in the continuation of the project.

It has been previously mentioned that ivory is slightly water absorbent and possesses a grain structure and for these reasons it cannot be regarded as an ideal standard to compare with the ulna trace. A more suitable standard could be made from a mixture of compounds to simulate the hydroxy apatite. By allowing the mixture to set in a water insoluble glue (such as casein glue to simulate protein), the artificial standard would be non absorbent and possess no macroscopic structure.

The densitomer gives a scan whose readings are proportional to the X ray absorption in the bone. To calculate the density of bone, (an assumption being made regarding the composition of bone) the path length of each scanned elemental strip of the bone has to be known. To obtain this information, tomographic equipment could be developed to give profile of the ulna at the position at which the densitomer scan was made. Standard X ray tomographic equipment cannot be used to obtain this information with any degree of accuracy, since its spatial resolution is a few millimetres which is comparable to the dimensions of the bone. The design and construction of high resolution tomographic equipment and a substitute for ivory is currently being pursued at the University.

Final conclusions.

The research work undertaken to design an inexpensive bone densitometer has been described in this thesis. The basic requirements of the densitometer were outlined in chapter 1 and it is useful to summarise the performance achieved and to compare it with that of equipment used by other workers.

Speed and Accuracy of Measurement.

The very high flux of photons ($\simeq 10^{11}$ photons mA^{-1} s^{-1} sr^{-1}) enables a sample measurement to be made every half cycle of the mains supply (10^{-2} s). With a scanning speed of 10 mm s^{-1}, an ulna may be scanned in approximately one second. The equipment has the advantage that as a scan is being made the result is simultaneously being recorded on X ray film. The speed with which the completed scan may be seen is therefore limited only by the time taken to secure the patient's arm in position (about one minute) and the two minutes necessary for the automatic processing of the X ray film.

The very many photons collected by the two detectors means that the final output signal is not subject to statistical limitations of accuracy as the radioisotope methods mentioned in chapter one. The number of photons reaching the detector measuring X ray absorption by the bone has been calculated to be $\simeq 10^{8}$ photons keV interval^{-1} s^{-1} for a 50 mA beam current. The statistical error is therefore $\simeq 0.01\%$ within one standard deviation.

The practical accuracy quoted in section 5.5 that the total X ray absorption of bone may be estimated to within ± 0.3 mm ivory equivalent (which is nearly the same as bone equivalent) has recently been improved. This has been brought about by making the external trigger to the oscilloscope short circuit proof. It had been found that two of the diodes in the resetting pulse generator had been damaged. The fluctuations in oscilloscope signal for constant X ray beam path of ivory and water is now nearly equal to the spot size on the oscilloscope screen. The scans now obtained of the ivory step wedge are superior to the radiographic measurements of a calcium sulphate step wedge used by Pridie (A). It is believed that measurements may now be made to ± 0.2 mm ivory equivalent. This is equivalent to an accuracy of 2% when measuring a cortical peak of 10 mm in the ulna. Comparative measurements for whole body neutron activation analysis is accurate to about 3%.

Spatial Resolution.

The densitometer makes a sample measurement of the X ray bone absorption every 10^{-2} second by sampling the X ray intensity through a 9.5 x 0.25 mm slit. The 9.5 mm length of the slit has the effect of giving an average of bone mineral content along the axis of the ulna, whilst the 0.25 mm width ensures that the densitometer has extremely good spatial resolution with the ability to observe the very interesting structure

in the medulla of the ulna.

This high spatial resolution is possible due to the very high intensity of the incident radiation. The resolution compares very favourably with those of radioisotope methods. For example, West (B) used a 10 x 2 mm collimation slit with a scanning speed of 0.28 mm s^{-1} to measure femoral bone density. Vogt et al (C - E) used a radiographic technique employing a microphotometer with a light beam of 10 microns x 1.25 mm which gave an error of about 2%. However, the speed of examining the radiograph was only 50 mm min^{-1}.

Convenience and Cost of the Equipment.

One of the first guidelines of the project was to construct a bone densitometer as inexpensively as possible and which could be easily and conveniently used with any full-wave rectified X ray set. The equipment has been constructed so that it may be easily attached and removed from an X ray tube head in order that the X ray set may be quickly used for routine radiography. The densitometer was mounted on a firm trolley so that this removal or attachment takes only one or two minutes.

During the course of the project the electronics was found to be so stable that once correctly adjusted no further adjustments were necessary. Very occassionally the oscillloscope beam brightness or the Y amplifier needed adjustment, but these elementary controls would be easily mastered by staff without special training.

The ease with which the densitometer may be used compares favourably with radioisotope and radiographic densitometry methods where special equipment is needed which requires skilled staff for operation. Neutron activation analysis also requires very complicated equipment with skilled staff.

The cost of all the electronics and materials used in constructing the densitometer has been estimated to be approximately £400. A commercial model might cost £4000 - £5000, but this is still small when compared with modern radiographic equipment. Running costs of the densitometer are negligible since only one 5X4 in sheet of X ray film is required per scan.

Clinical applications

Although the equipment has been used to measurements on several volunteers, it has yet to be tested in clinical practise. Patients undergoing any therapy which directly or indirectly affects the skeleton should be obviously chosen to be scanned with the densitometer. Those patients suffering from osteoporosis, osteomalacia, rickets, hypoparathyroidism, kidney disorders or vitamin D deficiency would be amongst those selected for study.

With any technique relying on comparative sequential measurements the variation expected with normal people must be known in order to specify a result which is not normal. Future clinical work with the densitometer must therefore include the scanning at regular intervals of a

large number of normal people of both sexes and all ages. The reproducibility of in vivo bone scans has been demonstrated but it remains to be seen whether any clinical use can be made of this, particularly of the structure in the medulla. This structure together with the physical dimensions and mineral content of the bone obtained from the scans could perhaps be linked with other clinical data - the level of calcium plasma in the blood, for example.

It is worthwhile recalling that the densitometer measures the total X ray absorption in the ulna and not the absorption due to a specific chemical element. It would therefore be worthwhile making parallel measurements on the same patients using techniques which give more specific results with respect to chemical composition, for example in vivo partial body neutron activation described by Cotto et al (F) and whole body activation by Weber and Andrews (G). The accuracy to which in vivo calcium may be determined using these methods is about 4 - 5%. Another method of using a neutron source is to make use of the ^{40}Ca (n, α) ^{37}Ar reaction and to collect and measure the radioactive ^{37}Ar expired. This technique has been used with animals and the possibility of using patients has been studied. A method to determine the electron density in bones by the scattering of γ rays has also been recently described by Clarke et al (H).

Although the densitometer has been designed to scan the ulna, the radius or metacarpal bones could equally as well be examined. For other bones, such as the os calcis,

the mechanical equipment would have to be redesigned to accept the bone or limb chosen for examination. However, it remains to be seen whether the examination of a peripheral bone is a better or worse than the whole body calcium measurements in giving a clinical guide as to the pathology of the skeleton. Such considerations as cost and convenience would obviously have to be bourne in mind if many patients are to be screened for bone diseases.

The overall performance of the densitometer has been given and compared with other equipment. It is believed that for a fast, accurate and inexpensive measurement of bone mineral in a peripheral part of the skeleton the instrument has several important advantages and it is hoped that it will shortly become established in its own field.

References:

A. Pridie R.B., Brit.J.Radiol. 40, 255, 1967

B. West, R.R. and Reed G.W. Brit.J.Radiol. 43, 886, 1970.

C. Vogt, F.B., Vose, G.P., Mack, P.B. and La Chorce, P.A. Amer.J.Roent. 100, 503, 1967

D. Vogt, F.B., Meharg, L.S. and Mack, P.B. Amer.J.Roent.105,870, 1969.

E. Vogt, F.B. and Mack, P.B. Amer.J.Roent., 113, 621, 1971

F. Cotto, G.R.D., McIntosh, J.A.R. and Macleod, M., Phys.Med.Biol., 18, 508, 1973

G. Weber, D.A. and Andrews, H.L. J.Nuc.Med., 13, 293, 1972.

H. Clarke, R.L. and Van Dyk, G., Phys,Med.Biol. 18, 532, 1973.

APPENDIX 1

Accuracy of the compensation for anode voltage fluctuations by the division technique.

This method of compensation has been fully discussed in section 1.5cii. In this appendix the accuracy of the division technique is calculated by considering peak sinusoidal voltages of 90 and 95 kVp respectively. The assumptions made regarding X ray sampling time and filtration of the two beams has also been described in section 1.5c ii.

For a narrow beam conditions, the attenuation of a monochromatic beam of X rays is given by the equation

$$I = I_o\, e^{-\mu_L(E)x} \qquad \text{A1.1}$$

where I = intensity of the attenuated beam,

I_o = initial beam intensity,

$\mu_L(E)$ = linear absorption coefficient at energy E,

x = thickness of the absorber.

For n absorbers placed in the path of the beam, the attenuated intensity becomes

$$I = I_o\, e^{-\sum_{i=1}^{n} \mu_{Li}(E)x_i} \qquad \text{A1.2}$$

where the subscript i refers to the i^{th} absorber.

The linear absorption coefficient for water, aluminium and bone have been taken to be that given in Fig.6.4. In the case of the monitor, the beam path is filtered by 45 mm water, 5mm bone and 1.5 mm aluminium. For the detector, the beam filtration was considered to be 40 mm water, 10 mm bone and 1.5 mm aluminium.

Answering Kramers law (equation 2.3) the instantaneous intensity dI emitted in the energy region E to E + dE will be

$$dI = K(E_{max} - E)\, dE \qquad \text{A1.3}$$

where K = constant

E_{max} = maximum photon energy.

For a full wave rectified sinusoidal voltage of angular frequency w radians sec^{-1} equation A1.3 becomes for any time t

$$dI = K(E_{max}|\sin wt| - E)\, dE \quad . \qquad \text{A1.4}$$

The intensity of the filtered beam when $wt = \frac{\pi}{2}$ will be

$$\int dI = K \int_{o}^{E_{max}} (E_{max} - E) e^{-\sum_{i=1}^{n} \mu_{ci}(E) x_i}\, dE \quad . \qquad \text{A1.5}$$

Equation A1.5 was calculated for the monitor and detector filtrations at peak anode voltages of 90 and 95 kVp. This was done numerically, by using 100 steps in the Simpson integration procedure (appendix 5) and using the absorption coefficients for water, aluminium and bone which are also given in appendix 4, table A6.2.

At 90kV, the X ray energy reaching the monitor is 12.071 arbitary units.

Similarly, at 90kV for the detector, 8.8026 arbitary units.

Similarly, at 95kV for the monitor, 13.702 arbitary units.

Similarly, at 95kV for the detector, 10.178 arbitary units.

Thus the ratio of

$$\frac{\text{X ray energy received by detector}}{\text{X ray energy received by monitor}}$$

$$= \quad 0.7292 \text{ at } 90kV \text{ and } 0.7428 \text{ at } 95kV.$$

$$\text{Percentage difference} = \frac{0.0136 \cdot 100}{0.7292}$$

$$= 1.87\ \%.$$

This is the theoretical limit of accuracy of the division technique for the assumed conditions of operation. The practical accuracy of the analogue divider was found to be about 3%, making the overall error about 5%. Because of this large error this method of compensation was not considered further.

Appendix 2.

Experimental procedures

This appendix describes in detail the infrequently used procedures for the equipment referred to in Chapter 4.

A.2.1. Alignment of the brass flange and the two detectors.

The stages are as follows:-

(1) Lock the monitor in position by the 6BA grub screw in the frame.

(2) Move the bottom detector until its collimating slit is vertically below the first slit of the top detector. This may be checked with a plumbline.

(3) Tightly screw the brass flange on top of the dural blocks, making sure that it is square to the main frame.

(4) Slide the X ray head onto the flange as far as possible. Switch on the field light and see that the light falls on the two detector slits.

(5) Check that the centres of the optical and X ray fields coincide using a ZnS or $CdWO_4$ screen.

(6) The centre of the X ray field should fall over the first collimator at the top detector. If not, adjust the two sets of dural blocks together with the brass flange.

(7) Inspect the X ray field arriving at the bottom detector. The centre of the field should be coincident with the collimating slit.

(8) Observe the output of the lower detector using 50kVp, 25mA. Move the detector longitudinally and slowly rotate in the vertical plane by a few degrees, noting the position at which the maximum signal occurs.

(9) Rearrange the rubber mounting of the lower detector until it remains in the optimum position noted in (8).

(10) Carefully remove the monitor and narrow the head collimating slits beneath this detector until the slit width is about 2mm.

(11) Replace and lock into position the top detector and check that there is no loss of signal from the output of the second detector. The X ray beam area on the lower collimating slit should be about 2mm × 15mm. Tighten the dural blocks in position and the three large screws at both ends of the monitor. Remove the locating grub screw and cover the hole with adhesive tape.

A.2.2. Adjustment of the electronic resetting pulse.

This pulse determines the time for which the two integrators and amplifiers are shorted in every half cycle. The control is situated in a panel near the motor. Its effect on the output of the amplifiers can be seen on the oscilloscope as a small positive step (≃0.1V). Fig.A.2.1 illustrates the output of either amplifier in the absence of detected X rays.

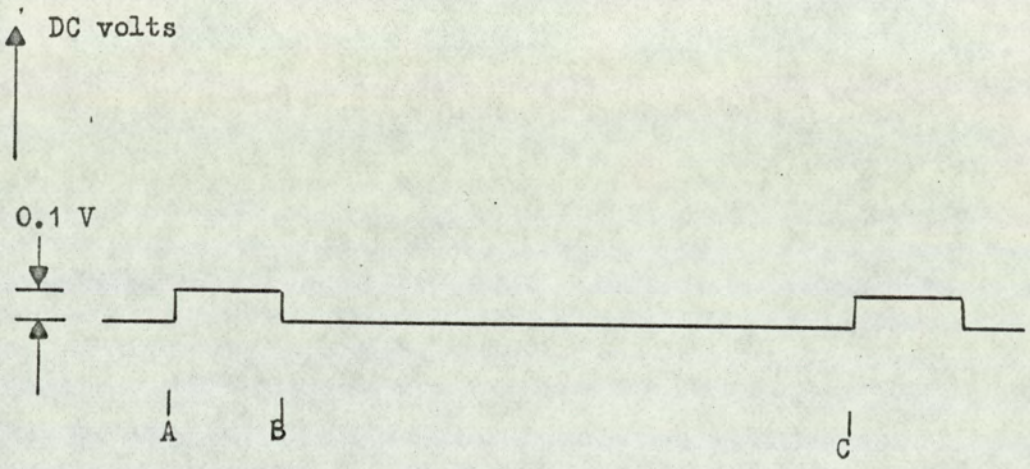

Fig.A2.1

The duration of the pulse may be easily adjusted by the following steps:-

(1) Adjust the time scan of the oscilloscope until one half cycle (AC) is 90mm on the screen. This gives the convenient scale of 5mm ≡ 10°.

(2) Adjust the control potentiometer until the duration of the resetting pulse, A B, is as required.

It should be noted that the minimum resetting duration in every half cycle is 10° for reasons which have been explained in Chapter 3, section 3.3. During the project, a 15± 2° resetting pulse has been used.

A.2.3. Adjustment of the phase control.

The phase control (which is adjacent to the pulse control), adjusts the phase of the resetting pulse so that the electronics may be discharged when the H T anode voltage is at a minimum. It therefore requires an observation of the instantaneous X ray intensity given by the X ray set (and caution on the operator's behalf not to overheat the tungsten anode or to become exposed to the X ray beam). Suitable equipment designed for this task has been described in Chapter 4. It enables the inverted and amplified waveform of the densitometer to be displayed on an oscilloscope. The adjustment may be made by the following steps:-

(1) Check that the oscilloscope is externally triggered by the pulse sent to the NPN Schmitt trigger (A long blue coloured lead makes this connection).

(2) Observe the output of either amplifier and adjust the time scan of the oscilloscope as in the resetting pulse adjustment until 90mm $\equiv 10^{-2}$ second. Note the x ordinates of the pulse.

(3) Place the X ray waveform detector in the bath of the X ray beam (this can be done without making an X ray exposure by using the optical field guide).

(4) Switch on the X ray set and observe the instantaneous X ray waveform.

(5) Adjust the height of the X ray tube head above the detector until a suitably sized waveform is observed for the peak anode voltage and beam current selected. Fig. A.2.2 illustrates a sketch of a typical waveform.

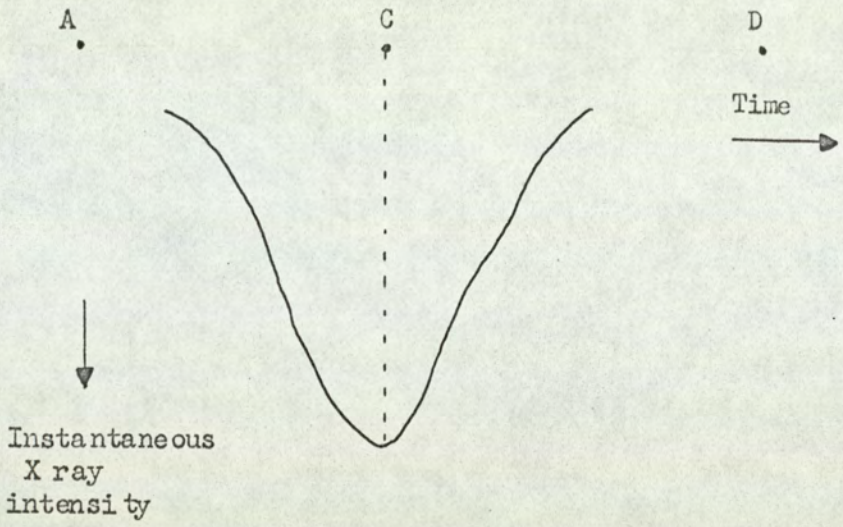

Fig. A2.2

let A = x time ordinate on the oscilloscope screen at which the resetting pulse is switched OFF (this corresponds to position B in Fig. A.2.1.)

D = A + 90mm.

C = x ordinate of the peak of the X ray waveform.

(6) Adjust the phase control until

AC = CD

The integration now commences when the HT anode voltage is a minimum i.e. when $t = 0$.

The accuracy with which the phase can be set can be considerably improved by increasing the vertical y amplification of the ascilloscope to obtain a larger gradient of the waveform at C. Usually the phase can be set to $\pm 3°$.

A.2.4. Setting the integration time.

This procedure may be made quickly by adjusting the left hand potentiometer control leading from the white electronic box. The necessary steps are

(1) Observe the signal output of the second detector on the oscilloscope using the time scan.

(2) Adjust the time scale as in A 2.2 until 90mm ≡ 180°.

(3) With 50mm depth of water in the bath, observe the output. A sketch of a typical oscilloscope trace is shown in Fig. A.2.3.

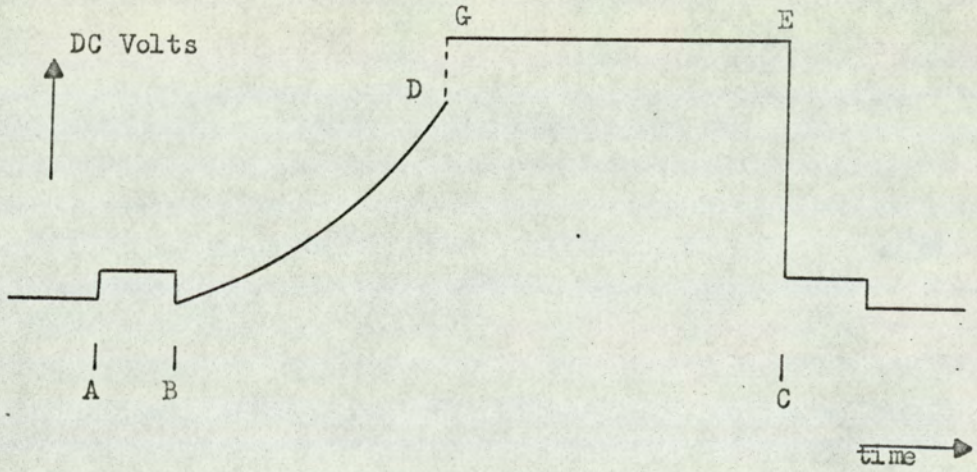

Fig. A2.3

AB = resetting pulse

AC = 90mm ≡ 1/2 cycle

BD = part of the integrated waveform

DG = termination of integration with DC adjustment of the signal

GE = signal held at constant DC level

(4) Adjust the integration time control as required.

(5) Check that neither detector signal is beyond the range of the amplifier at D.

(6) Place a radiopaque object in the beam path of the second detector. The output should be as sketched inFig.A.2.4.

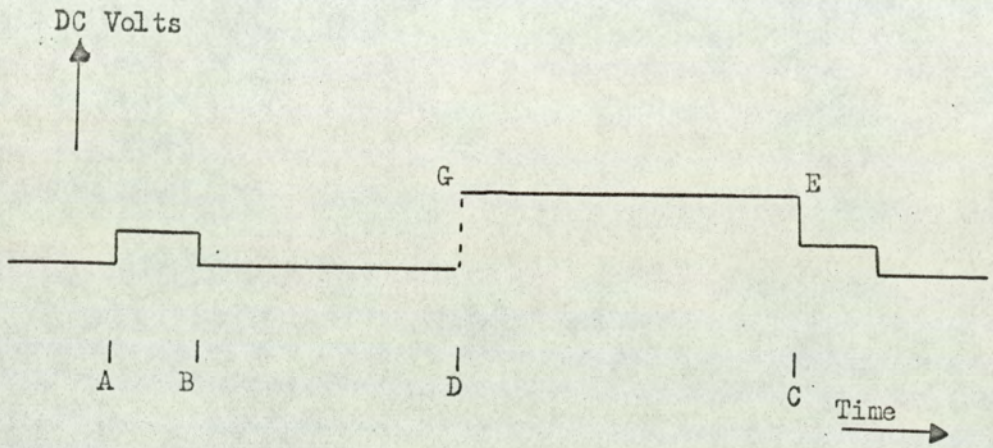

Fig. A2.4

This permits a more accurate setting of position D. This position will be seen to vary slightly as the monitor compensates for peak anode voltage fluctuations. The integration time can usually be set to ± 3°.

A.2.5DC adjustment of the reference line.

The potentiometer for the reference line is situated in the small die cast box near the oscilloscope. The circuit is shown in Fig.A.2.5.

(1) Observe the output of the second detector with a 50mm depth of water in the bath on the time scan of the oscilloscope.
Note the level of GE in Fig. A.2.3.

(2) Switch S1 (Fig.A.2.5) to observe the DC level of the potentiometer output. Adjust as necessary. This can be conveniently set at about 16 volts above the amplifier zero base line ABC (Fig.A.2.3 and A.2.4)

(3) Switch S1 back to observe the detector output. Also switch the oscilloscope to the *xy* scan.

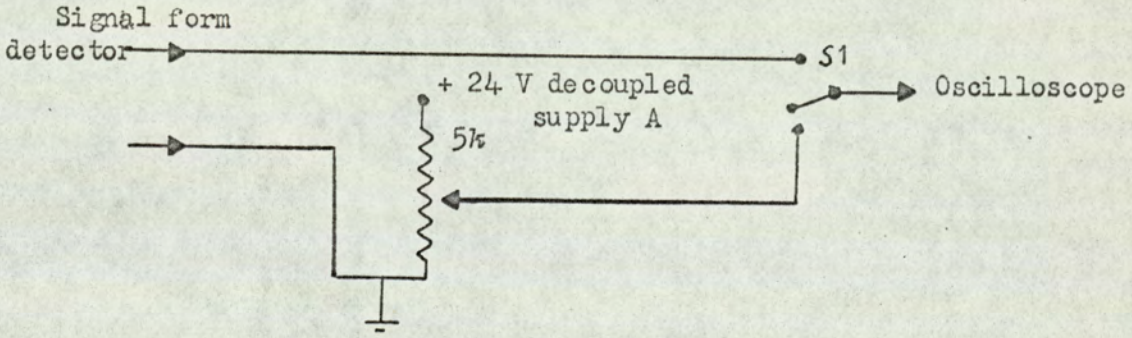

Fig. A2.5

A2.6 Equipment to measure the instantaneous X ray intensity.

The circuit shown in Fig.A2.6 is that used to determine the instantaneous X ray intensity emitted from an X ray generator. The equipment is shown in a photograph in Fig.4.3b.

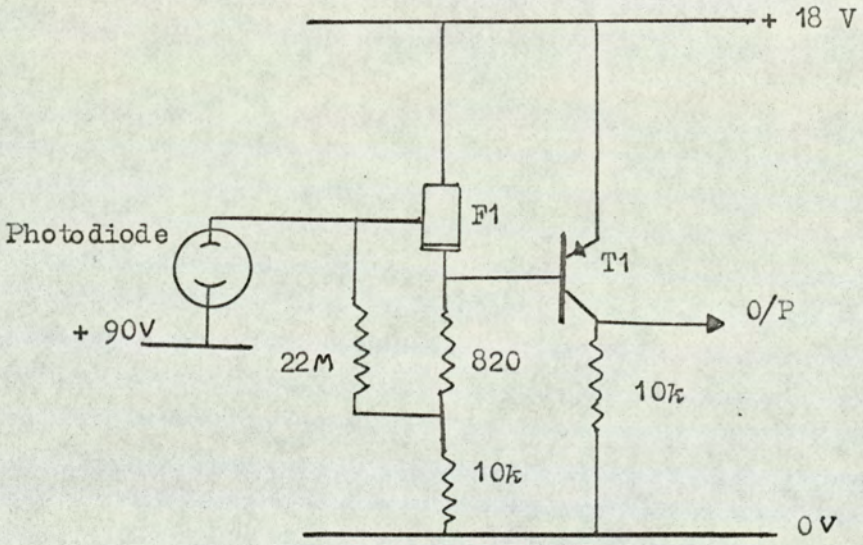

Fig. A2.6

Photodiode	92 AV
F1	2N 3821
T1	2N 4062

Appendix 3

The following tables are experimental results which are mentioned in Chapter 5.

TABLE A3.1

Signal Voltage Measurements

Signal voltages at 70 and 74 kVp

BX mm ivory

Trace Number	0	3	4	5	6	7	8	9	10	11	12
697	12.3	10.6	9.95	9.45	9.05	8.65	8.20	7.85	7.5	7.15	6.85
698	11.25	10.6	9.95	9.45	9.05	8.65	8.25	7.85	7.55	7.15	6.9
Δ	.05	0	0	0	0	0	-0.05	0	-.05	0	-.05
699	12.7	10.95	10.3	9.75	9.4	8.95	8.55	8.15	7.8	7.45	7.1
700	12.55	10.9	10.25	9.75	9.35	8.9	8.5	8.15	7.8	7.45	7.15
Δ	.15	.05	.05	0	.05	.05	.05	0	0	0	-.05
701	16.0	13.8	13.0	12.25	11.75	11.2	10.6	10.15	9.65	9.2	8.75
702	15.95	13.75	13.0	12.35	11.85	11.3	10.8	10.3	9.85	9.45	9.05
Δ	.05	.05	0	-0.1	-0.1	-0.1	-0.2	-0.15	-0.2	-0.25	-0.3
703	19.0	16.3	15.4	14.5	13.9	13.3	12.7	12.1	11.6	11.0	10.6
704	18.9	16.3	15.4	14.6	14.0	13.4	12.7	12.2	11.7	11.1	10.7
Δ	0.1	0	0	-0.1	-0.1	-0.1	0	-0.1	-0.1	-0.1	-0.1
705	12.5	10.85	10.2	9.65	9.3	8.85	8.45	8.05	7.7	7.35	7.05
706	12.2	10.6	10.0	9.55	9.15	8.7	8.3	7.95	7.65	7.35	7.05
Δ	0.3	0.25	0.2	0.15	0.15	0.15	0.1	0.05	0	0	0.05
707	12.95	11.15	10.4	9.9	9.5	9.05	8.6	8.2	7.85	7.55	7.20
708	12.4	10.8	10.2	9.75	9.35	9.0	8.55	8.2	7.9	7.6	7.35
Δ	0.55	0.35	0.2	0.25	0.15	0.05	0.05	0	-0.05	-0.05	-0.15

TABLE A3.2

Signal Voltages at 80 and 84 kVp

BX mm ivory

Trace number		0	3	4	5	6	7	8	9	10	11	12
678		10.95	9.3	8.65	8.25	7.9	7.45	7.1	6.75	6.45	6.1	5.85
679		10.85	9.3	8.65	8.25	7.85	7.5	7.1	6.75	6.45	6.1	5.85
	Δ	0.1	0	0	0	0.05	-0.05	0	0	0	0	0
680		12.7	10.9	10.15	9.65	9.2	8.75	8.3	7.95	7.55	7.15	6.88
681		12.65	10.9	10.25	9.7	9.25	8.8	8.35	7.95	7.55	7.2	6.88
	Δ	0.05	0	0.1	0.05	-0.05	-0.05	-0.05	0	0	-0.05	0
682		18.4	15.9	14.95	14.15	13.55	12.95	12.3	11.75	11.25	10.7	10.15
683		18.1	15.65	14.8	14.05	13.45	12.85	12.2	11.7	11.15	10.6	10.15
	Δ	0.3	0.35	0.15	0.1	0.1	0.1	0.1	0.05	0.1	0.1	0
684		11.75	10.35	9.85	9.4	9.05	8.75	8.4	8.1	7.75	7.5	7.2
685		11.7	10.4	9.85	9.45	9.15	8.75	8.45	8.15	7.85	7.55	7.25
	Δ	0.05	-0.05	0	-0.05	-0.1	0	-0.05	-0.05	-0.1	-0.05	-0.05
686		13.4	11.85	11.25	10.75	10.4	9.95	9.55	9.2	8.85	8.5	8.2
687		13.4	11.85	11.25	10.8	10.45	10.05	9.6	9.25	8.95	8.6	8.3
	Δ	0	0	0	-0.05	-0.05	-0.1	-0.05	-0.05	-0.05	-0.1	-0.1
689		16.75	14.8	14.05	13.4	12.9	12.4	11.85	11.45	11.0	10.55	10.2
690		16.65	14.75	14.0	13.4	12.9	12.45	11.9	11.45	11.0	10.6	10.2
	Δ	0.1	0.05	0.05	0	0	-0.05	-0.05	0	0	-0.05	0
691		19.5	19.2	16.3	15.6	15.0	14.4	13.8	13.3	12.8	12.2	11.7
692		19.3	17.1	16.3	15.5	15.0	14.4	13.8	13.3	12.8	12.3	11.8
	Δ	0.2	0.05	0	0.05	0	0	0	0	0	-0.1	-0.1
693		20.6	18.2	17.2	16.4	15.7	15.1	14.4	13.8	13.3	12.7	12.2
694		20.4	18.1	17.2	16.4	15.9	15.2	14.6	14.1	13.5	13.0	12.5
	Δ	0.2	0.1	0	0	-0.2	-0.1	-0.2	-0.3	-0.2	-0.3	-0.3
695		21.7	18.8	17.9	17.1	16.5	15.7	15.0	14.5	13.9	13.3	12.8
696		21.5	18.9	18.0	17.3	16.7	16.0	15.4	14.8	14.2	13.6	13.0
	Δ	0.2	-0.1	-0.1	-0.2	-0.2	-0.3	-0.4	-0.3	-0.3	-0.3	-0.2

TABLE A3.3

Signal Voltages at 90 and 95 kVp

BX mm ivory

Trace Number	0	3	4	5	6	7	8	9	10	11	12
754	9.3	8.2	7.75	7.35	7.1	6.8	6.5	6.3	6.05	5.8	5.6
755	9.30	8.15	7.70	7.35	7.05	6.85	6.55	6.3	6.05	5.8	5.6
Δ	0	0.05	0.05	0	0.05	-0.05	-0.05	0	0	0	0
756	13.7	12.1	11.5	10.9	10.5	10.1	9.7	9.3	9.0	8.6	8.3
757	13.7	12.1	11.5	11.0	10.6	10.2	9.8	9.4	9.0	8.6	8.4
Δ	0	0	0	-0.1	-0.1	-0.1	-0.1	-0.1	0	0	-0.1
758	9.1	8.1	7.7	7.4	7.2	6.9	6.7	6.4	6.2	6.0	5.8
759	9.1	8.1	7.7	7.4	7.1	6.9	6.7	6.5	6.3	6.0	5.8
Δ	0	0	0	0	0	0	0	-0.1	-0.1	0	0
630	13.0	11.4	10.65	10.1	9.7	9.25	8.8	8.4	8.0	7.6	7.2
631	12.7	11.15	10.45	9.95	9.6	9.15	8.65	8.3	2.9	7.5	7.15
Δ	0.3	0.25	0.2	0.2	0.1	0.1	0.15	0.1	0.1	0.1	0.05
632	16.9	14.9	13.95	13.35	12.75	12.40	11.65	11.15	10.65	10.15	9.75
633	16.8	14.8	14.0	13.35	12.85	12.25	11.75	11.25	10.7	10.3	9.8
Δ	0.1	0.1	-0.05	0	-0.1	0.15	-0.1	-0.1	-0.05	-0.15	-0.05
634	21.9	19.2	18.2	17.4	16.7	16.0	15.2	14.7	14.1	13.4	12.8
635	21.8	19.4	18.1	17.5	16.9	16.2	15.5	14.9	14.3	13.6	13.1
Δ	0.1	-0.2	0.1	-0.1	-0.2	-0.2	-0.3	-0.1	-0.2	-0.2	-0.3
667	11.2	9.65	9.25	8.9	8.6	8.3	7.95	7.65	7.4	7.1	6.8
668	11.15	9.75	9.1	8.8	8.5	8.25	7.95	7.65	7.4	7.05	6.85
Δ	0.05	-0.1	0.15	0.1	0.1	0.05	0	0	0	0.05	-0.05
669	12.7	11.1	10.65	10.2	9.75	9.4	9.05	8.7	8.4	8.1	7.7
670	12.6	11.25	10.75	10.25	9.9	9.6	9.2	8.85	8.5	8.15	7.85
Δ	0.1	-0.15	-0.1	-0.05	-0.15	-0.2	-0.15	-0.15	-0.1	-0.05	-0.15
673	14.15	12.4	11.85	11.3	10.9	10.55	10.15	9.7	9.35	9.05	8.65
672	14.2	12.65	11.6	11.2	10.8	10.35	9.95	9.6	9.25	8.9	8.55
Δ	-0.05	-0.25	+0.25	+0.	0.1	0.2	0.2	0.1	0.1	0.15	0.1

TABLE A3.4

Signal Voltages at 100 and 105 kVp

BX mm ivory

Trace number	0	3	4	5	6	7	8	9	10	11	12
650	11.4	10.14	9.75	9.25	9.0	8.65	8.35	8.1	7.75	7.5	7.2
651	11.25	10.1	9.65	9.3	8.95	8.65	8.35	8.05	7.8	7.5	7.2
Δ	0.15	0.05	0.1	0.05	0.05	0	0	0.05	0.05	0	0
648	15.35	13.75	13.15	12.65	12.2	11.8	11.4	10.95	10.6	10.25	9.8
649	15.15	13.65	12.95	12.50	12.1	12.65	11.25	10.85	10.5	10.1	9.8
Δ	0.2	0.1	0.2	0.1	0.1	0.15	0.15	0.10	0.10	0.15	0.0
655	16.7	14.75	14.1	13.55	17.05	12.55	12.0	11.6	11.15	10.75	10.3
656	16.55	14.75	14.05	13.45	12.95	12.5	12.0	11.55	11.15	10.75	9.9
Δ	0.15	0	0.05	0.10	0.10	0.05	0	0.05	0	0	0
653	21.0	19.0	18.1	17.5	16.9	16.3	15.7	15.2	14.7	14.2	13.7
654	21.0	19.0	18.1	17.4	16.9	16.3	15.8	15.2	14.8	14.2	13.8
Δ	0	0	0	0	0	0	-0.1	0	-0.1	0	-0.1
657	12.45	11.2	10.7	10.2	9.8	9.5	9.15	8.85	8.45	8.15	7.8
658	12.45	11.2	10.75	10.3	9.95	9.65	9.3	8.95	8.55	8.35	8.0
Δ	0	0	-0.05	-0.1	-0.15	-0.15	-0.15	-0.1	-0.1	-0.2	0.2
659	15.75	14.2	13.55	13.05	12.5	12.15	11.7	11.2	10.85	10.5	10.1
660	15.75	14.2	13.55	13.05	12.6	12.2	11.75	11.25	10.95	10.6	10.1
Δ	0	0	0	0	-0.1	-0.05	-0.05	-0.05	-0.1	-0.1	-0.0
661	17.7	16.0	15.3	14.75	14.2	13.8	13.3	12.8	12.45	11.95	11.5
662	17.85	16.1	15.4	14.85	14.35	13.85	13.4	12.9	12.5	12.05	11.6
Δ	-0.15	-0.1	-0.1	-0.1	-0.15	-0.05	-0.1	-0.1	-0.05	-0.1	-0.1
664	20.6	18.6	17.8	17.1	16.5	16.0	15.4	14.8	14.3	13.8	13.3
665	20.7	18.7	17.9	17.2	16.7	16.1	15.5	15.0	14.5	14.0	13.5
Δ	-0.1	-0.1	-0.1	-0.1	-0.2	-0.1	-0.1	-0.2	-0.2	-0.2	-0.2

TABLE A3.5

Trace Number	Peak voltage kVp	Beam Current mA	Integration time T2 degrees	'Scope setting volts cm^{-1}
697	70	100	80	1
698	74	100		1
699	70	100	83	1
700	74	100		
701	70	100	90	1
702	74	100		1
703	70	100	100	2
704	74	100		2
705	70	50	120	1
706	74	50		1
707	70	50	125	1
708	74	50		1

TABLE A3.6

Trace Number	Peak voltage kVp	Beam current mA	Integration time T_2 Degrees	'Scope Setting volts cm^{-1}
678	80	100	67	1
679	84	100		1
680	80	100	70	1
681	84	100		1
682	80	100	80	1
683	84	100		1
684	80	50	83	
685	84	50		1
686	80	50	90	1
687	84	50		1
689	80	50	100	1
690	84	50		1.
691	80	50	110	2
692	84	50		2
693	80	50	120	2
694	84	50		2
695	80	50	130	2
696	84	50		2

TABLE A3.7

Trace Number	Peak voltage kVp	Beam current mA	Integration time T2 Degrees	'Scope Setting volts cm^{-1}
754	90	100	60	1
755	95	100		1
756	90	100	69	2
757	95			2
758	90	50	73	1
759	95	50		1
630	90	50	80	1
631	95	50		1
632	90	50	90	1
633	95	50		1
634	90	50	100	2
635	95	50		2
667	90	25	100	1
668	95	25		1
669	90	25	110	1
670	95	25		1
673	90	25	120	1
672	95	25	120	1

TABLE A3.8

Trace Number	Peak voltage kVp	Beam current mA	Integration time T2 Degrees	'Scope Setting volts cm^{-1}
650	100	50	63	1
651	105	50		1
648	100	50	70	1
649	105	50		1
655	100	50	75	1
656	105	50		1
653	100	50	80	2
654	105	50		2
657	100	25	90	1
658	105	25		1
659	100	25	100	1
660	105	25		1
661	100	25	110	1
662	105	25		1
664	100	25	120	2
665	105	25		2

TABLE A3.9

Normalized signal voltages at 70 and 74 kVp

		BX	mm ivory								
Trace No.	T2	0	3	4	5	6	7	8	9	10	11	12
697	80	6.15	5.3	4.97	4.72	4.52	4.37	4.1	3.92	3.75	3.57	3.42
698		5.62	5.3	4.97	4.72	4.52	4.32	4.12	3.92	3.77	3.57	3.45
699	83	6.35	5.47	5.15	4.87	4.7	4.47	4.27	4.07	3.9	3.72	3.50
700		6.23	5.45	5.12	4.87	4.67	4.45	4.25	4.07	3.9	3.72	3.57
701	90	8.0	6.9	6.5	6.12	5.87	5.60	5.3	5.07	4.82	4.6	4.37
702		7.97	6.87	6.5	6.17	5.92	5.65	5.4	5.15	4.92	4.72	4.52
703	100	9.5	8.15	7.7	7.25	6.95	6.65	6.35	6.05	5.8	5.5	5.3
704		9.45	8.15	7.7	7.3	7.0	6.7	6.35	6.1	5.55	5.55	5.35
705	120	12.5	10.85	10.2	9.65	9.3	8.85	8.45	8.05	7.7	7.35	7.05
706		12.2	10.6	10.0	9.55	9.15	8.7	8.3	7.95	7.65	7.35	7.05
707	125	12.95	11.15	10.4	9.9	9.5	9.05	8.6	8.2	7.85	7.55	7.20
708		12.4	10.8	10.2	9.75	9.75	9.0	8.55	8.2	7.9	7.6	7.35

TABLE A3.10

Normalised signal voltages at 80 and 84 kVp

BX mm ivory

Trace Number	T2	0	3	4	5	6	7	8	9	10	11	12
678	67	5.47	4.65	4.32	4.12	3.95	3.72	3.55	3.37	3.22	3.05	2.9
679		5.42	4.65	4.32	4.12	3.92	3.75	3.55	3.37	3.22	3.05	2.9
680	70	6.35	5.45	5.07	4.82	4.60	4.37	4.15	3.97	3.77	3.57	3.4
681		6.32	5.45	5.12	4.85	4.62	4.4	4.17	3.97	3.77	3.6	3.4
682	80	9.2	7.95	7.49	7.07	6.77	6.47	6.15	5.87	5.63	5.35	5.0
683		9.05	7.82	7.4	7.02	6.72	6.42	6.1	5.85	5.57	5.3	5.0
684	83	11.75	10.35	9.85	9.4	9.05	8.75	8.4	8.1	7.75	7.5	7.2
685		11.7	10.4	9.85	9.45	9.15	8.75	8.45	8.15	7.85	7.55	7.2
686	90	13.4	11.85	11.25	10.75	10.4	9.95	9.55	9.2	8.85	8.5	8.2
687		13.4	11.85	11.25	10.8	10.45	10.05	9.6	9.25	8.95	8.6	8.3
689	100	16.75	14.8	14.05	13.4	12.9	12.4	11.85	11.45	11.0	10.55	10.2
690		16.65	14.75	14.0	13.4	12.9	12.45	11.9	11.45	11.0	10.6	10.2
691	110	19.5	19.2	16.3	15.6	15.0	14.4	13.8	13.3	12.8	12.2	11.7
692		19.3	17.1	16.3	15.5	15.0	14.4	13.8	13.3	12.8	12.3	11.8
693	120	20.6	18.2	17.2	16.4	15.7	15.1	14.4	13.8	13.3	12.7	12.2
694		20.4	18.1	17.2	16.4	15.9	15.2	14.6	14.1	13.5	13.0	12.5
695	130	21.7	18.8	17.9	17.1	16.5	15.7	15.0	14.5	13.9	13.3	12.8
696		21.5	18.9	18.0	17.3	16.7	16.0	15.4	14.8	14.2	13.6	13.1

TABLE A3.11

Normalized signal voltages at 90 and 95kVp

Bx mm Ivory

Trace No.	T2	0	3	4	5	6	7	8	9	10	11	12
754	60	4.65	4.10	3.86	3.68	3.55	3.4	3.26	3.15	3.03	2.9	2.8
755		4.64	4.07	3.85	3.68	3.53	3.41	3.26	3.15	3.03	2.9	2.8
756	69	6.85	6.05	5.75	5.45	5.25	5.05	4.85	4.65	4.5	4.3	4.15
757		6.85	6.05	5.75	5.5	5.3	5.1	4.9	4.7	4.5	4.3	4.2
758	73	9.1	8.1	7.7	7.4	7.2	6.9	6.7	6.4	6.2	6.0	5.8
759		9.1	8.1	7.7	7.4	7.2	6.9	6.7	6.5	6.3	6.0	5.8
630	80	13.0	11.4	10.65	10.1	9.7	9.25	8.8	8.4	8.0	7.6	7.2
631		12.7	11.15	10.45	9.95	9.5	9.15	8.65	8.3	7.9	7.5	7.15
632	90	16.9	14.9	13.95	13.35	12.75	12.40	11.65	11.15	10.65	10.15	9.75
633		16.8	14.7	14.0	13.35	12.85	12.25	11.75	11.25	10.7	10.3	9.8
635	100	21.8	19.4	18.1	17.75	16.9	16.2	15.5	14.9	14.3	13.6	13.1
667	100	22.4	19.3	18.5	17.8	17.2	16.6	15.9	15.3	14.8	14.2	13.6
668		22.3	19.5	18.2	17.6	17.0	16.5	15.9	15.3	14.8	14.1	13.7
669	110	25.4	22.2	21.3	20.4	19.5	18.8	18.1	17.4	16.8	16.2	15.4
670		25.2	21.5	21.5	20.5	19.8	18.4	18.4	17.7	17.0	16.3	15.7
673	120	28.3	24.8	23.7	22.6	21.8	20.3	20.3	19.4	18.7	18.1	17.3
672		28.4	25.3	23.2	22.4	21.6	19.9	19.9	19.2	18.5	17.8	17.1

TABLE A3.12

Normalised signal voltages at 100 and 105 kVp

		BX mm Ivory										
Trace No.	T2.	0	3	4	5	6	7	8	9	10	11	12
650	63	11.4	10.15	9.75	9.25	9.0	8.65	8.35	8.1	7.75	7.5	7.25
651		11.25	10.1	9.65	9.3	8.95	8.65	8.35	8.05	7.8	7.5	7.25
648	70	15.35	13.75	13.15	12.65	12.2	11.8	11.4	10.95	10.6	10.25	9.85
		15.5	13.65	12.95	12.50	12.1	11.6	11.25	10.85	10.5	10.1	9.8
655	75	16.7	14.75	14.1	13.55	13.05	12.55	12.0	11.6	11.15	10.75	10.3
656		16.55	14.75	14.05	13.45	12.95	12.5	12.0	11.55	11.15	10.75	10.3
653	80	21.0	19.0	18.1	17.5	16.9	16.3	15.7	15.2	14.7	14.2	13.7
654		21.0	19.0	18.1	17.4	16.9	16.3	15.8	15.2	14.8	14.2	13.8
657	90	24.9	22.4	21.4	20.4	19.6	19.0	18.3	17.7	16.9	16.3	15.7
658		24.9	22.4	21.5	20.6	19.9	19.3	18.6	17.9	17.1	16.7	16.1
659	100	31.5	28.4	27.1	26.1	25.0	24.3	23.4	22.4	21.7	21.0	20.2
660		31.5	28.4	27.1	26.1	25.2	24.4	23.5	22.5	21.9	21.2	20.3
661	110	34.4	32.0	30.6	29.5	28.4	27.6	26.6	25.6	24.9	23.9	23.0
662		35.7	32.2	30.8	29.7	28.7	27.7	26.8	25.8	25.0	24.1	23.2
664	120	41.2	37.2	35.6	34.2	33.0	32.0	30.8	29.6	28.6	27.6	26.6
665		41.4	37.4	35.8	34.4	33.4	33.2	31.0	29.0	29.0	27.0	27.0

APPENDIX 4.

The following tables are theoretical results which are mentioned in chapter 6.

For clarity most of the results have been written with the exponent of ten after the number to be multiplied e.g.

$1.764 - 4 = 1.764. \ 10^{-4}$.

The meaning of various symbols and their units are as follows

Symbol	Unit	Meaning of symbol
$S1$	Degrees	Lower limit of time integration .
$S2$	Degrees	Upper limit of time integration.
T1	seconds	$S1$ expressed in seconds for sinusoidal frequency 50Hz .
T2	seconds	$S2$ expressed in seconds for the same frequency .
TDASH	seconds	New upper limit of time integration when the amplitude of the voltage changes. See equation 6.11 .
ΔT	Degrees	T2- TDASH expressed in degrees .
$Vmin(=E_{min})$	Kilovolts	Lower limit of energy integration.
$V_{max}(=E_{max})$	Kilovolts	Upper limit of energy integration.
V'_{max}(=EDASH)	Kilovolts	$\frac{105}{100} \times V_{max}$.
ψ	Percent	Percentage error in the solution of equation 6.11. See also equation 6.16.
χ	Percent	Percentage error due to 5% increase in anode voltage. See equation 6.19.
XB	mm	Thickness of bone(= ivory)above the monitor.
XW	mm	Path length of water above the monitor.
BX	mm	Thickness of bone above the detector.
WX	mm	Path length of water above the detector.
G1	arbitary	The monitor signal. See equation 6.8.
G_{11}	arbitary	The monitor signal when the anode voltage is V'_{max} . See equation 6.15.

Symbol	Unit	Meaning of symbol
G_2	arbitary	The detector signal. See equations 6.9 and 6.17.
G_{22}	arbitary	The detector signal when the anode voltage is V_{Max}. See equation 6.18.
ρ	$kg\ m^{-3}$	Density of bone considered.
$\rho(x)$	$kg\ m^{-3}$	Density of bone taken to be $x\ kg\ m^{-3}$.
ΔCa	Percent	Percentage change of calcium in the bone. See equation 6.23.
$G(y)$	Arbitary	The detector signal when there is a change of calcium content in the bone of $y\%$.
P.C.	Percent	Percentage change in the detector signal. See equations 6.20, 6.23.

TABLE A6.1

E = electron energy (keV)

r = range of electron in tungsten (gm/cm^2)

R = range of electron in tungsten (mm)

d = depth of bremsshrahlung production (mm)

D = photon distance through the tungsten (mm)

E	r	R	d	D
10	1.6078 - 6	8.3304 -7	2.0826 - 7	7.2630 - 7
20	6.7862 - 4	3.5162 -6	8.7904 - 7	3.0656 - 6
30	1.5101 - 5	7.8244 -6	1.9561 - 6	6.8218 - 6
40	2.6135 - 5	1.3541 -5	3.3853 - 6	1.1806 - 5
50	3.9561 - 5	2.0498 -5	5.1244 - 6	1.7871 - 5
60	5.5120 - 5	2.8560 -5	7.1399 - 6	2.4900 - 5
70	7.2602 - 5	3.7618- 5	9.4044 - 6	3.2797 - 5
80	9.1832 - 5	4.7581 -5	1.1895 - 5	4.1484 - 5
90	1.1266 - 4	5.8374 -5	1.4594 - 5	5.0894 - 5
100	1.3497 - 4	6.9930 -5	1.7483 - 5	6.0970 - 5

Shown in Fig.6.1.

TABLE A6.2

Linear absorption coefficients of various substances used in the calculations.

Photon energy keV	Water cm^{-1}	Bone cm^{-1}	Aluminium cm^{-1}	2% NaCl sol. cm^{-1}
10	5.09 0	7.84 1	7.13 1	5.84 0
20	7.77 -1	1.11 1	1.13 1	8.94 -1
30	3.74 -1	3.75 0	3.86 0	4.08 -1
40	2.73 -1	1.89 0	1.80 0	2.92 -1
50	2.33 -1	1.20 0	9.93 -1	2.46 -1
60	2.10 -1	8.75 -1	8.13 -1	2.22 -1
70	1.96 -1	7.01 -1	6.87 -1	2.06 -1
80	1.85 -1	5.97 -1	5.93 -1	1.95 -1
90	1.77 -1	5.29 -1	5.22 -1	1.86 -1
100	1.70 -1	4.81 -1	4.65 -1	1.78 -1

Shown in Figs. 6.4 - 6.6.

TABLE A6.3

V_{max} = 80 kVp V_{min} = 10 kVp BX = 10 mm WX = 40 mm.

G_1G_2 Shown in Figs.6.7 , 6.9 (G_2 only)

$\chi - \phi$ " " Fig. 6.11

ΔT " " Fig. 6.16.

G_1	G_{11}	G_2	G_{22}	S2	ϕ	χ	$\chi - \phi$	T2	TDASH	ΔT^o
3.6365 -4	3.6403 -4	7.9705 -5	8.0864 -5	30	1.0630 -1	1.4489 0	1.3426 0	1.6667 -3	1.5892 -3	-1.3945 0
4.7129 -3	4.7119 -3	1.6929 -3	1.7117 -3	40	-2.2029 -2	1.1070 0	1.1290 0	2.2222 -3	2.1172 -3	-1.8906 0
2.1136 -2	2.118 -2	9.4942 -3	9.5855 -3	50	-8.5470 -2	9.6243 -1	1.0479 0	2.6416 -3	2.6416 -3	-2.4512 0
5.7302 -2	5.7277 -2	2.9034 -2	2.9330 -2	60	-4.2696 -2	1.0210 0	1.0637 0	3.3333 -3	3.1608 -3	-3.1055 0
1.1622 -1	1.1613 -1	6.3228 -2	6.3900 -2	70	-7.3993 -2	1.0630 0	1.1370 0	3.8889 -3	3.6709 -3	-3.9238 0
1.9484 -1	1.9493 -1	1.1068 -1	1.1217 -1	80	4.8765 -2	1.3427 0	1.2939 0	4.4444 -3	4.1693 -3	-4.9531 0
2.8482 -1	2.8485 -1	1.6595 -1	1.6849 -1	90	1.0688 -2	1.5290 0	1.5183 0	5.0000 -3	4.6455 -3	-6.3809 0
3.7480 -1	3.7477 -1	2.2123 -1	2.2531 -1	100	-8.3771 -3	1.8443 0	1.8443 0	5.5555 -3	5.0895 -3	-8.3887 0
4.5342 -1	4.5358 -1	2.6868 -1	2.7503 -1	110	3.4905 -2	2.3620 0	2.3271 0	6.1111 -3	5.4836 -3	-1.1295 1
5.1234 -1	5.1241 -1	3.0288 -1	3.1183 -1	120	1.3714 -2	2.9567 0	2.9430 0	6.6667 -3	5.7985 -3	-1.5627 1
5.4851 -1	5.4851 -1	3.2242 -1	3.3417 -1	130	2.9822 -4	3.6442 0	3.6439 0	7.2222 -3	6.0093 -3	-2.1833 1
5.6493 -1	5.6487 -1	3.3022 -1	3.4420 -1	140	-1.0570 -2	4.2346 0	4.2452 0	7.7778 -3	6.1115 -3	-2.9993 1
5.6928 -1	5.6934 -1	3.3183 -1	3.4693 -1	150	1.0037 -2	4.5499 0	4.5399 0	8.3333 -3	6.1403 -3	-3.9474 1

TABLE A6.5

V_{max} = 90 kVp V_{min} = 60 kVp BX = 10 mm
WX = 40 mm

S1 = 43°

$\chi - \phi$ shown in Fig.6.11.

G_1	G_{11}	G_2	G_{22}	S2	ϕ	χ	$\chi - \phi$	T2	TDASH	ΔT
1.45583 -3	1.4584 -3	1.0676 -3	1.0722 -3	50	1.7776 -1	4.2658 -1	2.4882 -1	2.7778 -3	2.6318 -3	-2.6270 0
1.4437 -2	1.4450 -3	1.0794 -2	1.0823 -2	60	9.3141 -2	2.6961 -1	1.7647 -1	3.3333 -3	3.1361 -3	-3.5508 0
4.6903 -2	4.6938 -2	3.5534 -2	3.5638 -2	70	7.4349 -2	2.9352 -2	2.1917 -1	3.8889 -3	3.6375 -3	-4.5254 0
9.8484 -2	9.8427 -2	7.5257 -2	7.5429 -2	80	-5.8262 -2	2.2836 -1	2.8662 -2	4.4444 -3	4.1207 -3	-5.8281 0
1.6166 -1	1.6154 -1	1.2415 -1	1.2453 -1	90	-7.3072 -2	3.0730 -1	3.8037 -1	5.000 -3	4.5732 -3	-7.6465 0
2.2483 -1	2.2495 -1	1.7304 -1	1.7401 -1	100	5.3272 -2	5.6043 -1	5.0716 -1	5.5555 -3	4.9835 -3	-1.0298 1
2.7641 -1	2.7640 -1	2.1276 -1	2.1417 -1	110	-2.2424 -3	6.6208 -1	6.6432 -1	6.1111 -3	5.3117 -3	-1.4389 1
3.0888 -1	3.0900 -1	2.3751 -1	2.3959 -1	120	4.1064 -2	8.7685 -1	8.3579 -1	6.6667 -3	5.5290 -3	-2.0479 1
3.2186 -1	3.2191 -1	2.4723 -1	2.4964 -1	130	1.6894 -2	9.7397 -1	9.5708 -1	7.2222 -3	5.6189 -3	-2.8860 1

TABLE A6.4

V_{max} = 90 kVp V_{min} = 10 kVp BX = 10 mm WX = 40 mm

G_1 G_2 shown in Fig.6.8, 6.9 (G_2 only)
$\chi - \phi$ " " Fig. 6.11
ΔT " " Fig.6.16.

G_1	G_{11}	G_2	G_{22}	S 2	ϕ	χ	$\chi - \phi$	T2	TDASH	ΔT°
1.1216 -3	1.1225 -3	3.1984 -4	3.2384 -4	30	7.8579 -2	1.2519 0	1.1733 0	1.6607 -3	1.5905 -3	-1.3711
1.0824 -2	1.0809 -2	4.5415 -3	4.5788 -3	40	-1.3832 -1	8.2140 -1	9.5292 -1	2.2222 -3	2.1189 -3	-1.8594
4.2261 -2	4.2244 -2	2.1199 -2	2.1383 -2	50	-3.9448 -2	8.6923 -1	9.0868 -1	2.7778 -3	2.6449 -3	-2.3926
1.0621 -1	1.0631 -1	5.8779 -2	5.9380 -2	60	9.5139 -2	1.0222 0	9.2706 -1	3.3333 -3	3.1660 -3	-3.0117
2.0600 -1	2.0586 -1	1.2093 -1	1.2202 -1	70	-6.8562 -2	9.0004 -1	9.6860 -1	3.8889 -3	3.6770 -3	-3.8145
3.3607 -1	3.3620 -1	2.0459 -1	2.0690 -1	80	3.8862 -2	1.1301 0	1.0912 0	4.4444 -3	4.1780 -3	-4.7969
4.8342 -1	4.8361 -1	3.0074 -1	3.0468 -1	90	4.0312 -2	1.3109 0	1.2706 0	5.5000 -3	4.6592 -3	-6.1348
6.3076 -1	6.3078 -1	3.9688 -1	4.0298 -1	100	3.8039 -3	1.5363 0	1.5325 0	5.5556 -3	5.1101 -3	-8.0176
7.6083 -1	7.6089 -1	4.8054 -1	4.8973 -1	110	7.6227 -3	1.9130 0	1.9054 0	6.1111 -3	5.5151 -3	-1.0729
8.6062 -1	8.6077 -1	5.4269 -1	5.5582 -1	120	1.7292 -2	2.4178 0	2.4005 0	6.6667 -3	5.8488 -3	-1.4722
9.2457 -1	9.2445 -1	5.8028 -1	5.9750 -1	130	-1.3804 -2	2.9687 0	2.9825 0	7.2222 -3	6.0823 -3	-2.0519
9.5601 -1	9.5579 -1	5.9693 -1	6.1784 -1	140	-2.3313 -2	3.5018 0	3.5251 0	7.7778 -3	6.2065 -3	-2.8284
9.6571 -1	9.6572 -1			150				8.3333 -3	6.2475 -3	-3.7546

TABLE A6.6

$\chi - \phi$ shown in Fig. 6.10

$S1 = 10°$ $S2 = 80°$ $G_1 = 1.9484\ -1$ $\phi' = 4.8765\ -2$

$V_{max} = 80$ kVp Vmin = 10kVp $G_{11} = 1.9493\ -1$

$T2 = 4.4444\ -3$ TDASH = $4.1693\ -3$ XB = 5mm XW = 45 mm

$\Delta T = T2 - TDASH = 2.7517\ -4$ $V'max = 84$ kVp

$= -4.953°$

G_2	G_{22}	BX	WX	χ	$\chi - \phi$
3.9961 -1	3.9370 -1	0	50	-1.4778 0	-1.5266 0
2.9113 -1	2.8873 -1	2	48	-8.2183 -1	-8.7059 -1
2.2117 -1	2.2066 -1	4	46	-2.3049 -1	-2.7925 -1
1.7258 -1	1.7313 -1	6	44	3.1966 -1	2.7089 -1
1.3723 -1	1.3839 -1	8	42	8.4153 -1	7.9276 -1
1.1068 -1	1.1217 -1	10	40	1.3427 0	1.2939 0
9.0263 -2	9.1914 -2	12	38	1.8281 0	1.7793 0
7.4281 -1	7.5990 -2	14	36	2.3010 0	2.2522 0

TABLE A6.7

$\chi - \phi$ shown in Fig. 6.10

$S1 = 10°$ $S2 = 80°$ $G_1 = 3.3607\ -1$ $\phi = 3.8862\ -2$

$V_{max} = 90kVp$ $V_{min} = 10kVp$ $G_{11} = 3.3620\ -1$

$T2 = 4.444\ -3$ $TDASH = 4.1780$ $XB = 5mm$ $XW = 45mm$

$\Delta T = -4.7969°$

G_2	G_{22}	BX	WX	χ	$\chi - \phi$
6.3141 -1	6.2337 -1	0	50	-1.2734 0	-1.31226
4.7812 -1	4.747 -1	2	48	-7.0631 -1	-7.4517 -1
3.7564 -1	3.7489 -1	4	46	-1.9919 -1	-2.3805 -1
3.0213 -1	3.0294 -1	6	44	2.6887 -1	2.3001 -1
2.4707 -1	2.4883	8	42	7.0955 -1	6.7069 -1
2.0459 -1	2.0690 -1	10	40	1.1301 0	1.0912 0.
1.7108 -1	1.7371 -1	12	38	1.5353 0	1.4964 0
1.4420 -1	1.4698 -1	14	36	1.9282 0	1.8893 0

TABLE A6.8

Calculated results shown in Fig. 6.10

S1 = 34° S2 = 80° G_1 1.9098 -1 ϕ = 3.7882 -1

V_{max} = 90 kVp V_{min} = 50 kVp G_{11} 1.9105 -1

T2 = 4.44444 -3 TDASH = 4.1502 -3 x = 5mm xW = 45mm

V_{max} = 94.5kVp

ΔT = 5.2969°

G_2	G_{22}	BX	WX	χ	$\chi - \phi$
2.6731 -1	2.6626 -1	0	50	-3.9141 -1	-4.2929 -1
2.3350 -1	2.3298 -1	2	48	-2.2276 -1	-2.6064 -1
2.0416 -1	2.0406 -1	4	46	-5.0009 -1	-8.7891 -2
1.7868 -1	1.7891 -1	6	44	1.2677 -1	-8.8888 -2
1.5653 -1	1.5701 -1	8	42	3.0751 -1	2.6963 -1
1.3725 -1	1.3793 -1	10	40	4.9214 -1	4.5426 -1
1.2046 -1	1.2128 -1	12	38	6.8058 -1	6.4270 -1
1.0582 -1	1.0675 -1	14	36	8.7273 -1	8.3485 -1

TABLE A6.9

Calculated results shown in Fig.6.10

$S1 = 43°$ $S2 = 80°$ $G_1 = 9.8484\ -2$ $\phi = -5.8262\ -2$

$V_{max} = 90kVp$ $V_{min} = 60kVp$ $G_{11} = 9.8427\ -2$

$T2 = 4.4444\ -3$ $TDASH = 4.1207\ -3$ $XB = 5mm$ $XW = 45mm$

$\Delta T = T2 - TDASH = 3.2378\ -4$ $V_{max} = 94.5kVp$

$= -5.8281°$

G_2	G_{22}	BX	WX	χ	$\chi - \phi$
1.2906 -1	1.2863 -1	0	50	-3.3411 -1	2.7585 -1
1.1581 -1	1.1555 -1	2	48	-2.2506 -1	-1.6424 -1
1.0394 -1	1.0383 -1	4	46	-1.1429 -1	-5.6028 -2
9.3315 -2	9.3314 -2	6	44	-1.8028 -3	+5.6459 -2
8.3792 -2	8.3886 -2	8	42	1.1241 -1	1.7067 -1
7.5257 -2	7.5429 -2	10	40	2.2836 -1	2.8662 -1
6.7606 -2	6.7840 -2	12	38	3.4605 -1	4.0431 -1
6.0747 -2	6.1030 -2	14	36	4.6547 -1	5.2373 -1

TABLE A6.10

$S2 = 80°$

Vmax kV	Vmin kV	A mm^{-1}
90	10	1.35 -1
80	10	1.61 -1
90	50	5.96 -2
90	60	3.74 -2

TABLE A6.11

Shown in Fig. 6.12.

Vmax = 80kVp Vmin = 10kVp

XB = 10mm

XW = 40mm S2 = 30°

ρ	G_2
1.3 3	1.2268 -4
1.4 3	9.8720 -5
1.5 3	7.9708 -5
1.6 3	6.4558 -5
1.7 3	5.2437 -5
1.8 3	4.2705 -5

TABLE A6.12

V_{max} = 80 kVp V_{min} = 10 kVp WX = 40 mm BX = 10 mm

Shown in Fig.6.13.

S2	ρ(1300)	ρ(1500)	ρ(1800)	P.C.
30	1.2268 -4	7.9708 -5	4.2705 -5	3.01
40	2.2781 -3	1.6929 -3	1.1035 -3	2.08
50	1.2029 -2	9.4941 -3	6.7530 -3	1.67
60	3.5614 -2	2.9034 -2	2.1635 -2	1.44
70	7.6096 -2	6.3227 -2	4.8419 -2	1.31
80	1.3168 -1	1.1068 -1	8.6164 -1	1.23
90	1.9612 -1	1.6595 -1	1.3044 -1	1.19
100	2.6055 -1	2.2123 -1	1.7471 -1	1.16
110	3.1613 -1	2.6868 -1	2.1246 -1	1.16
120	3.5662 -1	3.0287 -1	2.3924 -1	1.16
130	3.8020 -1	3.2241 -1	2.5412 -1	1.17
140	3.8995 -1	3.3022 -1	2.5977 -1	1.18
150	3.9211 -1	3.3183 -1	2.6083 -1	1.19

TABLE A6.13

Shown in Fig. 6.13.

V_{max} = 90kVp V_{min} = 10kVp WX = 40 mm BX = 10 mm

S2	p(1300)	p(1500)	p(1800)	P.C.
30	4.5818 -4	3.1984 -4	1.9033 -4	2.51
40	5.8601 -3	4.5415 -3	3.1463 -3	1.79
50	2.6071 -2	2.1199 -2	1.5739 -2	1.46
60	7.0411 -2	5.8779 -2	4.5322 -2	1.28
70	1.4259 -1	1.2093 -1	9.5376 -2	1.17
80	2.3890 -1	2.0459 -1	1.6360 -1	1.10
90	3.4916 -1	3.0073 -1	2.4246 -1	1.06
100	4.5941 -1	3.9688 -1	3.2132 -1	1.04
110	5.5572 -1	4.8054 -1	3.8955 -1	1.04
120	6.2791 -1	5.4269 -1	4.3961 -1	1.04
130	6.7225 -1	5.8027 -1	4.6919 -1	1.05
140	6.9246 -1	5.9693 -1	4.8178 -1	1.06
150	6.9786 -1	6.0115 -1	4.8474 -1	1.06

TABLE A6.14

V_{max} = 90 kVp

V_{min} = 10 kVp

XB = 5 mm

XW = 45 mm

$\varsigma 2$ = 40°

Shown in Fig. 6.14.

ΔCa	G_2
-10	1.1109 -2
-8	1.1049 -2
-6	1.0990 -2
-4	1.0933 -2
-2	1.0878 -2
0	1.0823 -2
2	1.0770 -2
4	1.0719 -2
6	1.0668 -2
8	1.0618 -2
10	1.0570 -2

TABLE A6.15

V_{max} = 80 kVp XB = 5 mm XW = 45 mm

V_{min} = 10 kVp

Shown in Fig.6.15.

S 2	G(-10)	G(0)	G(10)	P.C.
30	3.8360 -4	3.6364 -4	3.4630 -4	5.13 -1
40	4.8686 -3	4.7129 -3	4.5751 -3	3.11 -1
50	2.1631 -2	2.1136 -2	2.0694 -2	2.22 -1
60	5.8352 -2	5.7301 -2	5.6360 -2	1.74 -1
70	1.1801 -1	1.1622 -1	1.1462 -1	1.46 -1
80	1.9749 -1	1.9484 -1	1.9245 -1	1.29 -1
90	2.8840 -1	2.8482 -1	2.8160 -1	1.19 -1
100	3.7931 -1	3.7480 -1	3.7075 -1	1.14 -1
110	4.5879 -1	4.5342 -1	4.4859 -1	1.12 -1
120	5.1844 -1	5.1234 -1	5.0684 -1	1.13 -1
130	5.5517 -1	5.4850 -1	5.4251 -1	1.15 -1
140	5.7193 -1	5.6493 -1	5.5863 -1	1.18 -1
150	5.7642 -1	5.6928 -1	5.6286 -1	1.19 -1

TABLE A6.16.

V_{max} = 80 kVp V_{min} = 10 kVp

XB = 10 mm XW = 40 mm

Shown in Fig.6.15.

S2	G(-10)	G(0)	G(10)	P.C.
30	8.7123 -5	7.9708 -5	7.3491 -5	8.55 -1
40	1.7828 -3	1.6929 -3	1.6150 -3	4.96 -1
50	9.8390 -3	9.4941 -3	9.1911 -3	3.41 -1
60	2.9839 -2	2.9034 -2	2.8321 -2	2.61 -1
70	6.4672 -2	6.3227 -2	6.1945 -2	2.16 -1
80	1.1289 -1	1.1068 -1	1.0872 -1	1.88 -1
90	1.6899 -1	1.6595 -1	1.6325 -1	1.73 -1
100	2.2509 -1	2.2123 -1	2.1779 -1	1.65 -1
110	2.7330 -1	2.6868 -1	2.6456 -1	1.63 -1
120	3.0814 -1	3.0287 -1	2.9818 -1	1.64 -1
130	3.2814 -1	3.2241 -1	3.1732 -1	1.68 -1
140	3.3619 -1	3.3022 -1	3.2489 -1	1.71 -1
150	3.3789 -1	3.3183 -1	3.2643 -1	1.73 -1

TABLE A6.17

V_{max} = 90 kVp XW = 45 mm XB = 5mm

V_{min} = 10 kVp

Shown in Fig. 6.15.

S 2	G(-10)	G(0)	G(10)	P.C.
30	1.1700 -3	1.1216 -3	1.0791 -3	4.05 -1
40	1.1109 -2	1.0823 -2	1.0570 -2	2.49 -1
50	4.3054 -2	4.2260 -2	4.1550 -2	1.78 -1
60	1.0778 -1	1.0621 -1	1.0481 -1	1.40 -1
70	2.0854 -1	2.0600 -1	2.0372 -1	1.17 -1
80	3.3972 -1	3.3607 -1	3.3279 -1	1.03 -1
90	4.8824 -1	4.8341 -1	4.7907 -1	9.48 -2
100	6.3676 -1	6.3076 -1	6.2535 -1	9.04 -2
110	7.6794 -1	7.6083 -1	7.5442 -1	8.88 -2
120	8.6871 -1	8.6062 -1	8.5333 -1	8.93 -2
130	9.3343 -1	9.2457 -1	9.1659 -1	9.11 -2
140	9.6538 -1	9.5601 -1	9.4757 -1	9.32 -2
150	9.7531 -1	9.6571 -1	9.5206 -1	9.45 -2

TABLE A6.18

V_{max} = 90 kVp XB = 10 mm XW = 40 mm

V_{min} = 10 kVp

Shown in Fig.6.15

S2	G(-10)	G(0)	G(10)	P.C.
30	3.4264 -4	3.1984 -4	3.0036 -4	6.61 -1
40	4.7292 -3	4.5415 -3	4.3773 -3	3.87 -1
50	2.1801 -2	2.1199 -2	2.0666 -2	2.68 -1
60	6.0052 -2	5.8779 -2	5.7648 -2	2.05 -1
70	1.2308 -1	1.2093 -1	1.1902 -1	1.68 -1
80	2.0774 -1	2.0459 -1	2.0178 -1	1.46 -1
90	3.0495 -1	3.0073 -1	2.9697 -1	1.33 -1
100	4.0217 -1	3.9688 -1	3.9217 -1	1.26 -1
110	4.8683 -1	4.8054 -1	4.7493 -1	1.24 -1
120	5.4985 -1	5.4269 -1	5.3630 -1	1.25 -1
130	5.8811 -1	5.8027 -1	5.7328 -1	1.28 -1
140	6.0518 -1	5.9693 -1	5.8957 -1	1.31 -1
150	6.0956 -1	6.0115 -1	5.9364 -1	1.32 -1

TABLE A6.19

Comparison of experimental and theoretical results.

Shown in Fig. 6.17

Peak voltage = 80 kVp $\quad\quad$ $S2 = 80^{o}$

X ray beam path = BX mm bone + (50 - BX) mm water .

	Experimental results	Theoretical results	
BX	Normalised signal	Arbitary signal	Normalised signal
0	9.2	3.9961 -1	9.20
2	-	2.8873 -1	6.65
3	7.95	-	-
4	7.49	2.2066 -1	5.08
6	6.77	1.7313 -1	3.99
8	6.15	1.3839 -1	3.19
10	5.63	1.1217 -1	2.58
12	5.07	9.1914 -2	2.12
14	-	7.5990 -2	1.75

TABLE A6.20

Shown in Fig.6.17

Comparison of experimental and theoretical results.

Peak anode voltage = 90kVp $\Omega 2 = 80°$

X ray beam path = BX mm bone + (50 - BX)mm water

BX	Experimental results	Theoretical results	
	Normalised signal	Arbitary signal	Normalised signal
0	13.0	6.3141 -1	13.0
2	-	4.7812 -1	9.84
3	11.4	-	-
4	10.65	3.7564 -1	7.73
6	9.7	3.0213 -1	6.22
8	8.8	2.4707 -1	5.08
10	8.0	2.0459 -1	4.21
12	7.2	1.7108 -1	3.52
14	-	1.4420 -1	2.97

TABLE A6.21

Comparison of experimental and theoretical results.

Shown in Fig. 6.18.

Peak voltage = 80kVp X ray beam path 5mm bone + 45mm water.

Experimental results		Theoretical results		
S2	Normalised signal	S 2	Arbitary signal	Normalised signal
		30	3.6365 -4	0.014
		40	4.7129 -3	0.18
67	4.12	50	2.1136 -2	0.80
70	4.82	60	5.7302 -2	2.16
80	7.07	70	1.1622 -1	4.39
83	9.40	80	1.9482 -1	7.35
90	10.75	90	2.8482 -1	10.75
100	13.4	100	3.7480 -1	14.15
110	15.6	110	4.5342 -1	17.11
120	16.4	120	5.1234 -1	19.34
130	17.1	130	5.4851 -1	20.70
		140	5.6493 -1	21.32
		150	5.6928 -1	21.49

TABLE A6.22

Comparison of experimental and theoretical results.

Shown in Fig. 6.20.

Peak anode voltage = 80kVp X ray beam path 10mm bone + 40mm ivory

Experimental results		Theoretical results		
S2	Normalised signal	S2	Arbitary signal	Normalised signal
		30	7.9705 -5	0.004
		40	1.6929 -3	0.09
67	3.22	50	9.4942 -3	0.51
70	3.77	60	2.9034 -2	1.51
80	5.63	70	6.3228 -2	3.37
83	7.75	80	1.1068 -1	5.90
90	8.85	90	1.6598 -1	8.85
100	11.0	100	2.2123 -1	11.80
110	12.8	110	2.6868 -1	14.33
120	13.3	120	3.0288 -1	16.15
130	13.9	130	3.2242 -1	17.19
		140	3.3022 -1	17.61
		150	3.3182 -1	17.70

TABLE A6.23

Comparison of experimental and theoretical results.

Shown in Fig. 6.19.

Peak voltage 90kVp X ray beam path 5mm bone + 45mm water.

Experimental results		Theoretical results			
S2	Normalised signal	S2	Arbitary signal		Normalised signal
		30	1.1216	-3	0.003
		40	1.0824	-2	0.30
60	3.68	50	4.2261	-2	1.17
69	5.45	60	1.0621	-1	2.93
73	7.4	70	2.0600	-1	5.69
80	10.1	80	3.3607	-1	9.28
90	13.35	90	4.8342	-1	13.35
100	17.4	100	6.3076	-1	17.42
110	20.0	110	7.6083	-1	21.01
120	22.9	120	8.6062	-1	23.77
		130	9.2457	-1	25.53
		140	9.5601	-1	26.40
		150	9.6571	-1	26.67

TABLE A6.24

Comparison of experimental and theoretical results.

Shown in Fig. 6.21.

Peak voltage = 90 kVp X ray beam path 10mm bone + 40mm water.

Experimental results		Theoretical results			
S2	Normalised signal	S2	Arbitary signal		Normalised signal
		30	3.1984	-4	0.01
		40	4.5415	-3	0.16
60	3.03	50	2.1199	-2	0.75
69	4.5	60	5.8779	-2	2.08
73	6.2	70	1.2093	-1	4.28
80	8.0	80	3.0459	-1	7.25
90	10.65	90	3.0074	-1	10.65
100	14.1	100	3.9688	-1	14.05
110	16.1	110	4.8054	-1	17.02
120	18.5	120	5.4269	-1	19.22
		130	5.8028	-1	20.55
		140	5.9693	-1	21.14

APPENDIX 5

In this appendix a typical computer programme to calculate theoretically the performance of the densitometer isgiven. The programmes used are referred to in Chapter 6. The important symbols are as given in Appendix 4 and where MUB(E), MUAL(E) and MUW(E) are the aborption coefficients for bone, aluminium and water respectively in cm^{-1} for a photon energy E keV.

```
0       'SEND TO' (ED. ASTD-DEFAULT (0) ,. PROGRAM)
0       'WORK'  (ED.WORK FILE  )
0           'BEGIN'
1           'REAL'
1          D1,D2,D3,D4,D5,D6,
1         CH,CO,CP,CAL,CCA,
1         RHOAL, RHOB;
1           D1      := 2.U16/1004.67 ;
3           D2      := 416/1004.67 ;
4           D3      := 185.85/1004.67 ;
5           D4      := 400.80/1004.67 ;
6         D5  : = 2.016/18.016  ;
7         D6  : = 16/18.016  ;
8
8         CH  : = 1.674  ;
9         CO  ; = 2.657  *  10  ;
10        CP  : = 5.143  *  10  ;
11        CAL : = 4.478  *  10  ;
12        CCA : = 6.655  *  10  ;
13        RHOAL    := 2.7  ;
14        RHOB :  = 1.5   ;
15        'COMMENT'
15        ALGORITHM 233  ;
15        'BEGIN'
15        'REAL''PROCEDURE'SIMPS(X,P,A,B,F) ;
16        'VALUE'P,A,B ;
17        'INTEGER'P ;
18        'REAL'X;A,B,F ;
19          'BEGIN'
19          'REAL''ARRAY'L[1 :P+1];
19          'INTEGER'I ;
20          'REAL'SUM,D ;
21          I :=0 ;
23          D :=(1/P)*(B-A) ;
24          'FOR'X: =A'STEP'D'UNTIL'B+1.08-6'DO'
25            'BEGIN'
25            I:=I+1 ;
27            L[1] :=F ;
28            'END' ;
29          SUM:=0 ;
30          'FOR'I:=1'STEP'2'UNTIL'P-1'DO'
31        'BEGIN'
31          SUM:=SUM+L[1]+4*L[1]+L[1+2] ;
33        'END' ;
34          SIMPS:=D*SUM/3 ;
35          'END' ;
35        'REAL''PROCEDURE'MUB(E) ;
37        'VALUE'E ;
38        'REAL'E ;
39        'BEGIN'
39        'REAL'
39        W1,W2,W3 ,
39        MMUH,MMUO,MMUP,MMUCA,
```

```
39          H1,H2,H3,O1,O2,O3,
39          P1,P2,P3,P4,
39          CA1,CA2,CA3,CA4,
39          TH,TO,TP,TCA;
39
39
39          W1    := LN(E) :
41          W2    := W1 * W1 ;
42          W3    :=W2  * W1 ;
43
43
43          H1      :=      2.44964 - 3.34953 * W1
43                          -4.71370 * 0.01 * W2
43                          +7.09962 * 0.001 * W3 ;
44
44          H2      :=      -1.19075 * 0.1 - 9.37086 * 0.1 * W1
44                          -2.00538 * 0.1 * W2
44                          +1.06587 * 0.01 * W3 ;
45
45          H3      :=      -2.15772 + 1.32685 * W1
45                          -3.05620 * 0.1 * W2
45                          +1.85025 * 0.01 * W3 ;
46           TH     :=     EXP(H1) + EXP(H") + EXP(H3);
47
47
47          O1      :=      1.17130 * 10 - 2.57229 * W1
47                          -2.05893 * 0.1 * W2
47                          +1.99244 * 0.01 * W3 ;
48
48          O2      :=      3.77239 - 1.48539 * 0.1 * W1
48                          -3.07124 * 0.1 * W2
48                          +1.67303 * 0.01 * W3 ;
49
49          O3      :=      -1.73679 + 2.17686 * W1
49                          -4.49050 * 0.1 * W2
49                          +2.64733 * 0.01 * W3 ;
50
50          TO      :=      EXP(O1) + EXP(O2) + EXP(O3) ;
51
51
51          P1      :=      1.15508 * 10 - 2.92200 * W1
51                          +2.54262 * 0.1 * W2 ;
52
52          P2      :=      1.33735 * 10 - 1.86342 * W1
52                          -3.39440 * 0.1 * W2
52                          +2.88858 * 0.01 * W3 ;
53
53          P3      :=      4.78525 + 1.68708 * 0.1 * W1
53                          -3.60383 * 0.1 * W2
53                          +1.97155 * 0.01 * W3 ;
54
54          P4      :=      -4.76903 * 0.1 + 1.46032 * W1
54                          -2.51331 * 0.1 * W2
54                          +1.07202 * 0.01 * W3 ;
55
55          TP      :=      EXP(P1) + EXP(P2) + EXP(P3) + EXP(P4) ;
```

```
56
56          CA1     :=      1.27044 * 10 - 2.55011 * W1
56                          -9.43195 * 0.01 * W2 ;
57
57          CA2     :=      1.42950 * 10 - 1.88644 * W1
57                          -2.83647 * 0.1 * W2
57                          +2.26263 * 0.01 * W3 ;
58
58          CA3     :=      5.32375 + 2.06685 * 0.1 * W1
58                          -3.61664 * 0.1 * W2
58                          +1.93328 * 0.01 * W3 ;
59
59          CA4     :=      -9.82420 * 0.01 + 1.32829 * W1
59                          -2.13747 * 0.1 * W2
59                          +7.73065 * 0.001 * W3 ;
60
60          TCA     :=      EXP(CA1) + EXP(CA2) + EXP(CA3) + EXP(CA4) ;
61
61          MMUH := (1/CH) * TH ;
62          MMUO := (1/CO) * TO ;
63          MMUP := (1/CP) * TP ;
64          MMUCA := (1/CCA) * TAC ;
65          MUB : = ((MMUH * D1) + (MMUO * D2)
65                    +(MMUP * D3) + (MMUCA * D4)) * RHOB ;
66          'END' ;
66
66
66          'REAL''PROCEDURE'MUW(E);
68          'VALUE'E;
69          'REAL'E;
70          'BEGIN'
70          'REAL'
70          W1,W2,W3,
70          H1,H2,H3,01,02,03,
70          MMUH,MMUO,TH,TO;
70
70          W1    := LN(E) ;
72          W2    := W1 * W1 ;
73          W3    := W2 * W1 ;
74
74
74          H1      :=      2.44964 - 3.34953 * W1
74                          -4.71370 * 0.01 * W2
74                          +7.09962 * 0.001 * W3 ;
75
75          H2      :=      -1.19075 * 0.1 - 9.37086 * 0.1 * W1
75                          -2.00538 * 0.1 * W2
75                          +1.06587 * 0.01 * W3 ;
76
76          H3      :=      -2.15772 + 1.32685 * W1
76                          -3.05620 * 0.1 * W2
76                          +1.85025 * 0.01 * W3 ;
77
77          TH      :=      EXP(H1) + EXP(H2) + EXP(H3);
78
78          01      :=      1.17130 * 10 - 2.57229 * W1
78                          -2.05893 * 0.1 * W2
78                          +1.99244 * 0.01 * W3 ;
```

```
79
79          02      :=      3.77239 - 1.48539 * 0.1 * W1
79                          -3.07124 * 0.1 * W2
79                          +1.67303 * 0.01 * W3 ;
80          03      :=      -1.73679 + 2.17686 * W1
80                          -4.49050 * 0.1 * W2
80                          +2.64733 * 0.01 * W3 ;
81          TO      :=      EXP(01) + EXP(02) + EXP(03) ;
82
82          MMUH :=(1/CH) * TH ;
83          MMUO :=(1/CO) * TO ;
84          MUW :=(MMUH * D5) + (MMUO *D6) ;
85          'END' ;
85
85
85          'REAL''PROCEDURE'MUAL(E);
87          'VALUE'E;
88          'REAL'E;
89          'BEGIN'
89          'REAL'
89          TAL,MMUAL;
89          'IF'E'LE'50'THEN'
90          TAL:=10 (-1.1535*LN(E)+5.729)
90          'ELSE'
90          TAL:=10 (-0.4755*LN(E)+3.0767);
91          MMUAL:=(1/CAL)*TAL;
92          MUAL:=MMUAL*RHOAL;
93          'END' ;
93
93
93
93          'REAL''PROCEDURE'V(A,B);
95          'VALUE'A,B;
96          'REAL'A,B;
97          'BEGIN'
97          V:=EXP(-(A*B));
99          'END' ;
99
99
99          'REAL''PROCEDURE'Y(C,D,E) ;
101         'VALUE'C,D,E ;
102         'REAL'C,D,E;
103         'BEGIN'
103         Y:=C*D*E;
105         'END' ;
105
105
105         'REAL''PROCEDURE'P(G,H,I);
107         'VALUE'G,H,I;
108         'REAL'G,H,I;
109         ''BEGIN'
109         'REAL'OMEGA;
109         OMEGA:=314.15926536;
111         P:=(G*SIN(OMEGA*I))-H;
112         'END' ;
112
112
```

```
112         'REAL''PROCEDURE'K(M,N);
114         ''VALUE'M,N;
115         'REAL'M,N;
116         'BEGIN'
116         'REAL'OMEGA;
116         OMEGA:=314.15926536;
118         K:=M*SIN(OMEGA*N);
119         'END';
119
119
119         'REAL''PROCEDURE'L(J,K);
121         'VALUE'J,K;
122         'REAL'J,K;
123         'BEGIN'
123         L:=J*K;
125         'END';
125
125
125
125         'REAL''PROCEDURE'BISEC(F,X,A,B,EPS);
127         'VALUE'A,B,EPS;
128         'REAL'F,X,A,B,EPS;
129         'BEGIN'
129         'REAL'Q;
129         X:=A; Q:=F; X:=B;
133         'IF'Q*F>0'THEN'
133         'BEGIN'
133         BISEC:=0;
135         'GOTO'BOX
135         'END';
136         Q:=(B-A)*SIGN(Q)/2;
137         X:=(A+B)/2;
138         EPS:=EPS/2;
139         'FOR'Q:=Q/2 'WHILE' ABS(Q) >EPS'DO'
140         X:=('IF'F>0'THEN'Q'EKSE'-Q)+X;
141         BOX:
141         'END'BISEC;
141
141
141         'REAL'
142         EDASH,EMAX,TDASH,DELTAT,
142         E,T,LLT,ULT,PHI,T1,T2,
142         OMEGA,DELTA1, DELTA2,EMIN,
142         WX,BX,CHI,
142         G1,G11,G2,G22,
142         XW,XB,XAL,S,S1,S2,THETA,
142         DTHETA,DDEGREE,DEGREE;
142
142         'INTEGER'
143         H,Q;
143
143
143         H:=50.0;
145         Q:=20.0;
146         DELTA1:=1.0&-6;
147         DELTA2:=1.0&-5;
```

```
148          S1:=43;
149          S2:=80;
150          T1 := S1/18000 ;
151          T2:=S2/18000;
152           OMEGA := 314.15926536;
153           THETA := OMEGA * T2 ;
154           DEGREE := THETA * 57.295779 ;
155
155          LLT:=0.8*T2;
156          ULT:=T2;
157          DELTAT:=1.0E-6;
158          'FOR'BX:=0.0'STEP'0.2'UNTIL'1.4'DO'
159          'BEGIN'
159          WX:=5.0-BX;
161          XW:=4.5;
162          XB:=0.5;
163          XAL:=0.15;
164
164
164          EMIN:=60;
165          EMAX:=90;
166          EDASH:=EMAX+0.05*EMAX;
167
167
167          G1:=SIMPS(T,H,T1,T2,
167               SIMPS(E,Q,EMIN,K(EMAX,T),
167               L(P(EMAX,E,T),Y(V(MUB(E),XB),
167               V(MUAL(E),XAL),V(MUW(E?,XW)))));
168          PRINT(G1,0,4);
169          NEWLINE(1);
170
170          BISEC(((G1-SIMPS(T,H,T1,TDASH,
170                        SIMPS(E,Q,EMIN,K(EDASH,T),
170                      L(P(EDASH,E,T),
170                      Y(V(MUB(E),XB),V(MUAL(E),XAL),
170                      V(MUW(E),XW)))))));
170                 TDASH,LLT,ULT,DELTAT);
171          PRINT(T2.0,4);
172          PRINT(TDASH,0,4);
173          PRINT(T2-TDASH,0,4);
174
174
174          DTHETA:=OMEGA*TDASH;
175
175          DDEGREE:=DTHETA*57.195779;
176
176
176          PRINT(DDEGREE:0,4);
177          PRINT(DDEGREE-DEGREE,0,4);
178          NEWLINE(1);
179
179
179
179
179          G11:=SIMPS(T,H,T1,TDASH,
179               SIMPS(E,Q,EMIN,K(EDASH,T),
179              L(P(EDASH,E,T),Y(V(MUB(E),XB),
179              V(MUAL(E),XAL),V(MUW(E),XW)))));
```

```
180         PRINT(G11,0,4);
181         NEWLINE(1);'
182
182         G2:=SIMPS(T,H,T1,T2,
182              SIMPS(E,Q,EMIN,K(EMAX,T),
182             L(P(EMAX,E,T),Y(V(MUB(E),BX),
182             V(MUAL(E),XAL),V(MUW(E),WX))));
183         PRINT(G2,I,4);
184         NEWLINE(1);
185
185
185         G11:=SIMPS(T,H,T1,TDASH,
185              SIMPS(E,Q,EMIN,K(EDASH,T),
185              L(P(EDASH,E,T),Y(V(MUB(E),BX),
185              V(MUAL(E),XAL),V(MUW(E),WX))));
186
186         PRINT(G22,0,4);
187         NEWLINE(1);
188
188         'IF'G1<10 -6'THEN'
188         PHI:=0.0
188         'ELSE'
188         PHI := 100*(G11-G1)/G1;
189
189
189         'IF'G2<10 -6'THEN'
189         CHI:=0.0
189         'ELSE'
189         CHI := 100*(G22-G2)/G2;
190
190
190         PRINT(EMAX, 0, 3) ;
191         PRINT(DEGREE, 0, 3) ;
192         PRINT(BX,0,1);
193         PRINT(WX,0,1);
194         NEWLINE(1);
195         PRINT(PHI,0,4);
196         PRINT(CHI,0,4);
197
197         NEWLINE(3);
198         'END';
199         'END';
200         'END'
```

REFERENCES

1. Hine, G,J. and Brownell,G.L., Radiation Dosimetry, Academic Press, 1956.

2. Fourman,P., Calcium Metabolism and the Bone, Blackwell Scientific Press,1960.

3. Dallemagne,M.J. and Fabry,C., p.14 in Liba Foundation Symposium, Bone Structure and Metabolism, Churchill, London, 1956.

4. Jurist,J.M., Phy.Med.Biol. 15, 417-434,1970.

5. Abendschein,W.and Hyatt,G.W., Clinical Orthopaedics and Related Research, 69, 294, 1970.

6. Rich,C., Clink,E., Smith,R., Graham B., and Ivanovich,P., p.137 in Progress in Development in Methods in Bone Densitometry N.A.S.A. Report SP-64, 1965.

7. Jurist,J.M. and Selle,W.A., The Physiologist, 8,203,1965.

8. Smith,R.W. and Keiper,D.A. American Jour.of Med.Electronics, 4, 156, 1965.

9. Cameron,J.R. Jurist,J.M. Sorencon,J.A. and Mazess,R.B., Aerospace Medicine, 40, 1119, 1969.

10. Ludwig, G.D., Jour.Acoust.Soc.Am., 22, 862, 1950.

11. Mack,P.B., Brown, W. and Trapp,H.D., Amer.Jour.of Roent, 61, 808, 1949.

12. Looser, E., Dtsch.Z.Chir., 152, 210, 1920.

13. Pugh,D.G.,Roentgenologic diagnosis of diseases of bone. Nelson, New York, 1954.

14. Nordin,B.E.C., p.29 in Progress in Development in Methods of Bone Densitometry,N.A.S.A.Report SP-64. 1965.

15. Simon,G., Principles of X ray Diagnosis,London 1965.

16. Weber,J. and van der Berge,D.J., Brit.Jour.Radiol.,42, 378, 1969.

17. Atkinson,P.J. and Weatherell,J.A.,Jour.Bone Jt.Surg.498, 781, 1967.

18. Mack,P.B.,Brown,W.N. and Birtley,W.B.Rev.Sci.Inst.22,67,1951.

19. Mack,P.B., Amer.Jour.Roent,82, 303, 1959.

20. Lanzl,L.H.and Strandjord,N.M.,p.257 in Symposium on low energy X and Y sines and applications, Oak Ridge National Laboratory,Report IIC-5, 1965.

21. Strandjord, N.M., Forland,M., Lanzl,L., Cos,A.B., p.308 in Conf.on progress in methods of bone mineralisation,CONF-68.0211, Feb.1968.

22. Anderson,J.B., Shimmins,J. and Smith,D.A., Brit. Jour. Radiol., 39, 443, 1966.

23. Cameron,J.R.and Sorenson,J.A., Jour.Nuc.Med.,8,268,1967.

24. Cameron,J.R.and Sorenson,J.A., p.87 in Conf.in Progress in Development of Methods in Bone Densitometry, N.A.S.A. Report SP 64, 1965.

25 Goldsmith,N.F., Johnston,J.O.,Vry,H., Vose,G. and Colbert,C., Jour.Bone and Joint Surg., 53A, 609, 1971.

26. Pridie,R.B., Brit.Jour.Radiol., 40, 251, 1967.

27. Börner ,W., Moll E., Rauh,E. and Reiners,C., p.169 in Bone Measurement Conference, CONF 700515, Chicago, May, 1970.

28. Horsman,A., Milner,R.M.and Balusu,L., Phy.Med.Biol.,16, 542, 1971.

29. Mason,R.L.and Ruthen,C., Science, 150, 221, 1965.

30. Exton-Smith,A.N., Millard,P.H. Payne, P.R.and Wheeler,E.F., p.154, Lancet, Nov.28, 1969.

31. Barnett E. and Nordin,B.E.C., Clin.Radiol., 11, 166, 1960.

32. Vogel, J.M. and Friedman,R.J., p.408 in Bone Measurement Conference,CONF 700515, Chicago, May 1970.

33. Horsman,A., Balusu,L.,Bently,H.B.and Nordin,B.E.C.,p.365 in Bone Measurement Conference , Chicago, May 1970.

34. Sorenson,J.A. and Cameron,J.R., Jour.Bone Joint Surg., 49A, 481, 1967.

35. Doyle, F H. Brit.Jour.Radiol., 34, 689, 1961.

36. Mazess,R.B., Invest.Radiol., 6 , 52, 1971 and 6 ,433,1971.

37. Cameron J.R., Mazess,R.B. and Sorenson,J.A., Invest.Radiol., 3, 141, 1968.

38. Johnston,C.C. p.283 in Conference on Progress in Methods of Bone Mineral Measurement,CONF.680211,Bethesda, U.S.A., Feb.1968.

39. Smith,D.M.Johnston,C.C. and Deiss,W.P., Jour.Clin.Invest., 45 , 1073, 1966.

40. Smith,D.M.Johnston,C.C. and Yu,P. p.398 in Bone Measurement Conference,CONF-700515,Chicago,May 1970.

41. Johnston,C.C and Smith,D.M., ANN.Intern.Med., 72, 829, 1971.

42. Smith,D.M., Johnston,C.C and Yu.P., Jour.Amer.Med. Assoc. 219, 325, 1972.

43. Sorenson, J.A. Mazess, R.B., Smith, E.L., Clark, J.L. and Cameron, J.R., University of Wisconsin, U.S.A., Report COO - 1422 - 29, 1968.

44. Evans, R.G., Pak, C.Y.C., Ashburn, W., and Bartter, F.C., Invest. Radiol., 4, 364, 1969.

45. Virtama, P., Telkka, A., and Helela, T., Brit. Jour. Radiol., 38, 360, 1965.

46. Barnett, E., and Nordin, B.E.C., Clin. Radiol.,11,166, 1960.

47. Nordin, B.E.C., Barnett, E. McGregor, J. and Nisbett, J., Brit. Jour. Radiol., 1, 1793, 1962.

48. Doyle, F.H., Gutteridge, D.H., Joplin, G.F and Fraser, R., Brit. Jour. Radiol, 40, 241, 1967.

49. Ort, M.G. and Cameron, J.R. University of Wisconsin, U.S.A. Report COO 142279, 1970.

50. Roos, B., Rosengnen, B. and Skoldborn, H., p. 243 in Bone Mineral Conference, CONF 700515, Chicago, May, 1970.

51. Kranendonk, D.H. and Jurist, J.M., University of Wisconsin, U.S.A. Report COO 1422,107, 1971.

52. Sigmon, B.A., p. 428 in Bone Measurement Conference, CONF 700515, Chicago, May, 1970.

53. Mayer, E.H.,Trostle, G.H., Ackerman, E., Schraer, H. and Sittler, O.D., Rad. Res., 13, 156, 1960.

54. Nilsson, B., p. 334 in Bone Measurement Conference, CONF 700515, Chicago, May, 1970.

55. West, R.R. and Reed, G.W., Brit. Jour. Radiol., 43,886, 1970.

56. Ulrey, C.T., Phy. Rev., 11, 401, 1918.

57. Schmeling, P., Measurement of Bone Mineral Content Using Radiation Sources, AB Atomenergi, Studsvik, Sweden, 1972.

58. Langham, W.H. Occup. Med. Section 5, 1961.

59. Gramerstfelder, C.C., Larson, M.V., Nielson, J.M., Roesch, W.C. and Watson, E.C., Health Physics, 9,757, 1963.

60. Maletskos, C.J., Keane, A.T. Littlefield, S and McClatchey, R.A., M.I.T. Radioactivity Centre Annual Prog.Rep. 1961.

61. Anderson, J., Osborn, S.B., Tomlinson, R.W.S., Newton, D., Rundon, J., Solomon, L. and Smith, J.W., Lancet, 1201, 19

62. Palmer, H.E., Nelp, W.B. and Murano, R. and Rich, C., Phy. Med. Biol., 13. 269, 1968.

63. Chamberlain, M.J., Fremlin, J.H., Peters, D.K. and Philip, H., Brit. Med. Jour., 2. 581, 1968.

64. Chamberlain, M.J., Fremlin, J.H., Holloway, I. and Peters, D.K., Int. Journ. App. Rad and Isotopes, 21. 725, 1970.

65. Boddy, K., Harden, R.Mc.G. and Alexander, W.D. Jour. Clin. Endocr. Metab,, 28, 294, 1968.

66. Boddy, K., Dennis, J.A. and Lawson, R.C., Phy. Med. Biol., 14, 471, 1969.

67. Cooke, A.M. Lancet, 1. 877, 929.

68. Virtama, P. in Symposium Ossium, Livingstone, 1970.

69. Guin, R. and Murray, R.B., Rhy. Rev., 131, 501, 1963.

70. Guin, R. and Murray, R.B., IRE Trans. Nuc. Sci., 9. 28, 1962.

71. Collinson, A.C. and Hill, R., Proc. Phy, Soc., 81. 883, 1963.

72. Kramers, H.A., Phil. Mag., 46, 836, 1923.

73. Heitler, W., Quantum Theory of Radiation, Oxford University Press, 1954.

74. Segrè, E., Experimental Nuclear Physics, Vols. 1 and 2. Wiley, 1954

75. Compton, A.H. and Allison, S.K., X-rays in Theory and in Experiment, Van Nostrand, New York, 1935.

76. Flügge, E., (ed.). Encyclopaedia of Physics, Vol. 30 (X-rays), Springer Verlag, Berlin, 1957.

77. Kulenkampff, H. and Schmidt, L., Ann. der Phy., 43, 494, 1943.

78. Kaye, G.W.C., Phil. Trans. Roy. Soc., A209, 237, 1908.

79. Duane, W. and Shimizu, T., Phy. Rev. 11. 491, 1918.

80. Kulenkampff, H. Handbuck der Physik, Geiger-Scheel, Vol.23, 443, 1926.

81. Kulenkampff, H. Ann. der Phy., 69, 548, 1922.

82. Dyson, N.A., Proc. Phy. Soc., 73, 924, 1959.

83. Unsworth, M.W. and Greening, J.R., Phy. Med. Biol, 15, 621, 1970.

84. Soole, B.W., Phy. Med. Biol., 16, 427, 1971.

85. Soole, B.W. and Jager, W.F., Phy. Med. Biol, 15, 107,1970.

86. Green, M., Proc. Phy. Soc., 83,435,1964.

87. Ham, W.R., Phy. Rev., 30, 1, 1910.

88. Davey, W.P., Jour. Franklin Instit. (U.S.A.), March, 1911.

89. Hanson, H.P. and Salem, S.I., Phy. Rev., 124, 16, 1961.

90. Stoddard, K.B., Phy. Rev., 48, 43, 1935.

91. Farr, R.F., Brit. Jour. Radiol., 28, 364, 1955.

92. Berger, M and Seltzer, Z., N.A.S.A. Report SP 3012, 1964.

93. Cosslett, V.E. and Thomas, R.N., Brit. Jour. App.Phy., 15, 1283, 1964.

94. Endelsock, E.A., Kreger, W.E., Mallet, W. and Schofield,N.E., Health Physics, 4, 1, 1960.

95. Saylor, W.L., Phy. Med. Biol., 14, 87, 1969.

96. Dixon, W.R. and Aitken, J.H. Can. Jour. Phy., 36, 1624,1958.

97. People, L.H.J. and Burt, A.K., Phy. Med. Biol., 14, 73, 1969.

98. Epp, E.R. and Weiss, H., Phy. Med. Biol., 11, 225, 1966.

99. Stanton, L., Basic Medical Radiation Physics, Meredith Corporation, U.S.A., 1969.

100. Hettinger, G. and Starfelt, N., Acta Radiol., 50, 381, 1958.

101. Cormack, D.V. Davitt, W.E., Burke, D.G., and Lawson, E.G., Brit. Jour. Radiol, 31, 565, 1958.

102. Wong, P.K.S., Raridon, R.J. and Tidwell, M., Brit. Jour. Radiol., 30, 70, 1957.

103. Storm, E., and Lier, D.W., Health Physics, 23, 73, 1972.

104. Cormack, D.V. and Burke, D.B., Radiology, 74, 743, 1960.

105. Ehrlich, M., Jour. of Res. National Bureau of Standards, 54, 107, 1955.

106. Stokes, G., Proc. Manchester. Lit. Phil. Soc., 1898.

107. Thomson, J.J., Phil. Mag., 45, 172, 1898.

108. Böhm, K., Ann. der Phy., 33, 315, 1938.

109. Horerjager, R., Ann. der Phy., 38, 33, 1940.

110. Sommerfeld, A., Phy. Z, 10, 969, 1909.

111. Botden, P.J.M., Combee, B and Houtman, J., Philips Tech. Rev., 14, 165, 1952.

112. Green, M. and Cosslett, V.E., Proc. Phy. Soc., 78, 1206, 1961.

113. Kodak Ltd., Fundamentals of Radiographic Photography, p.25,1967.

114. Whiddington, R., Proc. Roy. Soc., A86, 360, 1912.

115. Webster, D.L., Proc. Nat. Acad. Sci., Washington, 13, 445, 1927 and 14, 330, 1928.

116. Hanson, H.P. and Cowan, D.J., Phy. Rev., 124, 22, 1961.

117. Burbank, B.G., Phy. Rev., 63, 139, 1943 and 66, 160, 1944.

118. Castaing, R. and Descamps, J., Jour. Phy. Radium, 16,304,1955.

119. Hettinger, G. and Starfelt, N., Acta Radiol, 50, 381, 1958.

120. Tothill, P., Brit. Jour. App.Phy. Ser.2, 1, 1093, 1968.

121. Evans, R.D., The Atomic Nucleus, McGraw Hill, 1955.

122. Hubbell, J.H. Photon Cross Sections, National Bureau of Standards, NBS 29, 1969.

123. Dearnaley, G. and Northrop, P.C., Semi-conductor Counters for Nuclear Radiations, Spon, London, 1966.

124. Kirpatrick, P. and Wiedmann, L., Phy. Rev., 67, 322, 1945.

125. Baker, L.C., and Buckingham, P.D.,Phy. Med. Biol., 10, 201, 1965.

126. Pallett, J.E., Phy. Med. Biol. 11, 533, 1966.

127. Brinkmann, P., Phy. Letters, 15, 305, 1965.

128. Harshaw Chemical Company, Ohio, U.S.A., Harshaw. Scintillation Phosphors, 1965.

129. Storey, R.S., Jock, W., and Ward, A., Proc. Phy.Soc., 72, 1, 1958.

130. Plyavin, I.K. Optika i Spektrosk, 4, 266, 1958.

131. Jones, D.A. and Ward, A., Proc. Phy. Soc., 75, 931, 1960.

132. Owen, R.B. Nucleonics, 17, 92, 1959.

133. Birks, J.B. The Theory and Practise of Scintillation Counting, Pergamon Press, 1967.

134. Axel, P., Rev. Sci. Inst., 25, 391, 1954.

135. Collinson, A., Liand Hill, R., Proc. Phy.Soc., 81,883, 1963.

136. Zerby, C.D., Meyer, A. and Murray, R.B., Nuc. Inst. Methods, 12, 115, 1961.

137. Jones, T.H., Nuc. Inst. Methods, 15, 55, 1962.

138. Kaiser, W.C., Baker, S.I., Mackay, A.J., and Sherman,I.S., I.R.E. Trans Nuc. Sci., N5-9, No 3, 22, 1962.

139. Smith, C.M.H., A Textbook of Nuclear Physics, Longhams,1964.

140. Snell, A.H.(ed.) Nuclear Instruments and their Uses, Vol.1, Wiley, 1962.

141. Jaundrell - Thompson, F., and Asworth, W.J., X ray Physics and Equipment, Blackwell Scientific Publications, 1956.

142. Holloway, A.F., Cambell, E.M. and Essenburg, A., Brit. Jour. Radiol., 45, 48, 1972.

143. Frigerio, N.A. Coley, R.F. and Sampson, M.J., Phy. Med. Biol., 17, 792, 1972.

144. Page 71 in Radiation Dose Measurements, European Nuclear Energy Agency, Stockholm, June, 1967.

145. International Commission of Radiological Protection, ICRP Publication 3, Pergamon Press, 1960.

146. Katz, L., and Penfold, A.S., Rev. Mod. Phy, 24, No. 1, 1952.

147. McMaster, W.H., Kerr Del Grando, N., Mallett, J.H., Hubbell, J.H. Lawrence Radiation Laboratory, Report, UCRL, 50174, Section II, Revision, I, May, 1969.

148. Katranoushov, I. and Dyankov, O., Brit. Jour. Radiol., 45, 210, 1972.

149. Vose, G.P., Chin. Orthop., 24, 206, 1962.

150. Gong, J.K. Arnold, J.S., and Cohn, S.H.,Anatomical Record, 149, 325, 1964.

151. Spiers , F.W., Brit. Jour. Radiol., 19, 52, 1946.

152. Wooldridge, R. and Ractliffe, J.F., An Introduction to Algol Programming, p. 62, Third edition, English Universities Press, 1968.

153. Collected Algorithms From C.A.C.M., Communications of the A.C.M., Colorado, U.S.A., 1962.

154. Davison, M. and Reekie, D., Phy. Med. Biol., 13, 643, 1968.

155. Hale, J. and Block, P., Phy. Med. Biol., 11, 557, 1966.

156. Hale, J. and Block, P., Phy. Med. Biol., 15, 123, 1970.

157. Jones, D.E.A., Phy. Med. Biol., 14, 495, 1969.